University of Sussex

Sensitivity of SNO+ to Supernova Neutrinos

Mark Stringer

Submitted for the degree of Doctor of Philosophy

University of Sussex

December 2018

Declaration

I hereby declare that this thesis has not been and will not be submitted in whole or in part to another University for the award of any other degree.

Signature:

Mark Stringer

UNIVERSITY OF SUSSEX

Mark Stringer, Doctor of Philosophy

Sensitivity of SNO+ to Supernova Neutrinos

Abstract

The Super-K experiment determined that neutrinos are massive particles by observing the oscillation of atmospheric neutrinos. The SNO experiment confirmed this measurement by observing neutrinos from the Sun. The SNO+ experiment is intended to study the nature of neutrino masses by replacing the heavy water used in SNO with scintillator. The main goal of the experiment is to search for neutrinoless double-beta decay within ^{130}Te. The SNO+ detector is much more sensitive to radioactive contamination than the SNO experiment. For this reason an external LED calibration system has been developed so the detector can be calibrated without risking contamination of the scintillator volume. This thesis describes the commissioning of this calibration system and its performance during the water phase of SNO+. The scintillator volume is separated from the surrounding detector via an acrylic vessel. As scintillator is less dense than water the position of the vessel is expected to shift throughout the lifetime of SNO+. A method to determine the position of the vessel using the external LED system is detailed as well as its performance. A measurement of the scattering length of the water surrounding the acrylic vessel using the same LED system is also presented. Calibration of the detector will also be performed using sources deployed within the vessel, and a study on the angular distribution of light from these sources and the effect of hardware upgrades is also presented. During the lifetime of the SNO+ experiment, the detector will be sensitive to neutrinos emitted from a supernovae within the Milky Way. A software framework was developed to accurately simulate the main interaction channels for supernova neutrinos within SNO+. The software was used to determine the burst trigger efficiency during the water phase as well as a procedure to follow in the case of the burst. One outstanding problem in the field of neutrino physics is the neutrino mass hierarchy; whether there are two heavy and one light or two light and one heavy neutrino mass eigenstates. Neutrinos from a supernova burst may be able to solve this problem. A simple study is performed to determine the sensitivity of various detectors. The same analysis is performed using the aforementioned software to explore any systematic effects which may alter the sensitivity.

Acknowledgements

I would firstly like to thank my supervisor Simon Peeters, his guidance has been crucial in the production of this thesis.

I would like to thank the James' (Waterfield and Sinclair) for their help introducing me to the TELLIE system. I would also like to thank Ed Leming for his support and patience when working with me to debug the TELLIE hardware. Clarence Virtue's provided valuable input for the Supernova studies presented in this thesis. I would also like to thank Belina Von Krosigk for providing me with the SNUGEN code.

Thanks also go to: Daisy and Lily Asquith, Cassie Churchwell, Fabrizio Miano, Martti Nirkko, Suf Shehu, James Waterfield, Nicola Abraham, Michal Rigan, Miro Mlejnek and all my other friends in Brighton both in and out of the EPP group, your moral support throughout my PhD was invaluable.

I would like to thank Carrie Regenstreif, Pouya Khaghani, Mike Schwendener, Jen Davidson, Andy Stripay, Doug Giblin, Kristina Donato, Caitlyn Darrach and everyone else who made Sudbury such a fun place to live for a year.

I would also like to thank my family for supporting me through my undergraduate and postgraduate studies.

Contents

List of Tables

List of Figures

Chapter 1

Introduction

The Standard Model originally assumed that neutrinos are massless. The observation of neutrino oscillations, the change of a neutrinos flavour between its point of creation and detection, which was discovered by the Super-K and SNO experiments, refutes this prediction. The neutrino masses must be a result of new physics beyond the Standard Model. Currently there are two main outstanding problems in neutrino physics: the determination of the neutrino mass hierarchy and the mechanism that generates the neutrino masses.

One possible mechanism to explain the neutrino masses is the see-saw mechanism, which predicts a heavy right-handed neutrino and light left-handed neutrinos. The see-saw mechanism requires that the Lagrangian for neutrinos has both a Dirac mass term as a result of coupling to the Higgs field, and another mass term known as the Majorana mass. If the neutrino has a Majorana mass then a process known as neutrinoless double-beta decay ($0\nu\beta\beta$) can occur. Chapter 2 provides an overview of the history of neutrino physics, the theory behind neutrino oscillations, and the possible explanation of their mass. The current status of experimental searches for $0\nu\beta\beta$ are also discussed.

The main physics goal of the SNO+ experiment is the search for neutrinoless double-beta decay in ^{130}Te. The detector is an upgrade of the SNO experiment, and a description of the detector hardware and physics goals throughout the experiment is given in Chapter 5. The detector consists of an acrylic sphere with inner radius of 6 m surrounded by a spherical geodesic structure containing an array of PMTs. Besides $0\nu\beta\beta$, other physics goals of the experiment are the search for nucleon decay and the study of solar, reactor and geo-(anti)-neutrinos. During all the phases of SNO+, the detector is sensitive to neutrinos produced by a supernova.

As the detector is an upgrade of the SNO experiment, an extensive calibration campaign must take place. One possible change between SNO and SNO+ is the angular

response of the PMT array. This is a result of the degradation of the light concentrators surrounding the PMTs, due to the extended submersion in ultra-pure water, which is chemically aggressive, throughout SNO. A calibration scan using sources deployed within the detector is proposed in Chapter 6 to cover the entire angular region of physics within the detector and perform a measurement of the response within this region to a significant accuracy.

New calibration hardware is also under development. One piece of hardware is a new laserball, (which acts as an isotropic light source), for use within the scintillator phase of the experiment. The new laserball features a thinner neck. A study of the improvement in the measurement of the angular response of the PMT array, as a result of this new neck is also shown in Chapter 6.

Another new piece of calibration hardware for the SNO+ experiment is the ELLIE system: an array of optical fibres external to the acrylic vessel (AV), coupled to LEDs and Lasers. The system is designed to perform the calibration of the detector without the requirement of deploying sources within the detector and risking radioactive contamination. The TELLIE subsystem is designed to perform the timing calibration of the PMT array of SNO+. Chapter 7 describes the hardware of the subsystem as well as the commissioning of the system. The performance of the system over an extended running period is also presented. Throughout the running time of SNO+, the fibres will be submerged in ultra-pure water (UPW). There was concern that the fibres would be degraded by the UPW over time. A study is presented of the results of an accelerated aging experiment of a TELLIE fibre submerged in UPW.

As well as performing the timing calibration of the PMT array, the TELLIE system can be used to position the acrylic sphere relative to the PMT array. The acrylic sphere is held in position using ropes. The scintillator used for SNO+ is less dense than water, making the AV buoyant. During the transition between water phase and scintillator phase, the tensions on the ropes are expected to change and the ropes are expected to change in length, altering the sphere's position. Some light is reflected off the sphere onto the PMTs surrounding the fibre. By calculating the reflected optical paths from fibre to PMT, a fit to determine the offset of the AV in the direction can be made. The method and results of this fit are discussed in Chapter 8. As well as light reflecting off of the acrylic sphere, a small amount of backscattered light in the external water can also produce PMT hits in the reflected region. The amount of scattered light depends on the scattering length of

the water. An analysis procedure to determine the scattering length of the external water was developed and the first results are also shown within Chapter 8.

Supernovae are large explosions which mark the end of a massive stars life, and can result in the star outshining its host galaxy. Approximately 99% of the energy released during a burst (which lasts O(10) s) is in the form of neutrinos, with the remaining 1% released as light and as kinetic energy of the ejected matter. Neutrinos are crucial to explain the mechanism for a supernova. Neutrinos transfer energy from the dense hot core of the star to the outer layers of the star, heating up the surrounding matter, causing an explosion. A description of the supernovae burst mechanism is included within Chapter 4. Despite the large neutrino fluence, the small cross section of neutrinos means that with current neutrino detectors, only neutrino bursts from supernovae within the Milky Way can be observed. Only one such supernova neutrino burst has been observed ever in 1987, with a total of 25 events seen in three detectors. The infrequency of supernova bursts and the low number of events means the kinematics of neutrino interactions within the detector must be well understood to correctly interpret the burst. Chapter 3 presents an overview of the kinematics of neutrino interactions in the energy range relevant for supernova neutrinos. A software package was developed by the author to convert event counts of various interactions into input for full detector simulation and is detailed within Chapter 9.

The large matter density within a supernovae can cause large changes to the observed neutrino flux via the MSW effect. Furthermore, the neutrino flux is so high within the supernova that neutrino-neutrino interactions can also induce oscillations, the phenomenology of both these phenomena is discussed in Chapter 4. Depending on the neutrino mass hierarchy, the observed neutrino spectra vary, hence the neutrino mass hierarchy could possibly be determined using a supernova burst. One possible oscillation effect is analogous to the adiabatic MSW effect within the Sun. A study of the sensitivity of SNO+, JUNO, and Super-K to the neutrino mass hierarchy using this effect is presented in Chapter 9, the estimated sensitivities are obtained using a toy MC. For SNO+, the limits obtained from a full detector simulation are also shown and compared with the toy study. Chapter 9 also presents a study into the sensitivity of the burst trigger as a function of supernova distance, which forms the lowest level trigger of any supernovae trigger. Full detector simulations are used to determine the burst trigger sensitivity. If a supernovae burst is observed the quick publication of results by the collaboration is vital. A simple cut

procedure in the case of a burst during the water phase of SNO+ is presented to separate supernovae neutrino events from detector backgrounds.

The thesis concludes with a summary of the main results of each of the studies described above, further possible studies beyond the scope of this thesis are also listed.

Chapter 2

Theory of Neutrino Physics

This chapter covers the physics of neutrino oscillations, the history of experimental searches for neutrino oscillations is also detailed. The effect of matter on neutrino oscillations, relevant to the study presented in Chapter 9 is covered in Section 2.2. The chapter concludes with a possible mechanism to explain the light neutrino masses, known as the Majorana mechanism. One signature of the Majorana mechanism is neutrinoless double-beta decay ($0\nu\beta\beta$). The search for $0\nu\beta\beta$ is the main experimental goal for SNO+.

The electron neutrino was predicted by Enrico Fermi to explain the spectrum of the electron produced in β-decay in 1934 [1]. Reines and Cowan subsequently discovered the anti-electron neutrino by searching for inverse beta-decay events (see section 3.2) at the Savannah River nuclear power plant in 1953 [2]. The muon neutrino was discovered in 1962 by studying neutrinos produced in pion decay and noting that they did not have the same signature as an electron interacting inside the detector [3]. The tau neutrino was discovered in the year 2000 by the DONUT experiment by using a high energy neutrino beam from the Tevatron [4].

The Standard Model does not predict a mechanism to generate neutrino mass and predicts their mass as zero; modifications have to be made to the model to accommodate neutrino masses. The measurements made by the SNO and Super-K experiments showed that neutrinos from the Sun and neutrinos produced from cosmic ray collisions with the atmosphere change their flavour as they propagate from their point of creation to their point of detection [5] [6]. This is only possible if neutrinos have mass. An interaction eigenstate is a mixture of mass eigenstates. As the neutrino propagates from its point of

creation to its point of detection its mass evolve via the Schrödinger equation. Due to the different masses of the eigenstates, the wavefunctions of the eigenstate have distinct wavelengths. Therefore, at the point of detection the mixture of the mass eigenstates is different from that of the flavour eigenstate the neutrino was created in. There is a chance the neutrino can therefore be detected in a different flavour eigenstate, i.e. the neutrino has oscillated to a different flavour. The discovery by SNO and Super-K of neutrino oscillations led to the award of the Nobel prize in physics in 2015 to A.B. McDonald and T. Kajita.

This chapter will first discuss the mathematics behind neutrino oscillations in vacuum, and the parameterisation of the oscillation phenomena. The effect of matter on the oscillations will also be discussed. The current experimental status and the experimental history of neutrino oscillations will be discussed. Finally, a mechanism to explain the neutrino mass is described and the current status of experimental searches of phenomena associated with the mechanism are discussed.

2.1 Neutrino Oscillations in Vacuum

Neutrinos change flavour as their flavour eigenstates do not correspond to a definite mass eigenstate. When a neutrino is produced during a weak interaction it is in a definite flavour eigenstate. During beta decay, when an electron is produced, we know that an anti-electron neutrino must be produced as well (Assuming Dirac neutrinos). All the flavour eigenstates must be orthogonal. If the definite flavour eigenstate is denoted as $|\nu_x\rangle$ and the mass eigenstates are denoted $|\nu_i\rangle$ then the mass and flavour eigenstates are linked by Eq. 2.1.

$$|\nu_x\rangle = \sum_j U_{x,j} \, |\nu_j\rangle \tag{2.1}$$

U is known as the Pontecorvo–Maki–Nakagawa–Sakata matrix (or PMNS matrix for short), and describes the mixing between the flavour and mass eigenstates.

A neutrino propagates through space as a superposition of the mass eigenstates. The time evolution of each mass eigenstate is given via the Schrodinger equation with solution given by Eq. 2.2, where m_j is the mass of the neutrino in its rest frame and τ is the time in the rest frame of the neutrino.

$$|\nu_j\rangle(\tau) = e^{-im_j\tau} \, |\nu_j\rangle \tag{2.2}$$

At the point of interaction the neutrino will be in the state given in in Eq. 2.3. If the neutrinos are massless particles then the plane wave prefactors would be unity for all values of τ therefore $|\nu_x\rangle = |\nu_x\rangle(\tau)$ i.e. no oscillations would take place. The propagation of a neutrino flavour state is shown in Eq. 2.3.

$$|\nu_x\rangle(\tau) = \sum_k e^{-im_k\tau} U_{x,k} |\nu_k\rangle \tag{2.3}$$

The probability amplitude of the neutrino interacting in a given flavour eigenstate is given by the inner product of the neutrino state and the flavour eigenstate, as shown in Eq. 2.5. To obtain the last part of the expression the fact that the neutrino mass eigenstates are orthonormal was used.

$$\langle\nu_y|\nu_x\rangle(\tau) = \sum_{j,k} U^*_{y,j} U_{x,k} e^{-im_k\tau} \langle\nu_j|\nu_k\rangle = \sum_j U^*_{y,j} U_{x,j} e^{im_j\tau} \tag{2.4}$$

Going from the neutrino rest frame to the lab frame the Lorentz transform $m_k\tau_k = Et - p_kL$ is used. If the neutrinos are ultrarelativistic, the approximation $p_j \approx E - m_j^2/2E$ can be made. Using this approximation and taking the absolute square of the amplitude the probability of a neutrino being produced in one flavour y and being detected as another flavour x is explained in Eq. 2.5.

$$\begin{aligned} P(x \to y) &= \sum_{j,k} U^*_{x,j} U_{y,j} U_{x,k} U^*_{y,k} e^{-i(Et - p_jL)} e^{i(Et - p_kL)} \\ &= \sum_{j,k} U^*_{x,j} U_{y,j} U_{x,k} U^*_{y,k} e^{-i(E(t-L) + \frac{m_j^2}{2E}L)} e^{i(E(t-L) + \frac{m_k^2}{2E}L)} \\ &= \sum_{j,k} U^*_{x,j} U_{y,j} U_{x,k} U^*_{y,k} e^{i(m_k^2 - m_j^2)\frac{L}{2E}} \end{aligned} \tag{2.5}$$

Assuming U is a unitary matrix, Eq. 2.5 can be written in the form shown in Eq. 2.6 [7]. The + sign in the equation corresponds to the case of neutrinos, whereas the - sign corresponds to the case of antineutrino oscillations. The antineutrino expression is obtained by assuming neutrinos are CPT invariant such that $P(\bar{x} \to \bar{y}) = P(y \to x)$ and using the relation $P(x \to y; U) = P(y \to x; U^*)$ [7].

$$P(\overset{(-)}{x} \rightarrow \overset{(-)}{y}) = \delta_{xy} - 4\sum_{j>k} \mathrm{Re}(U^*_{x,j}U_{y,j}U_{x,k}U^*_{y,k})\sin^2\left((m^2_j - m^2_k)\frac{L}{4E}\right)$$
$$\pm 2\sum_{j>k} \mathrm{Im}(U^*_{x,j}U_{y,j}U_{x,k}U^*_{y,k})\sin\left((m^2_j - m^2_k)\frac{L}{2E}\right) \quad (2.6)$$

Eq. 2.6 shows that if neutrinos were massless and $m_i = 0$ then there would be no oscillation. Furthermore, if there is no mixing between the mass and flavour eigenstates, U would be a diagonal matrix and any value that gave $U_{x,j}$ a non zero value would require that $U_{y,j}$ would be zero for $y \neq x$.

2.1.1 The PNMS matrix

The PNMS matrix links the flavour eigenstates to the mass eigenstates of the neutrinos. The mass splittings determine the frequency of the neutrino oscillation and the mixing matrix parameters describe the amplitude of the neutrino oscillations. Neglecting any sterile neutrinos, there are three flavour eigenstates and three mass eigenstates. Hence, the PNMS matrix is a 3×3 matrix. The fact that neutrino oscillations have been seen indicates that there are off diagonal elements in the matrix. The mixing is parameterised by three angles, θ_{12}, θ_{13} and θ_{23} (where $c_{ij} = \cos(\theta_{ij})$ and $s_{ij} = \sin(\theta_{ij})$). There are also three CP violating phases δ, ϕ_1 and ϕ_2. The usual parameterisation of the PNMS matrix is given in Eq. 2.8. The matrix is written as the product of four matrices: the first matrix can be measured by the atmospheric neutrino experiments; the second matrix contains the CP violating term δ, which has not yet been accurately determined. The matrix also contains the mixing angle θ_{13} which, until recent measurements by reactor experiments [8], had a very large uncertainty. The third matrix contains the parameters measured by the solar neutrino experiments and the final matrix contains the CP violating Majorana terms, ϕ_1 and ϕ_2, which are not measurable through neutrino oscillations [7].

$$U = \begin{array}{c} \\ e \\ \mu \\ \tau \end{array} \begin{array}{c} \begin{array}{ccc} \nu_1 & \nu_2 & \nu_3 \end{array} \\ \begin{pmatrix} U_{e,1} & U_{e,2} & U_{e,3} \\ U_{\mu,1} & U_{\mu,2} & U_{\mu,3} \\ U_{\tau,1} & U_{\tau,2} & U_{\tau,3} \end{pmatrix} \end{array} \tag{2.7}$$

$$= \underbrace{\begin{pmatrix} 1 & 0 & 0 \\ 0 & c_{23} & s_{23} \\ 0 & -s_{23} & c_{23} \end{pmatrix}}_{\text{Atmospheric}} \times \underbrace{\begin{pmatrix} c_{13} & 0 & s_{13}e^{-i\delta} \\ 0 & 1 & 0 \\ -s_{13}e^{-i\delta} & 0 & c_{13} \end{pmatrix}}_{\text{Reactor \& Accelerator}} \times \underbrace{\begin{pmatrix} c_{11} & s_{12} & 0 \\ -s_{12} & c_{12} & 0 \\ 0 & 0 & 1 \end{pmatrix}}_{\text{Solar}} \times \begin{pmatrix} e^{i\phi_1} & 0 & 0 \\ 0 & e^{i\phi_2} & 0 \\ 0 & 0 & 1 \end{pmatrix} \tag{2.8}$$

2.2 Neutrino Oscillations in Matter: The MSW effect

As neutrinos pass through matter they exchange W and Z bosons with neutrons, protons and electrons in the matter. All flavours of neutrinos can exchange Z bosons with neutrons and protons whereas only the electron flavour neutrinos can exchange a W boson with electrons. As the Z boson exchange is common to all flavours each neutrino mass eigenstate has its effective mass shifted by the same amount and there is no effect on neutrino oscillations. The case is not the same for the W exchange of electron flavour neutrinos that add a potential to the Schrödinger equation shown in Eq. 2.9 [9]. The + sign is for neutrinos and the - sign is for antineutrinos.

$$V = \pm\sqrt{2}G_F N_e \tag{2.9}$$

The vacuum Hamiltonian in the two flavour approximation is given in Eq. 2.10 [7], the addition of matter effects by adding the term $V/2$ to the electron flavour term and $-V/2$ to the non-electron flavour term.

$$H_{\text{vac}} = \frac{\Delta m^2}{4E} \begin{pmatrix} -\cos 2\theta & \sin 2\theta \\ \sin 2\theta & \cos 2\theta \end{pmatrix} \tag{2.10}$$

$$H_{\text{mat}} = \frac{\Delta m^2_{mat}}{4E} \begin{pmatrix} -\cos 2\theta_{\text{mat}} & \sin 2\theta_{\text{mat}} \\ \sin 2\theta_{\text{mat}} & \cos 2\theta_{\text{mat}} \end{pmatrix}$$
$$= H_{\text{vac}} + \frac{V}{2} \begin{pmatrix} 1 & 0 \\ 0 & -1 \end{pmatrix} \tag{2.11}$$

By rearranging H_{mat} into the form of H_{vac} the relations in Eqs. 2.12 and 2.13 are obtained [7]. A resonance condition is met when $\cos 2\theta = \frac{2V}{\Delta m^2/E}$ at this point $\sin^2 2\theta_{\text{mat}}$ will have a value of one meaning it will be possible for one flavour of neutrinos to evolve entirely into another flavour under the correct conditions [10][11].

$$\Delta m^2_{\text{mat}} = \Delta m^2 \sqrt{\sin^2 2\theta + (\cos 2\theta - \frac{2V}{\Delta m^2/E})^2} \tag{2.12}$$

$$sin^2 2\theta_{\text{mat}} = \frac{\sin^2 2\theta}{\sin^2 2\theta + (\cos 2\theta - \frac{2V}{\Delta m^2/E})^2} \tag{2.13}$$

The matter effect is shown pictorially in Figure 2.1. At very high densities the matter effect is dominant and the ν_e will be produced in the heaviest mass eigenstate. The other flavours ν_x do not have the additional potential seen by the ν_e flavours, and will be produced in the lightest mass eigenstates at very high densities. The resonance condition occurs when the flavour eigenstate (dashed lines) cross.

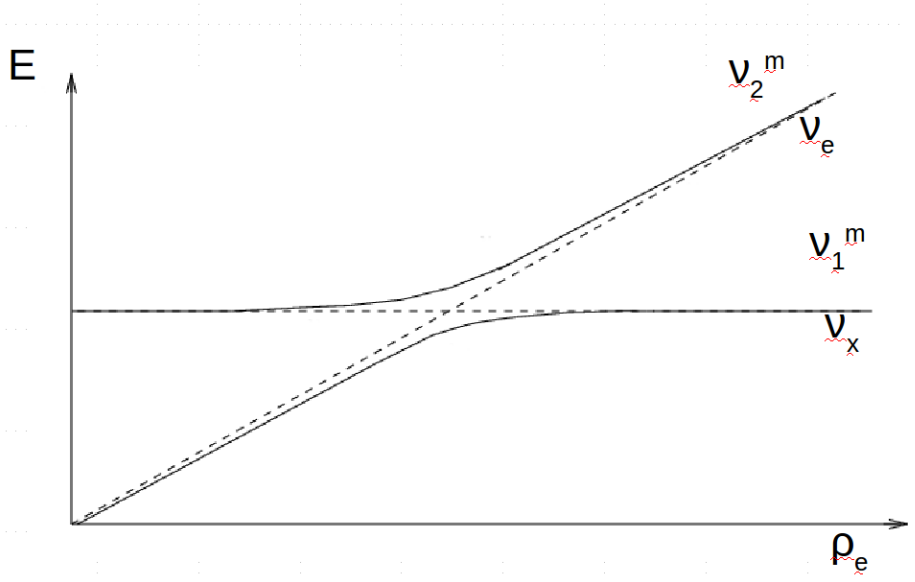

Figure 2.1: A diagram of the MSW effect ρ indicates the density of the surrounding matter, E is the total energy of the neutrino. The solid lines indicate the mass eigenstates. The dashed lines indicate the flavour eigenstates.

The three flavour MSW effect can also be calculated [12][13], often the two flavour approximation is sufficiently accurate.

2.3 Measuring the neutrino oscillation parameters.

The current[1] best fit values for the neutrino mass splittings and mixing angles can be seen in Tab. 2.1.

[1]This combined analysis was performed in 2017, the parameters are expected to change when the Noνa January 2018 results are added.

Mass Hierarchy	θ_{12} (°)	θ_{13} (°)	θ_{23} (°)
Normal	$34.5^{+1.1}_{-1.0}$	$8.44^{+0.18}_{-0.15}$	41.0 ± 1.1
Inverted	"	$8.41^{+0.16}_{-0.17}$	50.5 ± 1.0
Mass Hierarchy	Δm^2_{21} ($10^{-5}\,\mathrm{eV}^2$)	$\lvert\Delta m^2_{31}\rvert$ ($10^{-3}\,\mathrm{eV}^2$)	δ (°)
Normal	7.56 ± 0.19	2.55 ± 0.04	252^{+56}_{-36}
Inverted	"	2.49 ± 0.04	259^{+47}_{-41}

Table 2.1: The current combined neutrino oscillation parameters [14].

Several neutrino sources provide neutrino fluxes over various energy ranges. Electron flavour neutrinos produced in the Sun have energy in the region 0.1 MeV to 10 MeV [15], the total spectrum is shown in Figure 2.2. Reactor antineutrinos produced in beta decays of the fission products also have energies in the range 2 MeV to 10 MeV [16]. Neutrinos produced in interactions of cosmic rays with the atmosphere and by accelerators have energies of several GeV.

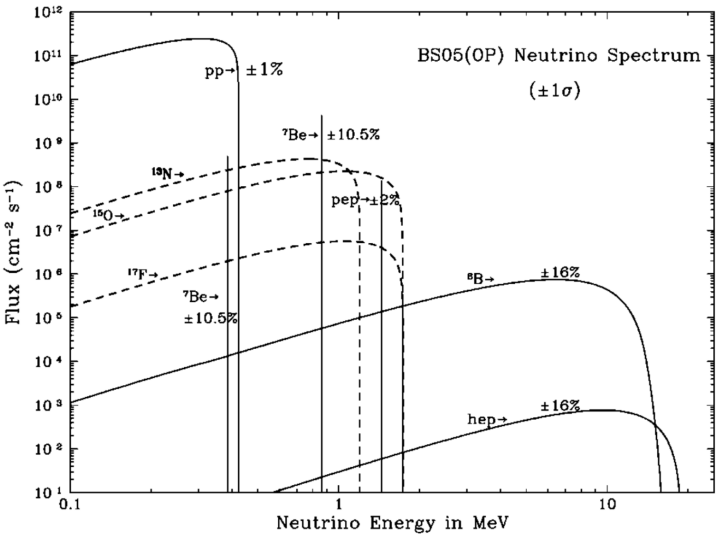

Figure 2.2: Energy spectrum for neutrinos produced in the Sun. Taken from [15].

The relation in Eq. 2.14 shows the oscillation phase in terms of the experimental setup. E is the energy of the neutrino source in GeV, L is the distance between the source and the detection point in km. Long baseline reactor and solar neutrino experiments are sensitive to mass splittings of $10^{-5}\,\mathrm{eV}^2$, whereas short baseline reactor experiments and accelerator neutrino experiments with baselines of O(100 km) are sensitive to mass splittings of $10^{-3}\,\mathrm{eV}^2$.

$$(m_j^2 - m_k^2)\frac{L}{2E} \approx 1.27(m_j^2 - m_k^2)[\mathrm{eV}^2]]\frac{L[\mathrm{km}]}{E[\mathrm{GeV}]} \tag{2.14}$$

The mass splitting and mixing is shown graphically in Figure 2.3. The colours of each bar represent the proportion of each flavour eigenstate in each mass eigenstate, the values of U_{xi}

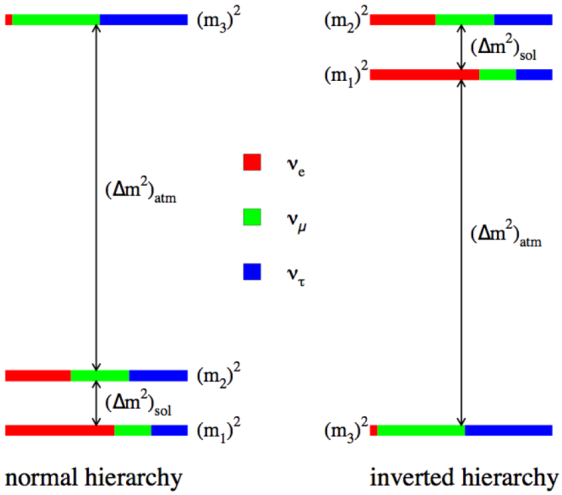

Figure 2.3: Representation of the current mass splitting measurements of the mass eigenstates, also shown is the mixing of the neutrino flavour eigenstates. Taken from [17].

At the time of writing the mass hierarchy is unknown, i.e. is the smaller mass splitting above or below the larger mass splitting. The scenario in which the smaller splitting lies above the larger one is known as the inverted hierarchy and the scenario where the smaller splitting is below is known as the normal hierarchy. The next generation of accelerator neutrino oscillation experiments intend to answer this question [18]. These experiments will compare the oscillation probabilities for both neutrinos and antineutrinos through the Earth, the MSW effect will shift the oscillation parameters via Eqs. 2.12- 2.13, as the potential V swaps its sign when exchanging neutrinos with antineutrinos the direction of the shift provides the sign of Δm^2.

2.3.1 The Solar Neutrino Problem

The neutrino spectrum from the Sun is predicted by standard solar models; these models can be refined by making heliosismological measurements of the Sun, as well as measurements of its luminosity, radius and the abundance of heavier elements on its surface.

Several experiments have measured ^{8}B neutrinos from the Sun due to their higher energy and relatively large flux. ^{8}B neutrinos are produced in β decay ($^8_5\mathrm{B} \rightarrow {}^8_5\mathrm{Be}^* + \mathrm{e}^+ + \nu_e$) [19], which is produced via the fusion of two helium nuclei via Eqs. 2.15 and 2.16.

$$^4_2\mathrm{He} + {}^4_2\mathrm{He} \rightarrow {}^7_4\mathrm{Be} + \gamma \tag{2.15}$$

$$^{7}_{4}\mathrm{Be} + p \rightarrow {}^{8}_{5}\mathrm{B} + \gamma \tag{2.16}$$

The first experiment to measure the ^{8}B flux from the Sun was the Homestake experiment [20]. The experiment consisted of 615 tonnes of C_2Cl_4 inside a tank at a depth of 1480 m in the Homestake gold mine in South Dakota. Incoming neutrinos from the Sun interact with the clorine via the interaction seen in Eq. 2.17.

$$\nu_e + {}^{37}_{17}\mathrm{Cl} \rightarrow {}^{37}_{18}\mathrm{Ar}^{*} \tag{2.17}$$

The isotope ^{37}Ar has a half life of $\approx$ 35 days, during their decay they produce a 2.82 keV Auger electron. During running of the experiment the ^{37}Ar is extracted chemically by passing helium through the tank. Pulse shape discrimination was used to reduce the backgrounds in the counters [20].

The experiment ran from 1970 to 1994, over the entire live time of the experiment 108 measurements of the ^{37}Ar were made. The ratio between the number seen and the number expected was ≈ 0.3 with a significance of 3σ [20] [21].

The Super-Kamiokande (Super-K) neutrino detector is a 50 ktonne water Cherenkov detector, the detector has a rock overburden of 1 km and is based in the Kamioka mine in Japan. The experiment detects the Cherenkov light (see Section 5.2.1) produced by $\nu - e$ scattering via the processes described in Section 3.3.

The large scale of the detector meant that it was able to measure the day night asymmetry as well as the seasonal variation in the number of solar neutrino events. The directionality possible with water Cherenkov detectors allows the reduction of backgrounds. Super-Kamiokande saw a deficit in the total number of ^{8}B with a ratio of ≈ 0.4 to that expected [21]. The day night asymmetry was found to be consistent with zero, the only change in flux was found to be seasonal and consistent with the variations in the distance between the Earth and the Sun caused by the eccentricity of the Earths orbit [22].

The SNO detector was also a water Cherenkov detector (a detailed description of the SNO(+) detector can be found in Chapter 5), unlike Super-K, the detection media used was heavy water. Heavy water is made up of two deuterons (The bound state of a proton and a neutron) and an oxygen. Electron flavour neutrinos can interact via the charged current interaction shown in Figure 2.4a, the emitted electron produced creates Cherenkov light in the detector. All flavours of neutrino can interact via the neutral current interaction shown in Figure. 2.4b, in this interaction the neutron produced is captured on another

deutron producing a 6.25 MeV γ ray which scatters off electrons which in turn produce Cherenkov light [21]. Like Super-K the $\nu - e$ scattering described in Section 3.3 interactions are accessible by all flavours of neutrino.

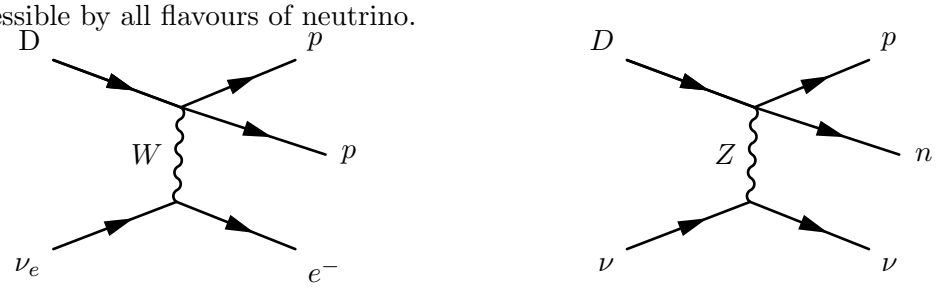

(a) The charged current interaction of electron neutrinos with a deuteron nuclei.

(b) Neutral current electron neutrino electron scattering.

Figure 2.4: Neutrino interaction processes in the SNO experiment. In all of the Feynman diagrams presented in this thesis time is assumed to move from left to right.

As SNO was sensitive to all flavours of neutrinos via a variety of interaction channels it was able to disentangle the electron flux from the muon and tau neutrino flux. It showed the missing flux was caused by the neutrinos changing flavour between their point of creation in the Sun and detection, and the total flux of neutrinos when summed over all flavours was consistent with the standard solar model.

The deficit of neutrinos is caused by matter induced oscillations within the Sun. Vacuum oscillations of the neutrinos are ruled out by the lack of seasonal variation associated with a change in baseline distance caused by the eccentricity of the Earths orbit. Matter effects within the Earth are not a significant contributor, consistent with SNO or Super-K not seeing a day night asymmetry in neutrino flux [23] [22]. The cause of the flavour change is the MSW-LMA resonance within the Sun.

The electron neutrino is mostly made up of the ν_1 and ν_2 mass eigenstates, a two flavour approximation is appropriate to use. Neutrinos produced in the Sun during fusion processes are all electron flavour neutrinos. The core of the Sun is very dense and therefore has a high electron density. The additional potential experienced by electron flavour neutrinos is given by Eq. 2.9. As the additional potential is much larger than the vacuum terms the Hamiltonian given in Eq. 2.11 will be approximately diagonal. As the sign of the potential is positive we know that the neutrino will be produced in the higher energy eigenstate ν_2. As the Hamiltonian is diagonal as the neutrino propagates towards the outer edge in the higher energy eigenstate and eventually exits the Sun in the higher energy vacuum eigenstate ν_2. The proportion of solar ^{8}B neutrinos detected as electron (approximately 1/3) gives the value of the solar mixing angle. As we know the neutrino exits the Sun in the heavier state the sign of Δm^2_{12} (if ν_1 was the heavier mass eigenstate

we would detect a flavour distribution proportional to that of ν_1), the sign of the mass splitting is not possible to measure with standard oscillation experiments.

2.3.2 Reactor neutrino experiments

The KamLAND experiment is a liquid scintillator detector based in Japan, it detects antineutrinos produced in fission reactors using the inverse beta decay interaction (see Section 3.2). The neutrino flux from 55 different reactors allows a much larger baseline of 180 km compared to other reactor experiments. The large baseline means the experiment is sensitive to the same mixing parameters as SNO and the other solar neutrino experiments. Figure 2.5 shows the survival probability of electron antineutrinos and clearly shows oscillatory behaviour. The experiment excluded no oscillations at a 5σ confidence.

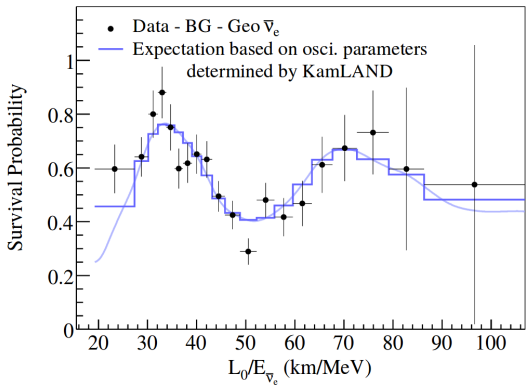

Figure 2.5: The oscillation of reactor neutrinos as seen by the KamLAND experiment [24]

Other reactor based experiments use a much shorter baseline to measure the mixing angle θ_{13}. The Daya Bay experiment based in China consists of six antineutrinos detectors at varying distances ranging from 350 m to 1.5 km, each detector uses 20 tonnes of liquid scintillator doped with gadolinium for improved neutron tagging. In 2012, the experiment ruled out a zero value for θ_{13} at a 5σ level. CP violation is only possible in neutrinos if all three mixing angles are non zero.

Future reactor experiments also hope to determine the mass hierarchy, JUNO [25] and RENO-50 [26], both detectors use liquid scintillator and will have a baseline of $\approx$50 km to the reactor, to account for this much longer baseline both experiments will be much larger than existing scintillator detectors with masses of 20 kT and 18 kT respectively.

In the case of the normal hierarchy the splitting will be given by $|\Delta m^2_{31}| = |\Delta m^2_{32}| + |\Delta m^2_{21}|$ whereas in the inverted hierarchy the splitting is $|\Delta m^2_{31}| = |\Delta m^2_{32}| - |\Delta m^2_{21}|$. The difference in splitting will produce a slight change in the phase of the oscillations as seen in Figure 2.6.

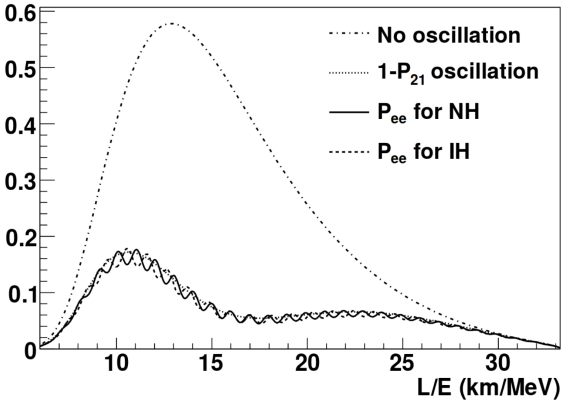

Figure 2.6: $\bar{\nu}_e$ survival probabilities for the normal and inverted hierarchy $\sin^2 2\theta_{13} = 0.1$ [27].

2.3.3 Atmospheric neutrino experiments

Cosmic ray interactions in the atmosphere also provide a source of neutrinos. Incoming cosmic rays (which are mainly protons) scatter off of nuclei in the atmosphere producing pions. The pions then decay to muons in the atmosphere via Eqs. 2.18 and 2.19.

$$\pi^+ \rightarrow \mu^+ + \nu_\mu \tag{2.18}$$

$$\pi^- \rightarrow \mu^- + \bar{\nu}_\mu \tag{2.19}$$

At lower energies (E $<$ 1 GeV) the majority of muons decay before reaching the Earth [21] via the interactions seen in Eqs. 2.20 and 2.21.

$$\mu^+ \rightarrow e^+ + \nu_e + \bar{\nu}_\mu \tag{2.20}$$

$$\mu^- \rightarrow e^- + \bar{\nu}_e + \nu_\mu \tag{2.21}$$

From Eqs. 2.18 to 2.19 the predicted ratio of the flux of lower energy atmospheric muon neutrinos to electron neutrinos is two [6]. At higher energies a smaller proportion of the muons decay before reaching the detector resulting in a reduction in the ratio.

The Super-K experiment studied atmospheric neutrinos produced on either side of the planet. Atmospheric neutrinos produced on the other side of the Earth were detected as upward going neutrinos, and had an oscillation baseline of $\approx 10^5$ km. Downward going neutrinos produced above the detector had a much shorter baseline of 15 km. The large

variation in baseline and high energy of the neutrinos meant Super-K to is sensitive to the larger mass splitting.

Super-K compared the expected interaction rate with no oscillations with the observerved data. The electron neutrino flux had very little disagreement with the no oscillations prediction, however the muon neutrino flux showed a significant deficit. Any reduction in muon neutrino flux must be associated with oscillations to tau neutrinos (sterile neutrino oscillation was ruled out due to matter effects within the Earth [28]). Figure 2.7 shows the double ratio of the atmospheric muon neutrino flux and the electron neutrino flux for the observed data and the non oscillation prediction made by MC.

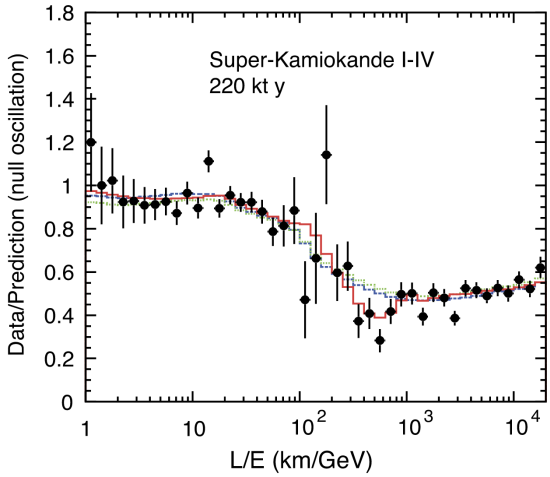

Figure 2.7: The ratio of the observed ratio between muon and electron neutrino atmospheric fluxes and the MC prediction with no oscillations as a function of L/E [29].

For downward travelling muon neutrinos oscillations have not started yet, so the data agrees with the prediction. For upwards travelling neutrinos the oscillations have averaged out so the ratio of observed events to predicted is given by $0.5 \times \sin^2\theta_{23}$, Super-K showed that the atmospheric mixing was maximal i.e. $\sin^2\theta_{23} \approx 1$. The atmospheric mass splitting was determined from the minimum point in Figure ref at approximately 500 km/GeV.

2.3.4 Summary

Neutrinos from various sources have shown definitively that neutrinos change flavour as they propagate through space. The mixing of the neutrinos has been found to be large unlike other mixings observed in the quark sector. Oscillations are only possible if neutrinos have mass; the next section describes a proposed mechanism to generate mass and its experimental signature.

2.4 Mechanisms to generate neutrino mass

As neutrino oscillation experiments have proven neutrinos are massive particles, additional terms have to be added to the Standard Model to explain the neutrino masses. In a charge-current weak interaction vertex the $(1-\gamma^5)$ term means only the left handed neutrinos and right handed antineutrinos are produced. Neutrinos could generate their mass via the coupling to the Higgs boson with the addition of a right handed neutrino field and a left handed anti neutrino field, these two additional fields do not couple to the weak interaction and are known as sterile. The neutrino mass term is then given by the standard Higgs coupling like the charged fermions as seen in Eqs. 2.22.

$$m_D = \gamma \langle \bar{H}^0 \rangle_0 \tag{2.22}$$

$$L_D = -\frac{m_D}{2}(\bar{\nu}_L \nu_R + \bar{\nu}_R^c \nu_L^c) + h.c. \tag{2.23}$$

From the experimental results detailed in the previous section we know the neutrino masses are much smaller than the other fermion masses in the standard model. If the neutrinos are Dirac particles, like all other particles in the standard model, and they get their masses via coupling to the Higgs mechanism then the coupling constant γ (shown in Eq. 2.22) must be much smaller than the constant for all other particles. The large difference from all other particles makes theorists suspect another mechanism might be responsible for the small neutrino masses. In the Dirac only regime the left handed neutrinos mixing and right handed neutrino mixing are separate, no neutrino produced in a weak interaction can oscillate into its sterile form [21].

As well as the standard known Higgs coupling, another mechanism can generate neutrino masses known as the Majorana mechanism. The Majorana mass has the effect of turning a particle into its own antiparticle. For charged fermions this is not possible because it would violate charge conservation. This is not an issue for neutrinos as they are electrically neutral. Furthermore, to conserve weak isospin only the right handed singlet can be added (which does not interact via the weak force). The Majorana mass Lagrangian can be seen in Eq 2.24; unlike the Dirac mass for the neutrino there is no prediction for the mass of the Majorana mass term M_{Maj}. The entire neutrino mass Lagrangian as a matrix can be seen in Eq. 2.25.

$$L_{\text{Maj}} = -\frac{M_{\text{Maj}}}{2}\bar{\nu}_R^c \nu_R + h.c. \tag{2.24}$$

$$L_{m_\nu} = -\frac{1}{2}(\bar{\nu}_L, \bar{\nu}_R^c) \begin{pmatrix} 0 & m_D \\ m_D & M_{\text{Maj}} \end{pmatrix} \begin{pmatrix} \nu_L^c \\ \nu_R \end{pmatrix} + h.c. \tag{2.25}$$

To get the physical mass eigenstates the matrix must be diagonalised, eigenvalues (i.e. the masses of the neutrino states) are given in Eq. 2.26

$$m_{1,2} = \frac{1}{2}\left(M_{\text{Maj}} \pm \sqrt{M_{\text{Maj}} - 4m_D^2}\right) \tag{2.26}$$

2.4.1 The see-saw mechanism

The see-saw mechanism can explain the light mass of the neutrinos relative to the other fermions in the standard model, whilst allowing the coupling constant to the Higgs to be the similar in size to that of all the other fermions. The value of M_{Maj} is not required to be small: setting $M >> m_D$ the eigenvalues of the matrix shown in Eq. 2.25 can be approximated using Eqs. 2.27 and 2.28. The corresponding eigenstates to these two eigenvalues can be seen in Eqs. 2.29 and 2.30 respectively.

$$m_1 \approx M_{\text{Maj}} \tag{2.27}$$

$$m_2 \approx \frac{m_D^2}{M_{\text{Maj}}} \tag{2.28}$$

$$N \approx (\nu_R + \nu_R^c) + \frac{m_D}{M}(\nu_L + \nu_L^c) \tag{2.29}$$

$$\nu \approx (\nu_L + \nu_L^c) - \frac{m_D}{M}(\nu_R + \nu_R^c) \tag{2.30}$$

One eigenstate N with a very large mass M_{Maj} will be made up mostly of the right handed sterile chiral state [19]. Whereas the other mass eigenstate ν will have a much lighter mass suppressed by heavy Majorana mass term and will be made up of the left handed chiral non-sterile state. From Tab. 2.1 the neutrino masses are at least of the order of a meV. If it is assumed that the neutrino couples to the Higgs with a similar strength as the other fermions, and therefore has a Dirac mass term m_D of the order GeV, then the heavy sterile neutrino field must have a mass of approximately 10^{11} GeV [19].

Acting with the charge conjugation operator on both ν and N, you obtain the relations $C\nu = \nu$ and $CN = N$, i.e. both the heavy and light neutrino are their own antiparticles.

If the neutrino is a Majorana particle, processes which violate lepton number by two will be permitted, a Majorana neutrino produced could be observed as either its particle or antiparticle, thus violating lepton number conservation. One of these processes is described in the next section. The possible Majorana nature of neutrinos can also be used to explain the matter antimatter asymmetry of the universe. If in the very early universe the heavy neutrinos are produced and subsequently exhibit CP violation, by decaying with different rates to the lighter neutrinos and their antiparticles an overall violation of lepton number in the early universe will occur [30]. The Standard Model sphaleron process [31] requires a conservation of $B - L$ but B and L are allowed to vary. Combining the CP violation of the heavy neutrinos and the sphaleron process an asymmetry in L can be turned into a asymmetry in B explaining the current matter anti-matter asymmetry.

2.5 Neutrinoless Double-Beta Decay

Certain isotopes can undergo a process known as double beta decay, this process occurs when a single beta decay is not possible due to conservation of energy. The process involves the simultaneous emission of two electrons and two electron antineutrinos as seen in Figure 2.8. The isotopes that undergo double beta decay ($2\nu\beta\beta$) are listed in Table 2.2.

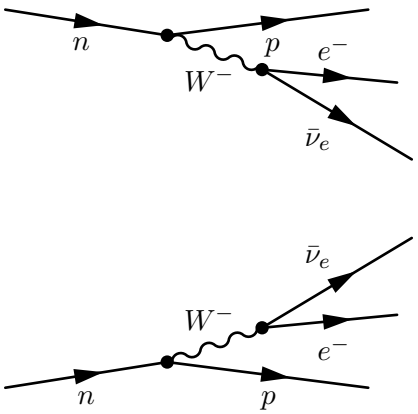

Figure 2.8: The Feynman diagram for double beta decay both initial neutrons exist in the same nucleus.

Isotope	**Abundance** (%)	**Q-value** (MeV)	$\boldsymbol{T^{2\nu}_{1/2}}$ (y)
^{48}Ca	0.187	4.267	$(4.39 \pm 0.58) \times 10^{19}$
^{76}Ge	7.75	2.039	$(1.43 \pm 0.53) \times 10^{21}$
^{82}Se	8.82	2.996	$(9.19 \pm 0.76) \times 10^{19}$
^{96}Zr	2.80	3.349	$(2.16 \pm 0.26) \times 10^{19}$
^{100}Mo	9.74	3.034	$(6.98 \pm 0.44) \times 10^{18}$
^{116}Cd	7.51	2.813	$(2.89 \pm 0.25) \times 10^{19}$
^{130}Te	34.1	2.528	$(7.14 \pm 1.04) \times 10^{20}$
^{136}Xe	8.86	2.458	$(2.34 \pm 0.13) \times 10^{21}$
^{150}Nd	5.64	3.371	$(8.37 \pm 0.45) \times 10^{18}$

Table 2.2: Isotopes that decay via the $2\nu\beta\beta$ process. Listed are the abundances of each isotope the Q-value of the decay and the. Only Isotopes with Q-values above 2 MeV are listed. The values for the half-lives and Q-values were obtained from [32] the abundances were obtained from [33]

If the neutrino has a Majorana mass term then lepton number violating processes are allowed. One process possible if the neutrino is Majorana in nature is known as neutrinoless double beta decay ($0\nu\beta\beta$), the lowest order Feynman diagram for this process can be seen in Figure. 2.9. The action of the Majorana mass term turns the outgoing antineutrino from one vertex into a incoming neutrino at the other vertex.

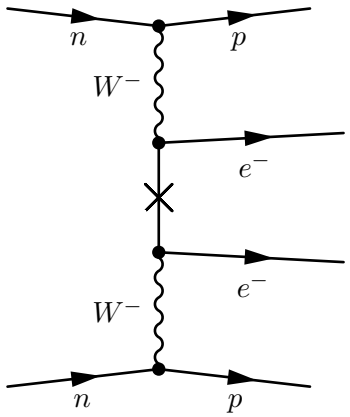

Figure 2.9: The Feynman diagram for neutrinoless double beta decay.

The emmitted antineutrino at one vertex will have mostly right handed helicity. There will be a small component that will have left handed helicity and will be able to couple as an antineutrino to the other weak vertex, with coupling strength proportional to m_i/E, where m_i is the neutrino mass [34]. The amplitude of the process will be the sum over all the mass eigenstates and is proportional to Eq. 2.32. The half life has to take into account the phase space of the electron energies and the nuclear matrix element for the process as shown in Eq. 2.33. The nuclear matrix element is a large source of uncertainty on the measurement of the value of $m_{\beta\beta}$ [35].

$$m_{\beta\beta} = \sum_i |U_{e,i}^2 m_i| \tag{2.31}$$

$$= \left| m_1 \cos^2\theta_{12} \cos^2\theta_{13} e^{i\phi_1} + m_2 \sin^2\theta_{12} \cos^2\theta_{13} e^{i\phi_2} + m_3 \sin^2\theta_{13} e^{-2i\delta} \right| \tag{2.32}$$

$$(T^0_{1/2}\nu)^{-1} = G_{0\nu} |M_{0\nu}|^2 |m_{\beta\beta}|^2 \tag{2.33}$$

The signal for $0\nu\beta\beta$ is given by two electrons with summed kinetic energy equal to the Q-value of the double beta decay as seen in Fig. 2.10. The electrons produced in $0\nu\beta\beta$ will have equal and opposite momenta.

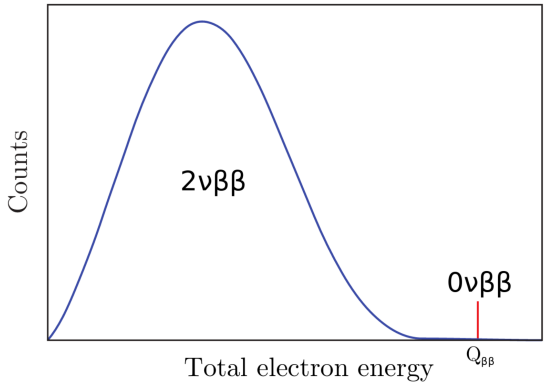

Figure 2.10: The energy spectrum of the summed kinetic energy of the electrons for double beta decay (blue) and neutrinoless double beta decay red [36].

2.5.1 Detecting Neutrinoless Double-Beta Decay

The limit an experiment can set on $0\nu\beta\beta$ is given by Eqs. 2.34 and 2.35 [36]. Eq. 2.34 is the background limited case, Eq. 2.35 holds for the zero background case where the number of background events in the ROI is of the order unity.

$$S_{0\nu\beta\beta} = \ln(2) \cdot \epsilon \cdot \frac{1}{n_\sigma} \cdot \frac{x\nu N_A}{\mathcal{M}_A} \cdot \sqrt{\frac{MT}{B\Delta}} \tag{2.34}$$

$$S^{0B}_{0\nu\beta\beta} = \ln(2) \cdot \epsilon \cdot \frac{x\nu N_A}{\mathcal{M}_A} \cdot \frac{MT}{N_S} \tag{2.35}$$

In both Eqs. 2.34 and 2.35 M is the detectors mass, N_A is Avogradros constant and $\mathcal{M}_A$ is the molecular mass of the detector compound. x is the proportion $0\nu\beta\beta$ element contained within each molecule and ν is the abundance of the $0\nu\beta\beta$ isotope within the element. T is the live time of the detector, ϵ is the detection efficiency. For Eq. 2.34 n_σ

is the level of confidence in the limit, and Δ is the energy resolution FWHM in the ROI. For Eq. 2.35 N_S is the number of events within the ROI.

There are several sources of backgrounds to $0\nu\beta\beta$ which can be split into three categories [37].

- Intrinsic radioactivity
- Cosmosgenic backgrounds
- $2\nu\beta\beta$ decay

Intrinsic Radioactivity

Intrinsic radioactivity is caused by small radioactive impurities inside the detector that decay in the signal region of $0\nu\beta\beta$. Many double beta isotopes decay with a small Q-value, so a double beta isotope with a larger Q-value is desirable. The intrinsic backgrounds are reduced by ensuring the detector is made up of radioactively pure materials. Other intrinsic backgrounds are caused by the ingress of radon gas inside the detector, this background can be reduced by making a fiducial volume cut as the gas is not expected to reach far inside the detector. Some daughters of the decay falling inside the signal region quickly go on to decay themselves. Their subsequent decays can be used to identify some events falling in the signal region as background.

Table 2.3 shows the backgrounds specific to the $0\nu\beta\beta$ search, and the method employed to reduce them.

Isotope(s)	Method of Reduction
External ^{208}Tl & ^{214}Bi	The hold down and PMT glass contain large amounts of these isotopes, a Fiducial volume cut and PMT timing cut reduce these.
Internal ^{238}U & ^{232}Th	The daughters of these particles ^{214}Bi and ^{212}Bi, decay with a characteristic $\beta - \alpha$ signal, one decay is subsequntly followed by another which can be used to tag these events thus removing the background

Table 2.3: The two main radioactive backgrounds to the $0\nu\beta\beta$ search in SNO+.

Cosmogenic Backgrounds

Cosmogenic backgrounds are caused by the radioactive activation of detector materials by cosmic rays. Having a large overburden reduces the cosmic ray flux, and therefore

this background. Cosmic muon activation events can be removed by having a muon veto region surrounding the detector and ignoring any events taking place in the detector for a certain period after a muon has passed through, these are mainly caused by interactions producing ^{11}C from carbon in the scintillator [35]. An irreducible cosmogenic background is caused by the ^{8}B neutrino flux from the Sun.

In SNO+ the cosmogenically activated isotopes which affect the $0\nu\beta\beta$ search are spallation products on the Tellurium (^{60}Co, ^{110m}Ag, ^{88}Y and ^{22}Na) [35], these will mainly be produced whilst the Tellurium is on the surface.

$2\nu\beta\beta$

The non-perfect energy resolution of the detectors used means some $2\nu\beta\beta$ events will fall into the energy region of $0\nu\beta\beta$ Eq. 2.36 [37] gives the approximate fraction of $2\nu\beta\beta$ events falling inside the $0\nu\beta\beta$ region, where ΔE is the energy resolution of the detector and Q is the Q-value of the nuclear decay, the energy deposited in the detector during a $0\nu\beta\beta$ event. m_e is the mass of the electron. A large Q value and a good energy resolution are crucial for detectors searching for $0\nu\beta\beta$.

$$F = \frac{7(\Delta E)^6}{Q^5 m_e} \tag{2.36}$$

2.5.2 Experimental techniques to detect $0\nu\beta\beta$

Several detection techniques exist to measure $0\nu\beta\beta$. SNO+ is a novel scintillator based experiment. Scintillator experiments like SNO+ benefit from being able to load a larger isotope mass inside the detector, due to their increased size. However scintillator detectors generally have poorer energy resolution. Scintillator detectors are often made up of a single instrument monolithic volume, whereas other detectors tend to be more modular in configuration.

Scintillator based detectors can achieve low backgrounds by performing a fiducial volume cut. Purification of the scintillator and isotope as well as extenstive cleaning of the detector apparatus also result in low backgrounds. In current scintillators the small amount Cherenkov light is masked by the prompt scintillation light meaning the event topology cannot be resolved. The development of slow and water based scintillators in which both components of the light are able to be distinguished are currently being investigated [38] [39].

Other techniques to measure $0\nu\beta\beta$ include the use of bolometers. Here, the isotope is

cooled down to a very low temperature. Any decays occurring in the detector will cause a temperature increase within the detector [40]. Bolometers have a very good energy resolution but are much less scaleable than scintillator based experiments. Ge can be used to construct ^{67}Ge rich diodes, which despite the low Q-value of the Ge double decay are still competitive due to their unique detection method. When an ionizing decay occurs within the detector an electron hole pair is created and creates a current pulse measurable by the detector electronics. Another detection method uses xenon time projection chambers, the topology of the events can be reconstructed in these types of detectors enabling a significant reduction in background events [41]. The NEMO detector allows the loading of various foils and can therefore attempt to detect $0\nu\beta\beta$ for multiple isotopes [42].

2.5.3 Current and near future limits on $0\nu\beta\beta$

Figure 2.11 shows the allowed values of $m_{\beta\beta}$ against the electron antineutrino mass, which is measured in tritium decays by the KATRIN experiment [43]. Figure 2.12 shows the allowed values of $m_{\beta\beta}$ against the sum of the neutrino masses that can be measured from cosmology. The current best limit on the sum of the neutrino masses ($\sum m_\nu$ <0.13 eV (95 % C.L.)) is obtained when combining Sloan digital sky survey data with Planck CMB measurements and Baryon Acoustic Oscillation (BAO) measurements [44].

For both Figures 2.11 and the thickness in the experiment limits of $m_{\beta\beta}$ is caused by the uncertainty in the values of the nuclear matrix elements and phase space factors (the value of $M_{0\nu}$ in Eq. 2.33).

The thickness of the allowed bands are mainly caused by the range of values possible for ϕ_1 and ϕ_2 which are unknown, another source of error is the uncertainties on the oscillation parameters themselves. Also shown is the future limit to be set by CUORE and SNO+ as well as the sensitivity of the SNO+-Phase 2 experiment.

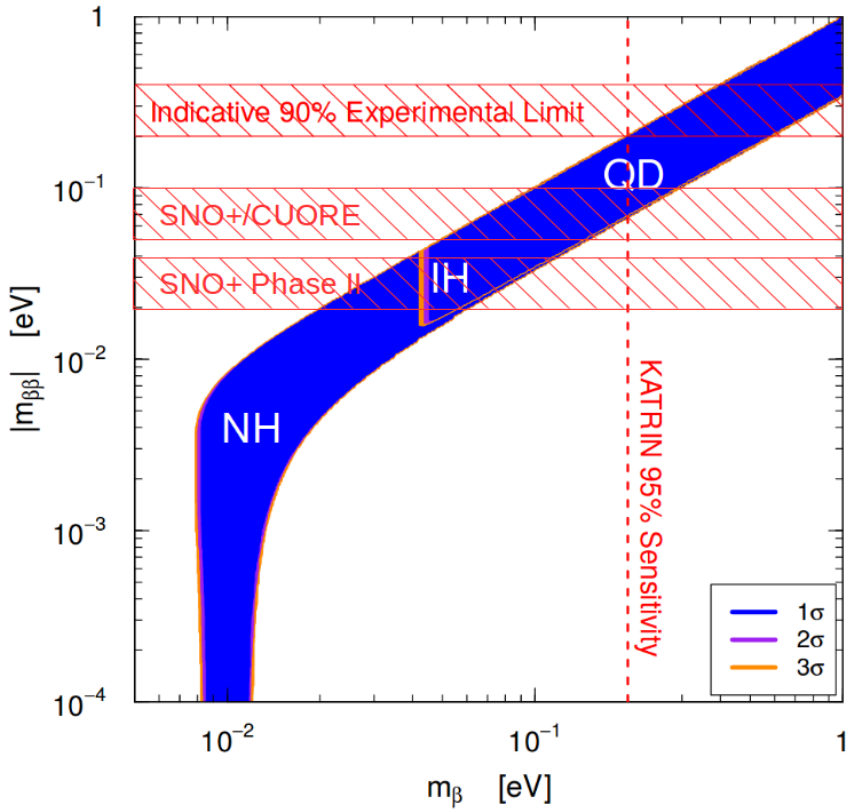

Figure 2.11: Values of $m_{\beta\beta}$ against the electron neutrino mass. Shown is the current double beta limit and limits from the CUORE and SNO+ experiments, as well as the predicted limit from SNO+-Phase 2. The expected sensitivity of KATRIN is indicated by the vertical dashed line. Plot modified from [45]

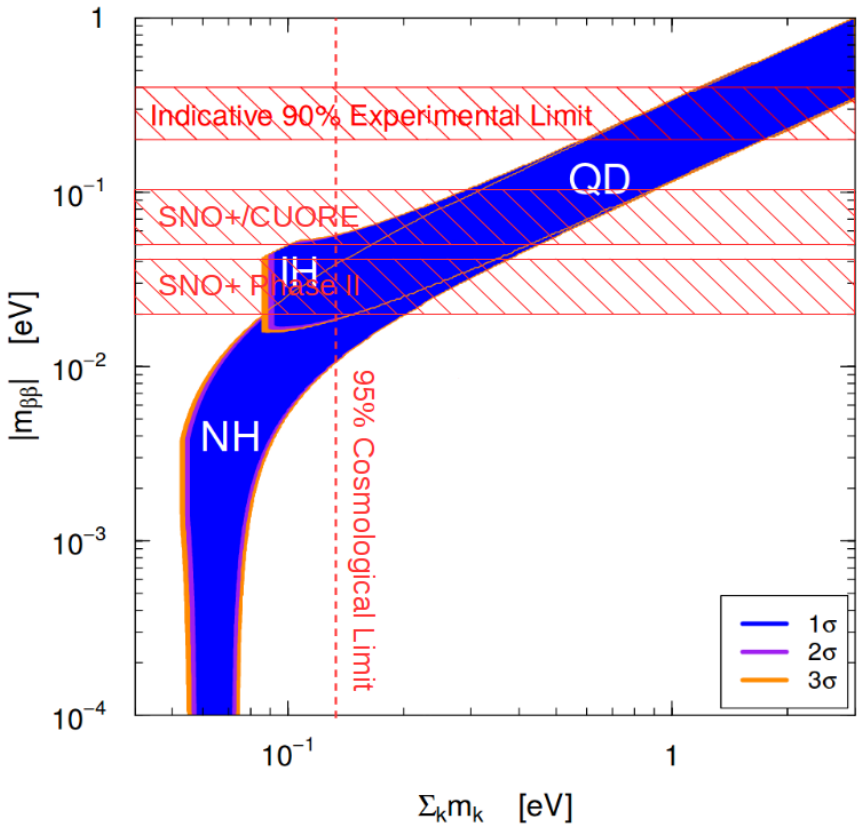

Figure 2.12: Values of $m_{\beta\beta}$ against the sum of the neutrino masses obtained. Shown is the current double beta limit and limits from the CUORE and SNO+ experiments, as well as the predicted limit from SNO+-Phase 2. The current limit on the sum of the neutrino masses from cosmology at a 95% confidence level is shown via the vertical dashed line. Plot modified from [45].

Chapter 3

Neutrino interactions

This chapter covers the interactions relevant to SNO+ in both its water and scintillator phases. The three interactions used in the studies presented in Chapter 9 (inverse beta decay, neutrino proton scattering and neutrino electron scattering) are described in detail with the kinematics of the interactions which are also included in the study. Interactions on nuclei, specifically ^{16}O and ^{12}C, which are relevant to SNO+ in the water and scintillator phases respectively are described, coherent interactions on nuclei as a whole are described for completeness.

3.1 Overview

Understanding the interaction cross sections between neutrinos and the targets in a detector is crucial to determine expected interaction rates. Some cross sections such as a neutrino scattering off of a electron are well understood and can be calculated using the Standard Model. Other interactions, including interactions with nucleons, require numerical evaluation and are a large source of systematic uncertainty. Fig 3.1 shows all the interactions relevant to SNO+, in both the water and scintillator phases.

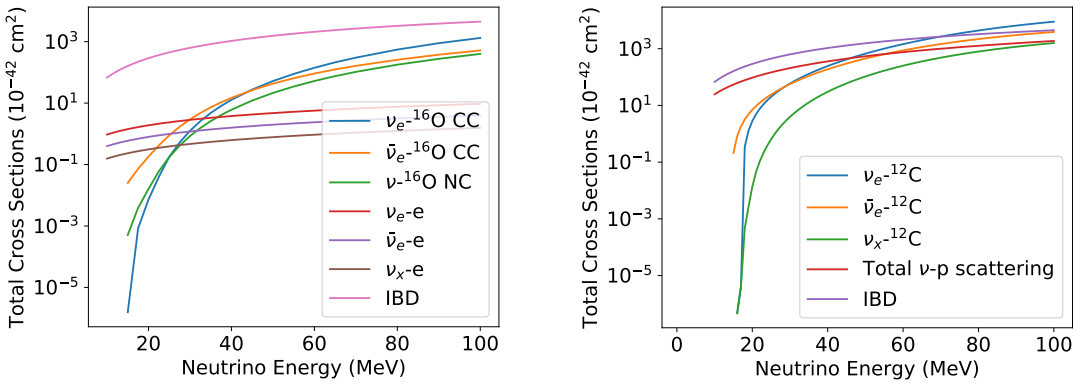

(a) Cross sections relevant for the water phase of SNO+.

(b) Cross Sections relevant for the scintillator phase of SNO+.

Figure 3.1: Interaction cross sections relevant to the SNO+ experiment. The $\nu - e$ scattering is also relevant during the scintillator phase but is omitted from the graph to make the graph to make it easier to read. There is no change in the size of the cross section between the phases.

The next sections describe the kinematics of the interactions at energies relevant to a supernovae neutrino burst.

3.2 Inverse-Beta Decay

The inverse-beta decay (IBD) process is shown in Eq. 3.1, during this process an electron anti-neutrino interacts with a proton via the exchange of a W^+ boson to produce a positron and a neutron. The positron promptly annihilates with an electron in the detector. The neutron thermalises before being captured by a nuclei after O(200 µs) [46]. This process has a threshold neutrino energy of $E_\nu = 1.806\,\text{MeV}$ [21].

$$\bar{\nu}_e + p \rightarrow e^+ + n \tag{3.1}$$

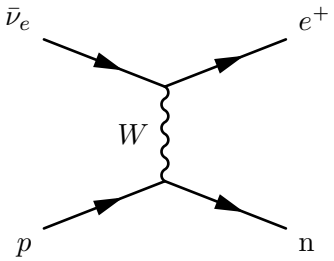

Figure 3.2: Feynman diagram for inverse beta decay.

A lowest order approximation to the cross section is given in Eq 3.2 [21]. This approximation neglects the nucleon recoil. A more accurate model is described in [47]. To

calculate the overall cross section for event rates in SNO+ the numerical approximation (accurate to the per mille level [47]) shown in Eq. 3.3 is used.

$$\sigma_{\text{IBD}} \approx 0.0952 \times 10^{-42} \left(E_e p_e\right) \tag{3.2}$$

$$\sigma_{\text{IBD}} \approx 10^{-43} p_e E_e E_\nu^{-0.07056+0.02018 ln E_\nu - 0.001953 ln^3 E_\nu} \tag{3.3}$$

$$E_e = E_\nu - \Delta \tag{3.4}$$

$$\Delta = m_n - m_p \approx 1.293\,\text{MeV} \tag{3.5}$$

$$p_e = \sqrt{E_e^2 - m_e^2} \tag{3.6}$$

A comparison of Eq. 3.2 and Eq. 3.3 can be seen in Fig. 3.3 at higher energies the difference between the calculations is significant.

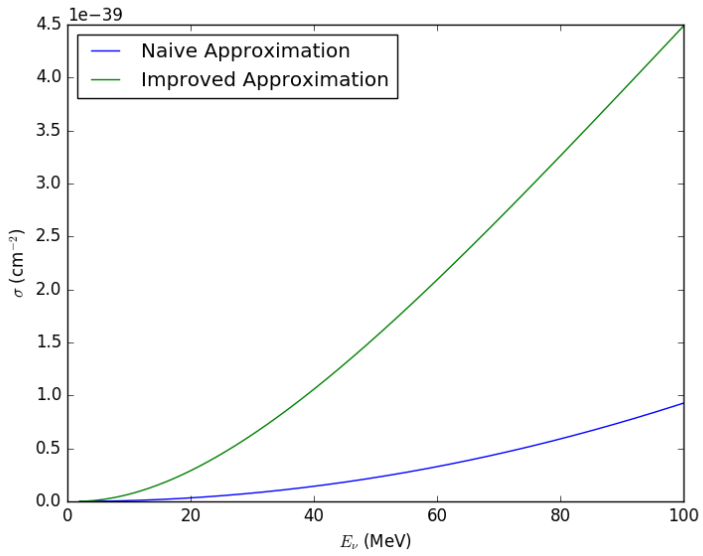

Figure 3.3: The naive cross section calculation from Eq 3.2, and the improved approximation calculated using Eq 3.3.

3.2.1 Kinematics

The kinematics of the interaction are calculated to NLO [21]. The approximate differential cross section as a function of the energy of the scattered positron is given in Eq. 3.7. $\mathcal{M}$ is the matrix element given in Eq. 3.8. m_p is the mass of the proton. G_F is the Fermi coupling constant and θ_C is the Cabbibo angle. Eqs. 3.7 to 3.21 are from [47].

$$\frac{d\sigma}{dE_e} = 2m_p \frac{G_F^2 cos^2\theta_C}{2\pi(s-m_p)^2}|\mathcal{M}^2| \tag{3.7}$$

$$|\mathcal{M}^2| = A - (s-u)B + (s-u)^2 C \tag{3.8}$$

The variables s, t and u are the standard Mandelstam variables, in the frame where the proton is initially at rest these are given by Eqs. 3.9 - 3.11. E_ν is the energy of the incoming neutrino, E_e is the energy of the scattered positron. m_n and m_e are the masses of the neutron and positron respectively.

$$s = 2m_p E_\nu + m_p^2 \tag{3.9}$$

$$s - u = 2m_p(E_\nu + E_e) - m_e^2 \tag{3.10}$$

$$t = m_n^2 - m_p^2 - 2m_p(E_\nu - E - m_e) \tag{3.11}$$

The values of A, B and C in Eq. 3.8, which are just terms to improve the readability of Eq. 3.8, are given in Eqs. 3.12 to 3.14. The variable Δ in Eq. 3.12 is the difference in mass between the neutron and the proton and has the approximate value 1.293 MeV and M is the mean nucleon mass, with approximate value 938.9 MeV.

$$A \approx \mathrm{M}^2(f_1^2 - g_1^2)(t - m_e^2) - \mathrm{M}^2\Delta^2(f_1^2 + g_1^2) - 2m_e^2\mathrm{M}\Delta g_1(f_1 + f_2) \tag{3.12}$$

$$B \approx t g_1(f_1 + f_2) \tag{3.13}$$

$$C \approx \frac{(f_1^2 + g_1^2)}{4} \tag{3.14}$$

The values for the form factors f_1, f_2 and g_1 are given in Eqs. 3.15 to 3.17. The value of $g_1(0)$ in Eq. 3.17 is set to 1.27 and M_A has been given the value of 1 GeV. The parameter ξ is the difference in the anomalous magnetic moments of the proton and the neutron and has a value of 3.706.

$$f_1(t) \approx 1 + \frac{2.5e - 6t}{\mathrm{MeV}^2} \tag{3.15}$$

$$f_2(t) \approx \xi \left[1 + \frac{3.4e - 6t}{\text{MeV}^2}\right] \tag{3.16}$$

$$g_1 = \frac{g_1(0)}{1 - t/M_A^2} \tag{3.17}$$

The differential cross section as a function of positron scattering angle relative to the incoming neutrino can be found using Eq. 3.18. The equation relating the scattering angle to the positron energy is given in Eq. 3.19. The positron momenta is given using the standard relation $p_e = \sqrt{E_e^2 - m_e^2}$.

$$\frac{d\sigma}{dcos\theta}(E_\nu, cos\theta) = \frac{p_e \epsilon}{1 + \epsilon\left(1 - \frac{E_e}{p_e} cos\theta\right)} \frac{d\sigma}{dE_e} \tag{3.18}$$

$$E_e = \frac{(E_\nu - \delta)(1 + \epsilon) + \epsilon cos\theta \sqrt{(E_\nu - \delta)^2 - m_e^2 \kappa}}{\kappa} \tag{3.19}$$

Fig 3.4 shows the angular distribution of the positron at various neutrino energies. For higher neutrino energies the direction of the scattered proton becomes more closely aligned with the incoming neutrino, although the distribution is close to isotropic.

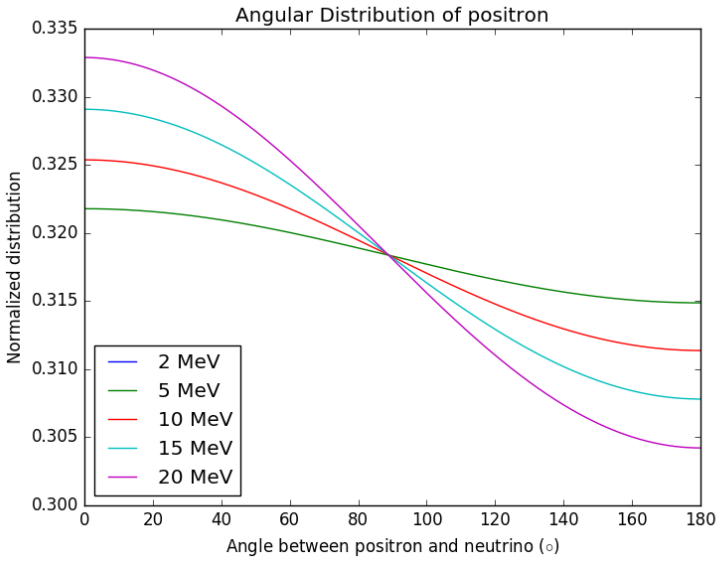

Figure 3.4: Normalised distributions of the angle of the emitted positron relative to the incoming neutrino shown for various neutrino energies.

The scattering momenta of the neutron p_n, shown in Eq. 3.20 is obtained via conservation of momenta and energy. The scattering angle of the neutron can be obtained from conservation of momentum perpendicular to the incoming neutrino direction as shown in

Eq. 3.21, where θ is the scattering angle of the positron, and ϕ is the scattering angle of the neutron.

$$p_n = \sqrt{(E_\nu + m_p - E_e)^2 - m_n^2} \tag{3.20}$$

$$p_n \sin\phi = p_e \sin\theta \tag{3.21}$$

3.3 Neutrino Electron Elastic scattering

Neutrino electron scattering can be calculated analytically via the standard model. At supernovae neutrino energies $E_\nu < O(100\,\text{MeV})$ only the electron neutrinos can scatter via both Z and $W^\pm$ boson exchange. Muon and tau neutrinos produced do not have enough energy to interact via charged current interactions, due to the muon and tau masses being greater than 100 MeV. The Feynman diagrams for neutrino electron scattering can be seen in Figures 3.5 to 3.7, and the cross sections can be found in Eqs. 3.22 to 3.25.

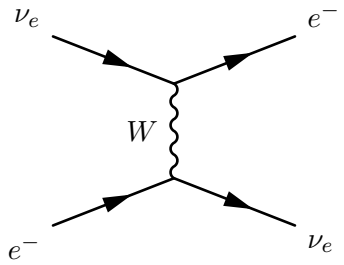

(a) Charged current neutrino electron scattering.

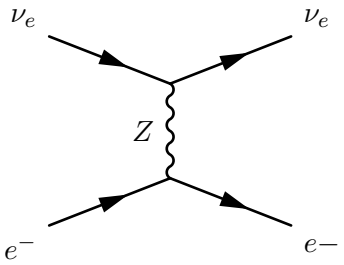

(b) Neutral current electron neutrino electron scattering.

Figure 3.5: The interaction channels available to ν_e for neutrino electron scattering.

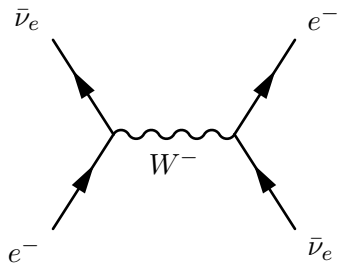

(a) Charged current anti electron neutrino electron scattering.

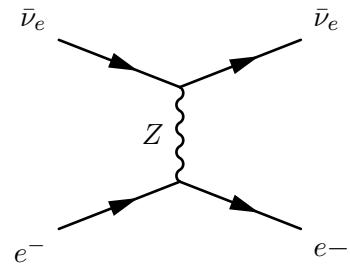

(b) Neutral current anti electron neutrino electron scattering.

Figure 3.6: The neutrino electron scattering channels available to $\bar{\nu}_e$.

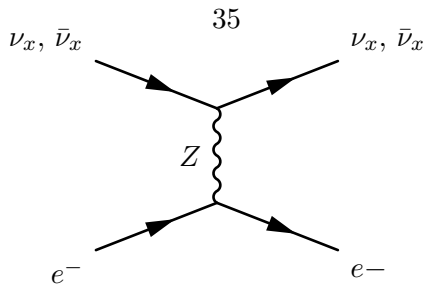

Figure 3.7: Neutral current neutrino electron scattering.

$$\sigma_{\mathrm{NC}-\nu} = \sigma_0 \left[\left(\frac{1}{2} - \sin^2\theta_W \right)^2 + \frac{1}{3}\sin^4\theta_W \right] \tag{3.22}$$

$$\sigma_{\mathrm{NC}-\bar{\nu}} = \sigma_0 \left[\frac{1}{3} \left(\frac{1}{2} - \sin^2\theta_W \right)^2 + \sin^4\theta_W \right] \tag{3.23}$$

$$\sigma_{\mathrm{CC}-\nu} = 2\sigma_0 \sin^2\theta_W \tag{3.24}$$

$$\sigma_{\mathrm{CC}-\bar{\nu}} = \frac{2}{3}\sigma_0 \sin^2\theta_W \tag{3.25}$$

The value of σ_0 is given by Eq. 3.26. θ_W is the Weinberg angle. The value of $\sin^2\theta_W$ used was 0.23.

$$\sigma_0(E_\nu) = \frac{G_F^2 2 m_e E_\nu}{\pi} \tag{3.26}$$

The total cross section for each neutrino flavour can also be written in a compact form seen in Eq. 3.27 [48], the + sign corresponds to electron flavour neutrinos, whereas the - sign corresponds to μ and τ flavour neutrinos. For neutrinos the values of c_1 and c_2 are 1 and $\frac{1}{3}$ respectively. For anti-neutrinos they are reversed with $c_1 = \frac{1}{3}$ and $c_2 = 1$.

$$\sigma_{tot} = \sigma_0 \left[c_1 \left(\frac{1}{2} \pm \sin^2\theta_w \right)^2 + c_2 \sin^4\theta_w \right] \tag{3.27}$$

3.3.1 Kinematics

The differential cross section for the scattering angle of the electron can be seen in Eq. 3.28 [21]. The value of σ_0 is given by Eq 3.26. Like the values of c in Eq. 3.27 the values of g_1 and g_2 depend on the type of neutrino. Table 3.1 shows the values of g for the neutrino flavours.

$\boldsymbol{\nu}$ **flavour**	$\boldsymbol{g_1}$	$\boldsymbol{g_2}$
ν_e	$\frac{1}{2} + \sin^2\theta_W$	$\sin^2\theta_W$
$\bar{\nu}_e$	$\sin^2\theta_W$	$\frac{1}{2} + \sin^2\theta_W$
ν_x	$-\frac{1}{2} + \sin^2\theta_W$	$\sin^2\theta_W$
$\bar{\nu}_x$	$\sin^2\theta_W$	$-\frac{1}{2} + \sin^2\theta_W$

Table 3.1: Values for g_1 and g_2 for each neutrino flavour.

$$\frac{d\sigma}{d\cos\theta} = \sigma_0 \frac{4E_\nu(m_e + E_\nu)^2\cos\theta}{[(m_e + E_\nu)]^2} \left[g_1^2 + g_2^2 \left(1 - \frac{2m_e E_\nu \cos^2\theta}{(m_e + E_\nu)^2 - E_\nu^2\cos^2\theta}\right)^2 - g_1 g_2 \frac{2m_e^2\cos^2\theta}{(m_e + E_\nu)^2 - E_\nu^2\cos^2\theta} \right]$$

The equation relating the scattering angle to the kinetic energy of the scattered electron is given in Eq. 3.28. The electrons kinetic energy is maximised when $\cos\theta$ is 1, i.e. the neutrino scattered backwards and the electron is scattered forward in the initial direction of the neutrino.

$$T_e = \frac{2m_e E_\nu^2 \cos^2\theta}{(m_e + E_\nu)^2 - E_\nu^2 \cos^2\theta} \tag{3.28}$$

3.4 Neutrino Proton Elastic Scattering

Neutrino proton elastic scattering involves the exchange of the Z boson between a neutrino and a proton. The charged current component is inverse beta decay, as described in Section 3.2. Unlike inverse beta decay, the boson exchange is not limited to a single flavour, neutrinos of all flavours can interact via this interaction. The total cross section for this equation is given in Eq. 3.29 [49]. For this calculation The value of c_v is given in Eq. 3.30. This value is an approximation: the full value also contains terms caused by the strange charge radius of the proton. The term contains a pre-factor q^2. At supernovae neutrino energies the value of q is small enough such that this can be neglected [49]. The value of c_A is the axial-vector coupling constant between the Z boson and the proton and is shown in Eq. 3.31. The term Δs is caused by the strange quark contribution to the protons spin, the current value of Δs has not been very accurately measured the current best fit value is $\Delta s = 0.152 \pm 0.0889$ [50]. The MicroBOONE experiment hopes to set make an improved measurement of this value and reduce the uncertainty to around one tenth of its current value [51]. Δs the value is set to the best fit value in the calculations

in this thesis (Chapter 9). G_F is the Fermi coupling constant and E_ν is the energy of the incoming neutrino.

$$\sigma = \frac{G_F^2 E_\nu^2}{\pi}(c_v^2 + 3c_A^2) \tag{3.29}$$

$$c_v = \frac{1 - 4\sin\theta_W}{2} \tag{3.30}$$

$$c_A = \frac{1.27 - \Delta s}{2} \tag{3.31}$$

3.4.1 Kinematics

The approximate differential cross section for neutrino proton scattering and the maximum scattering energy can be seen in Eqs. 3.32 and 3.33 [49]. The scattering direction of the proton can also be found in [49], although in scintillator based detectors (the only detector medium which can see proton scattering) the scattering direction of the of the proton cannot be seen.

$$\frac{d\sigma}{dT_p} = \frac{G_F^2}{2\pi E_\nu^2}\left[(c_v + c_A)^2 E_\nu^2 + (c_v - c_A)^2 (E_\nu - T_p)^2 - (c_v^2 - c_A^2) M_p T_p\right] \tag{3.32}$$

$$T_p^{\max} = \frac{2E_\nu^2}{M_p + 2E_\nu} \tag{3.33}$$

3.5 Neutrino Interactions with Nuclei

The SNO+ detector volume also contains nuclei. In the water phase ^{16}O nuclei are present, and in scintillator phase neutrino interactions on carbon nuclei are possible. Unlike the interactions previously described these cannot be determined analytically and numerical approximations must be made.

3.5.1 Coherent Nuclear Elastic Scattering

Coherent nuclear elastic scattering takes place when an incoming neutrino scatters elastically via the exchange of a Z boson of an entire nuclei. The process only happens for low energy neutrinos where the neutrino is unable to distinguish the individual nucleons making up the nucleus, due to its large de Broglie wavelength. Dark matter experiments [52]

and $0\nu\beta\beta$ searches [53] will be sensitive to this interaction. The cross sections for the individual nucleons add coherently this causes the total cross section to increase proportionally with the neutron number of the nucleus squared [54]. So despite the small size of experiments performing these searches a surprisingly large number of neutrinos can be detected. Coherent elastic scattering was first observed experimentally in 2017 by the COHERENT experiment [55].

The differential cross section as a function of scattering angle is given in Eq. 3.34 [54].

$$\frac{d\sigma}{d\Omega} = \frac{G_F^2}{4\pi^2} E_\nu^2 (1 + \cos\theta) \frac{Q_w^2}{4} F(Q^2)^2 \tag{3.34}$$

The value of F is the nuclear form factor which reflects the ability of the neutrino to interact with the nucleons rather than the nucleus as a whole, and is shown in Eq. 3.35 [54]. The factor Q_w accounts for the coherent adding of the single nucleon cross sections in the nucleus. Q is the momentum transfer from the neutrino to the nucleus and is given by $Q^2 = 2E_\nu^2(1 - \cos\theta)$, where θ is the scattering angle of the neutrino and E_ν is the energy of the neutrino. The recoil kinetic energy can be obtained from the expression $T = \frac{Q^2}{2m}$ where m is the mass of the nucleus.

$$F(Q^2) = \frac{3\left(\frac{\sin(QR_0)}{(QR_0)^2} - \frac{\cos(QR_0)}{QR_0}\right)}{QR_0} \times \exp\left[-\frac{(Qs)^2}{2}\right] \tag{3.35}$$

$$Q_w = N - (1 - 4\sin^2\theta_W)Z \tag{3.36}$$

R_0 is the nuclear radius given by $R_0^2 = (1.2 \times A^{1/3}) - 5s^2$ fm and s is the nuclear skin thickness with value 0.5 fm. N and Z are the neutron and proton count of the nucleus respectively.

3.5.2 Inelastic Interactions with Nuclei

The form factor F shown in Eq. 3.35 decreases with energy, causing the coherent cross section to decrease. Instead of interacting with the nucleus as a whole higher energy neutrinos begin to interact with individual nucleons within the nucleus.

If a neutrino interacts with an individual nucleon via a neutral current interaction it is possible that there is sufficient energy to promote the nucleon to a higher energy level within the nucleus. The nucleus will then decay to its ground state via the emission of γ-rays. This interaction is available to all flavours of neutrino. If the neutrino is high

enough energy, nucleons can be ejected from the nucleus.

$$\nu + X \rightarrow \nu' + X* \rightarrow X + \gamma \tag{3.37}$$

$$\nu + X \rightarrow \nu' + Y + n/p \tag{3.38}$$

For electron and anti-electron flavour neutrinos charged current interactions are also possible. For anti-electron neutrinos a proton inside the nuclei can be turned into a neutron with the emission of a positron. In the case of electron flavour neutrinos a neutron can be turned into a proton with the emission of an electron. Often the remaining nuclei are radioactively unstable and decay, the subsequent decays can possibly be used to tag events [56].

To calculate the total cross section for these interactions the effects of the other nucleons must be calculated. Furthermore, for the charged current interactions the effect of the attraction of the ejected charged lepton and the remnant nucleus must also be considered. These interactions are not very well understood currently and there exist various methods of calculating the cross sections at different energy levels [57]. As the neutrino energy increases the effects of the other nucleons become less significant.

Neutrino Interactions with ^{16}O

During the water phase of SNO+ the ^{16}O atoms in the water will act as targets for incoming neutrinos. The two charged current interactions and their thresholds are shown in Eqs. 3.39, 3.40.

$$\bar{\nu}_e + {}^{16}\mathrm{O} \rightarrow {}^{16}\mathrm{N} + e^+ \quad (E_\nu > 11.4\ \mathrm{MeV}) \tag{3.39}$$

$$\nu_e + {}^{16}\mathrm{O} \rightarrow {}^{16}\mathrm{F} + e^- \quad (E_\nu > 15.4\ \mathrm{MeV}) \tag{3.40}$$

The ^{16}N nuclei decays via β^- decay 68% of the time. This decay consists of an electron with decay endpoint energy 4.3 MeV and a 6.14 MeV γ ray associated with the newly produced ^{16}O decaying to its ground state. 26% of the time the decay occurs directly to the ground state of ^{16}O, releasing and electron with endpoint energy 10.4 MeV. The remaining decay modes consist of decays to higher exited levels of ^{16}O, resulting in a lower energy electron and either a single or a cascade of γ rays as the ^{16}O dexcites [58].

The ^{16}F nuclei decays immediately via the emission of a proton with energy 538 keV. The newly formed ^{15}O state then decays with a half life of 2.04 m by β^+ decay with a endpoint of ≈2.8 MeV.

Neutral current interactions can also happen on oxygen nuclei. If the neutrino has energy of more than 25 MeV then a proton or neutron can be ejected from the nucleus [59]. If a neutron is ejected the nuclei ends in a ^{15}N which is radioactively stable. If a proton is ejected then the nuclei becomes a ^{15}O which in turn decays via the β^+ decay described above.

Neutrino Interactions with ^{12}C

In scintillator based detectors interactions can take place with carbon nuclei present in the scintillator molecules, like the oxygen interactions charged current interactions will be available to both ν_e and $\bar{\nu}_e$ and are shown in Eqs. 3.42 and 3.41 respectively. Neutral current scattering will be available to all flavours of neutrino via Eq. 3.43.

$$\bar{\nu}_e + {}^{12}\mathrm{C} \rightarrow {}^{12}\mathrm{B} + e^+ \quad (E_\nu > 13.9\ \mathrm{MeV}) \tag{3.41}$$

$$\nu_e + {}^{12}\mathrm{C} \rightarrow {}^{12}\mathrm{N} + e^- \quad (E_\nu > 17.9\ \mathrm{MeV}) \tag{3.42}$$

$$\nu_e + {}^{12}\mathrm{C} \rightarrow {}^{12}\mathrm{C}^* \rightarrow {}^{12}\mathrm{C} + \gamma \tag{3.43}$$

Like the interactions on oxygen the two isotopes produced 3.41 and 3.42 are unstable. ^{12}B decays via β^- decay with a half life of 20.2 ms. The decay to the ground state has Q value of 13.37 MeV. It is also possible to decay to an exited state of ^{12}C [60]. ^{12}N decays after the via β^+ decay with a half life of 11.0 ms, and a Q value of 17.34 MeV [60] to the ground state of ^{12}C, decays to an exited state are also possible. The interaction cross section for the ^{12}N channel have been measured by the KARMEN and LSND experiments [61] [62].

The neutral current interaction on carbon shows a distinctive feature: the scattering of a neutrino can excite the nucleus, which then decays via the emission of a 15.1 MeV γ ray, producing a distinct spike in the energy spectrum (see Eq. 3.43). The cross section was measured by KARMEN at a neutrino energy of 29.8 MeV via pion decay at rest [63]. The cross section was found to be 3.2 ± 0.5 (stat) ± 0.4 (sys) $\times 10^{-42}$ cm^2.

The theoretical expectations for the interaction cross sections shown in Eqs. 3.41 to 3.43

are shown in Figure 3.8. The figure also shows the measured values of the cross sections where applicable.

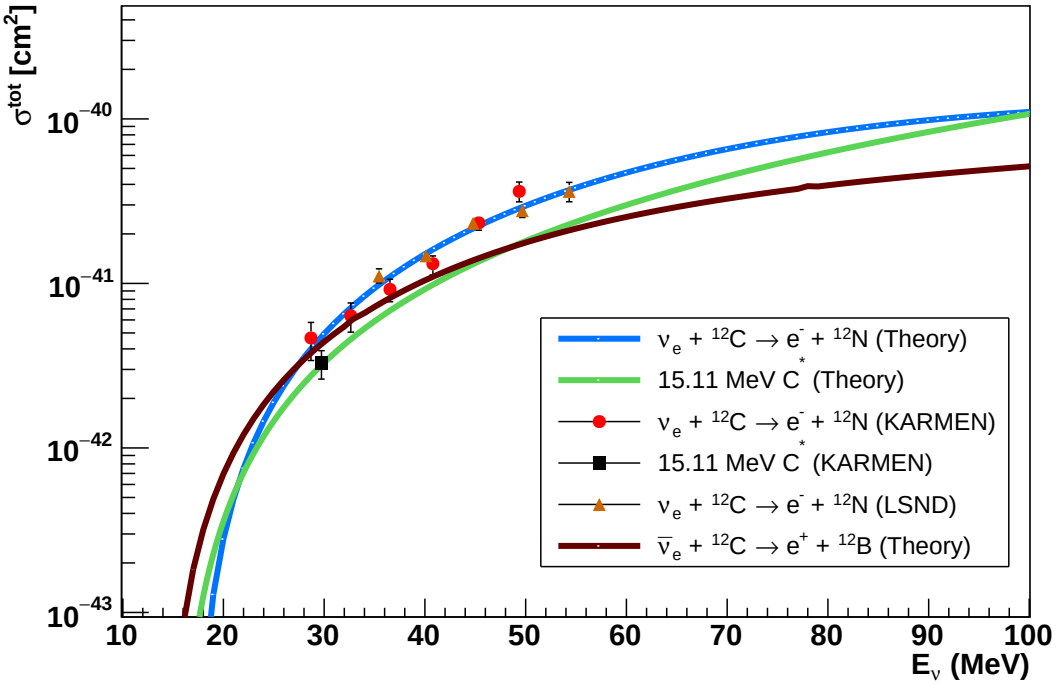

Figure 3.8: Cross sections of ν-^{12}C interactions. The theoretical cross sections are indicated by solid lines, the measured cross sections by KARMEN and LSND are shown as points.

Other neutral current interactions can take place on ^{12}C which cause the release of nucleons from the nucleus, the cross sections for these interactions are shown in Figure 3.9 [64] if a neutron is emitted this can mimic an IBD event [65].

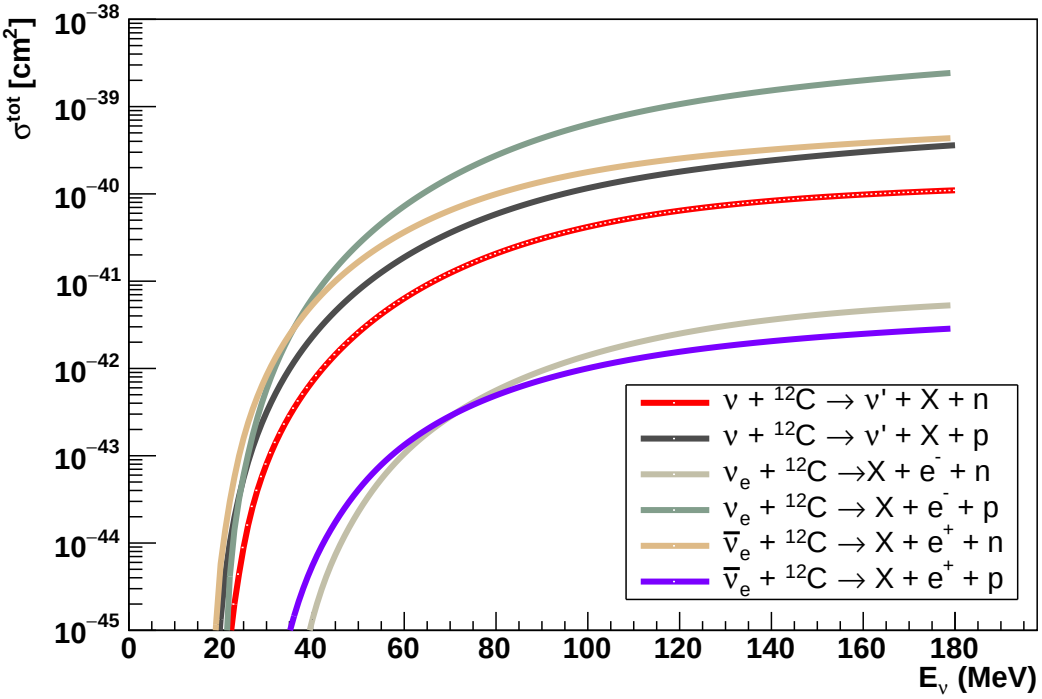

Figure 3.9: Cross sections of ν-^{12}C interactions. ν indicates a NC interaction available to all flavours of neutrino, X means the cross section is summed over all final states.

3.6 Conclusion

This chapter summarises the various interaction channels relevant to the detection of neutrinos from a supernova. The most important interactions for large scale neutrino detectors are the inverse beta decay (IBD) and neutrino electron ($\nu - e$) scattering interactions. Scintillator detectors are also able to observe the neutrino proton scattering ($\nu - p$) channel. These three interaction channels are used in the analysis described within Chapter 9. Both $\nu - e$ and IBD interactions are well understood and are accurate to the per mille level. The $\nu - p$ interaction has some uncertainty in its cross section associated with the measurement of Δs and is less well understood.

Interactions with nuclei are also possible. These can involve interactions with nuclei as a whole, which can produce a signal visible in dark matter experiments and low temperature bolometers. The cross section for this interaction is well understood. Neutrinos can also interact with individual nucleons within the nucleus, resulting in a variety of final states, including unstable isotopes which decay to produce a secondary signal within the detector. Due to the complexity of these interactions they can only be modelled numerically and the interactions either have larger uncertainties (The best neutrino nucleus cross

sections have been measured for ^{12}C and have errors of approximately 10%) or no information on the cross-sections is available. There is even less information on the kinematics of these interactions.

Chapter 4

Theory of Supernovae Bursts

This chapter describes the theory of supernova bursts. The chapter starts by overviewing the stellar conditions required for a core collapse supernova. The chapter then describes the explosion mechanism and the neutrino heating mechanism in detail as well as describing the neutrino emission from the supernova. The chapter then describes the SASI and LESA phenomena observed in simulations. The chapter then describes oscillation effects present in a supernova, of particular importance are the matter effects described in Section 4.6.1, which are used within the sensitivity studies in the final chapter. The chapter then follows with the predicted distribution of SN within the Milky Way and measurable properties of a SN using neutrinos. The chapter concludes with an overview of the only SN neutrino burst observed SN1987A and the diffuse SN background.

Supernovae are superluminous events associated with the end of a massive stars life. During the burst the star can outshine its host galaxy. Certain types of supernovae occur in binary systems and are caused by runaway fusion and do not emit any significant number of neutrinos. However, the majority of supernovae occur via the core collapse mechanism, releasing 99% of the stars gravitational binding energy as neutrinos [1] over a time period of O(10) s. The emission of these neutrinos is thought to be crucial to explosion via the heating of the outer regions of the star by neutrinos. Simulations where neutrinos are neglected were unable to cause the observed explosions by the core bounce alone.

Despite the large distance and miniscule interaction cross section of the neutrinos the flux is high enough to cause a burst of events in terrestrial detectors. Such an event has only been detected once in 1987 [66] [67] [68].

[1] the remaining 1% is released as optical light and kinetic energy of the ejected outer layers

As well as providing information about the mechanism of the burst, the unique conditions of incredibly high matter density and incredibly high neutrino flux[2] can be used to test the properties of the neutrinos, including their mass hierarchy.

In this chapter the various types of star which are able to undergo various types of core collapse supernovae are discussed, and a brief overview of their lifetimes is given. The explosion mechanism for the lightest mass SN (Supernovae) progenitors is then discussed. A description of the most common type of core collapse and the role of neutrinos in the explosion is explained, with reference to the observed neutrino spectra. The current status of simulations of supernovae is also described.

Neutrinos produced in a supernovae also oscillate in regions of very high matter density and neutrino flux, the effect of these conditions on the observed neutrino spectrum are described.

The detection of the neutrinos for the last (and only) observed SN neutrino burst is detailed, as well as physics knowledge obtained. The expected distance distribution for SN within the Milky Way is described, as well as the expected rate of SN within the Galaxy. Finally the diffuse supernovae background (DSNB), a neutrino flux produced by all the previous supernovae throughout history is described.

4.1 Lifetime of a star

Throughout the lifetime of a star the inwards gravitational pressure is matched by the outwards radiation pressure produced by the fusion of elements at the stars core. For the majority of its lifetime it generates outwards radiation pressure via the fusion of two protons (from the hydrogen plasma) into a deuteron. As the fusion takes place the number of protons in the core becomes depleted, the outwards radiation pressure then drops and the core contracts further until it becomes hot enough to fuse helium. Further fusion processes beyond helium can also take place provided the star is massive enough. The fusion processes of heavier elements are less efficient (i.e. less energy is released per fusion) than hydrogen fusion. As less energy is released per fusion interaction, to keep the inwards gravitational pressure balanced with the outwards radiation pressure the rate of fusion processes must increase, there is also less material to fuse. This results in the exponential decrease in the lifetime of subsequent burning stages, as shown in Figure 4.1.

[2] the flux is so high that neutrino-neutrino scattering must be considered.

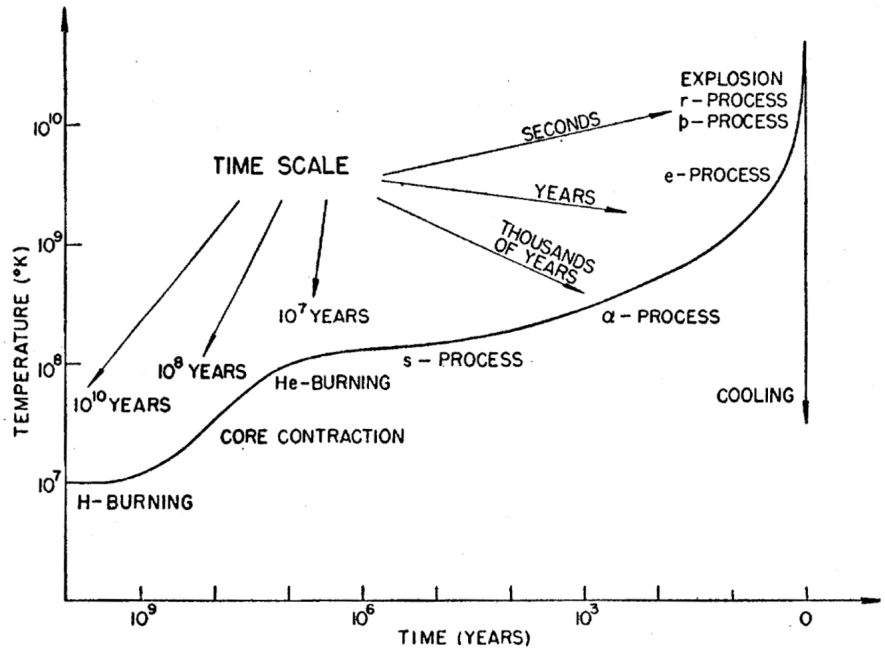

Figure 4.1: Pictographic representation of the core temperature against lifetime of a star which undergoes a SN explosion. The s process indicates "slow" neutron capture taking place on the core. The α process indicates when α particles capture on nuclei to form heavier elements. The e process indicates the point at which nuclear statistical equilibrium is reached in the core. The p process occurs when proton captures or neutron emission occurs on nuclei, and the r process indicates the rapid neutron capture on elements in the core. Taken from [69].

Figure 4.2 shows the evolution of various mass stars. For stars with masses lower than 8 solar masses a SN explosion cannot take place, as the core of these stars does not become massive enough to exceed the Chandrasekhar mass limit [70] and overcome the electron degeneracy pressure. Very low mass stars (with masses less than approximately half a solar mass) directly go to a white dwarf from the main sequence of hydrogen burning [71]. For stars with masses between $0.5M_{\odot}$ and $8M_{\odot}$ towards the end of the stars lifetime a red giant is formed. The area surrounding the helium core is heated up and the outer region begins to expand, eventually the outer layers of the star are lost due to stellar winds and slowly cooling white dwarf remains. It should also be noted that the rate of fusion in more massive stars is higher, and therefore they have shorter lifetimes.

Stars above 8 solar masses undergo a supernovae (SN) explosion forming a neutron star (NS) or a black hole (BH). The route to the explosion mechanism depends on the mass of the progenitor, although the mechanism of the collapse is largely the same for all progenitors. All core collapse supernovae release large numbers of neutrinos during their collapse $L_{\nu} \approx 10^{53}$ erg which accounts for approximately 99 % of the binding energy released [72]. The remaining 1% being visible light and ejecta energy.

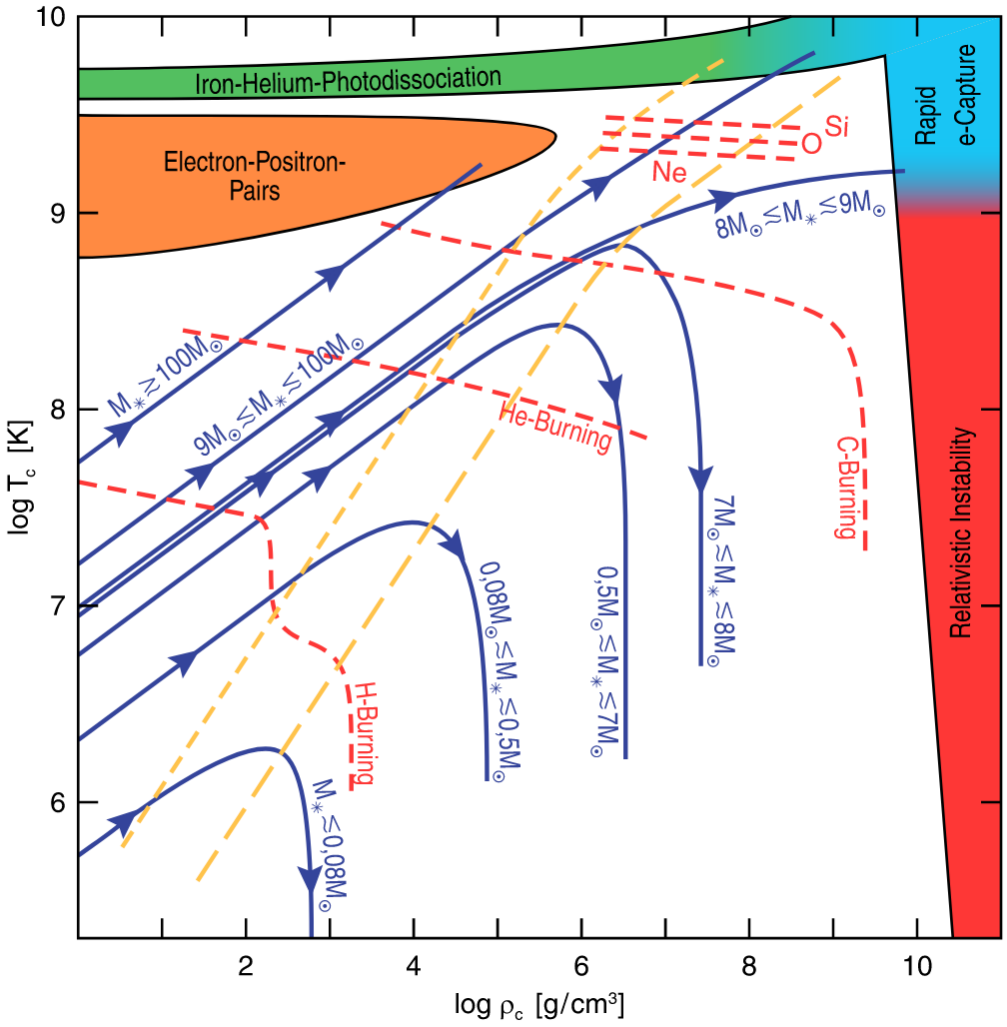

Figure 4.2: Figure showing the core densities and temperatures for various stellar masses. The red dashed lines indicate the conditions at which the fusion processes of different elements start. The short dashed yellow line shows the point at which degeneracy begins to take place, the long dashed line indicates the point at which hard electron degeneracy is reached. The colored regions indicate the core conditions for which various SN take place. Taken from [73].

4.2 Electron Core Collapse Supernovae

More massive stars can begin fusing heavier elements. A star with mass between 8 and 10 solar masses collapses via electron core collapse, because in a star of this mass, the core cannot become hot enough to fuse elements past neon in its core. Electron core collapse supernovae are thought to contribute to approximately 30% of the total SN rate [74]. As the rate of fusion reduces, the outwards radiation pressure also decreases. The electron degeneracy pressure, due to the Pauli exclusion principle begins to contribute . Eventually it becomes energetically favourable for electron captures to take place on the neon and

magnesium nuclei in the core [73]. These captures reduce the outwards degeneracy pressure of the electrons resulting in a collapse. As the surrounding matter falls in, the temperature of the core increases and allows oxygen fusion to take place [75]. The core enters a state of nuclear statistical equilibrium (NSE) and further electron captures take place, reducing the degeneracy pressure further. Eventually the NSE will contract enough to form a protoneutron star (PNS). The remainder of the collapse and subsequent explosion is via the same mechanism as for the iron core collapse supernovae described in the next section.

Due to the cooler core of the supernovae the neutrino spectra produced tends to have lower energy [76][77].

4.3 Iron Core Collapse Supernovae and the Neutrino driven delayed explosion mechanism

In this section the explosion mechanism of a supernovae is described and the role of neutrinos within the explosion is described. The neutrino spectra produced by supernovae are also described and the differences in the spectra for different neutrino flavours is also detailed.

4.3.1 Pre-SN Neutrinos

In stars with masses over 9 solar masses fusion of heavier elements up to silicon is possible. The burning of elements heavier than carbon occurs at approximately 10^9 K. At these temperatures electron position pair production is possible by producing neutrinos via the interaction $e^+e^- \rightarrow \nu\bar{\nu}$. The process is most prominent in the silicon burning phase, which lasts approximately two days before the supernovae explosion occurs with neutrinos of mean energy 1.8 MeV being produced [78]. The neutrino luminosity for pre-SN neutrinos is shown in Figure 4.3. The neutrinos produced during this early burning phase can be used to provide an early warning for an imminent neutrino explosion [79][80]. It should also be noted that this early burning neutrino signal is not seen for the lighter mass stars described in section 4.2, and could possibly be used to distinguish between the initial collapsing mechanism if a supernovae is observed at a close enough distance.

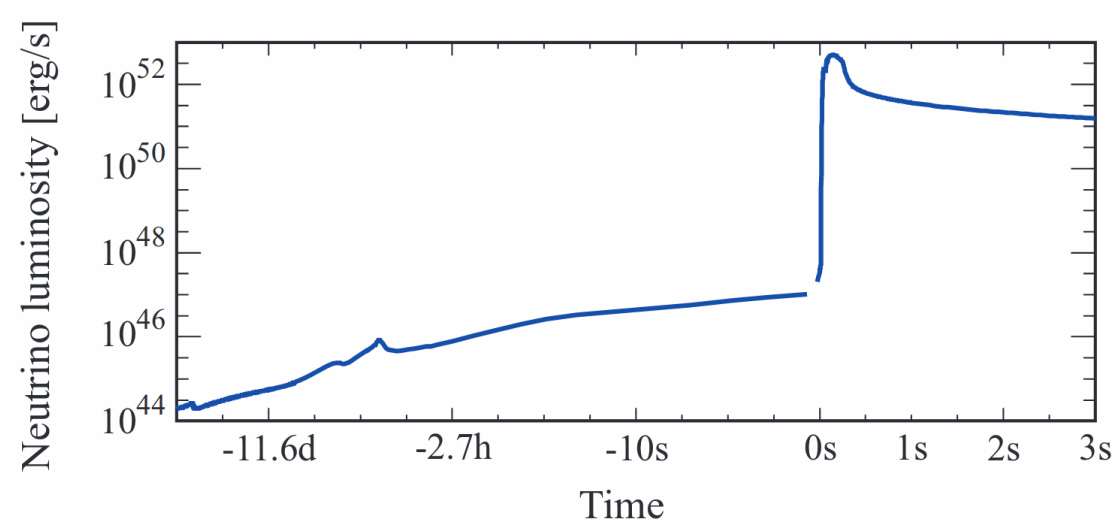

Figure 4.3: The simulated neutrino emission from a supernova before the core bounce due to Si fusion within the core [79].

4.3.2 SN Neutrino Emission Before the Core Bounce

As well as the production of neutrinos at these high temperatures nuclei can be broken down via photodisintigration and an NSE is formed in the core where nuclei are broken up into alpha particles which in turn fuse to produce different nuclei. Alpha particles in the core fuse with ^{28}Si to form ^{56}Ni as shown in Eq. 4.1.

$$^{28}\text{Si} + 7\,^{4}\text{He} \rightarrow ^{56}\text{Ni} \tag{4.1}$$

As ^{56}Ni is the tightest bound nucleus in the fusion chain of a star, fusion to heavier elements beyond this point is an endothermic process and the outwards fusion pressure begins to reduce. As the core begins to compress, the temperature increases and photons begin to break down nuclei into smaller nuclei and free protons. This requires a large amount of energy and cools the core of the star. The reduction in temperature causes a reduction in pressure and the surrounding matter begins to fall inwards. The degeneracy pressure of the electrons provides an outwards pressure to match the inwards gravitational pull. Eventually, it becomes energetically favorable for electron captures to occur on the remaining ^{56}Ni in the core and on free protons, at this point in time the surrounding matter is not dense enough to become opaque to the neutrinos which exit the star removing further energy from the core. This neutrino emission is shown as the small peak before the neutronisation burst in Figure 4.4.

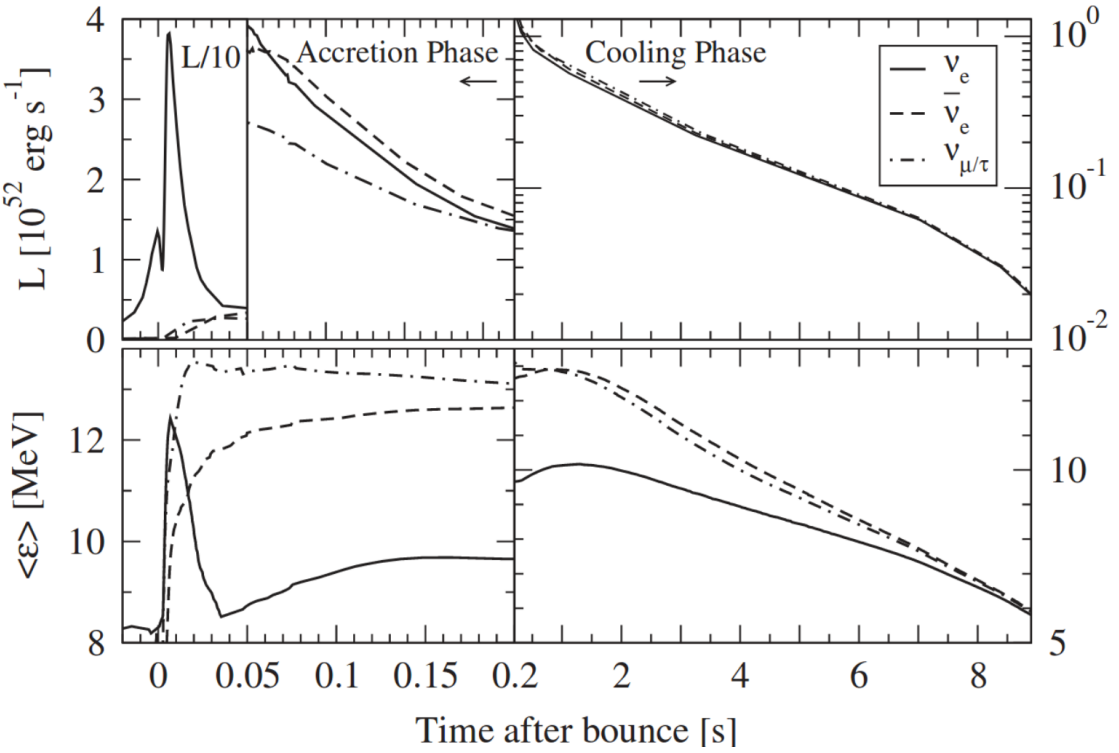

Figure 4.4: The neutrino emission from a core collapse supernovae. Neutrino oscillations are neglected. Taken from [76]. The top panel shows the total energy per second released as neutrinos (1 erg = 10^{-7} J). The bottom panel shows the mean neutrino energy for the various flavours.

4.3.3 The Core Bounce and Subsequent Neutronisation burst

As the surrounding matter falls in it becomes dense enough to block any neutrino transmission, the core continues to fall inwards past nuclear matter density. Eventually, the repulsive part of the strong nuclear force takes over causing the inward-falling matter to bounce outwards, forming an outwards shockwave, the shockwave breaks down the nuclei in the core into free nucleons. The free electrons capture on the liberated protons creating the neutronisation peak (the large peak of electron flavour neutrinos seen in Figure 4.4). The breakdown of the nuclei uses up a large amount of the shockwaves energy and it slows before it stops propagating outwards completely. The neutrinos produced in the neutronisation burst have not yet been able to leave the core before the shock stalls [73] and do not cause the shockfront to stop.

4.3.4 The Neutrino Heating Mechanism

After the shockfront stops it begins to fall inwards under gravity. The still proton and electron rich PNS continues to release neutrinos of all flavours via pair production processes and nucleon bremsstrahlung. During the accretion phase the PNS is still rich in

protons and electrons, electron captures on protons create ν_e and positrons produced in pair production processes can capture on neutrons to produce an additional $\bar{\nu}_e$ flux, this results in the slightly increased luminosity of ν_e and $\bar{\nu}_e$ compared to ν_x (which collectively denotes ν_μ and ν_τ neutrinos for reasons described below) seen towards the end of the accretion phase in Figure 4.4. At early times the PNS has a high electron (and ν_e) degeneracy pressure so the $e^- e^+$ and $\nu_e \bar{\nu}_e$ pair production processes are suppressed resulting in a slower rise time of $\bar{\nu}_e$ in the accretion phase compared to ν_x [81].

As the neutrinos move outwards, they scatter frequently until the density of the surrounding matter is low enough for their scattering length to exceed the radius of the star and they can exit freely. The scattering results in a transfer of energy from the neutrinos to the surrounding matter. The energy transferred to the matter by the neutrinos causes an increase in temperature of the inward-falling matter causing it to expand outwards and reviving the explosion.

$$\nu + X \rightarrow \nu' + X \tag{4.2}$$

$$\nu_e + n \rightarrow p + e^- \tag{4.3}$$

$$\bar{\nu}_e + p \rightarrow n + e^+ \tag{4.4}$$

The neutrino heating takes place via the interactions shown in Eqs. 4.2 to 4.4. The temperature of the core is not hot enough to readily generate neutrinos with high enough energies to create μ and τ particles via charged current interactions[3], so only the neutral current scattering indicated in Eq. 4.2 takes place. Often these flavours and their antiparticles are grouped together and denoted as ν_x. It should be noted that the interaction cross section of ν_μ, ν_τ and their antiparticles do differ slightly [83], which may have an effect on the explosion dynamics. However, currently there is no experimental method to distinguish neutrinos and their antiparticles via neutral current interactions. In contrast to the muon and tau flavour neutrinos, the electron flavour neutrinos can interact via the additional channels shown in Eqs. 4.3 and 4.4 resulting in an increased coupling to matter [84] [73].

[3]More recent simulations have taken into account muon production [82]

4.3.5 The Neutrino Energy Spectra

Previously it was thought that the increased electron flavour coupling would result in a neutrino spectrum with energy hierarchy $\langle \nu_e \rangle < \langle \bar{\nu}_e \rangle < \langle \nu_x \rangle$ [85]. The difference in the mean ν_e and $\bar{\nu}_e$ energies being caused by the excess of neutrons surrounding the core after the neutronisation burst. However, more recent simulations have shown average energies with a time dependent hierarchy $\langle \nu_e \rangle < \langle \bar{\nu}_e \rangle \approx \langle \nu_x \rangle$ [86]. At early times before the neutronisation of the core the interaction in Eq. 4.4 can occur readily, resulting in a lower $\langle \bar{\nu}_e \rangle$ between t=0 and t=0.2 in Figure 4.4 (t=0 or t_0 is defined as the point of core bounce). However, as the explosion continues and the core becomes increasingly more neutronised, the reaction becomes increasingly Pauli blocked and the only interaction channels available are the neutral current interactions. Therefore, the mean energy is similar to that of the ν_x as seen for t ¿0.2 s. After the neutronisation burst, there are a large number of neutron targets and the interaction shown in Eq. 4.3 results in an increased coupling between the core of the star and the escaping neutrinos. This increased coupling results in a lower emission energy than for $\bar{\nu}_e$ and ν_x. Eventually at very late times, greater than 6 seconds post bounce in Figure 4.4, this charged current process for ν_e becomes Pauli blocked by electron degeneracy pressure leaving only the neutral current interactions and the average energy becomes similar to that of the $\bar{\nu}_e$ and the ν_x.

4.4 Pair Instability Supernovae

For very massive stars $M > 70 M_{\odot}$, when temperature in the core exceeds 10^9 K, photons in the core have high enough energy to pair produce positrons and electrons as shown in Eq. 4.5.

$$\gamma \rightarrow e^+ e^- \tag{4.5}$$

The thermal energy of the core is converted to the rest mass energy of the positrons and electrons and a sharp temperature drop in the core occurs. The core then collapses inwards rapidly due to the large mass of the progenitor. This causes a rapid temperature increase and the explosive fusion of heavier elements in the core.

For the lightest pair production supernovae with masses in between $70 M_{\odot}$ and $140 M_{\odot}$ the explosive fusion is not large enough to cause a total explosion of the star [87]. Instead only the outer layers are ejected, this process results in a series of bursts with a periods of 1 to 10.000 yr [88], the luminosity of these bursts roughly scales with mass [87]. The

stars end up having very large iron cores and often end up collapsing to black holes [88]. For progenitors in between $140M_{\odot}$ and $260M_{\odot}$, the initial instability interaction causes a burst strong enough to cause the star to explode [88] [73].

For very massive stars ($M > 260M_{\odot}$) the neutrino pair production produces a collapse straight to a black hole, the reignition of fusion is not enough to overcome the inwards gravitational pull of such massive progenitors [89]. If the core is very heavy, photodisintegration can occur reducing the core temperature and causes a collapse straight to black hole [90][89].

In the case of rotating progenitors, if a black hole is formed the surrounding accretion disc can produce a large number of neutrinos $\mathrm{O}(10^{55}\,\mathrm{erg})$ over a period of a few seconds [91] [73].

4.5 Simulations of Supernovae

Simulations of supernovae in 1D have only resulted in explosions for the lowest mass progenitors which undergo electron core collapse as described in Section 4.2. For more massive Fe core collapse progenitors, no 1D simulation could produce an explosion with just neutrino heating of the outer core [92]. Several mechanisms exist in multidimensional simulations, which were not possible in simple 1D simulations. In multidimensional simulations, plumes of neutrino heated matter are produced. This convection increases the time that matter spends in the neutrino heating layer and transfers energy to the shock front fuelling the explosion [93] [94]. The neutrino heated plumes can be seen in Figure 4.5.

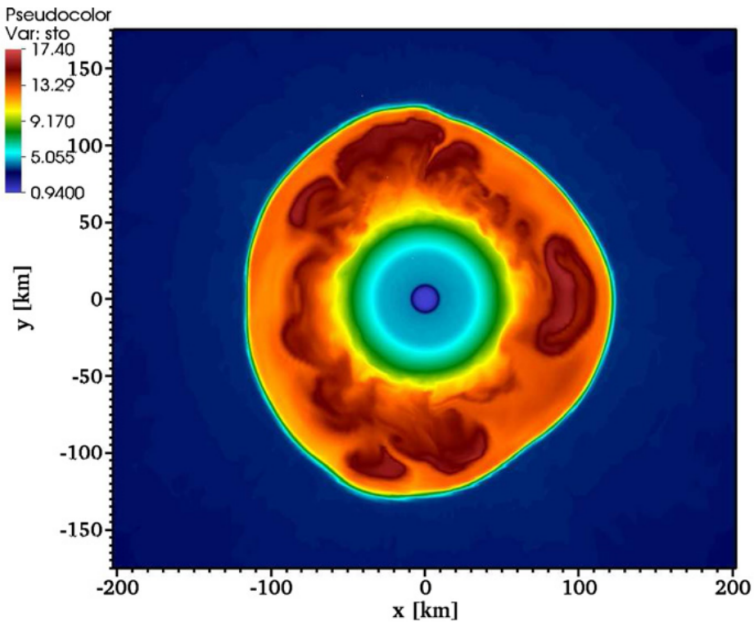

Figure 4.5: Entropy heat map of a 2D slice of a 3D supernovae simulation. The neutrino heated plumes can be seen as the dark red plumes. The central purple region is the proto neutron star. The inner blue region is the cooling region where the scattering of neutrinos cools the matter and heats up the neutrinos. The green band is known as the gain radius where the cooling and heating rate of the neutrinos is balanced. The light blue band surrounding the red region is the shock front. Taken from [95].

Another phenomena seen in 2D simulations is known as SASI (Standing Accretion Shock Instability [96]). As accreting matter meets the shock front, it pushes it inwards and in response an acoustic wave is generated within the dense region of the PNS back towards the shock front. The produced acoustic wave produces further deformation in the accreting region, resulting in an feedback loop with exponentially increasing amplitude. The same effect can be demonstrated in simple tabletop water based experiments [97]. To initiate SASI a small inhomogeneity in the accreting matter must occur, this could be provided by infalling matter [96]. Simulations of SASI instabilities in 3D result in spiralling modes of the accreting matter and can possibly explain the production of pulsars without a initially rotating star [98]. SASI instabilities also can increase the efficiency of energy transfer from the neutrinos to matter aiding the explosion [99].

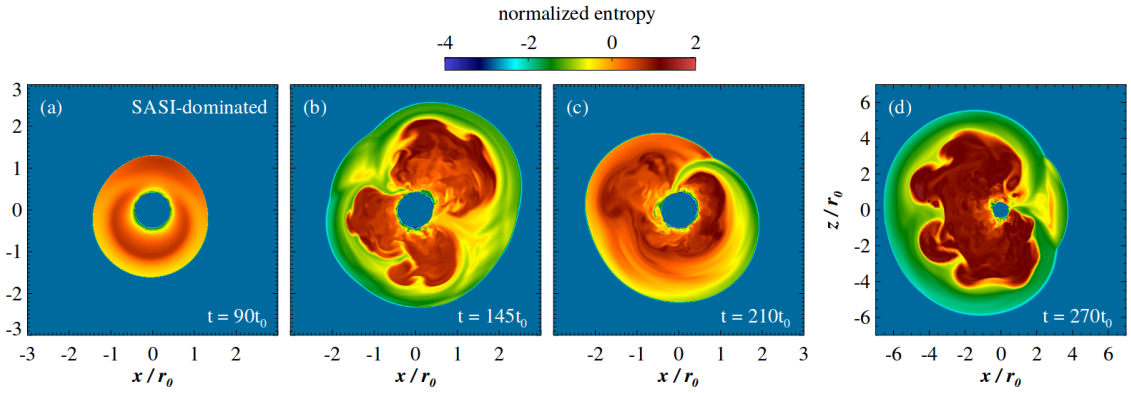

Figure 4.6: 2D slice of a supernovae simulation at various times. Pictures a and b show a sloshing mode SASI where the volume surrounding the core moves back and forth in an axis. Pictures c and d show a spiral mode SASI which is thought to produce pulsars. In d the shock front runaway has started after neutrino heating. $r_0 = 100$ km and $t_0 = 1.7$ ms. Taken from [100].

SASI also has an effect on the amount of matter infalling on to the protoneutron star this in turn effects the neutrino flux emitted from the star. The SASI effects have been shown to cause modulations in the event rate expected to be seen in large water Cherenkov detectors like IceCube [101]. The size of the modulations is effected by how close to the plane of SASI sloshing the detectors are positioned. The left panel in Figure 4.7 shows the maximal modulation in the IceCube detector, which occurs when the detector is on the plane of SASI oscillations. The right panel shows minimal modulation which occurs when the detector is perpendicular to the plane of the initial SASI oscillations. The drop in luminosity seen at 250 ms is associated with moving from one fusion shell to another and alters the plane of SASI oscillations, this is why the oscillations appear reduced in the left panel and enhanced in the right panel. The effect from SASI is very small, the SNO+ detector will not be sensitive to this phenomena, even the much larger proposed Hyper-K experiment will have limited sensitivity. Only the very large IceCube experiment will have a reasonable change of observing this effect.

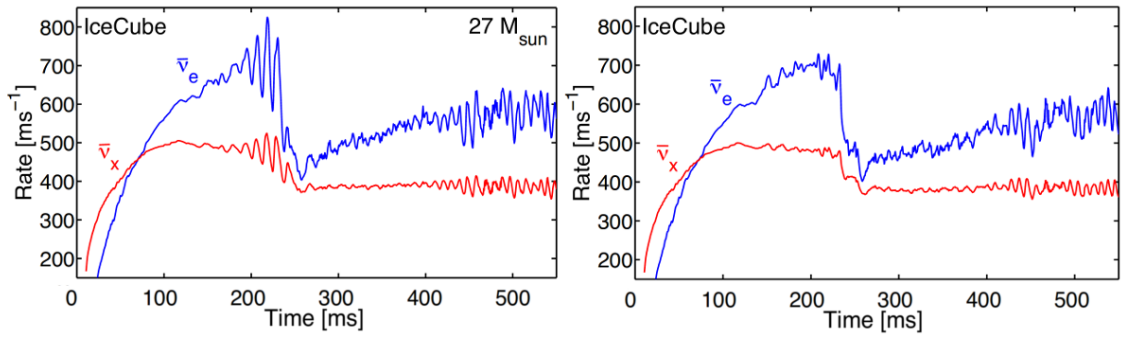

Figure 4.7: Expected event rate as a function of time for IceCube for a supernovae $27M_{\odot}$ at 10 kpc with SASI. The left panel shows when the detector is on the plane of the SASI modulations, the right panel shows when the detector is perpendicular to the plane of SASI oscillations. Modified from the plots in [101].

A more recent phenomena seen in 3D simulations is known as LESA (Lepton-number Emission Self-sustained Asymmetry [102]). The effect produces an asymmetry in emission of ν_e and $\bar{\nu}_e$ at approximately the 10%-20% level. The effect is thought to be caused by interactions between the neutrinos and matter close to the core of the star. If there is a small asymmetry in lepton number in the core then in one direction anti-neutrinos will be emitted favourably to the opposite direction. As the interaction between the electron anti neutrinos and surrounding matter is slightly stronger than that of the electron neutrinos, the shock front is pushed out slightly further in the direction of excessive $\bar{\nu}_e$ emission. This in turn deflects more matter towards the opposite hemisphere increasing the lepton number on that side. Furthermore, the increased accretion on this hemisphere causes increased convection of lepton rich matter from the core of the star maintaining the lepton number asymmetry and also the emission dipole. Currently LESA is an area under study to verify that it is not caused by any numerical approximations made in simulations [72].

4.6 Neutrino Oscillations in Supernovae

In the previous sections, we have not considered any neutrino oscillation effects on the neutrino spectrum. It turns out that the interactions of the neutrinos with the matter can have a significant effect on the spectrum and result in a full flavour conversion of the emitted neutrinos. Furthermore, at the core of the supernovae the neutrino density is so high that neutrino neutrino interactions must also be considered [103].

4.6.1 Neutrino Matter Interaction

As neutrinos propagate from the core of the exploding star to its edge, neutrinos interact with the matter enabling oscillations via the MSW effect, as shown in Eq. 2.13. Due to the high densities inside a supernovae, two MSW resonances can occur: the H resonance occurs when the potential term V is equal to the larger (atmospheric) mass splitting, the L resonance occurs when the potential term is equal to the solar mass splitting [104]. As there is a large difference in the atmospheric mass splitting and the solar mass splitting the regions of the star in which these resonances occur are separated hence a study can be approximated by the two flavour MSW effect.

Over time the position and size of the shock fronts varies and the neutrino mechanism is intrinsically coupled with the burst itself. Hence, it is difficult to uncouple any oscillation effects across the entire burst. The following results look at early times in the burst where large matter discontinuities have not had a chance to build up and the behaviour of the SN is relatively model independent.

Effect on the Neutronisation burst

The neutronisation burst is described as a standard candle of the SN burst and is unaffected by the mass of the progenitor [105] [106]. Modern simulations using different equations of state result in approximately 2% differences in the peak of the neutronisation burst [107]. Furthermore, as the neutronisation burst occurs before a sufficiently dense shock front has been created and the MSW effect can be approximated in an adiabatic way provided that $\sin^2\theta_{13} > 10^{-3}$ [105]. Neutrino self interactions described in the next section will also have no effect on the oscillation probabilities [72].

The resonant MSW effect seen here is similar to that of the solar neutrinos and shown in Figure 2.1. At the core of the supernovae, where the electron density is high enough, electron flavour neutrinos will be born in the highest energy mass eigenstate in the three flavour regime. In the normal hierarchy this is labeled ν_3, whereas in the inverted hierarchy the heaviest mass eigenstate will be ν_2 as shown in Figure 2.3. The neutrinos will then propagate to the edge of the star in this mass eigenstate. If the neutrino hierarchy is normal and the neutronisation burst ν_e leave the star as ν_3 then they will be detected at Earth as mainly ν_μ and ν_τ and the neutronisation burst will be heavily suppressed due to the small ν_e component of ν_3. If the neutrino hierarchy is inverted, then the neutronisation burst will be somewhat suppressed but not completely due to the larger proportion of ν_e in ν_2. The mixture of electron neutrinos seen at the Earth is shown in

Eqs. 4.6 and 4.7 [105] [104] where F_ν is the flux of a certain neutrino flavour seen at the Earth and F_ν^0 is the neutrino flux produced in the burst. The neutrino flux at the surface of a progenitor in for either mass hierarchy and in the no oscillations case can be seen in Figure 4.8.

$$F_{\nu_e} = F^0_{\nu_x} \qquad \text{(Normal Hierarchy)} \tag{4.6}$$

$$F_{\nu_e} = \sin^2\theta_{12} F^0_{\nu_e} + \cos^2\theta_{12} F^0_{\nu_x} \qquad \text{(Inverted Hierarchy)} \tag{4.7}$$

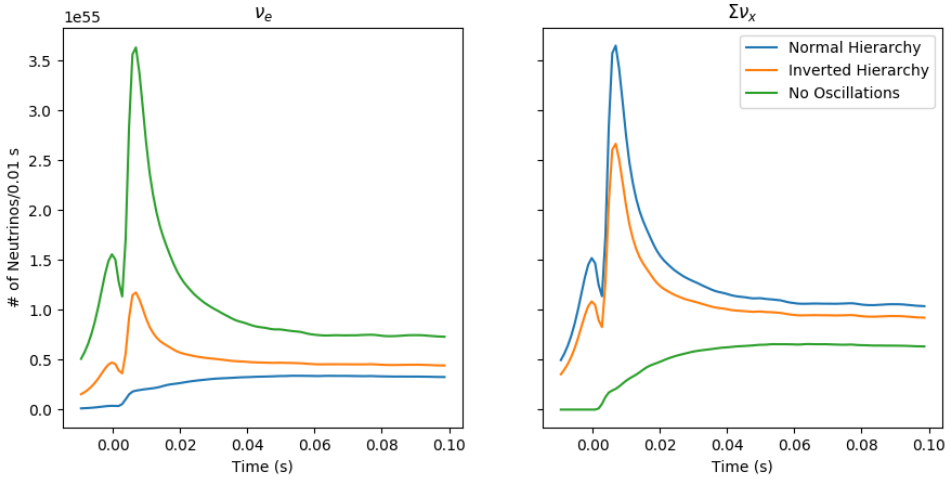

Figure 4.8: The ν_e and $\sum \nu_x$ flux produced from the surface of the progenitor during the time surrounding the core bounce. The fluences are shown for either mass hierarchy and the no oscillation case.

Neutrino Rise Time

As mentioned previously, the rise time of the luminosities of ν_x and $\bar{\nu}_e$ during the accretion phase is different. This effect is much more prominent in larger mass stars due to the longer accretion phase in an Fe-core collapse supernovae (which lasts up to approximately 0.1 s) [108]. Furthermore, the slower density variation of the Fe-core produces an increased suppression of collective neutrino oscillations (described in the next section) due to the matter effect [108]. Figure 4.9 shows the density of the SN as a function of radius. At small times, the shock front is behind the resonance region, which allows one to assume an adiabatic transition. At later times, the shock front begins to cross the resonance region and the matter effect can no longer be considered adiabatically.

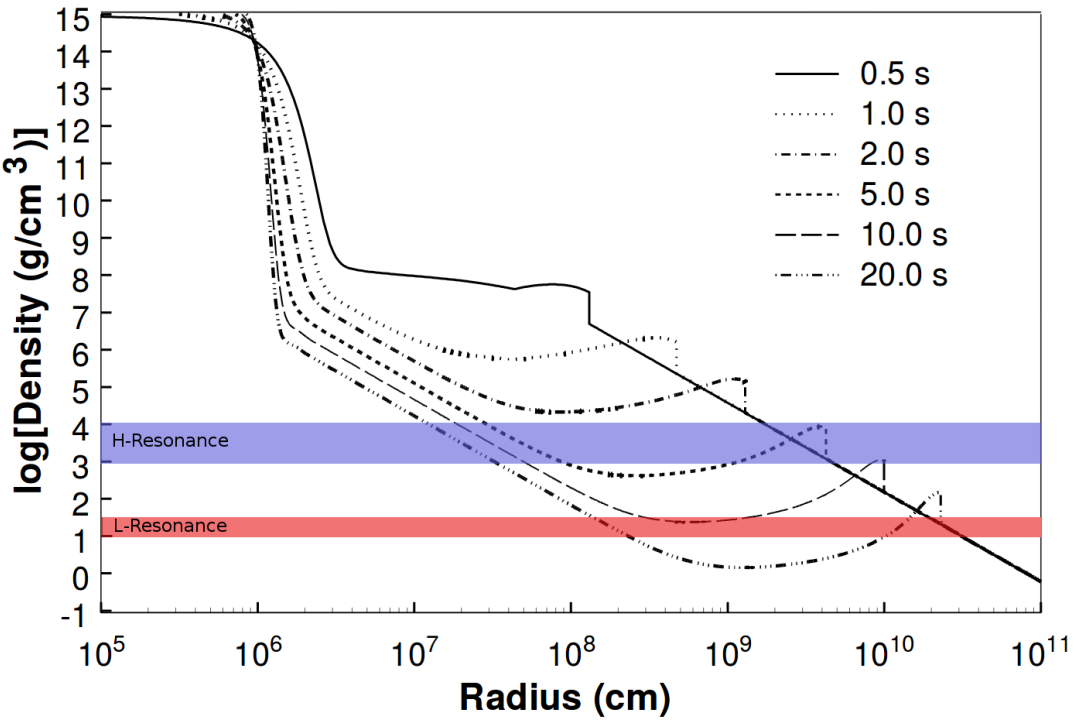

Figure 4.9: The density profile of a supernovae at different stages in the explosion, the sharp discontinuity in the plot which varies with time is the shock front, the sharp discontinuity at 10×10^6 cm is the surface of the PNS, also shown is the MSW resonance layers. The H-resonance corresponds to the atmospheric splitting. The L-resonance corresponds to the solar splitting. Resonance densities obtained from [104]. Plot modified from [109].

For anti-neutrinos the MSW potential gains a minus sign, so $\bar{\nu}_e$ will be in the mass eigenstate ν_1 in the normal hierarchy and ν_3 in the inverted hierarchy. Assuming adiabatic propagation of the neutrinos in the normal hierarchy the $\bar{\nu}_e$ will arrive as ν_x in the inverted hierarchy and a mixture of $\bar{\nu}_e$ and ν_x as seen in Eqs. 4.8 to 4.11 [105] [104], the factor 4 in Eqs. 4.9 and 4.11 accounts for the summing up of the four non electron flavour neutrinos.

$$F_{\bar{\nu}_e} = \cos^2\theta_{12} F^0_{\bar{\nu}_e} + \sin^2\theta_{12} F^0_{\nu_x} \qquad \text{(Normal Hierarchy)} \tag{4.8}$$

$$4F_{\nu_x} = F^0_{\nu_e} + \sin^2\theta_{12} F^0_{\bar{\nu}_e} + (2 + \cos^2\theta_{12}) F^0_{\nu_x} \qquad \text{(Normal Hierarchy)} \tag{4.9}$$

$$F_{\bar{\nu}_e} = F^0_{\nu_x} \qquad \text{(Inverted Hierarchy)} \tag{4.10}$$

$$4F_{\nu_x} = \cos^2\theta_{12} F^0_{\nu_e} + F^0_{\bar{\nu}_e} + (2 + \sin^2\theta_{12}) F^0_{\nu_x} \qquad \text{(Inverted Hierarchy)} \tag{4.11}$$

The event rates in IceCube (which are mainly determined by the $\bar{\nu}_e$ IBD interaction) for various progenitor models in both mass hierarchies are shown in Figure 4.10. For all models the rise time is distinguishable based on the hierarchy.

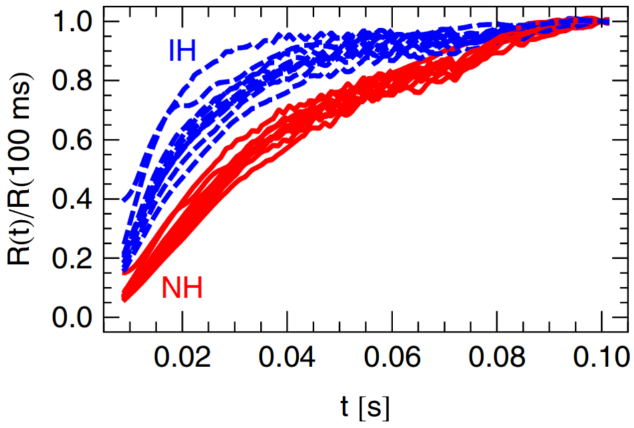

Figure 4.10: The event rates in the IceCube detector during the accretion phase of the Supernovae as a function in time for various models. The event rate is dominated by the IBD interaction Taken from [81].

Earth Matter Effects

The Earth can also produce matter effects on the spectrum if it shadows the SN burst [104], i.e. the neutrinos have to pass through the Earth before being detected, which has a probability of approximately 0.5. The standard MSW matter effect will alter the spectrum of the neutrinos. The Earth effect will only alter the neutrinos in the inverted hierarchy and only the anti-neutrinos in the normal hierarchy. This is due to the fact that in the normal hierarchy the neutrinos (in the early phases of the burst) will arrive as ν_3 matter eigenstate and due to its small mixing with the ν_e state the matter effect will be negligible and the flux will be the same as shown in Eq. 4.6 after passing through the Earth. The same principle applies for $\bar{\nu}_e$ in the inverted hierarchy.

The flux seen by the neutrinos after passing through a distance L through the mantle of the Earth is shown in Eqs. 4.12 and 4.13 [110] [104].

$$\begin{aligned} F^{\oplus}_{\nu_e} = & \sin^2\theta_{12} F^0_{\nu_e} + \cos^2\theta_{12} F^0_{\nu_x} \\ & + (F^0_{\nu_e} - F_{\nu_x}) \sin(2\theta^m_{12} - 2\theta_{12}) \sin^2\left(\frac{\Delta m^2_{12} \sin(2\theta_{12})/\sin(2\theta^m_{12})}{10^{-5}\mathrm{eV}^2} \frac{L}{10^3\mathrm{km}} y\right) \end{aligned} \tag{4.12}$$

(Inverted Hierarchy)

$$F^{\oplus}_{\bar{\nu}_e} = \cos^2\theta_{12}F^0_{\bar{\nu}_e} + \sin^2\theta_{12}F^0_{\bar{\nu}_x}$$
$$+(F^0_{\bar{\nu}_e} - F_{\bar{\nu}_x})\sin\left(2\bar{\theta}^m_{12} - 2\theta_{12}\right)\sin^2\left(\frac{\Delta m^2_{12}\sin(2\theta_{12})/\sin(2\theta^m_{12})}{10^{-5}\mathrm{eV}^2}\frac{L}{10^3\mathrm{km}}y\right) \quad (4.13)$$

(Normal Hierarchy)

$$y = \frac{12.5\mathrm{MeV}}{E} \quad (4.14)$$

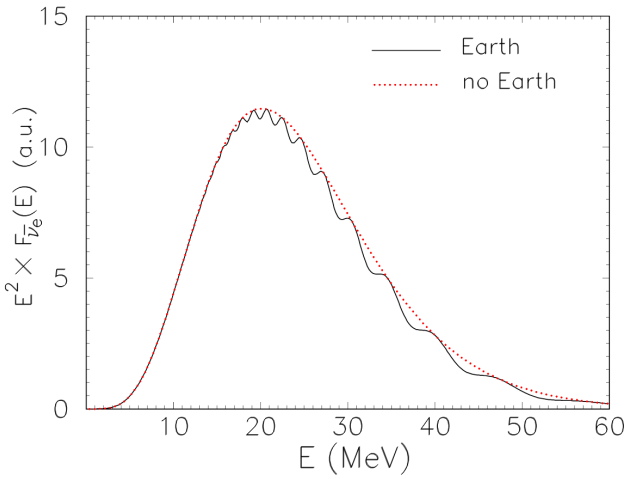

Figure 4.11: The effect of the Earth on the SN spectrum detected via the IBD interaction (Assuming a normal mass hierarchy). Taken from [72].

The flux after passing through the Earth will have an oscillatory energy dependence due to the third terms in both Eqs. 4.12 and 4.13 as shown in Figure 4.11. It has been proposed to perform a Fourier analysis on the spectrum of the neutrinos detected from a supernovae burst with a single detector in order to determine the mass hierarchy [111], although more recent simulations of the supernovae have revealed this is not possible even for next generation detectors (DUNE, Hyper-K, LENA) at 10 kpc, due to the cooler spectrum of neutrinos. A determination of the mass hierarchy would only be possible at a few kpc or closer for an Argon TPC [110]. This study also looked at the sensitivity when combining the results of two large water Cherenkov detectors (Hyper-K and IceCube), with one being unshadowed by the Earth and found even at 0.2 kpc the change in the ratio of events due to Earth matter effects was 1.7 %.

4.6.2 Neutrino Self Interactions

Another effect on the supernovae spectrum is the effect of neutrino neutrino scattering via the exchange of a Z boson. At the core of a supernovae, the neutrino number density is high enough such that these scatterings become common enough to produce an MSW like effect. Each individual neutrino has an additional potential term due to all the other neutrinos in the core. The potential behaves in the same way as the electron potential shown in Eq 2.9. This neutrino-neutrino potential is shown in Eq. 4.15. The neutrino neutrino interactions also alter the spectrum produced via the pair production process: $\nu_e\bar{\nu}_e \rightarrow \nu_x\bar{\nu}_x$. The interaction term between neutrinos is thought to cause coherent oscillations of neutrinos with the same frequency [112].

$$\mu \propto (1 - v_i \cdot v_j) \tag{4.15}$$

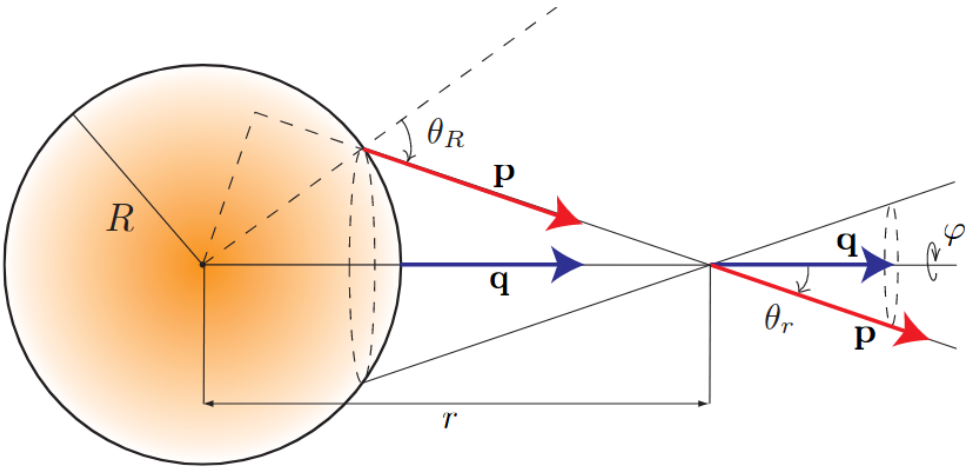

Figure 4.12: Schematic of the neutrino neutrino interactions present in a supernovae burst. Taken from [72].

The dense core produced during a Fe-core collapse suppresses neutrino-neutrino induced oscillation at early times during the burst. The neutrino-neutrino potential effects all flavours equally and acts to make all oscillations have the same frequency and oscillate coherently. The neutrino flux at a given point within the core will be made up of neutrinos which were created with different momenta and at different radii within the core. The path length of each neutrino will be different. This can be seen in Figure 4.12: the propagation length of neutrino **p** is longer than that of neutrino **q** before the neutrinos interact. Due to the matter the oscillation phases will significantly differ. The coherence caused by the neutrino self interactions is overwhelmed by the decoherence caused by dense matter [108].

This is not the case for lighter electron core collapse supernovae due to their less dense cores. Transformations via the pair production process are also suppressed due to the low number of $\bar{\nu}_e$ surrounding the core at early post bounce times [112] [113]. The neutronisation burst is unaffected by the neutrino neutrino interactions as the initial flux is largely made up of electron flavour neutrinos [72].

The signature produced by neutrino neutrino interactions are known as spectral splits and swaps. In simple singular angle approximations (where θ_R in Figure 4.12 is given a fixed value) the effect was only seen in the inverted neutrino hierarchy, with little alteration to the spectra in the normal hierarchy [72]. However, more recent multi-angle calculations (where θ_R in Figure 4.12 is allowed to vary) have shown that the process is possible in either hierarchy, although the features differ depending on the hierarchy seen in Figure 4.13.

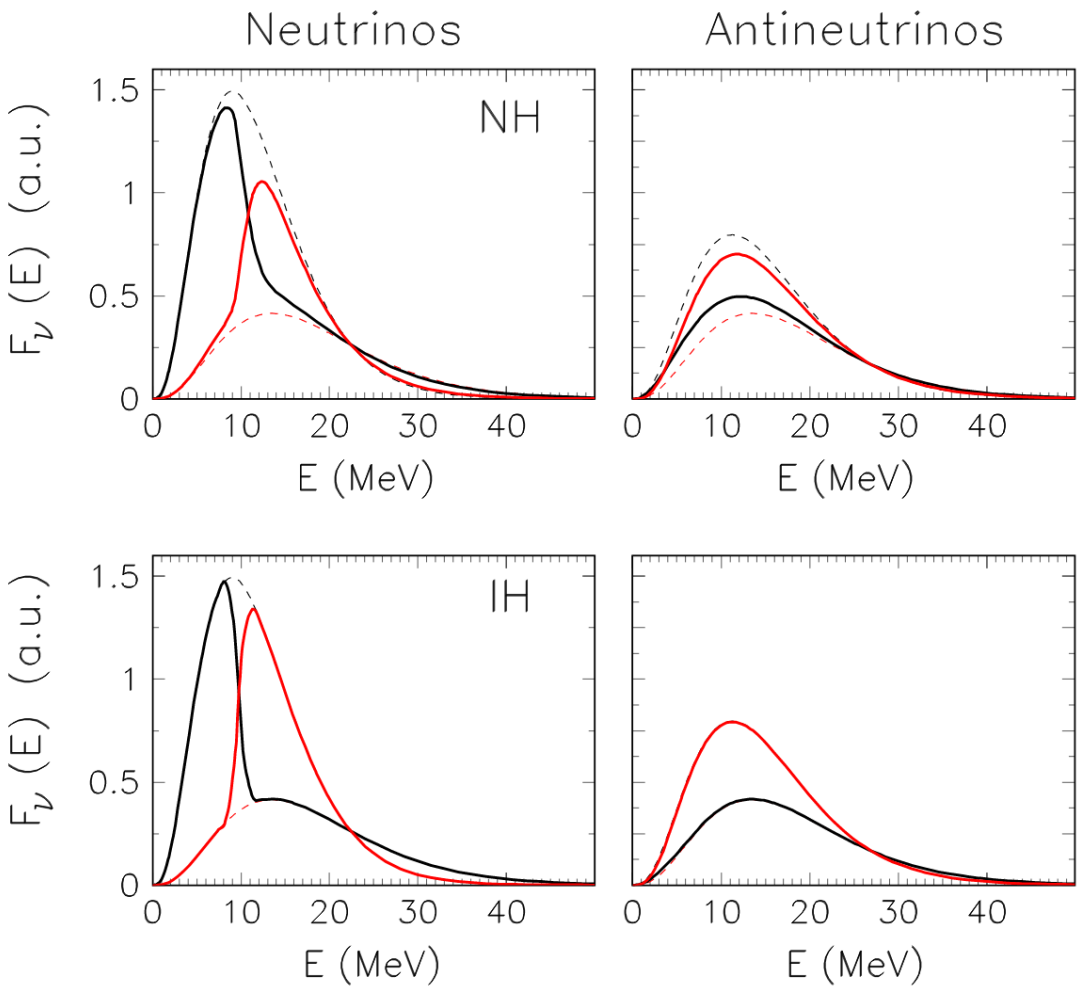

Figure 4.13: Collective oscillation effects using a multi angle calculation. The dashed lines indicate the unaltered flux. The solid lines indicate the flux after collective oscillations. The black lines correspond to ν_e the red lines correspond to ν_x. Taken from [114].

A spectral swap is characterised by the exchange of the two flavours across the neutrino

spectrum from the supernovae. A complete spectral swap can be seen in the lower right panel of Figure 4.13; the initial $\bar{\nu}_e$ flux has been completely swapped with the $\bar{\nu}_x$ flux. A partial swap is shown in the upper right panel.

A spectral split is characterised by the swapping of the spectrum around a certain energy value (in the case of Figure 4.13 around 10 MeV). In the inverted hierarchy case the splitting is complete. At energies higher than the splitting energy the spectra are completely swapped, whereas in the normal hierarchy the splitting is only partial.

Neutrino-neutrino interactions are still an active area of research and further detail on these effects and the sensitivity of SNO+ to these effects can be found in [115].

4.7 Distribution of Galactic Supernovae

4.7.1 Distance distribution

The calculated distance distribution of supernovae in from the Sun be seen in Figure 4.14. The distribution is peaked at approximately 9 kpc, corresponding to the central region of the Milky Way. (The centre of the Milky Way was assumed to be 8.7 kpc when producing Figure 4.14). More recent studies place the distance from the Sun to the centre at (8.2 ± 0.1) kpc [116], indicating the peak of the PDF in Figure 4.14 may in fact be at a smaller distance. Often the value of 10 kpc is used when determining a neutrino detector's response to a typical supernovae burst [117] [118] [48].

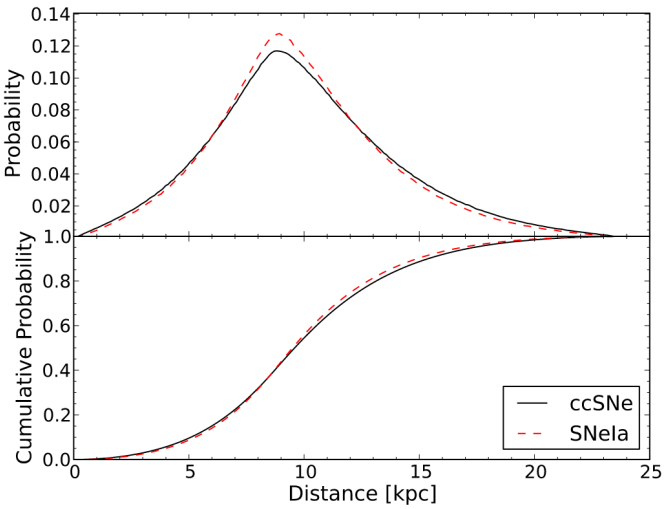

Figure 4.14: Modeled distance distribution of supernovae within the Milky Way. Taken from [119].

4.7.2 Time distribution

The rate of supernovae has been estimated using multiple methods. A study of supernovae in the last millennia revealed six possible candidates all within 5 kpc [120]. Usually only five are considered due to the poor recording of the candidate seen in 1658 [121] [119]. Older studies showed a SN rate of $2.5\pm^{0.8}_{0.5}$ per century [121]. More recent studies have shown a slightly increased rate of $3.4\pm^{7.8}_{2.5}$ [119] per century.

An estimate of the supernovae rate was also made by looking at the content of ^{26}Al within the Galaxy. ^{26}Al is produced in Supernovae explosions and has a half-life of 7.2×10^5 yr and decays with a 1.8 MeV γ emission. The rate obtained corresponded to a supernovae rate of 1.9 ± 1.1 per century [122]. Neutron star distributions can also be used to calculate the rate of core collapse supernovae, as neutron stars are produced in core collapse supernovae. The rate predicted from the neutron star distribution is significantly higher than other measurements with a value of 5.7 to 10.8 per century depending on the model used [123]. The rate of supernovae in other galaxies can also be used to predict a supernovae rate in the Milky Way. The Lick observatory supernovae search predicts a rate of 2.8 ± 0.6 per century using this method [124].

Various methods predict rates between 1 and 10 supernovae per century, the widely used rate for supernovae within the Milky way is one every 30 years.

4.8 Measurable Supernovae Properties with a Supernovae neutrino burst

As well as providing information on the mass hierarchy and other properties of neutrinos, the neutrino burst from a supernovae provides the unique opportunity to measure properties of the explosion mechanism and verify the effects seen in simulations. The detection of the neutrino signal several hours before the optical signal also can provide an early warning to astronomers.

4.8.1 SNEWS: Supernovae Early Warning System

The burst of neutrinos seen from SN1987A arrived two and a half hours before the optical signal was seen by astronomers [125]. SNEWS (SuperNovae Early Warning System) [126] is a collaboration of neutrino detectors designed to take advantage of the early arrival time of neutrinos to issue a warning to the astronomical community that a galactic supernovae is imminent and give them time to prepare . The rate of false alarms is designed to be 1

per century. This limit is obtained by checking for coincidences between experiments. If a SNEWS alert is issued, the position of the supernovae in the sky can then be estimated using Super-K to approximately 2.3° at a SN distance of 10 kpc [118], which may allow astronomers to identify a progenitor.

4.8.2 Composition of fusion shells of progenitor

As mentioned previously, the progenitor towards the end of its lifetime forms an onion like structure corresponding to fusion shells, closer to the core the shells are more dense to fuse heavier elements. During the accretion phase of the supernovae burst these shells subsequently fall onto the surface of the PNS, fuelling the neutrino emission. As subsequently less dense shells fall onto the Proto-Neutron Star (PNS), the rate of matter acretion drops and the neutrino luminosity decreases. The sharp drop seen at 250 ms in Figure 4.7 is associated with the transition from the Si burning shell to the O burning shell [101]. The distribution of these drops can therefore be used to determine the composition of the progenitor.

4.8.3 Measurement of the neutron star radius.

The total luminosity of neutrinos can be used to link the radius and the mass of the neutron star. The total binding energy $\mathcal{E}_B$ is given as the sum of the neutrino energies shown in Eq 4.16 [127].

$$\mathcal{E}_B = \mathcal{E}_{\nu_e} + \mathcal{E}_{\bar{\nu}_e} + 4\mathcal{E}_{\nu_x} \tag{4.16}$$

The link between the radius and the mass of the neutron star is given by Eq. 4.17, G is the gravitational constant, M and R is the mass and radius of the neutron star respectively. The limits on the mass of the neutron star can be obtained by comparing simulation results with the amount of ^{56}Ni ejected from the star [127] [128].

$$R = \frac{0.6GM^2}{\mathcal{E}_B} + \frac{r_s}{4} \tag{4.17}$$

r_s is the Schwarzschild radius given by Eq. 4.18.

$$r_s = 2\frac{GM}{c^2} \tag{4.18}$$

The Super-K experiment can measure the value of $\mathcal{E}_B$ to an relative accuracy of 11 % by counting the total number of events from a SN at 10 kpc. Assuming the total energy is split

equally between all flavours of neutrino, the accuracy improves to approximately 3 % [127]. It should be noted that this requires the distance to the supernovae to be known accurately via other means.

4.8.4 Black Hole Formation

The formation of a black hole can also can also produce interesting effects in the neutrino signal. For very massive stars the collapse inwards is straight to a black hole with no core bounce and no neutrino burst is detected. However, some massive stars (of order $40M_{\odot}$) can undergo a core bounce producing a neutrino burst. In this case, the accretion rate post bounce is high enough that the PNS collapses into a black hole 0.5 to 1.5 s post bounce (depending on the Equation Of State (EOS)) [129]. The neutrino spectra obtained from simulation show two significant differences from an Fe core collapse which produces a PNS. The most distinct difference is the sharp cut off of the neutrino signal, as shown in Figure 4.15 at 1.3 s, this is associated with the moment of black hole formation post bounce, it is expected that the neutrinosphere will be absorbed into the BH less than 1 ms after this point [129]. The second feature is the rise time in neutrino energies post bounce to much higher energies, with average energies reaching as high as 50 MeV (Shown in the left panel of Figure 4.15). This is associated with the increase in temperature of the PNS as it is compressed by the infalling matter.

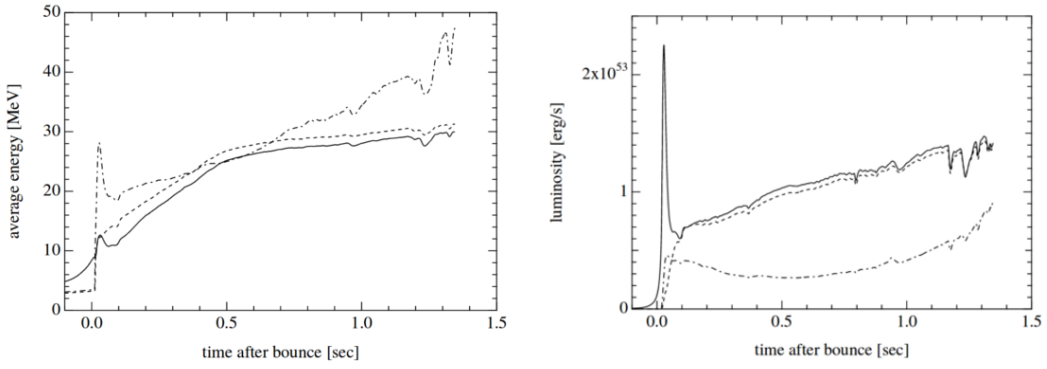

Figure 4.15: The neutrino spectra produced from a $40M_{\odot}$ progenitor using the Shen Equation of state [130]. The left panel shows the average energy of each flavour and the right hand plot shows the luminosity of each flavour. The solid line indicates ν_e the dashed line indicates $\bar{\nu_e}$ and the dash dotted line indicates ν_x Taken from [129].

4.9 SN1987A

The only detection of neutrinos associated with a supernovae occurred on the 24^{th} of February 1987. The burst was seen using optical telescopes and was a type II supernovae. The supernovae progenitor was Sanduleak-69 202 [131] located in the Large Magellenic Cloud approximately 50 kpc from Earth.

A signal was seen by four neutrino detectors on Earth: two water Cherenkov detectors and two liquid scintillator detectors. The water Cherenkov detectors Kamiokande-II [66] based in the Kamioka mine in Japan and the IMB [67] (Irvine-Michigan-Brookhaven) experiment located in a mine in Ohio. The two liquid scintillator detectors that saw a signal were the Baksan scintillation telescope [68] in southern Russia and the LSD experiment [132] at the Mont-Blanc laboratory in the Mont-Blanc road tunnel.

The Kamiokande experiment with a fiducial volume of 2.14 ktonne saw a total of 12 events with energies in the range 6.3 to 35.4 MeV. The IMB experiment had a fiducial volume of 3.3 ktonne. Unfortunately, one of the PMT power supplies was broken during the burst resulting in a higher energy threshold of approximately 20 MeV. The detector electronics also experienced significant dead time between events and a total of 8 events were seen, it was estimated that the total number of events inside the detector was 22 [67]. The Baksan experiment had a much lower fiducial volume of 0.2 ktonne, and detected neutrinos via IBD. It saw a total of 5 events. It should be noted that the backgrounds in Baksan were significantly higher than that of the two Cherenkov detectors and the burst itself could not be distinguished from random background coincidences without using the Cherenkov detectors to provide a time window.

The most accurate timing was given by the IMB experiment, which had a resolution of 50 ms. The uncertainty on the Kamiokande experiment was 1 minute. The Baksan scintillation telescope had a design time resolution of 2 s. It was discovered the clock recording the time of events had shifted by 54 s. Taking this error into account, the events were still consistent with those seen by the IMB and Kamiokande experiments. The distribution of the events associated with SN1987A in these three detectors can be seen in Figure 4.16.

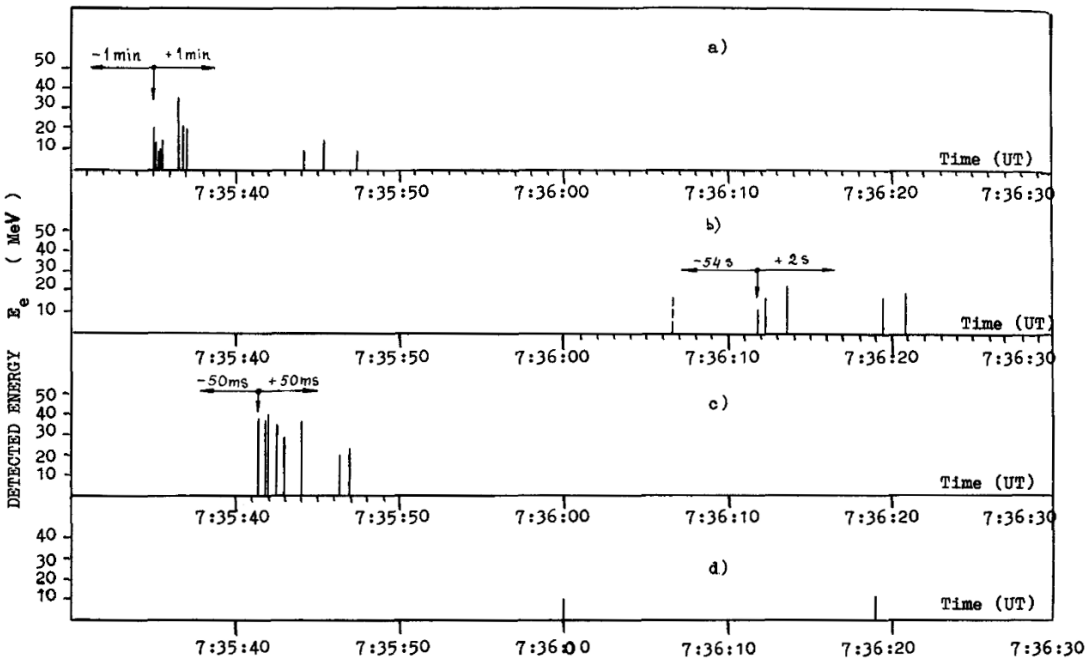

Figure 4.16: The distribution of events associated with SN1987A in the Kamiokande (a), IMB (b), and Baksan (c) experiments. Panel (d) shows the LSD events during the same period. Taken from [68].

The burst of events detected by the LSD experiment were detected 4 hours and 47 minutes before the other detectors. Some authors claim that this event was in coincidence with gravitational wave detection [133] [134] [135], although their statistical method has been strongly disputed [136]. Models have been made involving fast rotating progenitors to explain the delayed mechanism [137]. Although generally the LSD signal and any associated gravitational wave signal was considered a random coincidence by the scientific community.

SN1987A also provided valuable information about neutrinos. By looking at the spectrum of neutrinos and their spread a new limit was set on the neutrino masses [138]. The comparison of the neutrino and optical signal also provided tests of special relativity [139].

4.10 The Diffuse SN-ν background

SN1987A proved that certain supernovae can produce neutrinos. As supernovae have been occurring throughout the universe at an estimated rate of 3 Hz [140], there is an isotropic background of O(MeV) neutrinos associated with these past SN. The background is known as the Diffuse Supernovae Neutrino Background (DSNB) [141].

The differential DSNB flux for neutrinos of energy E_ν when seen at a detector is shown

in Eq. 4.19 [141], the first term is the average neutrino flux from a supernovae ϕ the $(1+z)$ terms account for the redshift of the spectra. It should be noted that there is no intrinsic distance factor within the distance integral, this is because the flux seen at a distance r goes as $1/r^2$, whereas the volume increases as $r^2 d\Omega$ where Ω is the solid angle. The second term $R_{\rm SN}(z)$ indicates the rate of supernovae as a function of distance and the final term is a correction applied due the expansion of the universe [141] (and is understood with negligible uncertainty).

$$\frac{d\phi(E_\nu)}{dE_\nu} = \int_0^\infty \left[(1+z)\phi(1+z)\right]\left[R_{\rm SN}(z)\right]\left[\frac{cdt}{dz}dz\right] \tag{4.19}$$

The rate of supernovae is determined from the star formation rate and the mass distribution of stars and is in Eq. 4.20 [141] where R_{SF} is the well measured rate of star formation [142]. Current measurements show the optically detected supernovae rate significantly differs from this predicted rate [143]. It is thought that this discrepancy is caused by supernovae being obscured by dust [144], or an increased proportion of dim supernovae [143]. A measurement of the DSNB could support or discredit this hypothesis. Searches for disappearances of bright progenitors are also underway to determine the number of optically dark but neutrino bright supernovae [145].

$$R_{\rm SN}(z) \approx \frac{R_{\rm SF}(z)}{143 M_\odot} \tag{4.20}$$

The current best limit on the DSNB was set by Super-K [146]. The current exclusion limit set by Super-K and the exclusion limit after six years of running with a Gd-loaded Super-K is shown in Figure 4.18. Assuming a SN rate of 10 Hz in the universe and the SN 1987A energy spectra the total DSNB interaction rate in Super-K is approximately $3\,{\rm yr}^{-1}$ [141]. Despite the fact that the only background to the DSNB is other neutrino sources, currently there isn't the statistics to resolve these from the other backgrounds. The main background in Super-K are low energy atmospheric ν_μ which produce μ below the Cherenkov threshold that the subsequently produce a Michel electron above the Cherenkov threshold. Low energy atmospheric ν CC and NC scattering also contribute to the backgrounds. Another small background is caused by μ and π particles [146].

Work is underway to load Super-K with Gd greatly enhancing the sensitivity to $\bar{\nu}_e$. A search for the DSNB will then only have backgrounds due to reactor neutrinos, and low energy atmospheric antineutrinos, as shown in Figure 4.17. It should be noted that

more modern estimates of the DSNB shift the signal towards the upper edge of the band [147] [148].

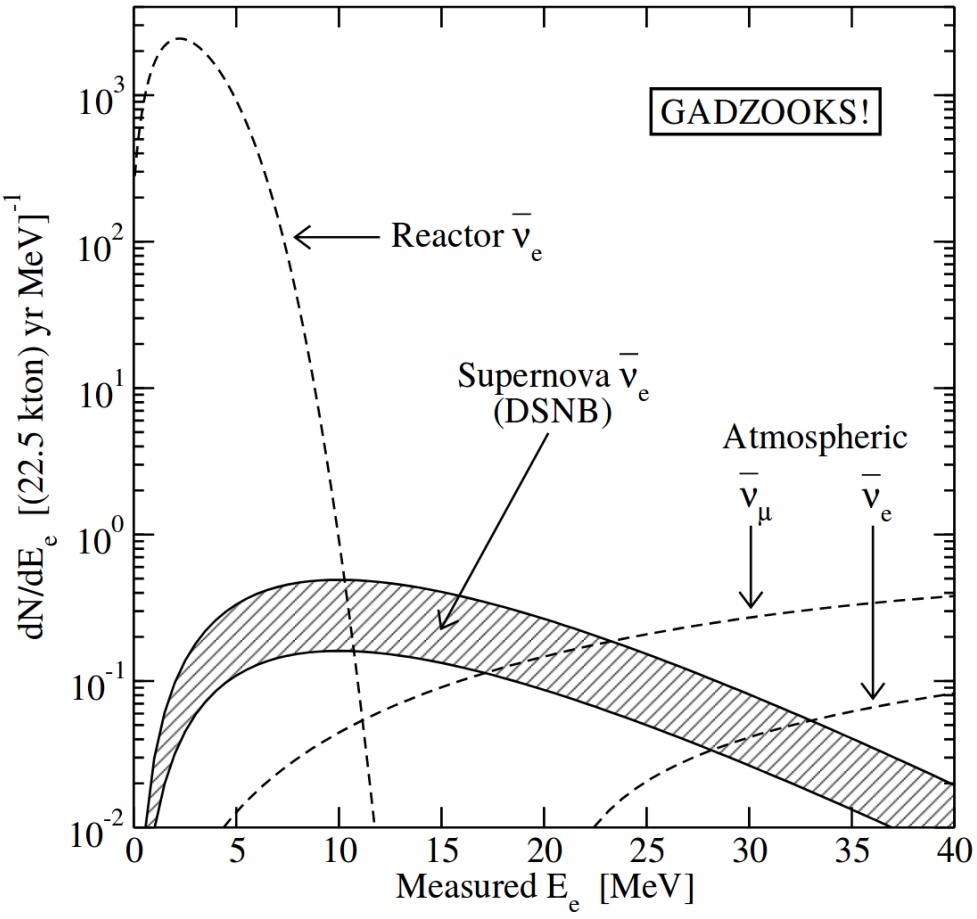

Figure 4.17: The backgrounds to the DSNB and the expected signal itself. Taken from [149].

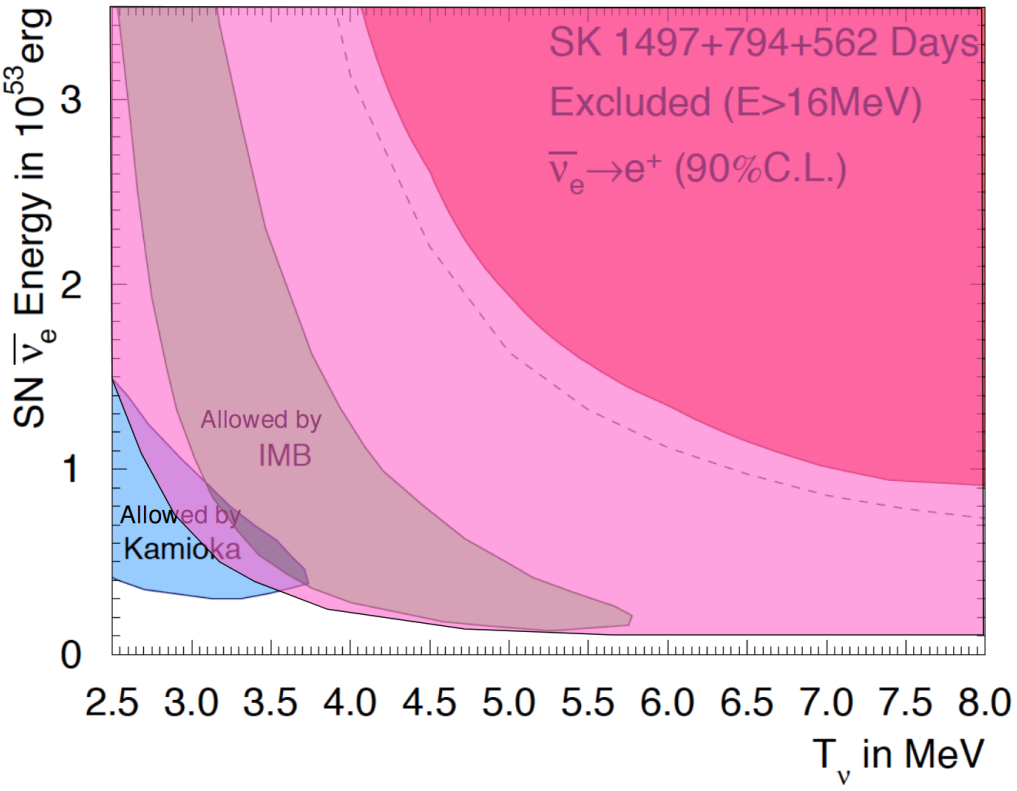

Figure 4.18: Exclusion plot for average neutrino temperature T_ν of neutrinos emitted against average luminosity of antineutrinos in a supernovae burst. The dark pink region shows the current limit set by Super-K, the translucent pink region is the limit possible after six years of running with a Gd loaded Super-K. Also shown are the allowed regions from the IMB and Kamioka measurements of SN1987A. Original plot from [146], Gd added plot from [147].

Chapter 5

The SNO+ Detector

This chapter describes the SNO+ detector. The description of the ropes and AV is particularly important for the AV positioning analysis described in Chapter 8. The effect of time walk on PMTs is also described. The calibration of time walk is the main purpose of the TELLIE system described in Chapter 6. The timing of the trigger system is also described, and is also of relevance to the TELLIE system. Finally the event construction is described, the upper limit to the event construction rate may become important if a supernova occurs close enough.

The following chapter describes the SNO+ detector. The physical structure of the detector is discussed. Following this the three phases of SNO+ , defined by the medium inside the AV, are detailed. The physics goals of each stage are discussed and the sensitivity of the experiment to $0\nu\beta\beta$ is described. The processes of Cherenkov emission and Scintillation are discussed, and the details of the PMT array are described. Finally the trigger system and data readout system of the detector are described.

5.1 Overview of the Detector

The SNO+ detector is a liquid scintillator experiment based at SNOLAB in Sudbury, Northern Ontario, Canada. The SNOLAB site is at a depth of 2070 m providing an overburden to cosmic rays of 6080 m.w.e. [150]. SNOLAB is a class 2000 clean room to prevent radioactive contamination of the experiments by the mine dust. The laboratory also hosts several dark matter experiments. The centre of the SNO+ detector is slightly higher at 2039 m below the surface of the Earth, this provides a overburden of approximately 6000 m.w.e [151]. The area surrounding the top of the detector is surrounded by a tent to prevent to prevent radon contamination of the detector.

The SNO+ detector uses an upgraded version of the SNO detector, the detector consists of a hollow acrylic sphere (known as the Acrylic Vessel (AV)) with inner radius 6 m and thickness 5.6 cm. The sphere is loaded with the detection medium used in the various phases of SNO+. At the top of the sphere, there is an acrylic cylinder leading up to the deck of the detector for the deployment of calibration sources and loading of material. The AV is held in place with ropes made from Tensylon [35].The hold up ropes are routed through tracks on plates (known as belly plates). The belly plates are thicker than the regular AV plates with thickness 11.4 cm. A picture of one of these plates is shown in Figure 5.1.

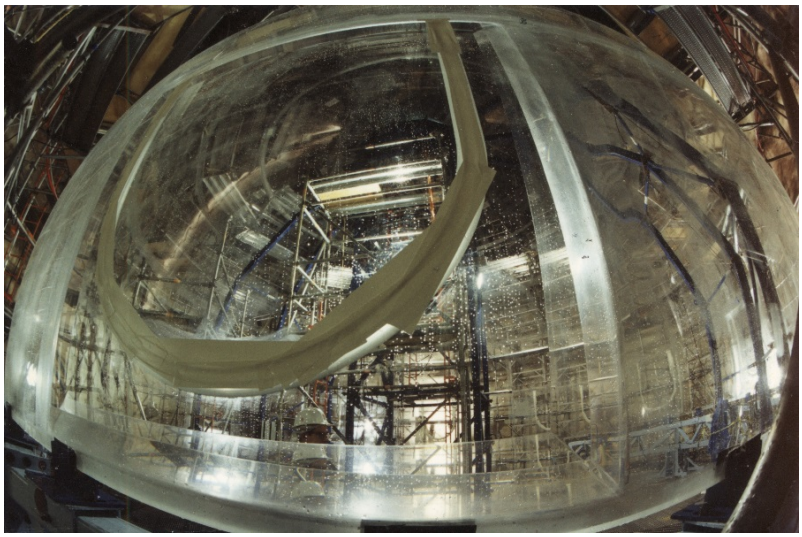

Figure 5.1: Image of a belly plate used to mount hold up ropes to the AV. Taken during the construction of SNO. The rope groove is covered with tape.

As the LAB scintillator used in SNO+ is less dense than water the rope system must be able to provide a downwards force. During the commissioning of SNO+ hold down ropes were installed over the top of the AV and mounted to the floor of the cavity. The hold down ropes are shown in Figure 5.2.

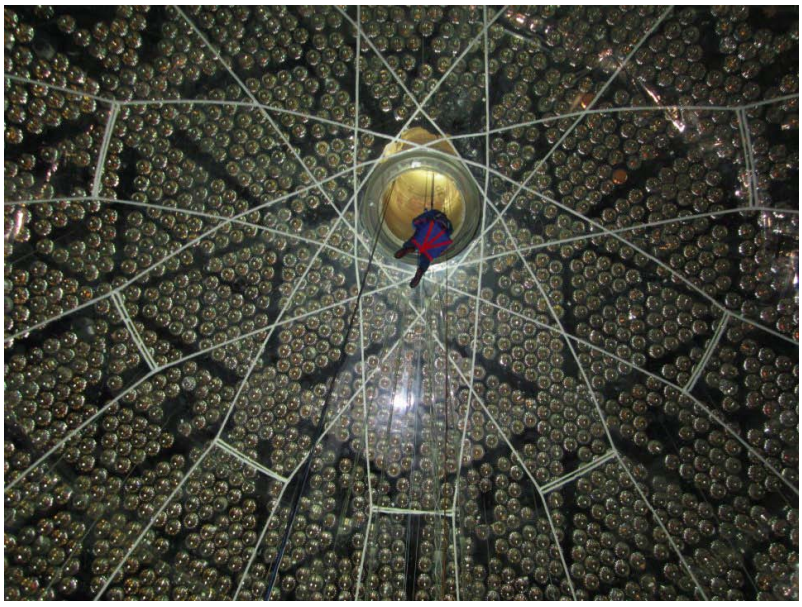

Figure 5.2: Image of the inside of the SNO+ detector, shown is the neck of the detector and the hold down ropes. Sussex PhD student James Sinclair is pictured descending into the vessel.

The acrylic sphere is surrounded by a stainless steel geodesic sphere with radius 9 m, known as the (PMT Support Structure (PSUP)). The PSUP supports the PMTs. The entire PSUP is suspended inside a barrel shaped cavern (known as the cavity) 22 m in diameter at its widest point and 30 m in height. The volume surrounding the AV is filled with 7,000 tonnes of ultra pure water (UPW), known as the external water. The cavity walls are coated with Urylon to reduce radioactive backgrounds from the rock. At the top of the cavern a deck as been installed, the deck holds the detector electronics as well as the systems for deployment of calibration sources. The detector, deck and cavity are all shown in Figure 5.3.

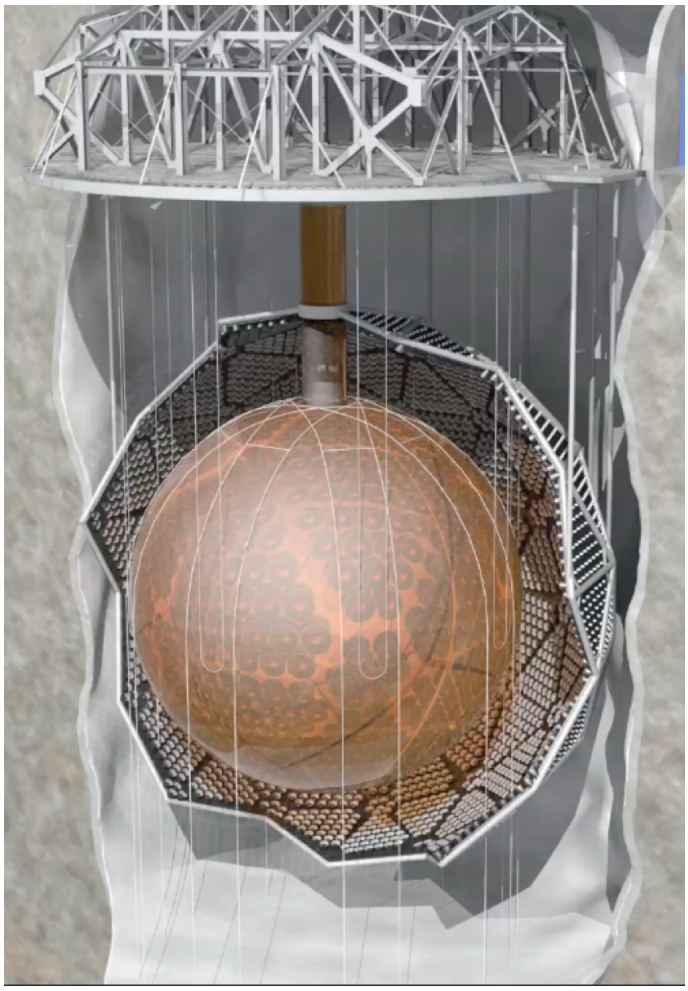

Figure 5.3: An artists impression of the SNO+ detector. A cutaway is taken of the PSUP to reveal the AV.

5.2 Loading Materials in SNO+

The SNO+ detector is split into three phases based on the medium loaded inside the acrylic vessel. The first phase the AV will be loaded with ultra pure water. After this, the UPW will be replaced with LAB liquid scintillator. For the final phase of the SNO+ experiment SNO+ will be loaded with Telluric Acid to search for neutrinoless double-beta decay in ^{130}Te.

5.2.1 Water Phase

The main physics goal of the water phase of SNO+ is the attempted detection of invisible nucleon decay. An extensive calibration campaign will take place to determine the optics of the detector and how they have changed since the end of the SNO experiment. During this phase, the detector will be sensitive to neutrinos from a supernova.

Neutrino Detection in Water

Cherenkov light occurs when a charged particle moves through a medium faster than the phase velocity of light in that medium. Light is produced in a cone centered about the particles direction. The opening angle of the cone is given in Eq. 5.1. Where n is the refractive index of the medium, and v is the velocity of the particle in the medium.

$$cos\theta = \frac{1}{n\beta} \tag{5.1}$$

$$T_p > M_p \left(\frac{1}{\sqrt{1 - \frac{1}{n^2}}} - 1 \right) \tag{5.2}$$

The minimum kinetic energy of required for a particle with mass M_p to emit Cherenkov radiation is given in Eq. 5.2. For electrons in water the Cherenkov threshold is 0.264 MeV whereas the Cherenkov threshold for protons and neutrons is approximately 480 MeV. It is for this reason that during the water phase of SNO+ the elastic scattering of neutrinos on electrons is detectable whereas the elastic scattering of protons is not detectable in SNO+ at supernovae neutrino energies.

A particle above the Cherenkov threshold produces a number of photons (N) per unit distance along its direction of travel (x) with wavelength (λ), Eq. 5.3 shows the number of photons per unit distance (x) per unit wavelength (λ) produced, α is the fine structure constant.

$$\frac{dN}{dxd\lambda} = 2\pi\alpha \left(1 - \left(\frac{1}{n\beta} \right)^2 \right) \frac{1}{\lambda^2} \tag{5.3}$$

Nucleon Decay

The primary physics goal of SNO+ during the water phase of SNO+ is the search for invisible nucleon decay. Invisible nucleon decay is predicted in theories which link the electroweak and strong forces [152]. The processes searched for are of the form $n/p \rightarrow \nu\nu\nu$ in ^{16}O. After the decay the nucleus is left in an exited state. The decay of the nucleus to its ground state releases a γ ray which is in turn detected.

In the case of proton decay, the nucleus is left in an exited state of ^{15}N. 41 % of the time this will de-excite via the emission of a 6.32 MeV γ particle [35] [153]. If a neutron decays the nucleus will be in an excited ^{15}O state, decaying to the ground state 44 % via a 6.18 MeV γ. The main backgrounds to the signal are solar neutrinos and ^{214}Bi/ ^{208}Tl in the external water. After 6 months of data taking the detector is expected to set a limit

of $O(10^{30})$ y [35]: twice that of the current best limit set by KamLAND [154]. SNO+ can set a better limit than SNO, as the D_2O in SNO had a additional NC interaction channel shown in Figure 2.4b, which acted as a background in the nucleon decay search.

5.2.2 Pure Scintillator Phase

During scintillator phase the detector will be used to study solar neutrinos and reactor antineutrinos. The detector will also be sensitive to a supernova during this stage. Calibrations to determine the optical model of the scintillator will also take place. The pure scintillator phase will also be used to verify the purity of the scintillator and check the backgrounds are at a suitable level for the Te loading in the next stage of SNO+.

Neutrino Detection in Scintillator

When a particle interacts with a scintillator molecule it excites it. A prompt de-excitation of the molecule, occurring over the course of a few ns, releases a photon. The scintillator compound used in SNO+ is known as linear alkyl benzene (LAB) and emits a spectra of light peaked in the UV range. Experiments therefore load the scintillator with various wavelength shifters, which are excited by the initial photon then de-excite. The two wavelength shifters used in SNO+ are PPO and bis-MSB. The spectra of the shifted light can be seen in Figure 5.4. Compared to water Cherenkov detectors the light yield is much higher, but the directionality obtained from the Cherenkov light is lost [155]. Cherenkov light is still produced in scintillator detectors, but the dexcitation of the scintillator occurs on a similar time scale as the emission of the Cherenkov light, the Cherenkov light cannot be distinguished from the scintillation light. As the number of photons produced by scintillation is much greater than the number of Cherenkov photons, the directional signal is lost in the isotropic scintillation light.

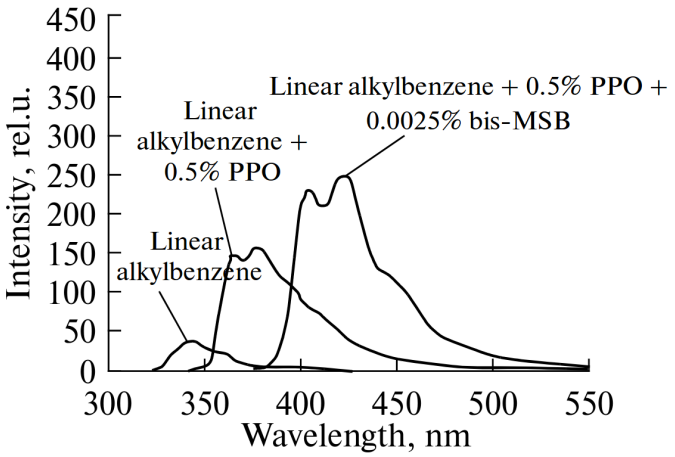

Figure 5.4: The fluorescence spectra produced by LAB and the spectra produced after the excitation and subsequent dexcitation after the light is wavelength shifted. Taken from [156].

Quenching in Scintillator

Quenching in scintillator describes processes that reduce the light output of scintillator when a particle excites it. There are two main types of quenching, impurity quenching and ionization quenching. Impurity quenching like the name suggests indicates the altering of the light output of the scintillator via impurities within it. If the impurities do not scintillate when exited then the overall light output of the scintillator is reduced. However if the impurities do dexcite via scintillation of light they alter both the wavelength distribution and the time profile of the scintillator.

Ionisation quenching occurs due to the different particles having different levels of ionisation inside a scintillator. Heavier particles are more ionising so excite the scintillator differently to lighter less ionising particles. More ionising particles deposit energy over much shorter distances then less ionising particles, the ionization of two scintillator molecules close to each other can recombine in a process which does not emit a photon, in turn reducing the light yield [48]. The relation between the amount of light produced and the energy deposited can be modelled using Birks' law shown in Eq. 5.4. The equation relates the true energy E deposited by a particle over a distance x with the observable energy ϵ, via a parameter k_B, known as the Birks' constant for the scintillator [157]. The Birks' constant for protons the scintillator used in SNO+ has been measured as 0.0096 ± 0.0003 cm/MeV and the use of the neutrino proton scattering as a detection channel for supernovae neutrinos has been discussed extensively in [158] [48].

$$\frac{d\epsilon}{dx} = \frac{\frac{dE}{dx}}{1 + k_B \frac{dE}{dx}} \tag{5.4}$$

Physics Goals

The physics goals of the scintillator phase of the SNO+ experiment are to measure low energy solar neutrinos, as well as the study of reactor and geo-antineutrinos. The pp chain which produces neutrinos with low energies upto approximately 0.3 MeV [15], was first detected by the Borexino experiment [159], if the ^{14}C impurity in the scintillator is low enough SNO+ would be able to make a precision measurement of the pp flux from the Sun [35]. Solar neutrinos with low energies such as the pep and pp neutrinos are dominated by vacuum oscillations, whereas the higher energy CNO and pep neutrinos are dominated by the matter effect, SNO+ hopes to examine the transition region between these effects. During this phase the detector will also be sensitive to a galactic supernova should one occur. Studies into the sensitivity of the detector to the supernova neutrino energy spectra using the IBD and $\nu - p$ scattering events are presented in [48].

Purity of the Scintillator

The scintillator first arrives at the SNOLAB surface lab via truck from Quebec, the short transit distance reduces the likelihood of cosmogenic activation. The scintillator is then transferred underground via mine cart to the underground purification plant. The underground purification plant cleans the LAB scintillator before it is transferred to the AV. The purification process involves several steps. Removal of impurities is performed by distilling the scintillator. Large particulates such as dust are removed by filtration. Metallic impurities are removed by metal scavengers. Further purification is performed by water extraction and steam and Nitrogen stripping. It is hoped the scintillator purification process produces a background level similar to that of Borexino [35]. More details on the purification system can be found in [160].

5.2.3 Scintillator + ^{130}Te Phase

The main physics goal of the SNO+ experiment is to attempt to determine the nature of neutrino masses and whether they are Dirac or Majorana particles. To do this it searches for neutrinoless double beta decay in the isotope ^{130}Te. The scintillator volume is loaded with unenriched Tellurium to a level of 0.5% by mass. The Tellurium is produced in China as Telluric acid and transferred to the SNOLAB site via ship, rather than aeroplane. This

is to reduce the amount of radioactive activation by cosmic rays. To further reduce the amount of contamination within the detector the acid is stored underground for a "cool-down" period, this allows the cosmogenically activated isotopes produced on surface to decay before loading. Before being loaded into the detector the acid is chemically purified.

The choice of ^{130}Te

Originally, SNO+ was intended to be loaded with Nd as the isotope used in the $0\nu\beta\beta$ search. The collaboration decided to use Tellurium for several reasons listed below [35].

- **High Isotopic Abundance:** Tellurium has a high natural abundance of its $0\nu\beta\beta$ isotope (34.08%), meaning no enrichment of the isotope is required.
- **Long $2\nu\beta\beta$ Half-life** Tellurium has a relatively long $2\nu\beta\beta$ half-life, reducing this background. The $2\nu\beta\beta$ background is especially important to liquid scintillator detectors because of their limited energy resolution. The double-beta half-life of ^{150}Nd has been measured as 9.11×10^{18} years [161], the measured half-life for ^{130}Te was found to be 8.2×10^{20} years [162], resulting in a approximate reduction in the $2\nu\beta\beta$ background of approximately a factor 90.
- **Te-Scintillator Cocktail Stability** The cocktail of liquid scintillator can allow Te loading up to 5% (by mass), and has been shown to be stable for 2 years with 0.3% loading.

Predicted $0\nu\beta\beta$ limit

The predicted limit, using a simple counting analysis, for $0\nu\beta\beta$ after 5 years of running with 0.5% loading of $^{\text{nat}}$Te is 1.9×10^{26} years. The sensitivity as a function of live time is shown in Figure 5.5 This corresponds to a value of $m_{\beta\beta}$ (Defined in Eq. 2.32) between 41 and 95 meV depending on the nuclear matrix element used. In the analysis a 3.3 m fiducial volume cut is made.

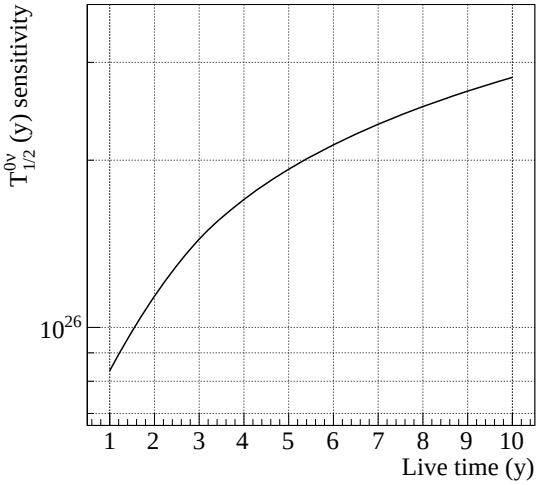

Figure 5.5: The sensitivity of SNO+ to $0\nu\beta\beta$ as a function of lifetime.

Figure 5.6 shows the signal expected after five years of running if $m_{\beta\beta}$ = 100 meV. The sources of the backgrounds are described in Section 2.5.1.

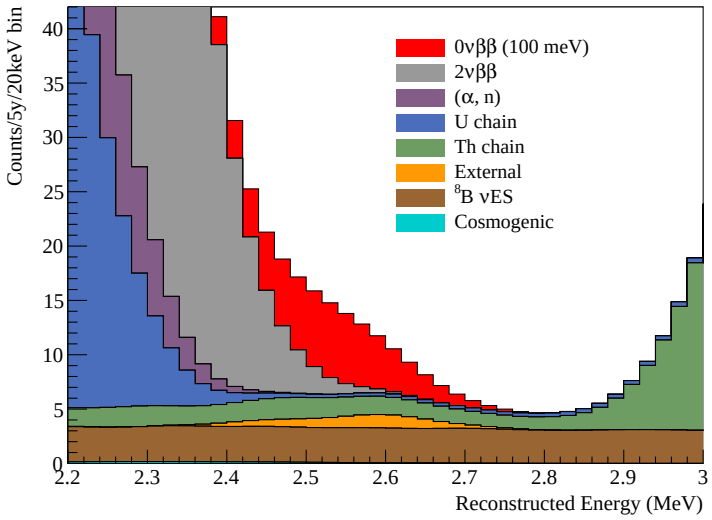

Figure 5.6: The expected signal and backgrounds after 5 y of running if $m_{\beta\beta}$=100 meV.

5.3 SNO+ Electronics

This section describes the electronics and the computing equipment used to convert the physics events occuring within the detector into measured data. The signal from detector broadly follows three steps. The detection of a signal via the PMTs. The propogation of the signal through the detector electronics which decide whether to record the PMT data

or not. The conversion of the measured PMT signals into a digital format for transfer offsite. All of thes steps are described in the following sections.

5.3.1 SNO+ PMTs

SNO+ uses the same Hamamatsu R1408 photomultiplier tubes as the SNO experiment. The PMTs can be divided into three categories: inward looking tubes (sometimes referred to as normal PMTs), outward looking PMTs (OWLS) and neck PMTs.

The Hamamatsu R1408 PMT is eight inches in diameter. There are approximately 9400 normal PMTs looking inwards within the detector [35]. Each normal PMT is mounted within a 27 cm concentrator to increase the PMT coverage to 54% [35]. An image of a SNO+ PMT and a concentrator are shown in Figure 5.7. These concentrators have degraded since the SNO experiment, and the angular response of the PMT has changed Section 6.4 describes the procedure for measuring and verifying the angular response of the PMTs. The transit time spread of the PMTs is 1.7 ns [151].

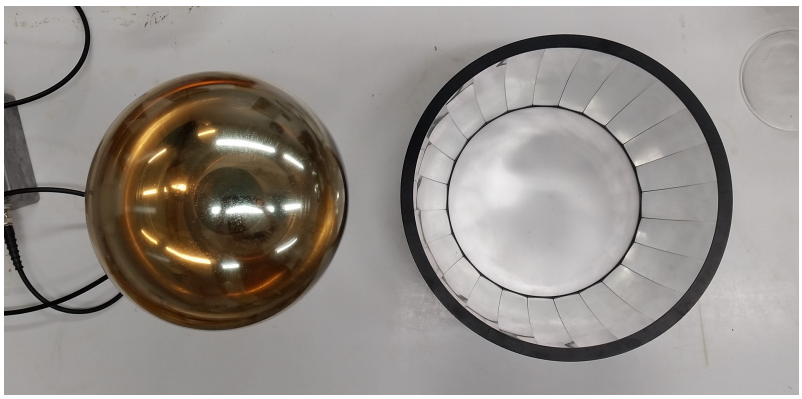

Figure 5.7: A PMT and concentrator used in the SNO+ experiment.

One hundred PMTs point outwards from the PSUP into the cavity. These are the OWL PMTs, they are designed to act as a cosmic muon veto. Two PMTs are installed within the neck to ensure there are no light leaks into the detector, they are also used to veto any event occurring within the neck of the detector which may misreconstruct within the inner AV otherwise.

All PMTs are connected to the detector electronics via a waterproof BNC cable which provides a both the HV to the PMT and cabling for the PMT signal. Compensation coils are installed in the walls of the cavity to cancel out the magnetic field of the Earth.

Several high quantum efficiency PMTs, of the proposed type used for SNO+-Phase 2 have been installed to monitor their performance. The HQE PMTs are approximately two times as efficient at 420 nm. The PMTs will be used to determine the performance of

SNO+-Phase 2 more accurately. The efficiency of the new PMTs as well as the measured efficiency of two standard PMTs used in SNO+ are shown below.

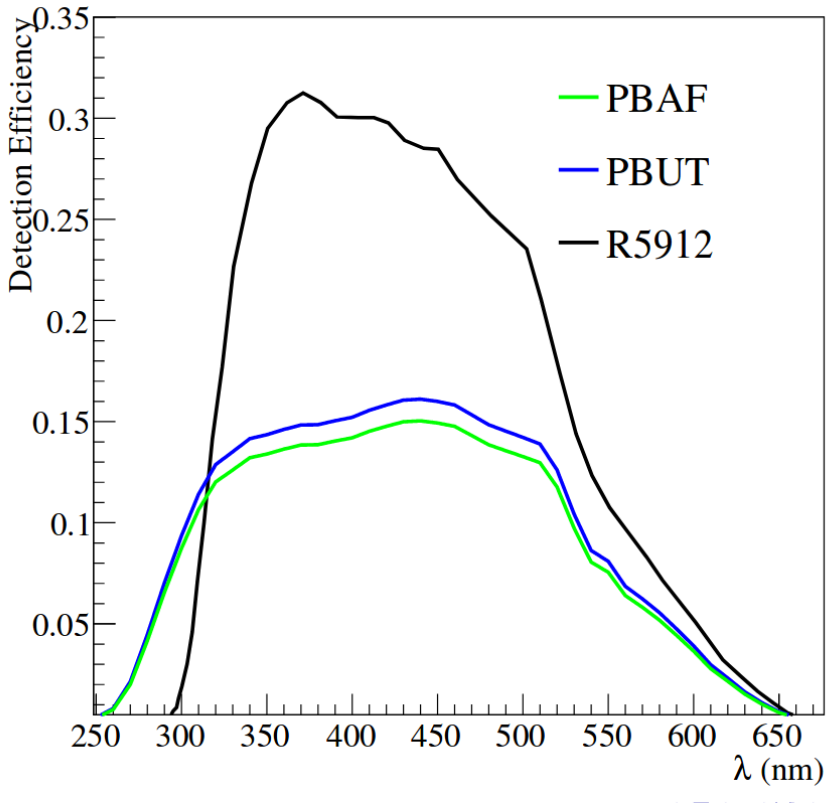

Figure 5.8: The efficiencies of two SNO+ standard PMTs (PBAF, PBUT) and the efficiency of the HQE PMT proposed for SNO+-Phase 2 as a function of wavelength. Taken from [163].

Time walk on PMTs

For a PMT to trigger in the SNO+ electronics it must pass a threshold value. The number of photoelectrons produced at the photocathode corresponding to a single photon hit on a PMT is determined by Poisson statistics. Depending on the number of photoelectrons produced the time at which the threshold value is crossed and the time at which the PMT records a hit is changed. The more photoelectrons liberated the earlier the pulse produced crosses the threshold and the earlier the PMT appears to have been hit. A single photoelectron pulse can be distinguished from multiple photoelectron pulse by its area (the amount of charge deposited at the anode). A graphic of time walk on a PMT pulse is shown in Figure 5.9.

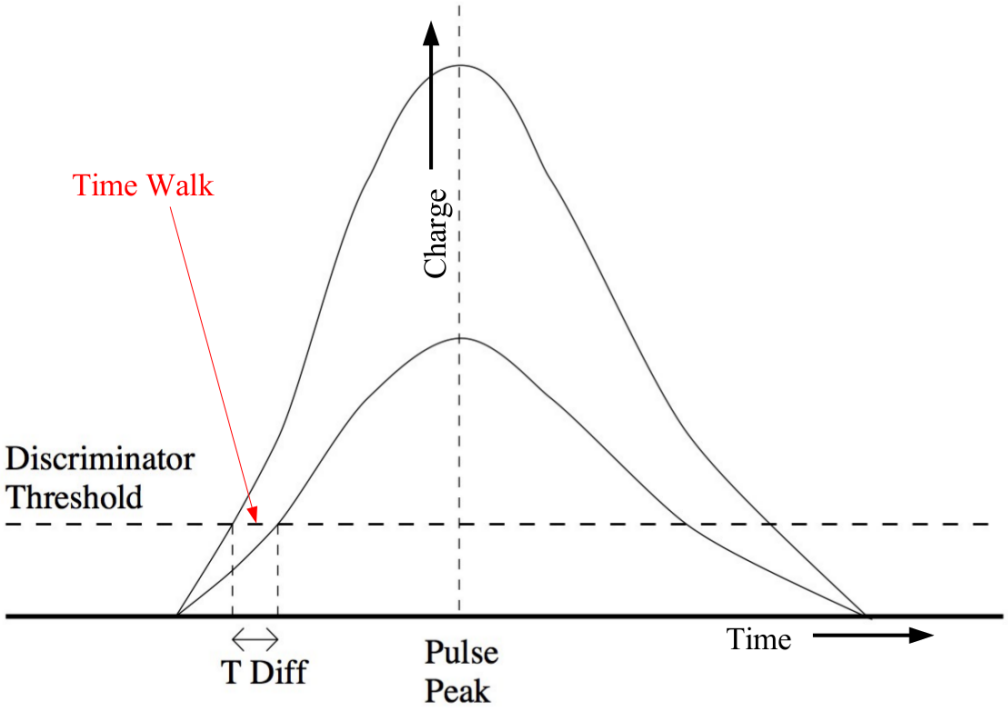

Figure 5.9: Schematic of time walk on a PMT pulse. Taken from [164], [165].

5.3.2 The SNO+ Trigger system

To record the data from the PMTs in SNO+, electronics exist on the deck above the detector. Every PMT is connected to a paddle card which provides HV voltage to a group of eight PMTs, and there are four paddle cards per PMT interface card. The PMT interface card can turn off the power to each paddle card to remove any faulty channels. A front end card mirrors the PMT interface card and has four daughterboards. Each daughterboard has two chips to set the thresholds of the eight channels, two chips to integrate the PMT pulses of the channels and eight CMOS chips (One for each channel) to record the point at which the PMT pulse passed threshold.

When a PMT passes its threshold value the front end card produces a 100 ns and a 20 ns square pulse, known as the N100 and N20 trigger pulses. The CMOS chip starts ramping to record the hit time of the PMT. The integrator chips integrate the pulses over different time windows. The QHS (Charge Hit Short Integration time) value is obtained by integrating the PMT pulse over 60 ns and the QHL (Long Integration Time) is integrated over 400 ns. QLX is an integration of a low gain copy of the PMT pulse, and can be integrated over either time window. After a channel is triggered it is locked out for 400 ns and will not generate another trigger pulse if it passes threshold. After the 400 ns has

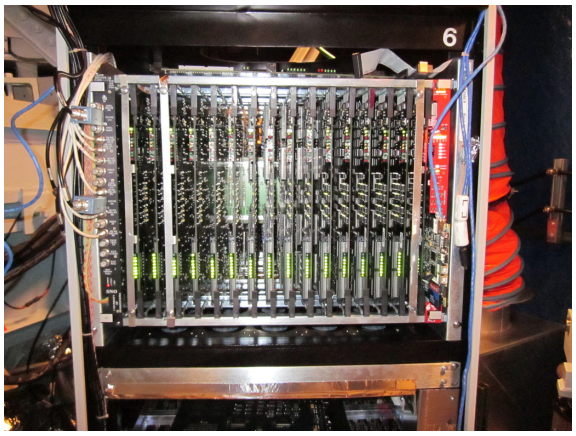

Figure 5.10: A single crate for the SNO+ experiment. The board on the leftmost side is the crate trigger card (CTC). The red board on the right is the XL3 (Described in the next section), the boards in between are the front end cards (FECs).

elapsed the time values and charge values are reset. A high and low gain copy of the PMT pulses (known as ESUMHI and ESUMLO) and the N100 and N20 pulses are summed and sent to the front end card. The front end card then sums the signals from each of the daughterboards. Outward looking tubes (OWLs) produce the same pulses as regular PMTs, these are summed separately.

In each crate, there are sixteen PMTICs and FEC cards, giving 512 channels per crate. The N100, N20 and ESUM pulses from all the FEC cards (excluding signals from OWL which are summed separately) in the crate are summed by the crate trigger card (CTC). The summed signals from the crate are then sent to the master trigger card analogue (MTCA).

The MTCA sums the signals from the individual crates. The MTCA also provides the ability to mask out any crates if necessary. There is one MTCA per trigger signal. The N100 signal is now the number of PMTs hit within a 100 ns time window. The ESUM signal is the sum of all the PMT pulses. The summed signal is sent from the MTCA to the MTCD the card detects whether the any of the summed trigger signals pass their corresponding predefined thresholds.

A schematic of the signal from the PMTs to the MTCA is shown in Figure 5.11.

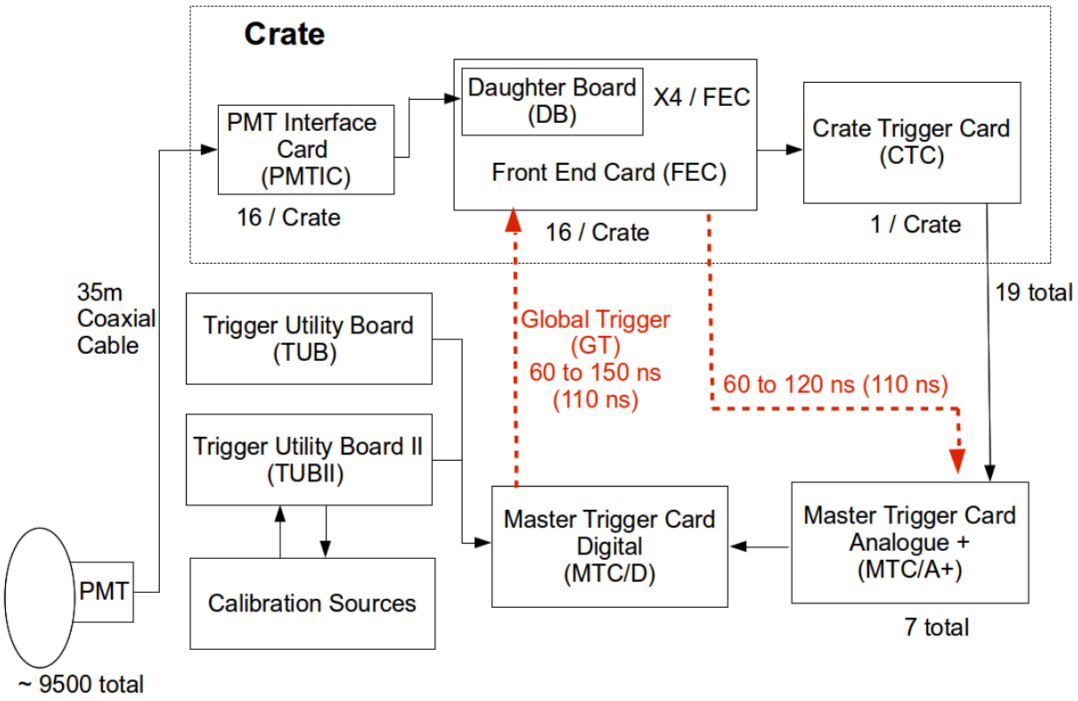

Figure 5.11: The signal paths from the PMT to the MTCA [166]. The 9500 PMTs represent the sum of the normal and OWL PMTs.

The total transit time of the signal from FEC to MTCD is 110 ns, it takes the same time to send a signal in the opposite direction. When a global trigger threshold is passed a signal is sent back to the channels, any channels which are locked out are read out and used to construct an event in the detector. A CAEN board is also used to digitise the ESUMHI signal. Any trigger signals passing threshold (regardless of whether they are masked in or out) within 10 ns either side of the trigger signal generating the global trigger will be masked into the trigger word of the event. Any masked in triggers which pass threshold after this will cause the missed trigger word to be set.

The global trigger signal is latched to a 50 MHz clock, hence there can be up to a 20 ns delay between the point at which a global trigger channel passes its threshold and the global trigger is issued. After a global trigger is issued there is a 450 ns delay before the next global trigger can be issued.

The event time is stored using the 10 MHz and 50 MHz clocks. The 50 MHz clock has a register of 43 bits and resets approximately every 2 days, it is designed to calculate the time in between events. The 10 MHz clock has a 53 bit register, and resets every 28.5 years. The clock is kept in sync using a GPS. The 10 MHz clock is used to define the time of the event relative to a fixed date, defined as midnight on the 1st of January 2010.

The only trigger not latched to the 50 MHz clock the External Async trigger. This

trigger is used with some calibration sources, when this trigger channel records a trigger there is no delay associated with waiting for the next 50 MHz clock tick, the trigger lock out window is extended slightly by the difference between the async trigger time and the next 50 MHz clock tick when compared to any of the other triggers.

The MTCD also has the ability to prescale the $N100_{LO}$ trigger such that only a certain proportion of events will generate a global trigger.

An image of the timing rack is shown in Figure 5.12.

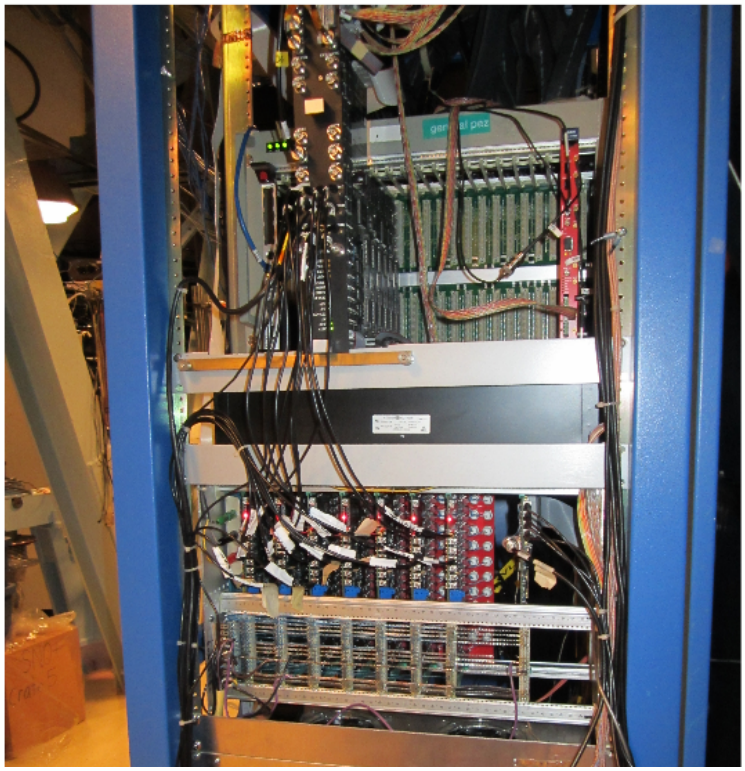

Figure 5.12: The timing rack of SNO+. The large dark grey card in the top create is the MTCD. The smaller red card next to it is the CAEN board. The MTCAs are the red boards in the lower crate.

5.3.3 Event Data Flow

If a global trigger is issued the PMT hits associated with the trigger are stored in 4 MB FEC FIFO memory. The digitised PMT hit is 96 bits long the components are listed below

- PMT LCN : 14 bits
- TAC : 12 bits
- QHS : 12 bits

- QHL : 12 bits
- QLX : 12 bits
- GTID : 24 bits
- CMOS Cell : 4 bits
- Other : 6 bits

The PMT LCN (Logical Channel Number) identifies the PMT that gave a signal. The channels are mapped to crates and cards via Eq. 5.5.

$$\text{LCN} = 512 \cdot \text{Crate} + 32 \cdot \text{Card} + \text{Channel} \tag{5.5}$$

TAC is the digitised hit time of the PMT, and ranges from 0 to 4095, as the trigger window is 400 ns long time resolution a PMT hit is approximately 0.1 ns. The charge of the PMT pulse integrated over varying time periods with varying gains (QHS,QHL,QLX) also take up 12 bits each. The location in which the analogue data was stored takes up 4 bits of memory, to allow debugging of the various CMOS cells. The lower 24 bits of the GTID are also stored with each PMT hit, and are used to ensure the PMT hits are kept in sync with the global triggers by checking the rollovers of the last 16 and 24 bits of the GTID are in sync. Six bits are used by the CMOS chip to inform of any errors associated with the chips as well as information if any data is stored within the CMOS chips or the CMOS chips memory is full.

The XL3 scans the FECs within its crate, if a FEC has data up to 120 PMT hits are copied to the XL3 memory. When 120 hits are stored within the XL3s memory they are transferred via TCP/IP to the builder. Each XL3 has a data transfer rate of 14 MB/s corresponding to approximately 2 million hits per second [167]. The XL3 is also responsible for controlling the voltage of the PMTs within the crate.

The builder organises the output of the XL3s, the CAEN and the MTC information into events by grouping together PMT bundles and trigger words with the same GTIDs the builder constructs ZDAB files from the events. The maximum output rate of the builder is approximately 400 kb/s.

The data rate of the builder and the electronics is important in the event of a supernova. A calibration source is being developed to mimic the signal produced by a supernova, to ensure the detector threshold is set high enough that the electronics and builder are not overloaded.

The built ZDAB files are then suitable for analysis with RAT. The files are stored on a nearline RAID array and transferred to the grid for offsite processing, to produce ROOT tuples from the ZDABs. A server exists onsite to run nearline data quality checks and inform operators on the correct operation of the detector.

Chapter 6

Calibration of the SNO+ detector

This chapter describes two of the deployed calibration sources used by SNO+, the Laserball and the ^{16}N source. A study is presented to verify the scans using these sources are able to determine the angular response of the detector PMTs. In the scintillator phase of SNO+ a new laserball will be used for the calibration, the new laserball has a thinner neck than the old laserball, and therefore less shadowing. A study is presented showing the change in the distribution of light by using the new neck. The data quality code for the laserball is also described. The external LED/Laser calibration system (ELLIE) is described as well as the nearline DQ scripts and website.

In order to understand the response of the detector to physics it must be calibrated. There are multiple devices designed to calibrate the SNO+ detector. The devices used can be divided broadly into two categories. Optical sources are used to monitor the optical properties of the detector media and the response of the PMT array and radioactive sources are used to determine the response of the detector to physics events of a certain energy at a certain position in the detector. The latter are used to verify the energy and position reconstruction algorithms. Due to the strict radiopurity requirements of SNO+, the ELLIE system was developed to enable calibration without needing to deploy any sources within the detector and risk contamination.

6.1 The Deployment System for Calibration Sources

Sources are positioned in the detector using a rope system known as the manipulator system. A schematic of the manipulator system is shown in Figure 6.2 calibration sources are lowered down the neck of the AV and are connected to the deck via an umbilical and

ropes. The umbilical provides the connections required to operate the source, for example the laserball umbilical shown in Figure 6.2 has a core of optical fibres to pipe the light from the laser into the laserball. The umbilical for the ^{16}N source has a tube to pipe ^{16}N gas into the source. The umbilical is surrounded in a silicone (tygothane for LAB compatibility during the scintillator phases [168]) tube to result in low radon emanation within the detector [169], similarly the manipulation ropes are made of Vectran ropes [151]. Figure 6.1 shows the manipulation ropes used to position the source. Ropes can be passed through the AV to allow positioning in both the X/Z and Y/Z planes, an offset in all three axes simultaneously is not possible. Furthermore, due to limitations on the tension of the ropes some positions within the AV are not reachable these are indicated by the shaded regions in Figure 6.1. Tubes (also shown in Figure 6.1) exist external to the AV to allow the deployment of sources within the external water [151].

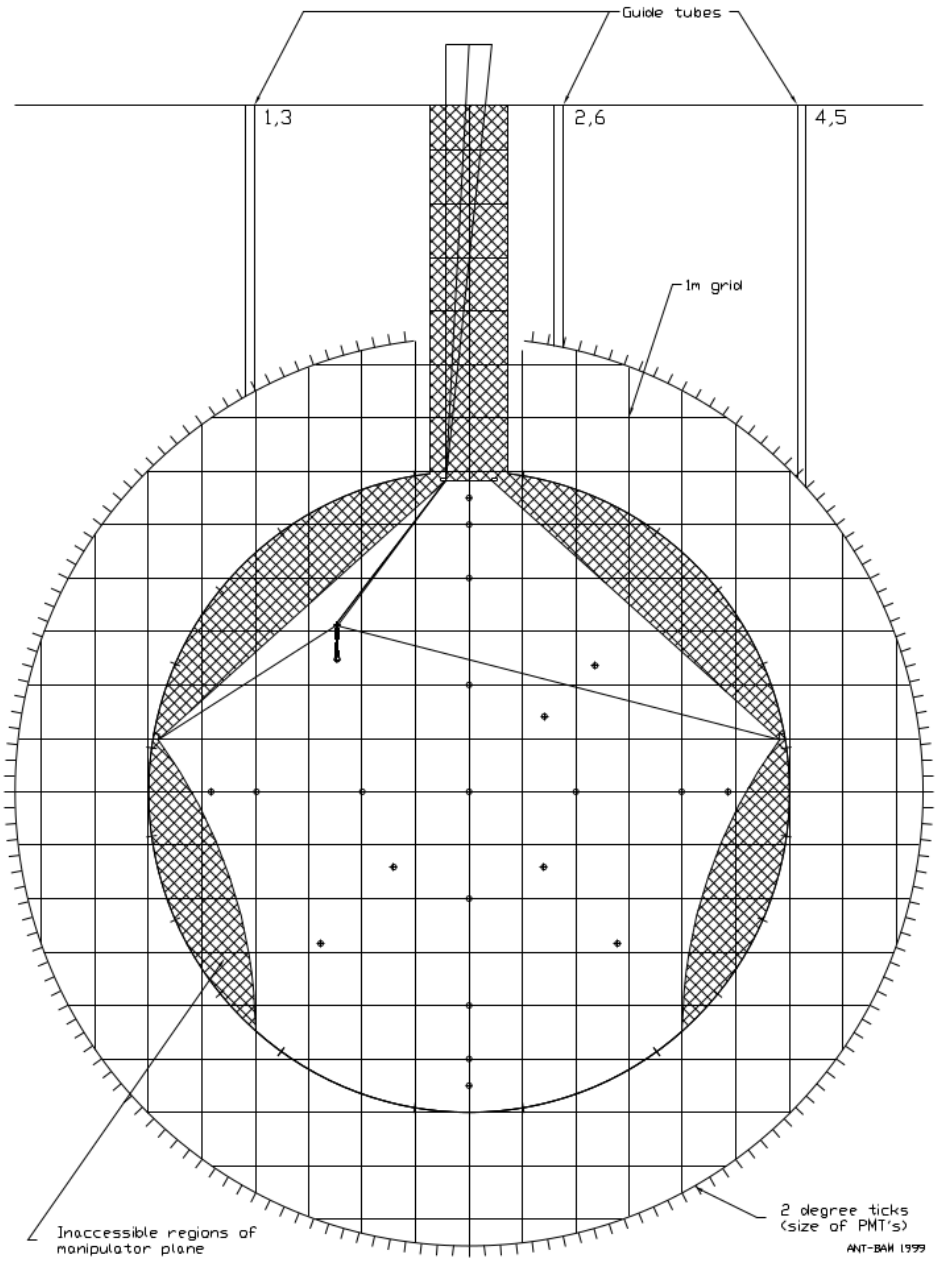

Figure 6.1: The manipulator rope system, the source cannot be deployed within the shaded regions due to the limits of the tensions on the ropes. Also shown are the guide tubes used place sources external to the AV. Taken from [170].

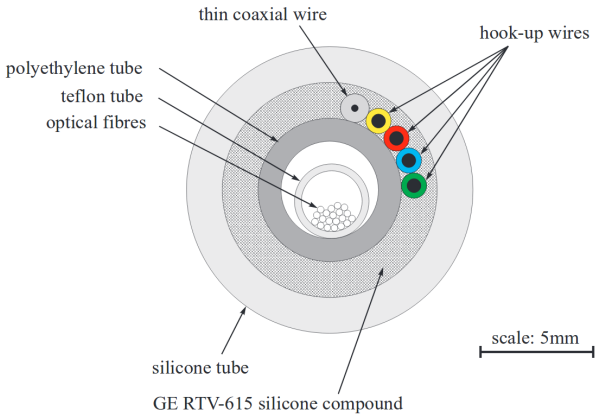

Figure 6.2: The umbilical for the laserball used in SNO and the water phase of SNO+, taken from [169].

6.2 The Laserball

The laserball acts as an isotropic light source within the detector it is used to perform the initial timing calibration of the SNO+ PMT array as well as the measurement of the optical properties of the detector.

The laserball itself consists of an optical fibre piped into a 10.9 cm quartz flask. The flask contains 50 µm glass spheres uniformly suspended in a silicone gel [169]. The glass spheres scatter light from the laser and produce an approximately isotropic source of light. To identify laserball pulses the source sends an trigger pulse to the EXTA input on the MTCD.

The light into the laser is provided by an N_2 gas laser with a wavelength of 337 nm and a pulse width of 0.6 ns [151], in order to provide coverage over multiple wavelengths the laser can be piped though various dye laser chambers. The available wavelengths are shown in Figure 6.3. The laserball increases the pulse width of light to approximately 2 ns [151].

In reality the laserball is not a perfectly isotropic light source. The stainless steel neck of the laserball, that is required attach the source to the manipulation systems, shadows the top of the laserball. During the construction of the SNO laserball the fibre was positioned slightly below the equator of the laserball resulting in a downwards favoured light distribution.

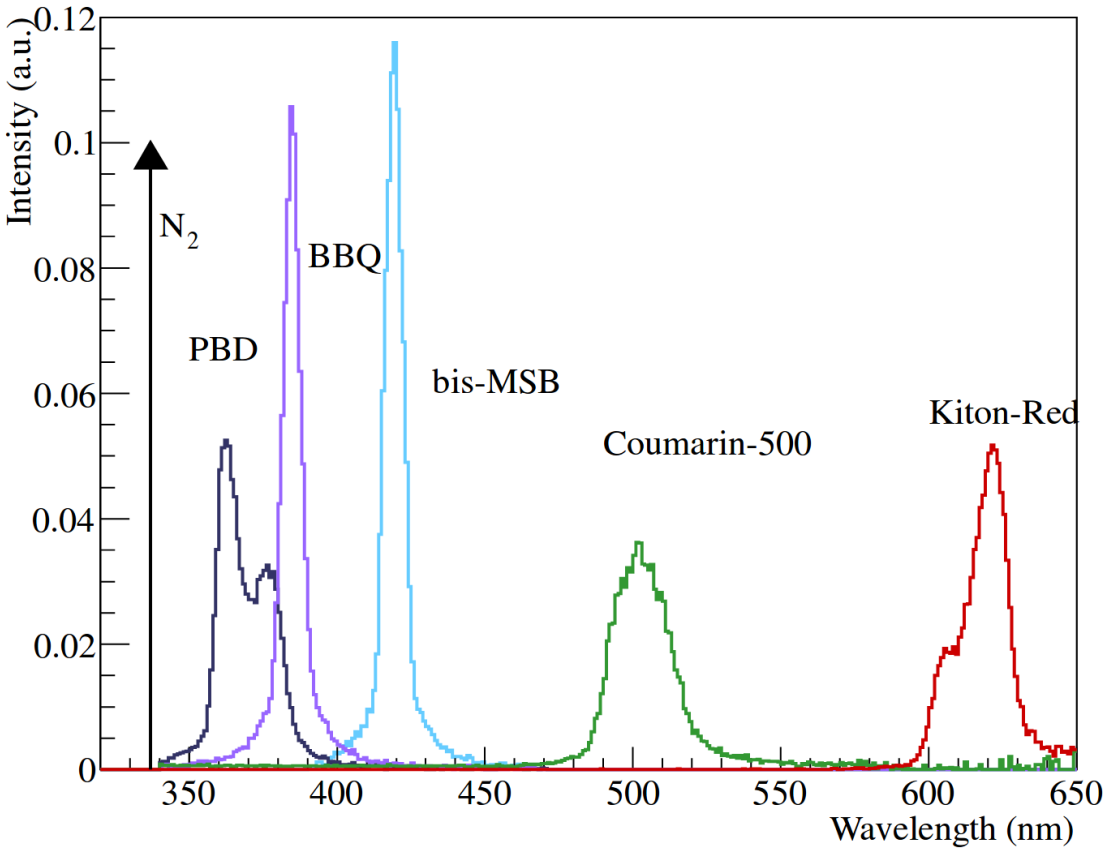

Figure 6.3: The wavelength distribution of various laser dyes used with the laserball and the 337 nm gas laser used in the SNO experiment. Taken from [171].

In SNO+, the laserball can provide two main calibrations of the detector: the PMT timing calibration (PCA), and the optical calibration of the detector (OCA). By placing the laserball in the centre of the detector the light arrives at the PMTs arrives at approximately the same time this can be used to determine the cable delays of the channels by measuring the apparent offset of the hit times. By comparing the charge deposited with the hit time of the PMT, the time walk of the PMTs can also be measured. The OCA is performed using the entire laserball scan by varying the position of the source the optical properties of the detector such as the attenuation of the media and the angular response of the PMTs can be obtained [172].

6.2.1 Simulation of the Scintillator Phase Laserball Neck

During the water phase of SNO+ the original laserball used for SNO was used. Due to radiopurity requirements a new laserball needs to be created for the scintillator phase of SNO+, the opportunity was taken to improve the design producing smaller neck shadowing. Figure 6.4 shows the schematics for the SNO laserball and the SNO+ laserball.

The original SNO laserball had a shadowing of approximately 30° [169] whereas the new laserball has shadowing of 7.3° [164].

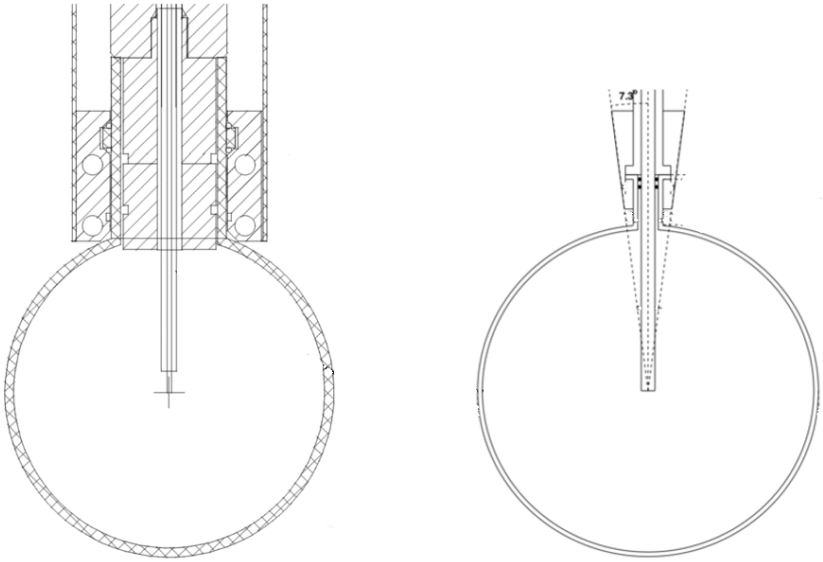

Figure 6.4: The left schematic is that of the SNO laserball and its neck, used throughout SNO and the water phase of SNO+. Taken from [169]. The right schematic shows the scintillator phase laserball and neck with reduced shadowing.

The Laserball Mask Function

In RAT, the anisotropy of the laserball is simulated by using a polynomial which acts as a PDF weighting the light distribution relative to the laserball neck. The polynomial is defined by sixth order polynomial in $(1 + \cos\theta)$, where θ is the angle between the photon and the neck. When $\theta = \frac{\pi}{2}$ the photons are going straight down and therefore unaffected by the neck. However, when a photon is travelling upwards and $1 + \cos\theta \approx 2$, there is a larger chance of the photon being shadowed by the source neck so the PDF is smaller.

Generating the new laserball mask

To generate the mask function, a simple 2D ray-tracing program was written. The laserball was treated as a circle of radius 10.9 cm, photons were generated at an angle ϕ relative to the surface normal according to a Lambertian distribution (defined by Eq. 6.1) uniformly on the edge of the circle. The path of the photon was extended to infinity and code was written to check if the photon intercepted the neck as shown in figure 6.5. The ratio of photons hitting and not hitting the neck were binned in θ (the angle relative to the neck). The points were then fitted to a sixth order polynomial to determine the mask function.

$$p(\phi) \propto \cos\phi \tag{6.1}$$

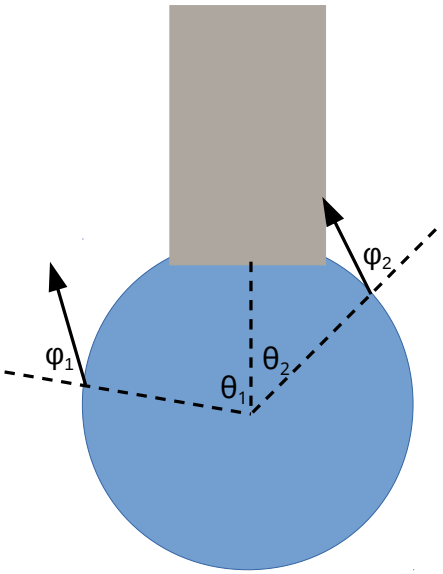

Figure 6.5: Graphic demonstrating the code used to determine the mask function.

The results of the simulation can be seen in Figure 6.6. The axis in Figure 6.6 spans from the horizontal up towards the laserball neck, for values with $1 + \cos\theta \approx 2$ where the neck shadowing has a significant effect the simulation of the old neck agrees well with the data from SNO. The data from SNO has been scaled such that the first data point (corresponding to angles of 180° relative to the neck, and therefore unaffected by it) is equal to 1. As expected, the mask function for the new neck shows an increase in the amount of light seen at small angles relative to the laserball neck.

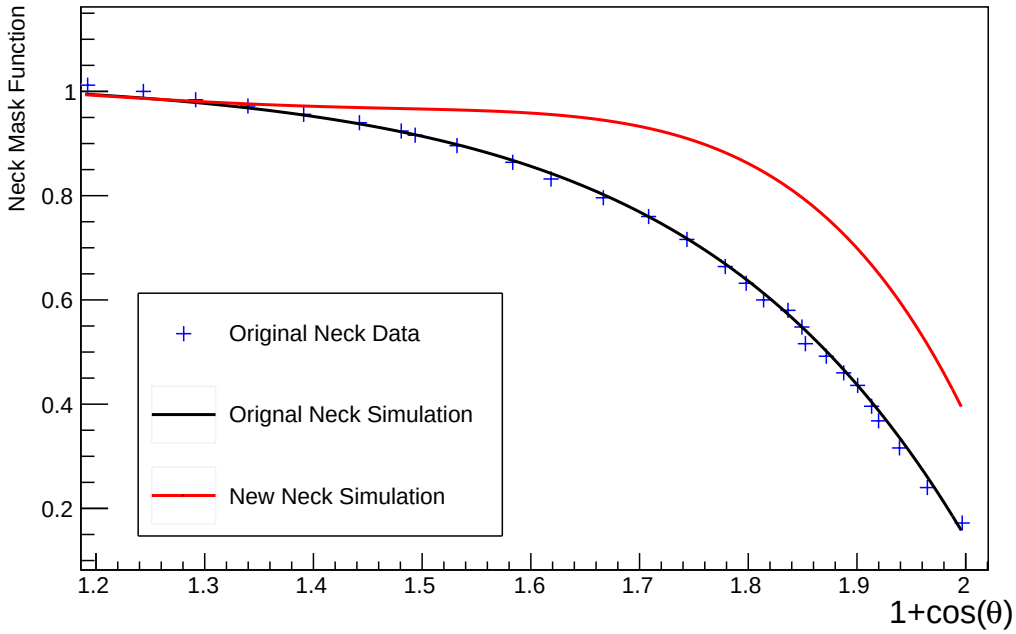

Figure 6.6: The laserball mask functions obtained from the laserball neck simulation. Also shown is the measured neck mask function of the old neck taken during SNO experiment [169]. θ is the angle relative to the vertical.

The fits were made to a 6th order polynomial, with the 0th order term being fixed to 1, as any light going directly downwards will not be affected by the neck. The polynomial fits to both necks are shown in Table 6.1.

Laserball Neck	p_1	p_2	p_3	p_4	p_5	p_6
Old Neck	0.041207	-0.572771	1.697651	-1.986543	1.046997	-0.217940
New Neck	0.291433	-2.608465	7.038575	-8.053912	4.140373	-0.792326

Table 6.1: The parameters for the neck polynomials obtained from the neck simulations.

Increase in the amount of light emitted

In simulation, the amount of light from the surface of the source (after any shadowing effects) is fixed. In reality, however, the number of photons entering the laserball is fixed and the total luminosity is effected by the shadowing. By approximating the laserball as an uniformly emitting source of light effect on the shadowing can just be approximated by the ratio of the unshadowed area of both necks as shown in Eq. 6.2. The limits of the two integrals are obtained from the shadowing angles described in Section 6.2.1.

$$\frac{\int_0^{\pi-\frac{\pi}{6}} \sin(\theta)d\theta}{\int_0^{\frac{43\pi}{45}} \sin(\theta)d\theta} \approx 0.937 \tag{6.2}$$

The old laserball produces approximately 94 % of the light from the new laserball at the same laser intensity.

6.2.2 The Laserball Data Quality Processor

To ensure a laserball scan is good enough quality to use in calibration analysis, checks are performed on the data. The checks are written in the form of a RAT processor and are performed on processed Summary Optical Calibration files (SOC) files. The channel hardware status (CHS) of the PMTs are also checked before using them in the quality checks. Several checks are performed by the processor.

NHit Checks

The NHit checks are designed to check the intensity of the laserball and its intensity stability throughout a run. The code also checks if the detector is in a suitable condition for a laserball run to be taken by checking the number of unhit PMTs.

- NHit Check - The number of hit PMTs per laserball pulse should be between 200 and 600.
- Number of Unhit PMTs - The number of unhit PMTs throughout the run should be less than 600.

QHS Checks

The QHS checks look at the charge spectrum of the PMTs. The QHS values for all normal PMTs are binned for all laserball triggered events. Several fits are then made to the histogram and the fit parameters are compared with expected values.

A Gaussian is fitted between 15 and 35 ADC counts. The mean value is then compared with the check parameters. The number of entries in the bin which the mean value falls into is used to define the maximum of the histogram. The peak value is used to find the 25 % and 75 % points on either side of the peak. On each side of the peak a linear fit is made between these points, the point at which the line passes half the maximum is used to define the half maximum points on either side of the peak. Figure 6.7 shows the QHS spectrum from a laserball run as well as the fits made to the spectrum.

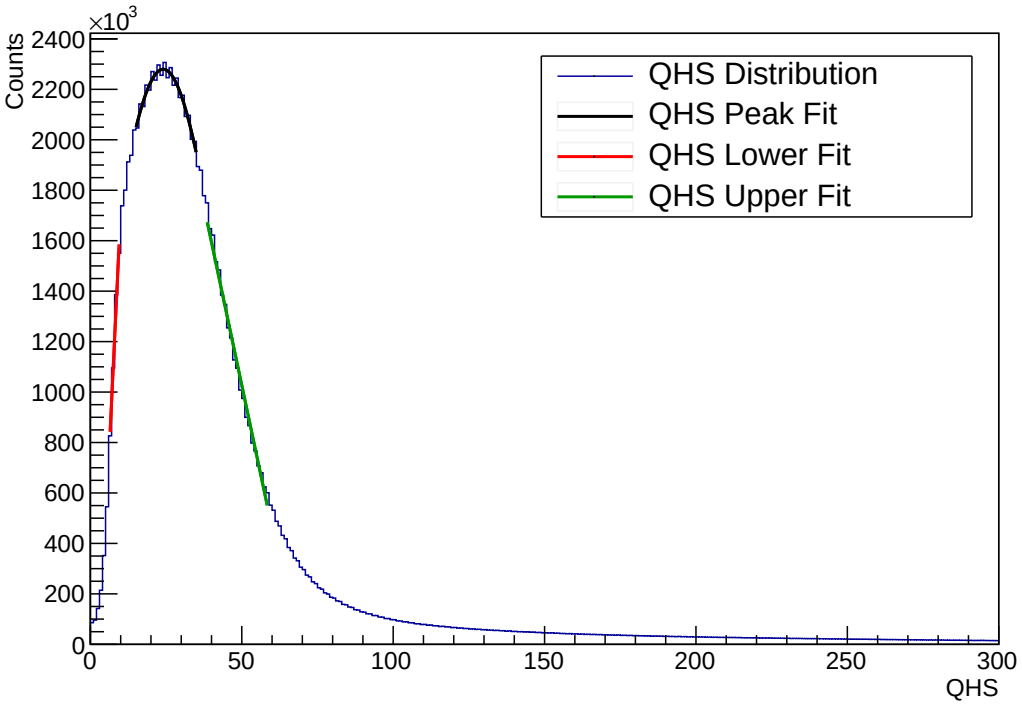

Figure 6.7: The QHS spectrum of PMT hits during a laserball run. Also shown are the fits used to determine the check parameters.

- QHS Peak Check - The peak of the QHS spectrum should be between 21 and 24 ADC counts.
- QHS Low Half Maximum - The half maximum on the left hand side of the peak should be between 8 and 10 ADC counts.
- QHS High Half Maximum - The half maximum on the right hand side of the peak should be between 43 and 46 ADC counts.

Occupancy Checks

The occupancy checks also check the stability of the laserball throughout the run. The occupancy of a PMT is defined as the proportion of laserball pulses that generate a hit on a PMT. The full occupancy is calculated by performing no cut on time, whereas the prompt occupancy only counts hits occurring within ± 4 ns of the peak hit time. The prompt and full occupancy for a laserball scan are shown in Figure 6.8.

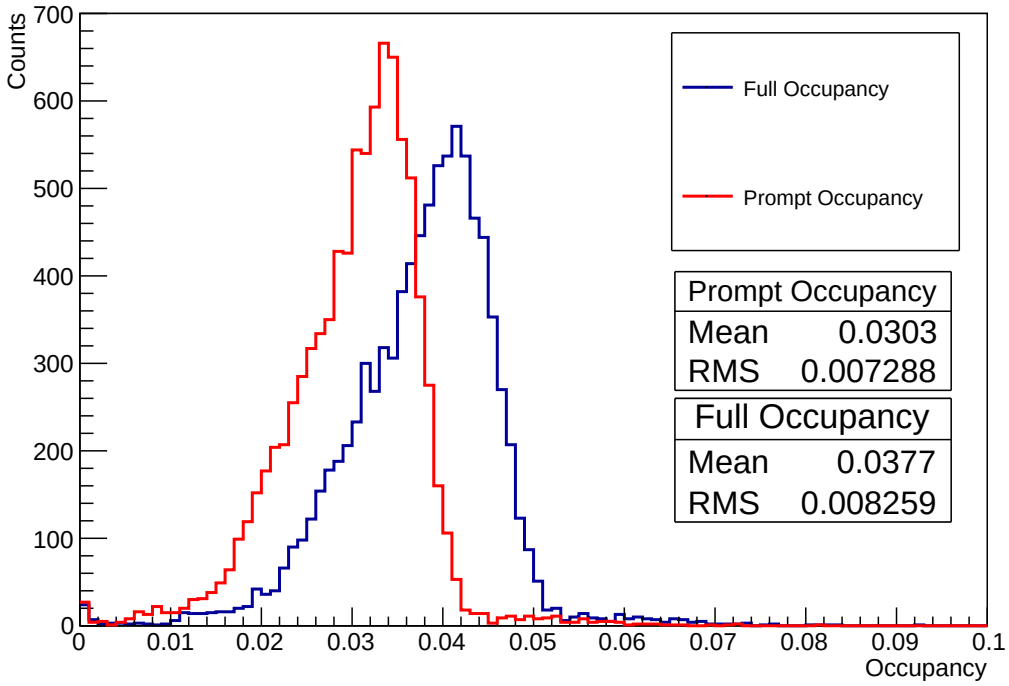

Figure 6.8: The distribution for prompt and full occupancies taken during a laserball calibration run.

- Mean Occupancy Check - The mean occupancy should be less than 0.08.
- Occupancy Spread Check - The spread on the occupancy should be less than 0.05.

Timing Checks

The timing checks verify the timing calibrations of the PMT array. The laserball produces an approximately isotropic pulse of light at a known position within the detector. The hit times of each of the PMTs throughout the run minus the time of flight of the light from the laserball to a particular PMT should therefore be approximately Gaussian. A fit to the distribution of hit times minus the time of flight is made using a Gaussian function and the mean value is checked. Figure 6.9 shows the hit time residuals of all the PMTs as well as the fit.

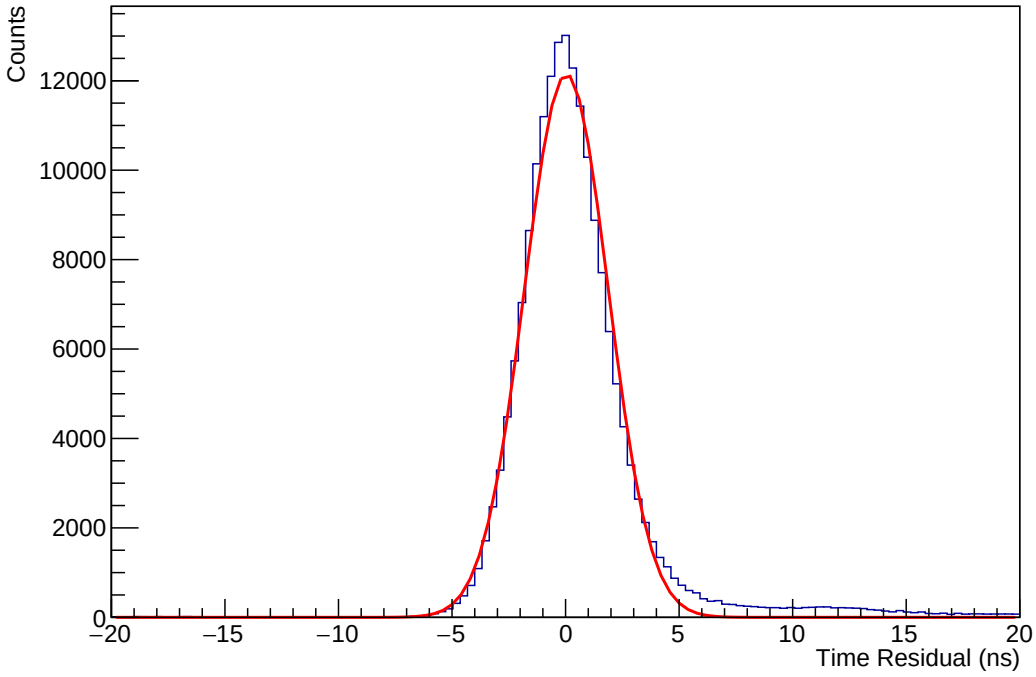

Figure 6.9: Residual of PMT hits during a laserball run, also shown is the Gaussian fit.

The code also performs checks on individual PMTs. For each individual PMT the prompt hit time is calculated by binning a histogram of hit times within ± 4 ns of the expected peak hit time and attempting to find a peak, if the average peak time or the uncertainty on the peak time is too large the channel is flagged. A crate map as shown in Figure 6.10 of the failing channels is made to indicate to the operator if something is wrong with a particular card or crate.

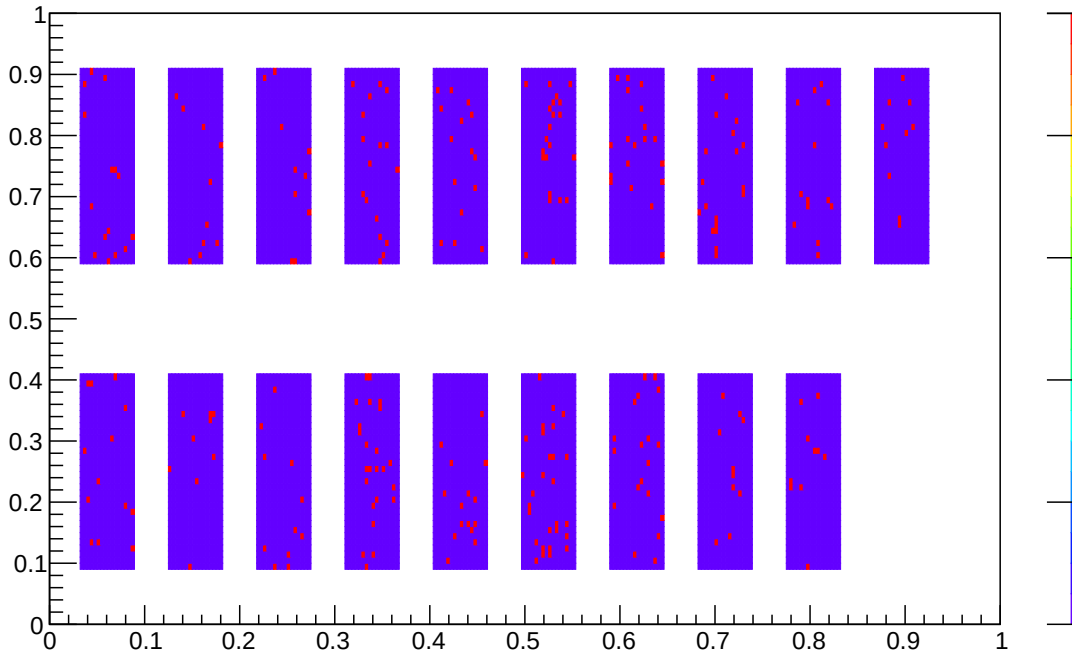

Figure 6.10: The crate map showing channels which failed the average peak time check. Good channels are marked purple whereas failing channels are marked red.

Source Position Checks

The source position checks compare the fitted position of the source with the position provided by the manipulator system. The fitted position is determined by minimising the time of flight residuals to the PMTs. Depending on whether the side ropes are being used to position the source the tolerance of the check changes. When the side ropes are used to position the source off of the Z axis the accuracy of the positioning of the source is reduced. The code checks if the X and Y positions are consistent with any of three ports on the UI. If the positioning is consistent the tolerance is reduced as the Z positioning is simply determined by lowering the source to the desired height.

- Position tolerance (no side ropes in use) - The difference between the fitted and manipulator positioning should be less than 2 cm.
- Position tolerance (side ropes in use) - The difference between the fitted and manipulator positioning should be less than 4 cm.

6.3 The ^{16}N source

The ^{16}N source was used to calibrate the energy response of the SNO detector and the SNO+ detector during its water phase. The source produces an 6.13 MeV γ-ray 66.2% of the time [173]). The γ-ray scatters off an electron in the detector the scattered electron then produces an optical signal within the detector via the Cherenkov effect described in Section 5.2.1. As the source produces γ-rays of a known energy its main purpose is to determine the response of the detector to interactions of a certain energy happening at a certain position within the detector. The ^{16}N isotope can also decay via the emission of a 7.1 MeV γ 4.8 % of the time, the remaining 28 % of the decays involve no γ ray being produced with the β particle.

^{16}N is initially produced by bombarding ^{16}O (in CO_2) with 14 MeV neutrons in a DT generator [173]. The ^{16}N (which has a half-life of 7.13 s) is then piped down a tube in the umbilical to the ^{16}N source. A schematic of the source is shown in Figure 6.11. The gas is piped into the chamber surrounded by the plastic scintillator shell, if an ^{16}N decays within the chamber the electron produced may interact with the plastic scintillator inside the source causing a flash of light seen by the PMT inside the source. The source PMT is connected to a specific channel in the detector which is used to tag the ^{16}N events.

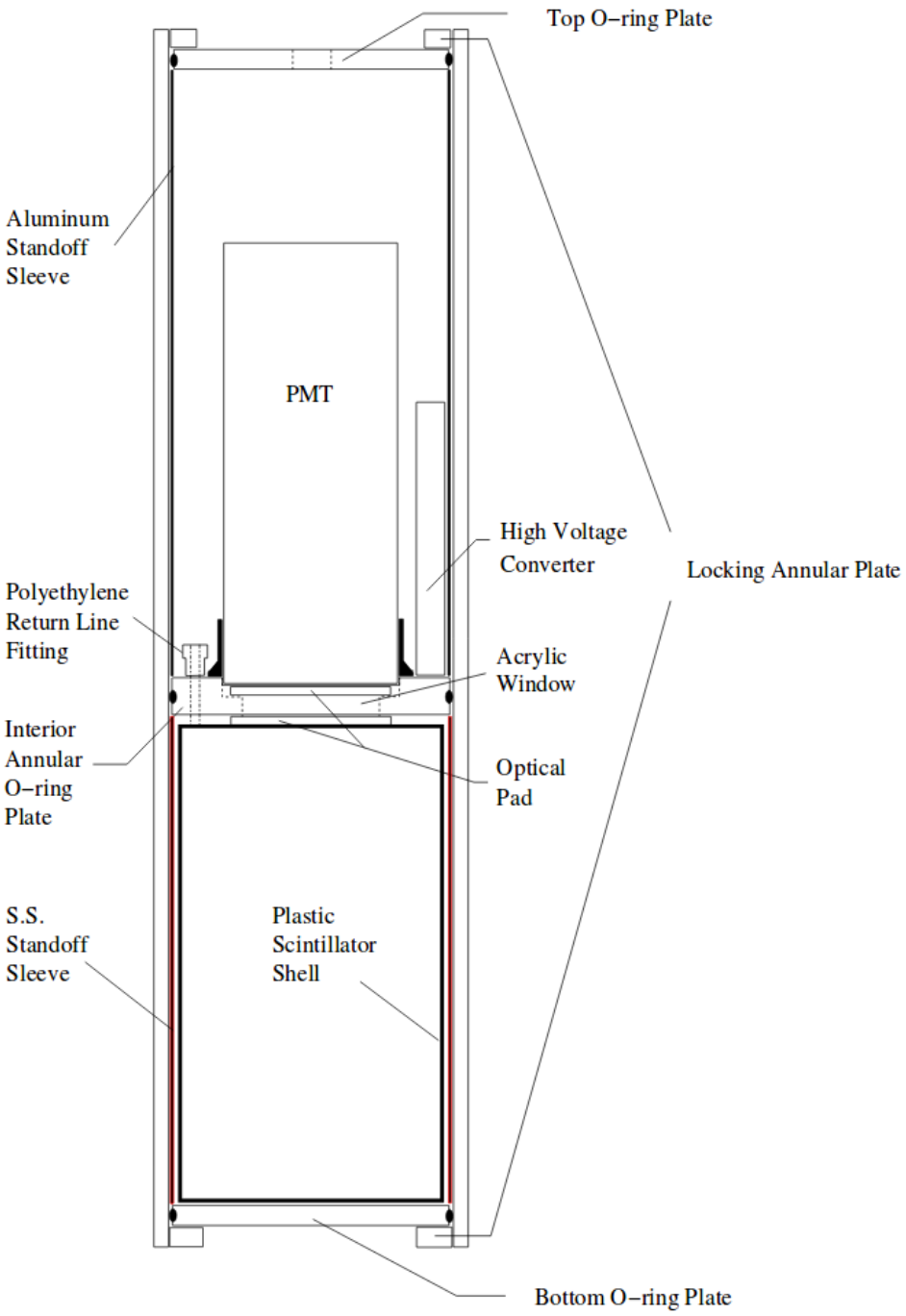

Figure 6.11: Schematic of the ^{16}N calibration source. Taken from [173].

6.4 Calibration of the SNO+ PMT array Angular response

The angular response of a PMT is defined as the number of photons incident on the PMT bucket which successfully produce a photoelectron at the cathode of the PMT as shown in Eq. 6.3. In order to successfully reconstruct physics events within the detector the

angular response of the PMTs must be well understood. Visual inspections of the light concentrators on the PMT bucket face found that some degradation of concentrators has occurred (as shown in Figure 6.12) as a result of being submerged in UPW during the course of the SNO experiment. Furthermore, throughout the commissioning period of SNO+ the detector has not been fully filled. This has resulted in the PMTs at the bottom of the detector being submerged for longer than those at the top, it is thought that there may be a height dependence on the angular response of the PMTs.

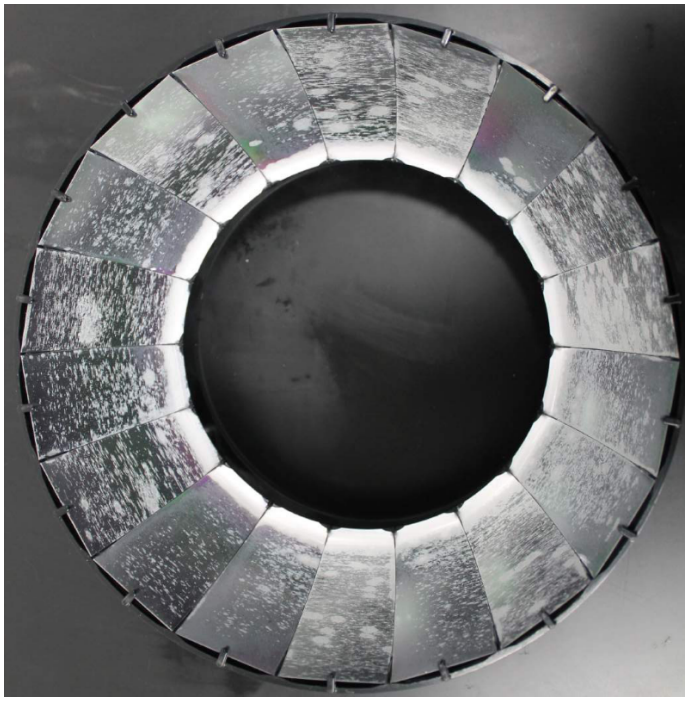

Figure 6.12: A badly degraded concentrator taken from the SNO+ experiment [174].

$$R(\theta) = \frac{N_{\text{p.e.}}(\theta)}{N_{\gamma}(\theta)} \tag{6.3}$$

The distribution of light from physics events within the detector can be approximated by a sphere within which photons are generated uniformly in volume and isotropically in direction. Figure 6.13 shows the normalised angular distribution of light relative to the normal of the PMTs for two spheres both centered at the centre of the detector. One sphere has radius of 3.5 m corresponding to the proposed $0\nu\beta\beta$ fiducial volume whereas the second sphere has radius of 6 m corresponding to the entire inner AV region.

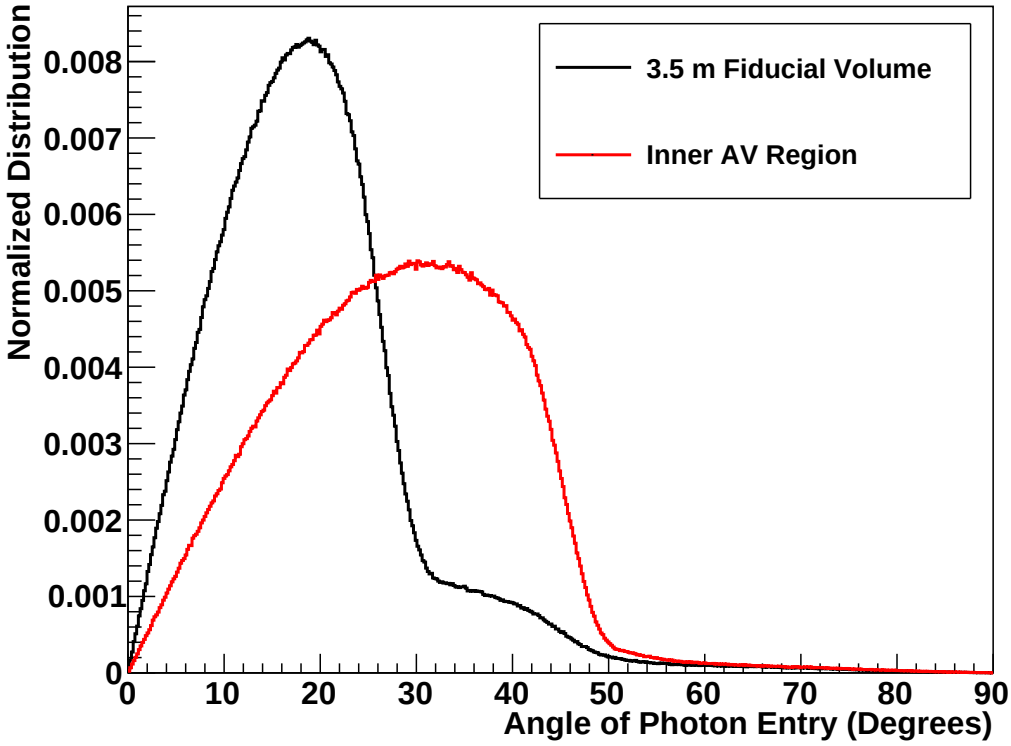

Figure 6.13: Angular distribution of light from two isotropic spheres of light centered at the origin, with radii 3.5 m and 6 m.

It can be seen from Figure 6.13 that the majority of light enters PMTs at angles less than 50° hence any calibration scans hoping to measure this should produce an angular distribution in the range 0° to 50°. The laserball scan will provide an initial measurement of the response of the PMTs, this in turn can then be verified using the ^{16}N source. Both scans should cover the entire 0-50° region, across the entirety of the detector.

The shoulder between 30° and 50° seen for the 3.5 m fiducial volume is a result of scattering of the light in the detector. Figure 6.14 shows the angle between the initial photon direction and the position of the PMT hit against the angle of entry on the PMT. The photons entering between 30° and 50° are a result of forward scattering and backscattering in the detector at larger angles.

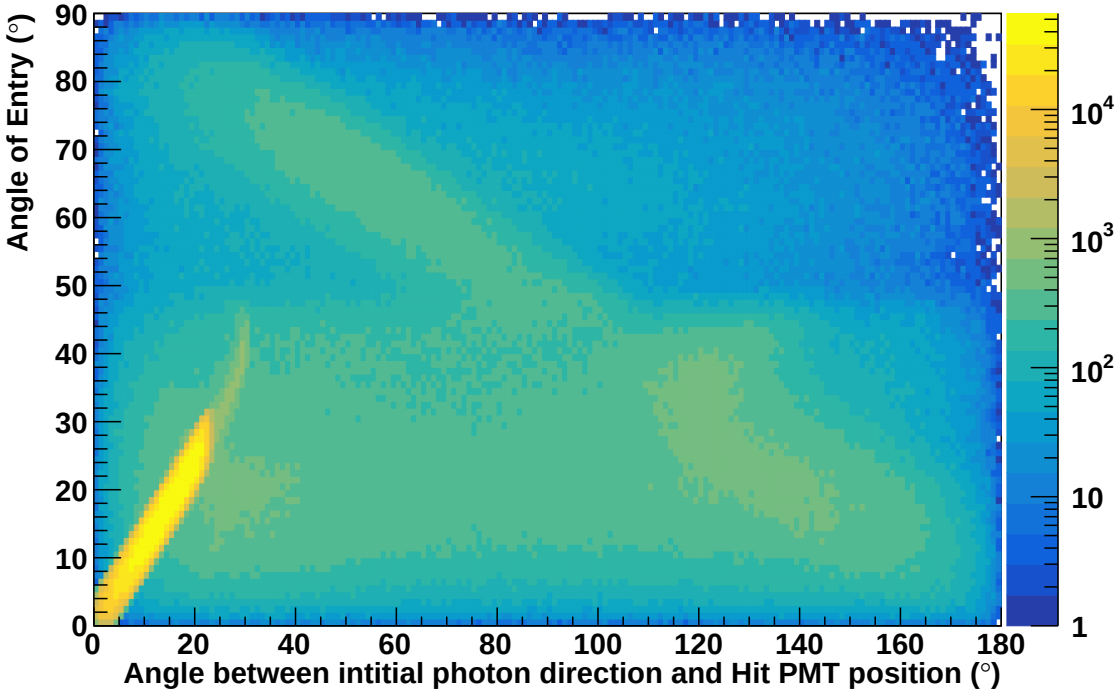

Figure 6.14: The angle between the initial photon direction and the hit PMT position against the angle of entry into the PMT bucket. The distribution shown is for an isotropic homogeneous sphere of light positioned in the center of the detector with radius 3.5 m.

6.4.1 Method

Scans were proposed by the calibration and optics groups of the SNO+ collaboration. The scan positions of the laserball scan was developed by the optics group. The ^{16}N scan was originally developed by Matt Mottram, with further developments made by me. The scan positions are shown in the appendices A.1 and A.3. RAT simulations were performed with the sources in the listed positions. The angle at which the photon enters the PMT bucket is stored for both photons which do and do not generate a photoelectron. The data is binned in angle relative to the PMT normal as shown in Figure 6.15. The angular response is calculated for each angular bin via Eq. 6.3. The uncertainties on each bin are Poissonian so the total uncertainty on the angular response is given by Eq. 6.4.

$$\sigma(R(\theta)) = \frac{N_{\text{p.e.}}}{N_\gamma}\sqrt{\frac{1}{N_{\text{p.e.}}} + \frac{1}{N_\gamma}} \tag{6.4}$$

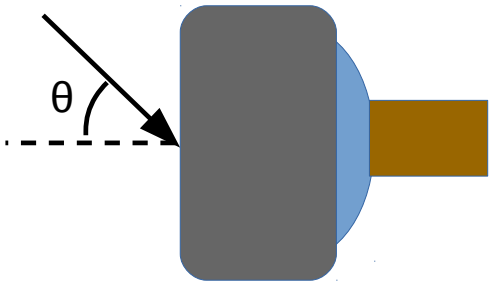

Figure 6.15: θ the angle of incidence on the PMT is used to define the angular response. The grey box is the concentrator, as seen in Figure 6.12

6.4.2 Measurement of the Angular Response using the Laserball

Simulations of the laserball positioned in the positioned detailed within appendix, all dye wavelengths shown in Figure 6.3, except for Kiton-Red are used at each position in the scan. The number of pulses simulated at each position is weighted by the amount of time spent at each position in the proposed scan. In the proposed scan the laserball is pulsed at a rate of 40 Hz, in the proposed scan the laserball should be positioned at the origin for 1 hour resulting in a total of 144×10^3 events. Due to computing limitations only 0.1 % of the proposed events were simulated. The number of photons per laserball pulse was set to 1×10^5. One degree bins were used to calculate the response.

Figure 6.16a shows the normalised angular distribution of light on the PMT array. Figure 6.16b shows the angular distribution of light for various components of the laserball scan. The central positions cause the large peak seen at low angles. At angles between 10° and 40° the internal AV scan provides the majority of the statistics. The guide tube positions external to the AV provide information on the response of the PMTs at high angles.

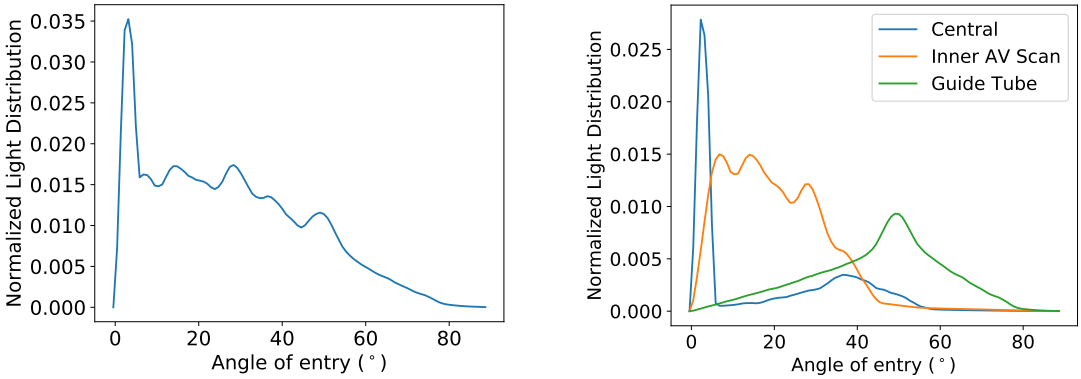

(a) Normalised angular distribution of light incident on the PMTs from the laserball scan.

(b) Normalised distribution of the response separated into various components of the scan.

Figure 6.16: The normalised light distributions from the laserball scan Figure 6.16a shows the overall distribution, whereas Figure 6.16b shows the distribution split into its constituents.

The angular response defined by Eq. 6.3 is shown in Figure 6.17a. The uncertainty on the angular response scaled by a factor of 10 is identified by the red band surrounding the line. The relative uncertainty on the angular response is shown in Figure 6.17b.

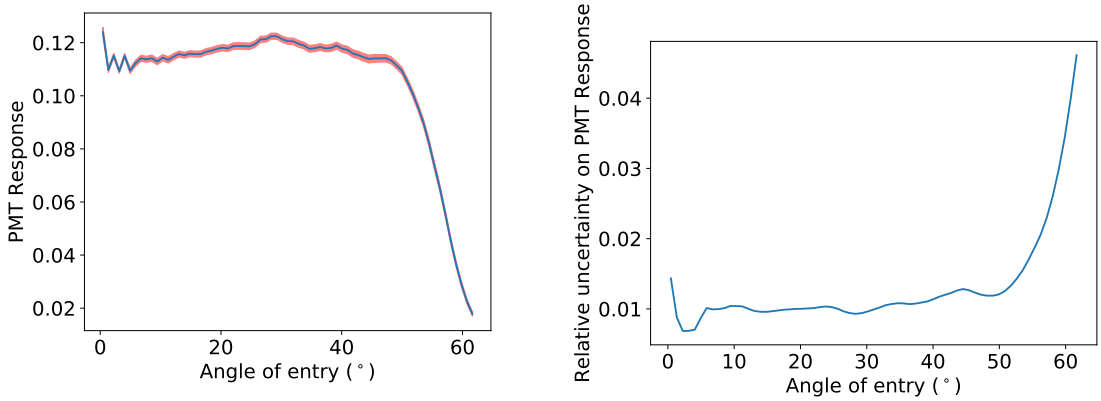

(a) Angular response as calculated by the laserball scan. The red band indicates the error on the measurement scaled up by a factor 10.

(b) Relative uncertainty on the angular response.

Figure 6.17: The measured angular response from the laserball and its relative uncertainty.

As mentioned previously it is possible there may be Z dependence on the response of the concentrators, the scans must produce adequate coverage over the entire height of the detector. PMTs were grouped via their position on the Z axis Figure A.1 in Appendix A shows the angular response for these PMTs.

6.4.3 Improvement in the measurement of the angular response by using the new laserball neck

In order to see the improvement of the measurement of the angular as a result of the new laserball neck simulations were run using the mask functions shown in Table. 6.1. Only the Coumarin-500 wavelength was simulated. For the old neck a total of 1×10^4 photons were simulated per pulse, for the new neck 10 672 photons were simulated per pulse , this is due to the reduced shadowing of the new neck described by Eq. 6.2.

The angular light distributions incident on the PMTs for the upper hemisphere of the detector produced by both necks are shown in Figure 6.18.

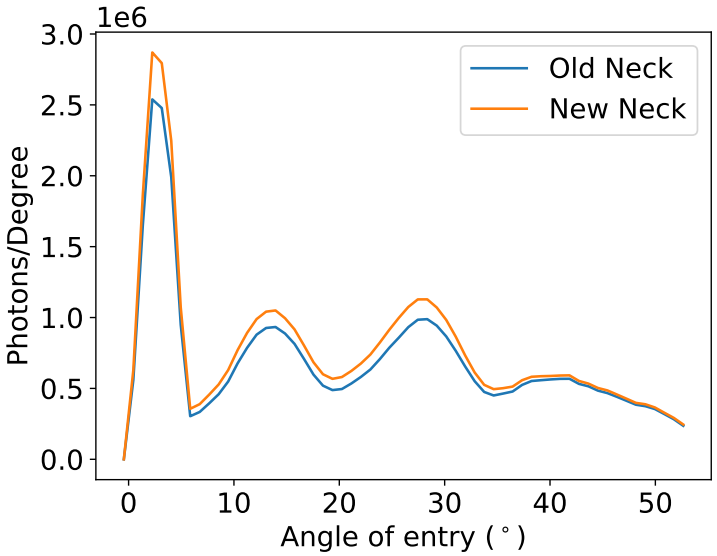

Figure 6.18: The angular distribution of light incident on the PMTs from both laserball necks for the upper hemisphere of the detector

The error on the measurement of the angular response for both necks and the error ratio of the necks for PMTs in the upper hemisphere of the detector is shown in Figure 6.19, the error ratio is approximately 93-94% for the new neck when compared to the old neck measurements up to 30°, past this angle the uncertainties are approximately equal for both the new and the old neck.

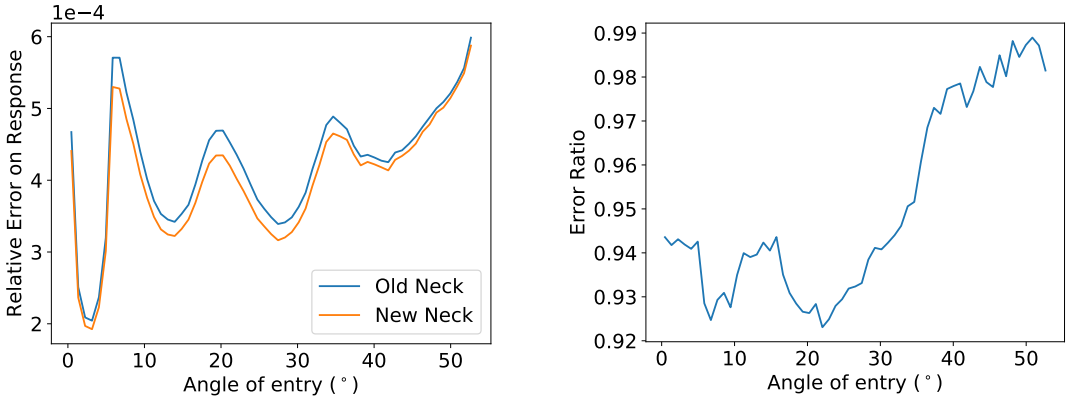

(a) Relative error on the angular response for both necks for PMTs in the upper hemisphere.

(b) Ratio of Errors from both necks (New Neck/Old Neck)

Figure 6.19: The relative uncertainties on the angular response from both necks and their ratio as a function of angle for PMTs in the upper hemisphere.

The new neck will have the most significant effect for PMTs at the top of the detector. Figure 6.20 shows the angular distribution of light for both necks for PMTs higher 5.4 m above the equator of the detector.

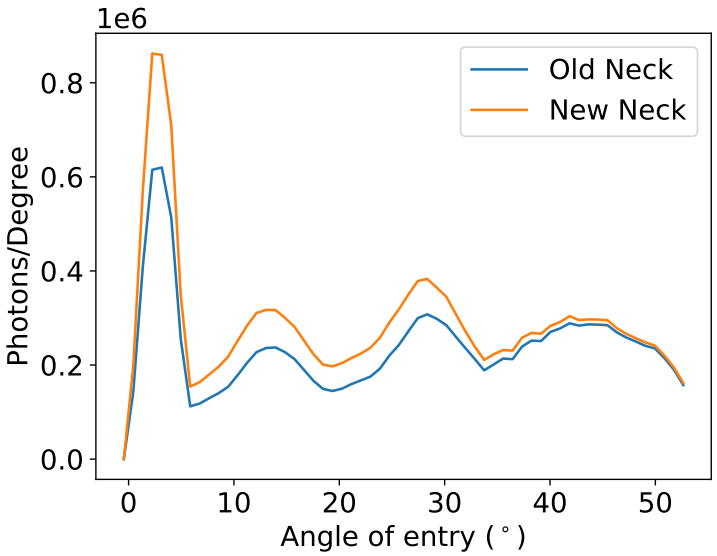

Figure 6.20: The angular distribution of light incident on the PMTs from both laserball necks for the PMTs above 5.4 m above the equator.

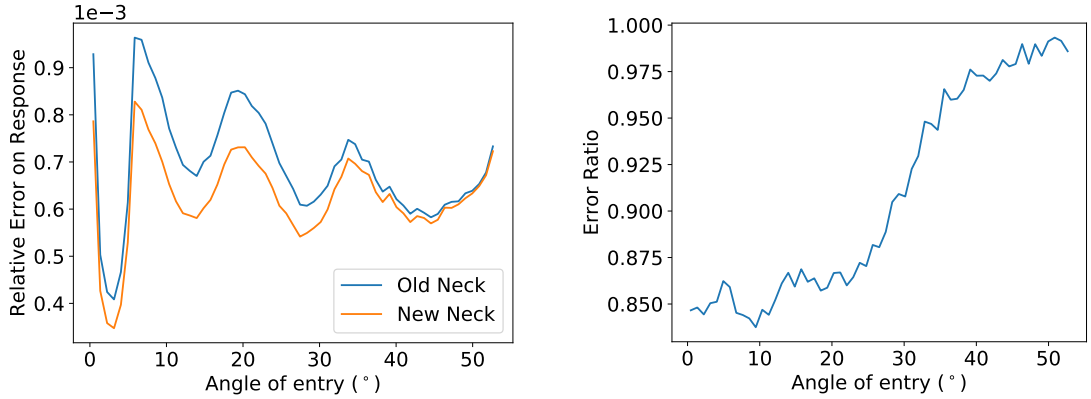

(a) Error on the angular response for both necks for PMTs near the top of the detector.

(b) Ratio of Errors from both necks (New Neck/Old Neck)

Figure 6.21: The relative uncertainties on the angular response from both necks and their ratio as a function of angle for PMTs above 5.4 m above the equator.

The relative uncertainties on the angular response for both necks and their ratios are shown in Figure 6.21. The new neck produces a 14% improvement in the angular response measurement for small angles, at 30° there is still a 10% reduction in error of the angular response. Past 30° the reduction in the error rapidly decreases, beyond 40° there is no real improvement when using the new neck relative to the old neck.

6.4.4 Verification of the Angular response using the ^{16}N Source

The same procedure was performed for the ^{16}N source using the scan positions detailed within Appendix A.3. In each position a total of 1×10^5 events were simulated. In the proposed scan the source is positioned at each location for 15 minutes. The flow of ^{16}N gas from the DT generator is tuned to obtain a tagged event rate of approximately 40 Hz, resulting in approximately 3.6×10^5 events in each position. The angular distribution of light can be seen in Figure 6.22.

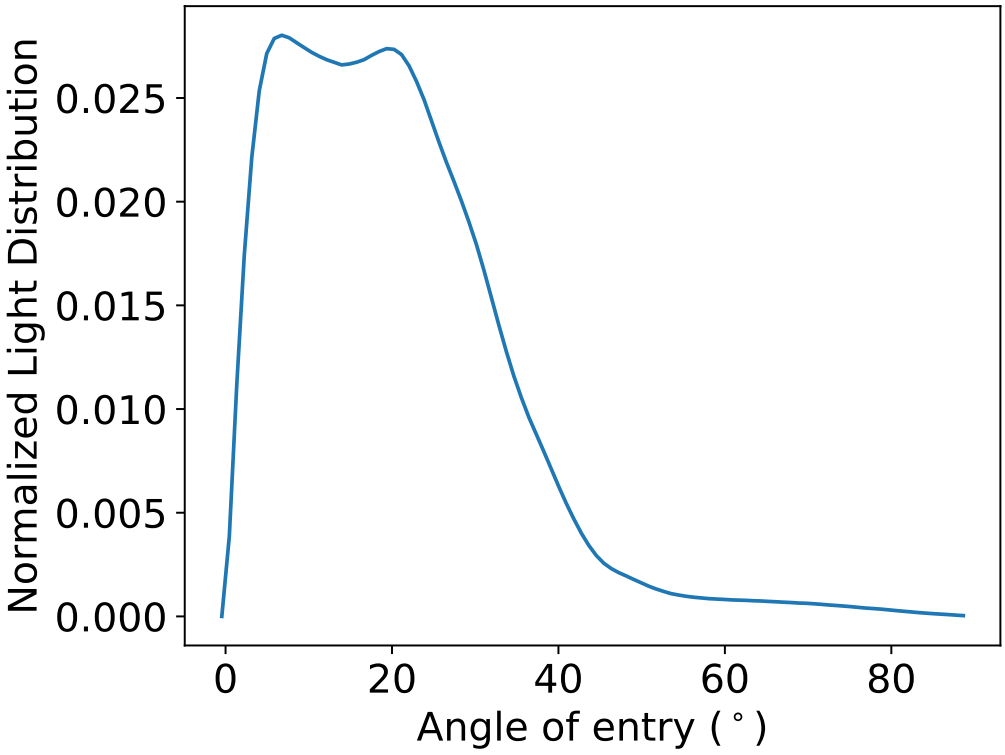

Figure 6.22: The angular distribution of light from the simulated ^{16}N scan.

The angular response and its uncertainty are calculated using using Eqs. 6.3 and 6.4, and are shown in Figure 6.23.

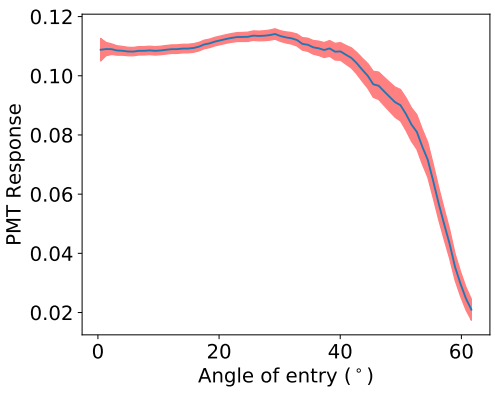

(a) Angular response as calculated by the ^{16}N scan.

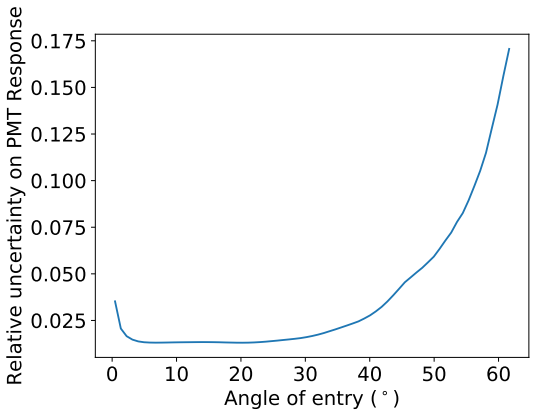

(b) Relative uncertainty on the angular response.

Figure 6.23: The relative uncertainty on the angular response from the simulated ^{16}N source scan.

6.4.5 Summary of the Measurement of the Angular Response

In conclusion, both the ^{16}N and laserball scan cover the entire angular physics angular distribution. The accuracy of the measurement of the angular response using the laserball, is reduced for PMTs at the top of the detector compared to those at the bottom. A new laserball neck was designed to increase the amount of light reaching the top of the detector. For the PMTs at the top of the detector an reduction in the error in the angular response measurement of approximately 10-15% is seen for angles smaller than 30°. At angles larger than this no improvement is seen relative to the old neck.

6.5 ELLIE

Every time a source is deployed within the detector there is a chance of radioactive contamination of the detector caused by radioactive isotopes leaching from the source or its manipulator ropes into the detector. Figure 6.24 shows the activity of ^{222}Rn measured by BiPo coincidences, after calibrations with a source deployed the activity increases significantly after calibration runs have been performed.

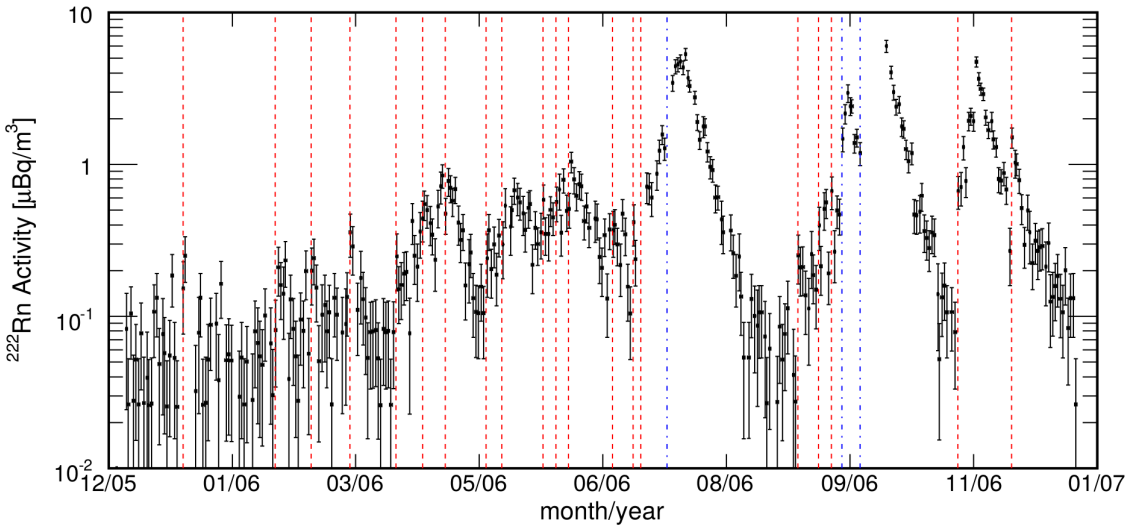

Figure 6.24: The activity of ^{222}Rn in the KamLAND detector over time. The red lines indicate where a calibration source was deployed on the central axis of the detector, and the blue lines indicate off axis deployment which requires additional manipulation ropes to be deployed within the detector. Taken from [175].

In order to meet the strict radiopurity requirements required to perform a $0\nu\beta\beta$ search with SNO+ several optical sources have been installed externally to the AV by mounting optical fibres to the PSUP this allows the optical calibration without the risk of radioactively contaminating the detector. This calibration system is known collectively as ELLIE

(External LED/Laser Light Injection Entity), and consists of three subsystems TELLIE, SMELLIE and AMELLIE. The subsystems are distinguished via their light sources and the type of fibre used to transport the light into the detector.

6.5.1 TELLIE

TELLIE is designed to perform a continuous timing calibration of the PMT array of SNO+, 92 PMMA fibres are mounted on the PSUP pointing across the AV each fibre covers a region of PMTs on the opposing face of the detector. The deck above the detector hosts the TELLIE driver systems which are tuned to inject O(1000) photons peaked at a wavelength of 506.2 nm into the detector per pulse, at this intensity approximately one photoelectron will be produced at each of the PMTs within the beamspot meaning a measurement of the time walk on the PMTs can be made. A PIN diode is attached to each LED to perform an internal measurement of the intensity of the LED.

When TELLIE fires, a trigger signal is sent to the detector electronics to tag TELLIE events. The tagging of TELLIE events allows the pulsing of TELLIE whilst taking physics data meaning the PMT array can be continuously calibrated.

6.5.2 SMELLIE

SMELLIE is the Scattering Module of the ELLIE system. It uses multiple fixed wavelength lasers with wavelengths of 375, 405, 440 and 500 nm and a super continuum laser, which can have a range of wavelengths from 400 to 700 nm with bandwidth of 10 nm [176]. A monitoring PMT receives some light via a beamsplitter and is used to monitor the pulse intensity on a per pulse basis. The lasers are routed into a fibre switch via 1 m patch fibres, fifteen 45 m fibres connect the switch and the mounting points in the detector, the fibres have a 50 µm quartz core. The fifteen fibres are mounted at five nodes inside the detector at angles of 0°, 10° and 20°. At the end of each of the fibres installed in the detector a collimator has been installed to reduce the opening angle of the light from 11° to approximately 3°. To measure the scattering distance in the detector, the ratio of scattered light and direct beam light to the total amount of light seen inside the detector will be compared with MC data produced with different scattering lengths.

6.5.3 AMELLIE

The AMELLIE system is used to measure the attenuation of the scintillator cocktail over time. The schematic of the AMELLIE light source is identical to a single TELLIE box

with 8 channels except for the replacement of the 506 nm TELLIE LEDs with different wavelength LEDs tuned for the scintillator cocktail used. As the cocktail had not yet been finalised during the commissioning of the AMELLIE system TELLIE 506 nm LEDs were used. Light is transmitted into the detector via quartz fibres with a wide opening angle of approximately 5°. The fibres are mounted at four nodes in the detector pointing at angles of 0° and 10° relative to the centre of the detector. The AMELLIE box is controlled using the same hardware in place for TELLIE. To measure the attenuation a similar procedure to SMELLIE is being developed by comparing the in beam to scattered light ratio with Monte Carlo.

6.5.4 Calibration of the angular response of the PMTs using the TELLIE reflected light

It was proposed that it may be possible to calibrate the angular response of the PMTs by comparing the occupancy of the PMTs in the direct beamspot with the PMTs in the reflected beamspot. To determine the feasibility of this simulations of two TELLIE fibres were run and the angular distribution of the photons entering the PMTs in the reflected and direct beamspot regions was obtained. The direct beamspot was defined as PMTs within 20.0° of the fibre direction, and the reflected beamspot was defined as the region of PMTs which were within a certain distance of the fibre, this range was taken from 0.5 m to 3.5 m in steps of 0.5 m. No timing cut was applied to either the direct or reflected light in the beamspots, the reflected beamspot will contain both far and near AV reflections, both beamspots will contain light from scattering in the detector. The two fibres simulated were FT040A (A fibre close to the equator of the detector) and FT079A (A fibre at the bottom of the detector).

Figure 6.25 shows the proportion of reflected photons relative to the number of photons in the direct beamspot as a function of the reflected light beamspot radius. Both fibres show a low ratio of reflected against direct light, the total proportion of reflected light is less than 5% of that seen in the direct beamspot. Any calibration will require very high statistics TELLIE data to infer anything about the angular response of the PMTs.

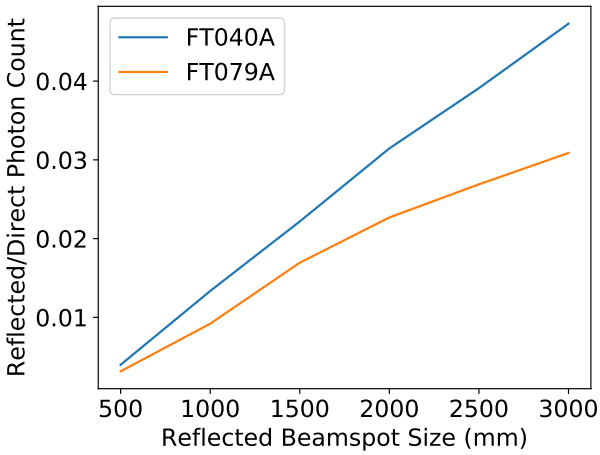

Figure 6.25: Ratio of reflected photon count to direct photon count for fibres FT040A and FT079A as a function of reflected cut distance.

The stacked angular distribution of reflected light from fibre FT040A for various reflected distance cuts is shown in Figure 6.26. As the reflected radius cut is increased light begins to enter the PMTs at higher angles. With the maximum distance cut, the majority of light enters the PMTs at angles smaller than 25° beyond this less than 1% of the total reflected light enters per degree. As the distance cut is reduced, the distribution becomes more sharply peaked with more light entering at smaller angles.

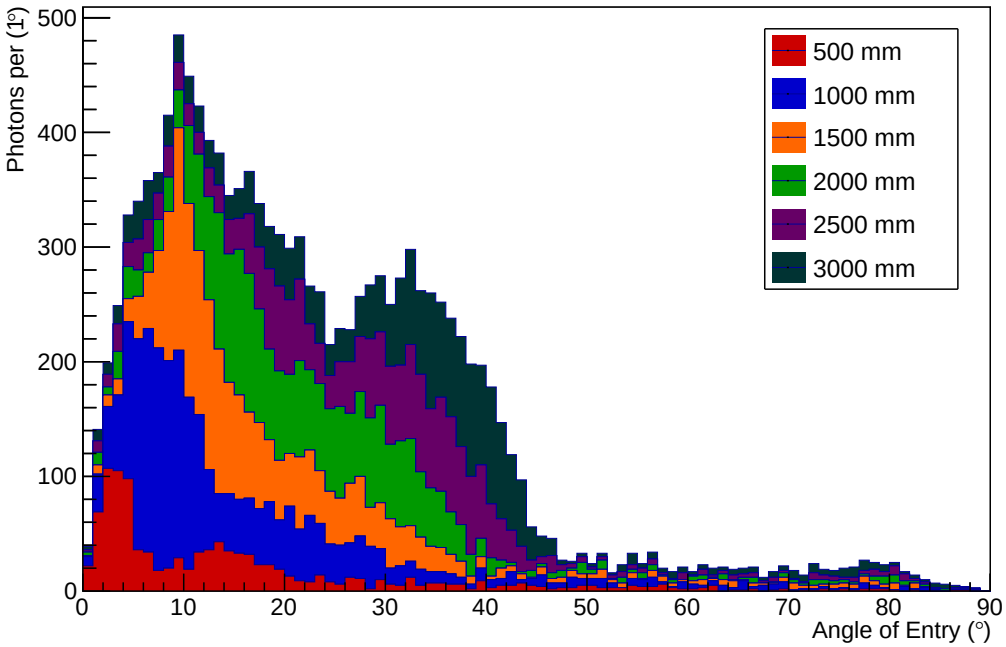

Figure 6.26: Angular distribution of reflected light off of the AV for PMTs within varying distance cuts of the fibre.

A comparison of the angular distributions for the two fibres is shown in Figure 6.27. FT079A is pointing towards the bottom of the AV which is a particularly featureless part of the AV, whereas as FT040A is at the equator of the detector, and the distribution of reflected light may be effected by the ropes and belly plates. The angular distribution of FT040A has significantly more light than FT079A at higher angles, it is expected that this is caused by reflection off an uneven part of the AV near the belly plates.

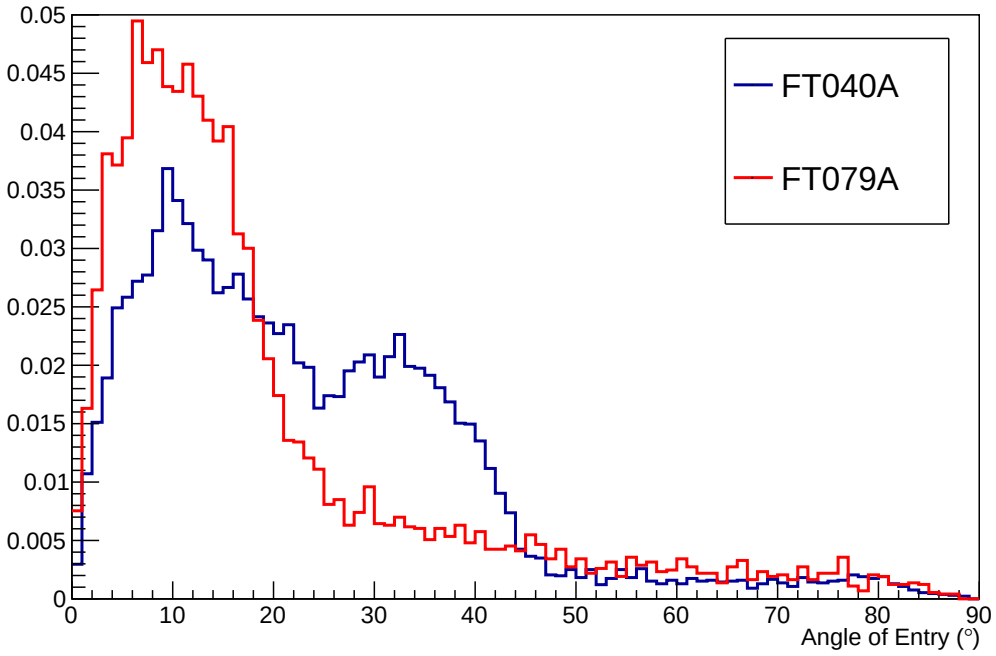

Figure 6.27: Comparison of the angular distribution of light entering the PMTs for both fibres when a 3.5 m distance cut is used.

Although the belly plates appear to cause light to reflect into PMTs at large angles, the low statistics of the reflected light represent a severe limitation in the measurement of the angular response with reflected light. A measurement of the angular response of the PMT array using TELLIE reflected light is not feasible.

6.5.5 The ELLIE nearline processors.

The ELLIE nearline processors are designed to perform the necessary tasks required immediately after a ELLIE run has completed. At the time of writing processors exist for both SMELLIE and TELLIE. The scripts serve two main purposes listed below.

- The upload of the run tables to RATDB

- The running of the data quality processors and the conversion of the output for display on a webpage.

The code first checks if the run is a TELLIE or SMELLIE run by examining its run type. If the run is a ELLIE run the code first uploads the the run information to the database. The code then constructs a rat macro from a template with the input files and the run settings. The code then runs the data quality processor on the input file, converts the output and transfers it to a webpage to be viewed by the operator.

The Data Quality Monitoring Webpage

The ELLIE data quality monitoring webpage displays the check results for each run, a detailed description of the checks performed by the TELLIE processor can be found in [166]. A list of recent TELLIE runs is shown any runs for which there is no DQ information as shown in Figure 6.28.

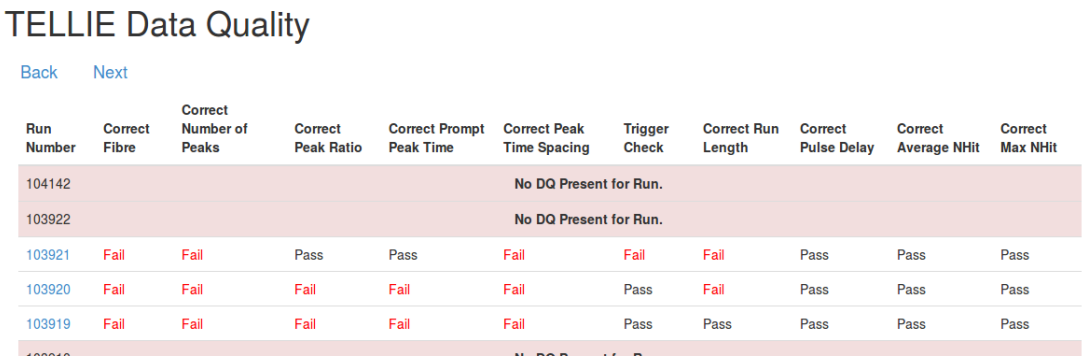
TELLIE Data Quality

Back Next

Run Number	Correct Fibre	Correct Number of Peaks	Correct Peak Ratio	Correct Prompt Peak Time	Correct Peak Time Spacing	Trigger Check	Correct Run Length	Correct Pulse Delay	Correct Average NHit	Correct Max NHit
104142					No DQ Present for Run.					
103922					No DQ Present for Run.					
103921	Fail	Fail	Pass	Pass	Fail	Fail	Fail	Pass	Pass	Pass
103920	Fail	Fail	Fail	Fail	Fail	Pass	Fail	Pass	Pass	Pass
103919	Fail	Fail	Fail	Fail	Fail	Pass	Pass	Pass	Pass	Pass

Figure 6.28: The overview of previous TELLIE runs. If the nearline process has failed the run is marked in red.

By clicking on a particular run a list of the check results for individual subruns are shown. Each TELLIE run is split into subruns consisting of 5000 shots each in order to make a PIN reading to monitor TELLIEs intensity. For an entire run to pass a given check, all subruns must also pass the same check. The subrun table is identical to that shown in Figure 6.28.

In the same way that choosing a particular run reveals information on the list of subruns clicking on a particular subrun reveals details about it. A list of statistics from the run is displayed (Figure 6.29) as well as a selection of the plots produced by the processor (Figure 6.30).

Run information for run 102300 subrun 6

Parameter	Value
Expected Number of TELLIE events	5000
Actual Number of TELLIE events	5000
Average NHit	38.5808
Greater Than 1000 Nhit Events	0
Fibre Firing	FT013A
Calculated Fibre Firing	FT017A
Number of TAC peaks (Should be 3)	3
Pre peak TAC count	2785
Prompt peak TAC count	2345
Late peak TAC count	1685
Run Time	7.3113417
Proportion of TELLIE events with correct pulse delay seperation	1

Figure 6.29: The statistics table detailing the results of the subrun.

TELLIE Data Quality Plots for run 102300 subrun 6

PSUP Hit Map

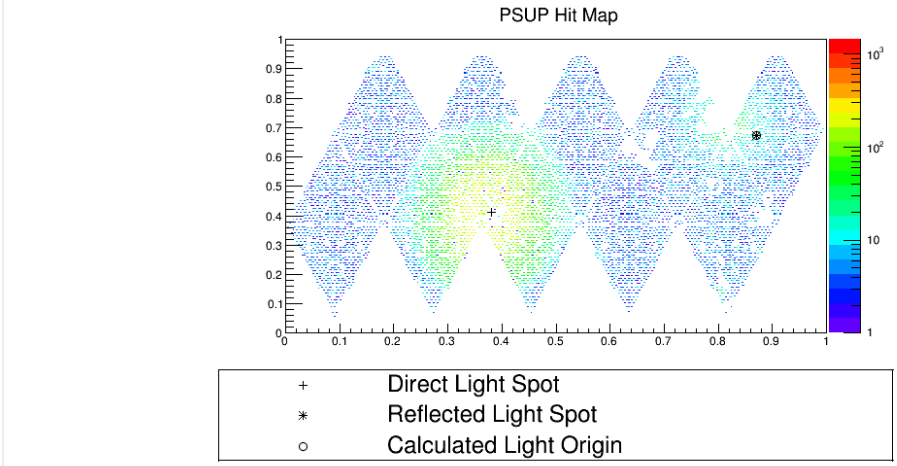

Figure 6.30: One of the plots produced by the data quality processor displayed on the web page.

Chapter 7

TELLIE

This chapter describes the Timing component of the External LED/Laser Light Injection Entity (TELLIE). The chapter first describes the operating procedure of TELLIE. A detailed description of the TELLIE hardware is then presented. The procedure to calibrate TELLIE is presented the results from stability tests of a TELLIE channel are also presented. In situ measurements of the performance of TELLIE are shown. The chapter concludes with a study into the effect of the extended submersion of the TELLIE fibres in UPW on their optical transmission properties.

7.1 Timing calibration using TELLIE

TELLIE is used to calibrate the timing of the PMT array of SNO+. The TELLIE system is designed to fire light at an intensity such that a single photon hits the PMTs. Due to mode mixing in the fibre described in Section 7.2.4 there is a correlation between the time at which light leaves the fibre end and the angle a photon leaves, this means that alone TELLIE cannot be used to determine the timing properties of the PMTs and must be used in conjunction with the laserball. Once the timing and angular correlations of a fibre have been calculated, the time walk on the PMTs can be found by plotting the charge deposited against the hit time of the PMT as shown in Figure 7.1. The increase in hit time for low charge hits identifies the time walk.

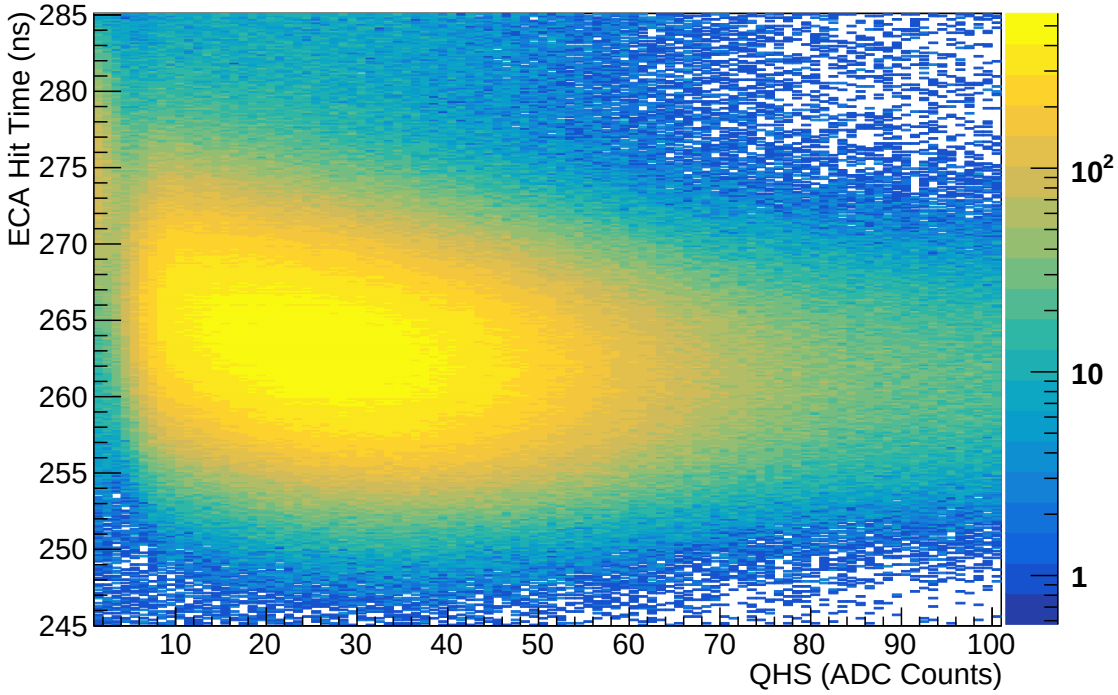

Figure 7.1: QHS against the ECA hit time of the PMTs in the TELLIE beamspot. Taken using fibre FT040A. Run number 101553.

7.2 TELLIE Hardware

TELLIE consists of 96 LEDs peaked at 506.2 nm. The 96 channels are divided between twelve boxes each with eight channels. A image of the inside of a TELLIE box is shown in Figure 7.2. Each channel consists of an LEDs which is driven by a push-pull driver and a PIN diode designed to internally monitor the light output of the LED. Each LED has its own driver board whereas each PIN board is shared between four channels. To transmit light into the detector PMMA optical fibres are used. In total there are 92 fibre positions in the PSUP facing radially inwards. The fibres have a wide enough beam spot such that if a fibre were to failed adjacent fibres would still cover the region of the failed fibre.

Figure 7.2: The internals of a TELLIE driver box. The eight small boards at the bottom of the image are the LED driver boards. The LEDs and the PIN diodes are encased in the brass fittings shown in the center of the image. The two larger boards at the top of the image are the PIN diode monitoring boards.

7.2.1 TELLIE LEDs

The TELLIE LEDs are peaked at 506.2 nm, the wavelength was selected to reduce Rayleigh Scattering and absorption in the scintillator cocktail as much as possible but still in a region of high quantum efficiency of the PMTs [166] [164]. The TELLIE spectrum along with the absorption length and the quantum efficiency of the SNO+ PMTs is shown in Figure 7.3.

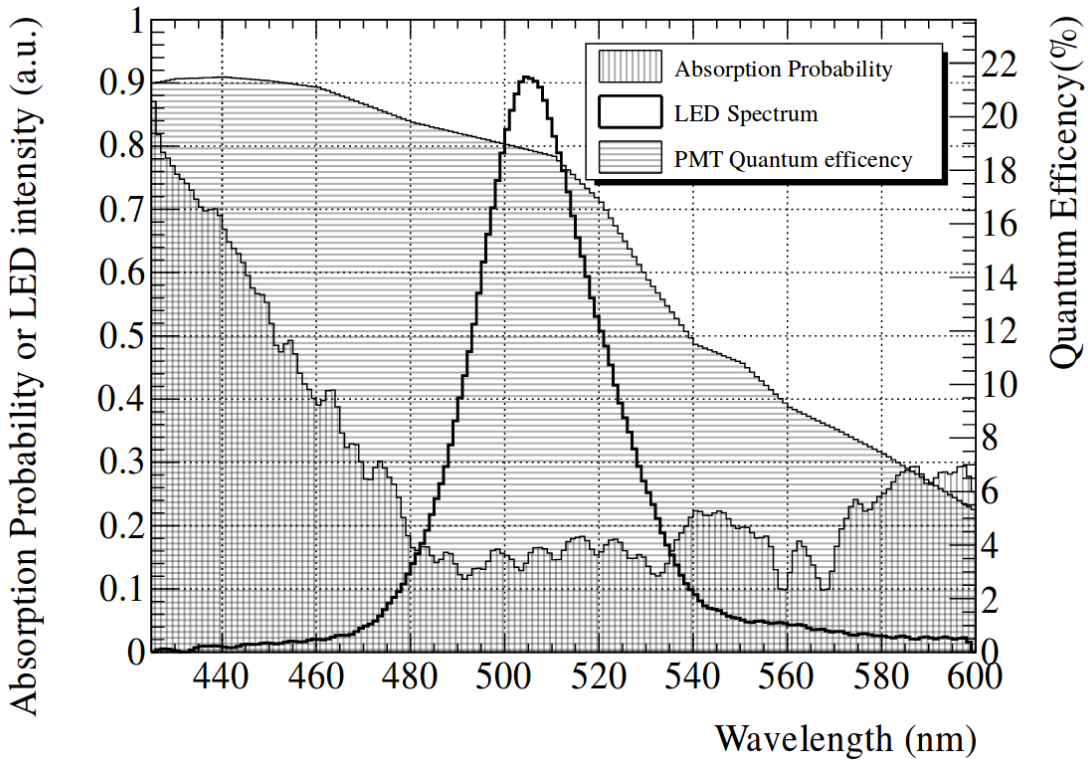

Figure 7.3: The LED spectrum of a TELLIE fibre overlayed with the absorption of the scintillator Tellurium cocktail and the quantum efficiency of the PMTs [177].

The lens of each LED is drilled out and a internal patch fibre is glued into the hole. The coupling is encased in a brass fitting with a PIN diode to prevent light leaks via the fibres. The coupling and the encasing are shown in Figure 7.4.

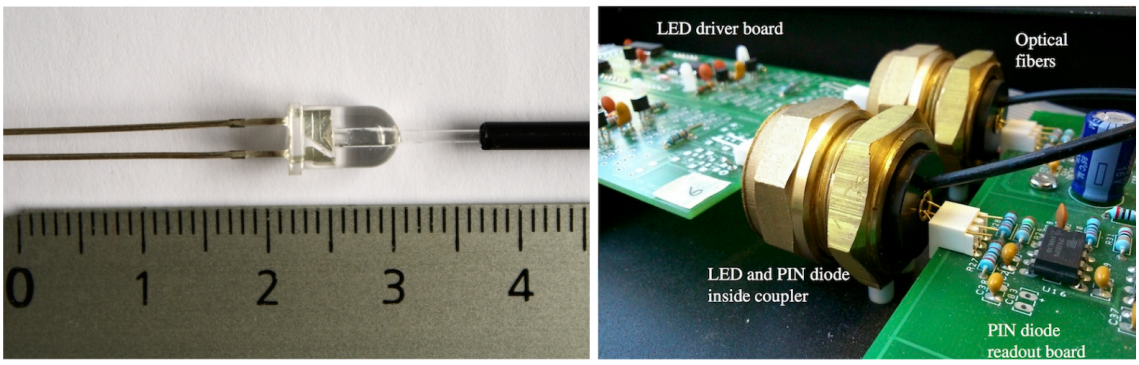

Figure 7.4: The LED coupling and the casing for the LED fibre couplings [177].

7.2.2 TELLIE push-pull driver

An image of the TELLIE driver board can be seen in Figure 7.5, each LED has its own driver board. The LED is attached to the driver via the white adapter to the right of the image. The driver board operates by first applying a potential difference across the

driver such that it is reversed biased, the size of the bias can be set via parameter I_{OP}. The potential difference is only applied for a limited amount of time which is tuned by a parameter I_{BW}. To the potential across the LED is reversed to allow current to pass though, causing the LED to emit light. After a certain amount of time the voltage is reversed back so the LED is once again reverse biased. By applying a reverse bias across the LED the fall time of the LED light pulse is reduced. The time which the potential is reversed is set using the parameter I_{PW}. Further details on the driver boards can be found in [164]. A simplified schematic of the voltage applied to the LED by the driver board as a function of time is shown in Figure 7.6

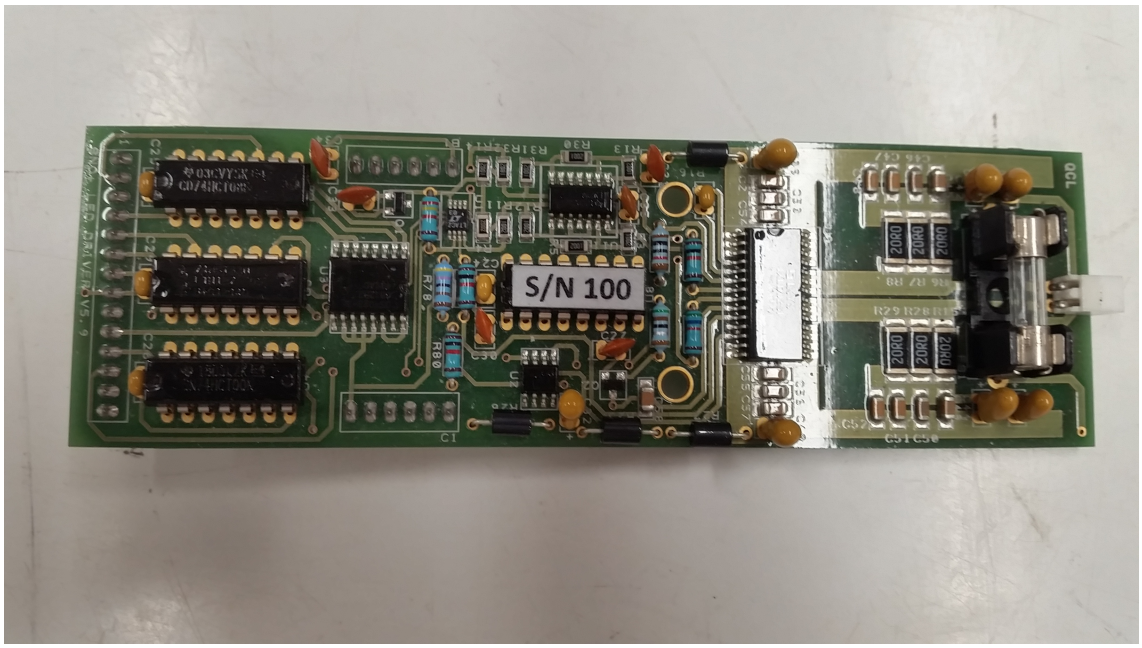

Figure 7.5: A TELLIE LED driver board.

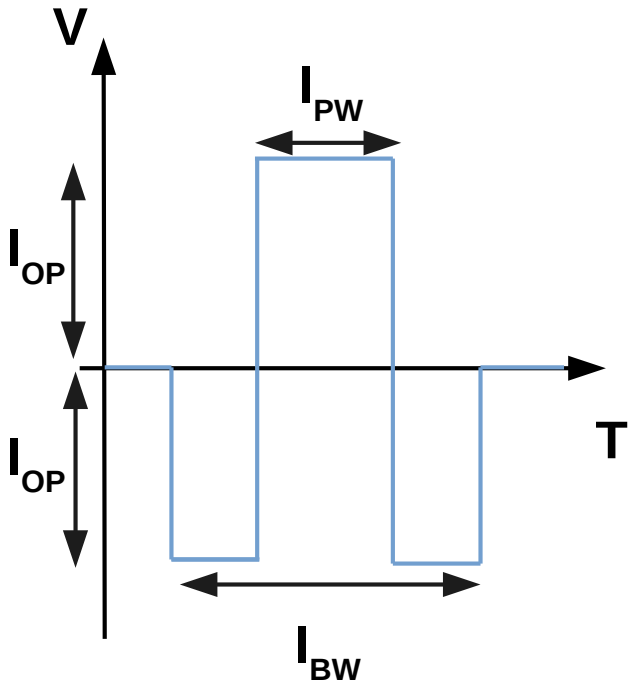

Figure 7.6: Schematic of the voltage across a TELLIE LED when it pulses, the parameters described in the text are labeled. A positive voltage means the LED is forward biased and the led is producing light.

For the normal operation of TELLIE the variables I_{OP} and I_{BW} are fixed at their maximum values, the intensity of the LED pulse is controlled by the parameter I_{OP} [164].

7.2.3 TELLIE PIN boards

The PIN boards provide an internal measurement to the intensity of light produced by TELLIE. The coupling between the LED and the fibre allows some light to spill out into the brass cone encasing the LED, in each cone a PIN diode has been installed. A PIN diode consists of a PIN junction, under a negative bias when a photon hits the intrinsic region of diode electron hole pairs are produced and are then swept across the diode creating a small current pulse. The pulse is then routed through two op-amps before a point on the pulse is read off by an 16-bit ADC. Adjustable potentiometers on the PIN board allow both the gain and pick-off point on the ADC to be tuned. The value returned by the ADC is sent to the PIC chip in the control box which calculates the average and RMS of the PIN readings over a pulse sequence (nominally 5000 pulses). Four channels share a single PIN board, an image of the PIN board is shown in Figure 7.7.

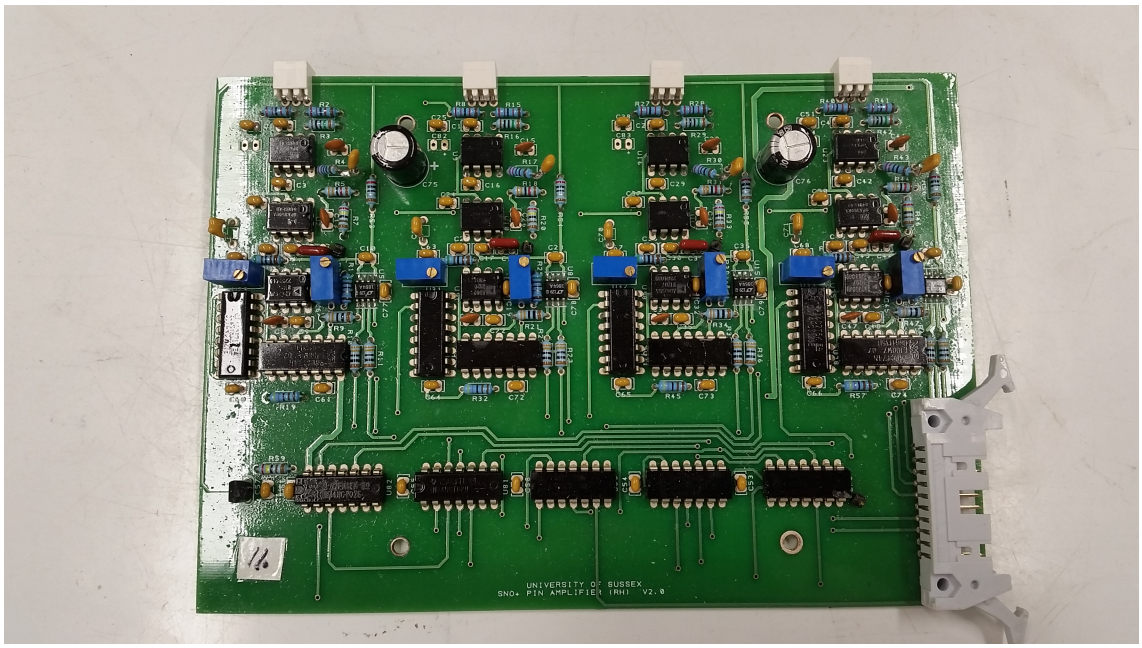

Figure 7.7: A TELLIE PIN board.

7.2.4 TELLIE Fibres

The fibres used by TELLIE are duplex Polymethylmethacrylate (PMMA) fibres, in the case one fibre is broken it is hoped the backup fibre can be used. PMMA fibres were chosen as they are cheaper than quartz fibres as well as being much more durable. The fibre diameter is also much wider than quartz fibres resulting in a much wider opening angle and a larger detector coverage per fibre. All fibres have the same length of 45.5 m. All fibres were tested before installation. At one end of the fibre there is an ST optical connection for attachment to the TELLIE patch panel. The end of fibre inside the detector is attached to a PMT bucket via a mounting plate as shown in Figure 7.8.

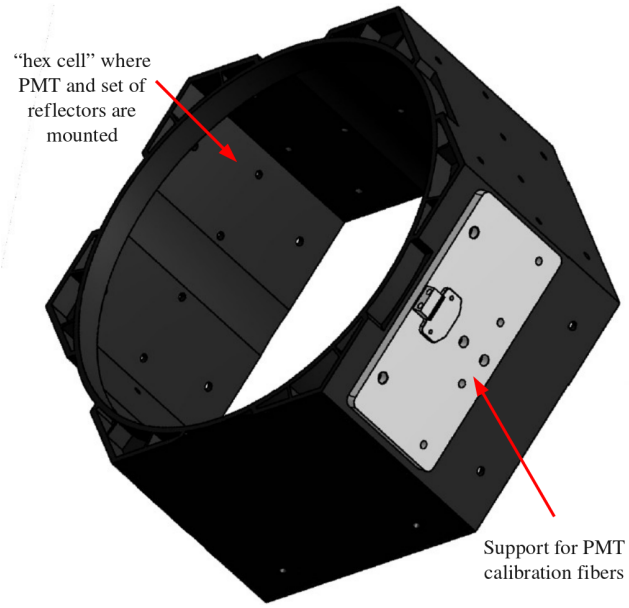

Figure 7.8: The mounting bracket for a TELLIE fibre on a PMT casing [177]

The fibres and their mounting points were tested for radioactivity before installation [177].

Mode Mixing in Fibres

The wide opening angle of TELLIE fibres means they are more susceptible to mode mixing in the fibres. Light emitted at larger angles has a longer path length within the fibre compared to light leaving at smaller angles. A simplified schematic of mode mixing is shown in Figure 7.9 This systematic needs to be corrected for before TELLIE can be used to calibrate the timing of PMTs within the detector.

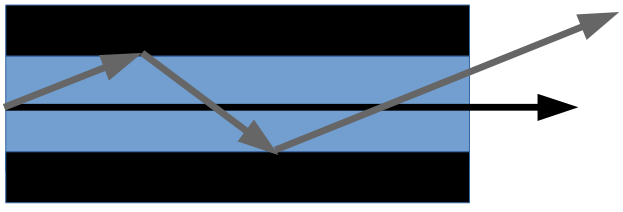

Figure 7.9: Simplified schematic of mode mixing within a TELLIE fibre. The ray of light emitted at low angles indicated by the black line has a shorter path length than the grey line.

7.3 The Calibration Procedure for TELLIE

The calibration procedure for TELLIE involved the determination of three variables as a response to changes in I_{PW}. The values are listed below:

- The light output of TELLIE.
- The PIN response.
- The time delay between the trigger signal and the light pulse.

The light output is measured to find the setpoints for use in TELLIE PCA running, the PIN reading response is measured to tune the PIN reading to a known number of photons. The time offset is measured to ensure the timing stability of TELLIE.

The original calibration procedure and code was developed by Ed Leming and others at Sussex and Lisbon. I performed several calibration runs of all the channels during my attachment at SNOLAB. I also added functionality to perform the slave mode calibrations as well as writing the code to perform the testing of TELLIE for an extended period of time.

A simplified schematic of the setup can be seen in Figure 7.10.

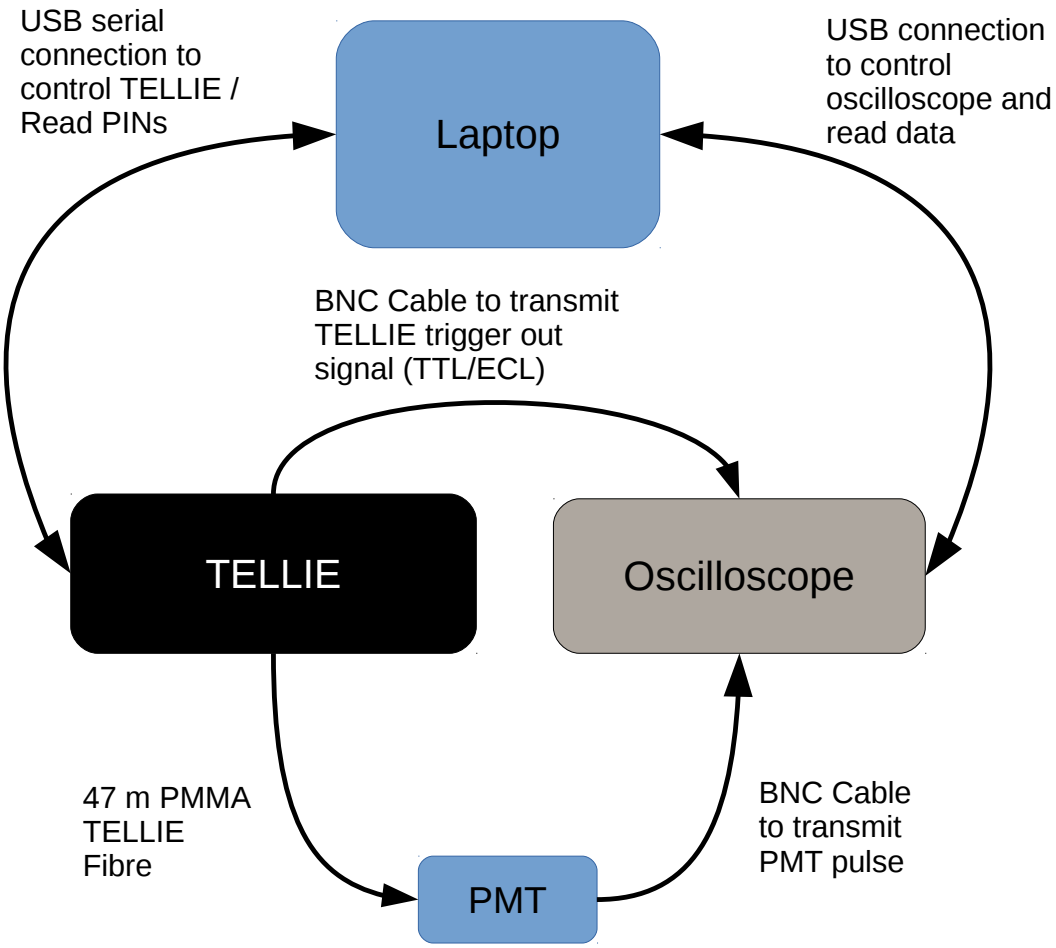

Figure 7.10: Simplified schematic of the TELLIE calibration setup.

Both the scope and TELLIE are controlled by the laptop, both are controlled via USB. The light produced via TELLIE is routed to a Hamamatsu H10721-210 desktop PMT [178] via a 45+2 m optical cable. The 2 m section mimics the patch cable between TELLIE and the patch panel, the remaining 45 m mimics the remainder. The two sections of fibre are connected by the same connection used on the patch panel. The fibre is setup to mimic the genuine path light has to taken from TELLIE to detector and correctly include any light losses incurred. The voltage across the PMT is varied depending on intensity setting of TELLIE.

Both the trigger out signal from TELLIE and the signal from the PMT are sent into the oscilloscope, the traces of which are transferred to the laptop. For calibrations TELLIE is set to generate TTL (Transistor Type Logic) pulses as the specification 0 V to 5 V is

more identifiable on the oscilloscope than the ECL (Emitter Coupled Logic) ($-0.75\,\mathrm{V}$ to $-1.6\,\mathrm{V}$). For the general use of TELLIE the ELLIE ECL triggering is used. During calibrations the scope is always set to trigger on the TELLIE trigger out signal.

The calibration of a TELLIE channel involves two sweeps though the $\mathrm{I_{PW}}$ settings of TELLIE, the first, known as a broad sweep iterates through the entire range of $\mathrm{I_{PW}}$ values. During the broad sweep the PMTs voltage is set to $0.5\,\mathrm{V}$, the sweep is intended to provide an overview of the response of TELLIE. The stepsize during the broad sweep is 250 $\mathrm{I_{PW}}$.

A second sweep is performed in the low intensity range of TELLIE with a smaller $\mathrm{I_{PW}}$ step size. During this second sweep the PMT voltage is increased to $0.7\,\mathrm{V}$. The starting point of the low sweep is determined by the point at which no light can be seen from the broad sweep. The sweep finishes when no light is detected by the PMT. The stepsize during the low sweep is 50 $\mathrm{I_{PW}}$.

The first step of collecting a datapoint in a sweep involves setting the voltage scale of the oscilloscope. TELLIE is pulsed continuously, and the oscilloscope was is set to be triggered on the PMT pulse. The code reduces the scale of each scope division keeping the trigger level (in divisions) constant, i.e. If the scaling was changed from $1\,\mathrm{V}$ to $0.5\,\mathrm{V}$, the trigger level is set to 3 divisions would change from $3\,\mathrm{V}$ to $1.5\,\mathrm{V}$. Ten triggers are collected, the DC offset is corrected for by subtracting the average of the first ten points on the trace (Which are noise) from the minimum value of the trace. The average value of the ten corrected minima is then used to set the scale by finding the scope division size which is smaller than 1/6 of the average.

After setting the scope scale a fixed number of pulses are made, these are used to make the PIN reading for a given $\mathrm{I_{PW}}$ value. TELLIE is then pulsed continuously at the same IPW value until 100 traces are collected. The traces are saved and analysed to obtain the pulse delay and the photon count. Throughout the calibration the oscilloscopes sample rate is set to its maximum value, $2.5\,\mathrm{GS/s}$ or $0.4\,\mathrm{ns/S}$.

The slave mode calibration is performed similarly to the master mode calibration, an Arduino was coded to generate a TTL pulse to trigger TELLIE.

7.3.1 Calculating the number of Photons per Pulse

The number of photons incident on the PMT is proportional to the area of the pulse generated by the PMT. To find the area of the pulse a time cut must first be defined. The code first determines the maximum shot noise on the PMT trace. This is obtained by looking at the start of PMT trace up to $40\,\mathrm{ns}$ before the PMT pulse, the maximum

absolute value of the trace in this region defines the noise level. A cut is then made based on when the pulse crosses 1.5 times this value with an additional $\pm 2\,\text{ns}$ tolerance. The region within the time cut is then integrated over using the trapezium rule. The average area of the 100 collected traces is then used to calculate the number of photons. The area under the PMT pulse (A) is converted to a number of photons (N_p) using Eq. 7.1, G is the gain of the PMT, ϵ_Q its quantum efficiency (determined from the datasheet at the peak TELLIE wavelength) and e is the charge of an electron. R is the impedance of the oscilliscope which was $50\,\Omega$.

$$N_p = \frac{A}{(G \cdot R \cdot \epsilon_Q \cdot e)} \tag{7.1}$$

Calculating the PMT gain

The PMTs gain needs to obtained at the two set voltages, 0.5 V and 0.7 V, in order to convert the size of the pulse to a number of photons. To do this a optical power meter is used in conjunction with a single channel TELLIE. Two sweeps are performed one with the power meter, and the other with the PMT.

The power meter makes multiple readings each reading integrates over a fixed time window. The number of photons is then given by Eq. 7.2. The first term is the power per pulse (P is the overall power η is the number of pulses during the integration time). The second term is the energy per photon where λ is the peak TELLIE wavelength and set to 506.2 nm.

$$N_{PM} = \frac{P}{\eta}\frac{hc}{\lambda} \tag{7.2}$$

A sweep is then made with the PMT in place of the power meter, for a given IPW the number of photons from TELLIE (N_{PM}) is assumed to remain constant. The gain of the PMT is then obtained via Eq. 7.3.

$$G = \frac{A}{N_{PM} \cdot R \cdot \epsilon_Q \cdot e} \tag{7.3}$$

7.3.2 Calculating the pulse delay

The pulse delay is the difference between the point at which the trigger out signal is received and the PMT detects a pulse of light. For both the trigger and the PMT pulse constant fraction discrimination is used. The code locates the point at which the trace passes 10% of its maximum value and uses this as the time of the pulse.

7.4 Stability of a single channel over time

A single channel was pulsed in master mode at a rate of 1 kHz for a period of 210 hours. The setup was the same as the standard TELLIE calibration. After 5000 pulses a PIN reading is made, 40 traces are also read out for each group of pulses. The number of traces read out is 40 due to the limited readout rate of the scope via USB. The photon count and pulse delay were calculated using the methods described in Sections 7.3.1 and 7.3.2 respectively. In total 66361 readings were taken corresponding to a reading once every 11.4 s. 5 s were spent pulsing, the remaining 6.4 s were spent processing the data.

Figure 7.11 shows the number of photons per pulse as a function time. There is a downwards trend over time, the shift is negligible over the time in which a TELLIE PCA run is taken (10 mins), but may have an effect if TELLIE and physics runs are interleaved.

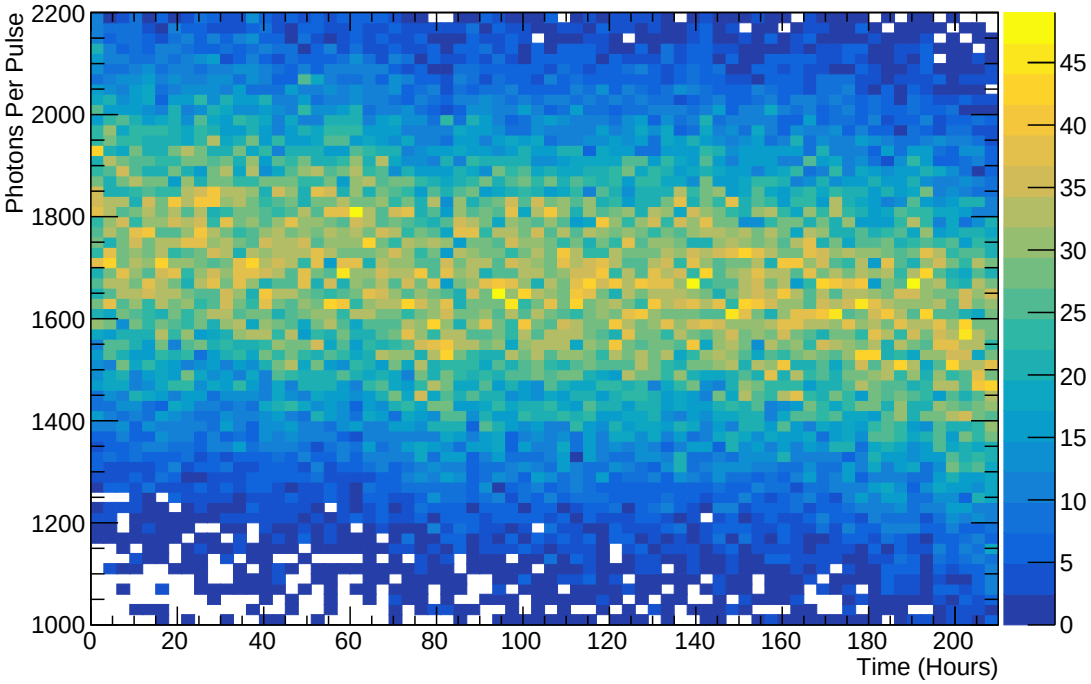

Figure 7.11: The calculated photon output of TELLIE over the extended running. The binwidths are 20 photons and 3 hours

Figure 7.12 shows the PIN readings over the extended run period. Several discontinuities are present in the readings over time. These have been seen in previous calibration runs and were present even after the replacement of PIN boards. It is suspected that the source of this is bad power, as the PIN signal is amplified through two op-amps any small changes in the voltages from the power supply can cause a large shift in PIN reading. When the extended run was performed TELLIE was plugged into the mains power of

SNOLAB. Although the power is filtered from regular mine power some instabilities have been seen. In the future TELLIE is expected to be installed on the SNO+ UPS system to hopefully remedy these issues.

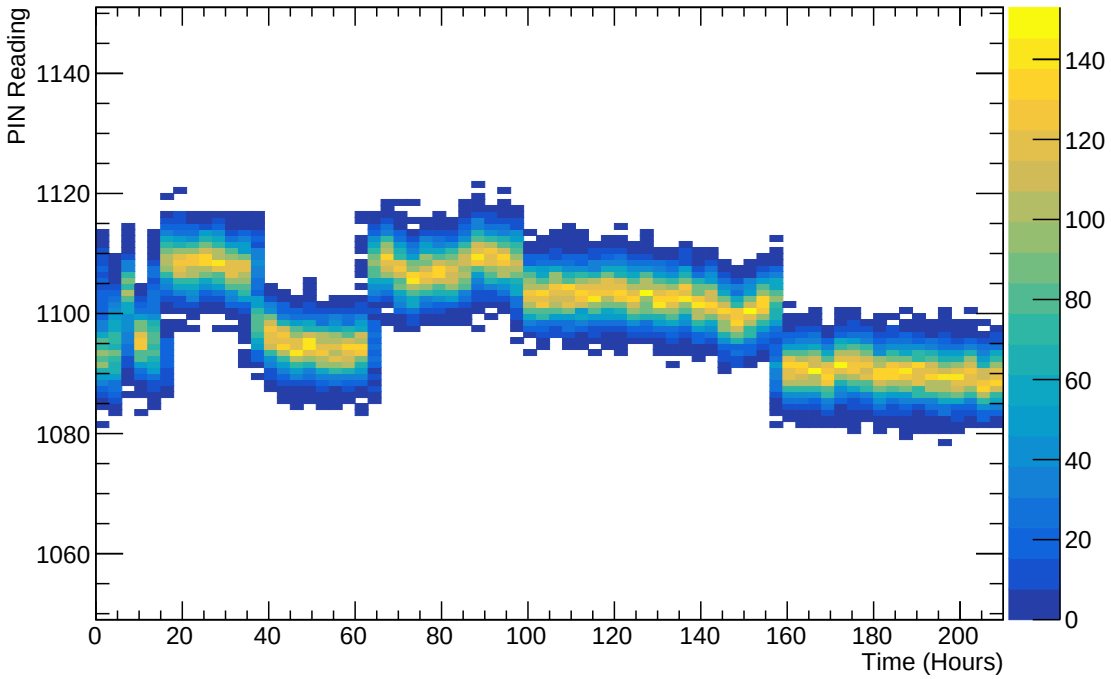

Figure 7.12: The measured PIN readings of TELLIE over the extended running.

Figure 7.13 shows the pulse delay as a function of time, it is stable over the entire period, the mean value fluctuates by less than 0.1 ns over the entire running.

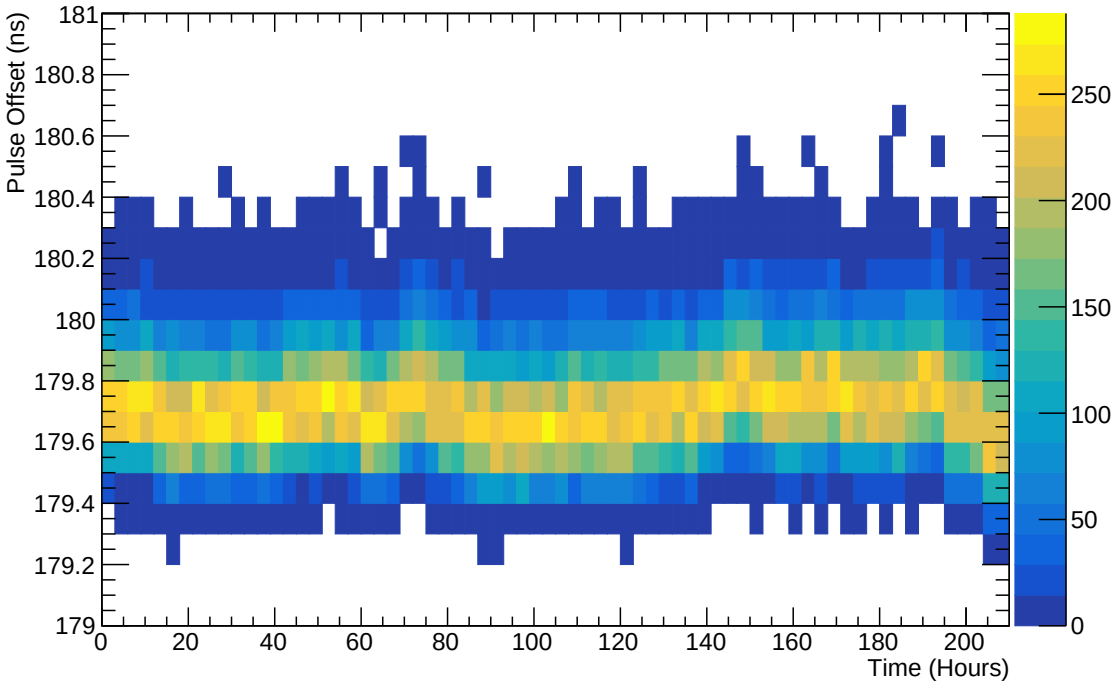

Figure 7.13: The pulse delay of TELLIE over the extended running.

All the trigger delays obtained during running were taken and binned a split Gaussian fit was then made, the rise time of the fit was 0.11 ns and the fall time was 0.19 ns. The fit and the histogram are shown in Figure 7.14. The average uncertainty on each trigger delay reading was 0.14 ns.

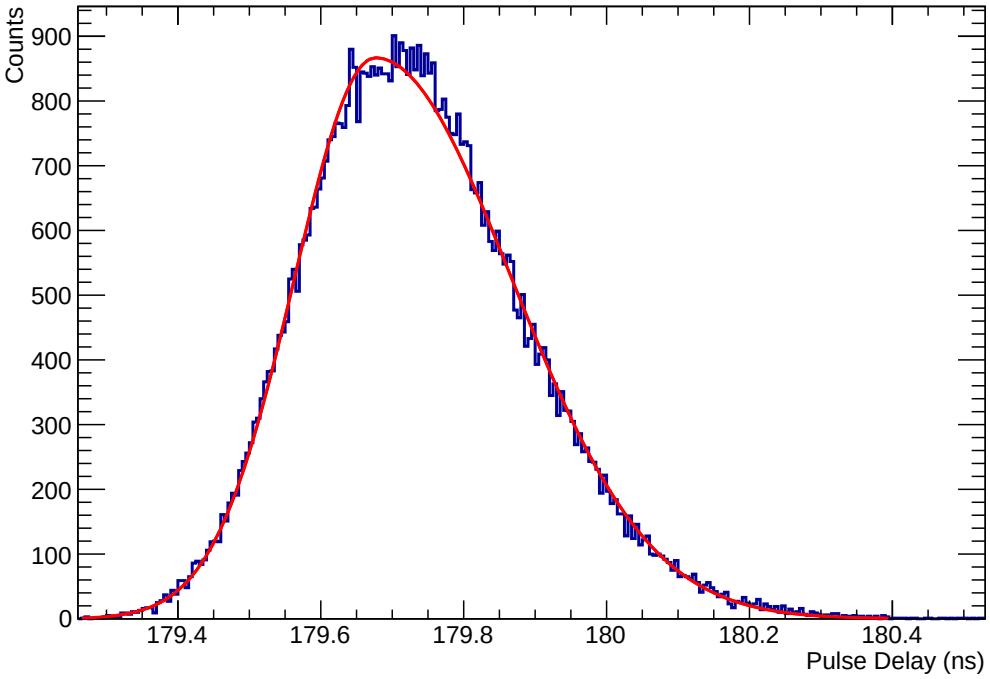

Figure 7.14: The distribution of average pulse delays obtained from the extended running of TELLIE and its fit to data.

An extended run test of TELLIE was performed, a shift in intensity was seen over time, although this was not enough to warrant concern for PCA calibrations. The PIN readings were shown to have large fluctuations over time, it is hoped that the installation of a UPS will remove these. The timing delay of the TELLIE pulses, which are crucial to any PCA calibration, were found to be stable over time.

7.4.1 Rate dependence of driver pulse shape

To measure the rate dependence on the pulse shape a TELLIE channel was pulsed 100000 times at the same intensity setting. The runs were taken immediately after each other to avoid any changes in detector state between measurements. The only setting that was varied between runs was the rate of pulsing. The pulse rates set in chronological order were 100 Hz, 200 Hz, 500 Hz and 1 kHz. Figure 7.15 shows the calibrated hit times of the prompt light in each of the runs. With an increase in rate a clear decrease in the rise time of the prompt light can be seen, the amount of light per pulse is also seen to increase.

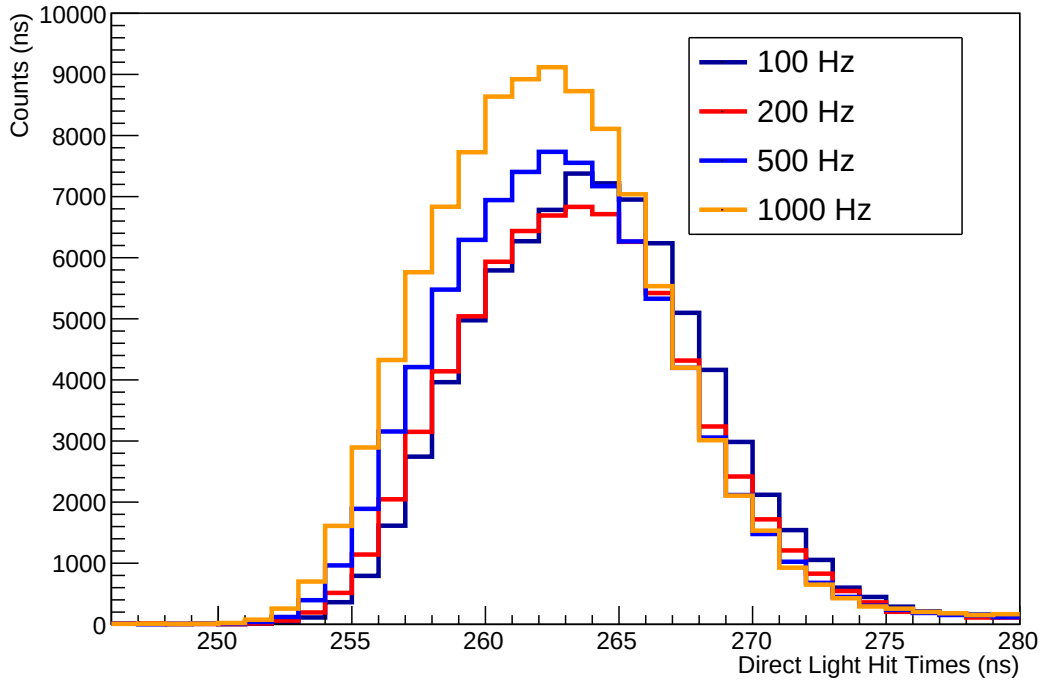

Figure 7.15: The prompt hit times for four successive TELLIE runs with rate being the only configuration parameter varied

7.4.2 Angular distribution of light from a fibre

The angular profile of a TELLIE beam was measured at the University of Lisbon, subsequently this measurement was used in simulation to estimate the in-situ performance of the fibres. One way to quantify the angular distribution of the fibres is to look at the occupancy of the PMTs as a function of angle relative to the fibre. Figure 7.16 shows the occupancy, defined as the proportion of TELLIE events in which a PMT is hit, as a function of angle relative to the fibre in data and simulation of the TELLIE fibre FT040A. The input distribution used to generate the photon directions in simulation is also shown.

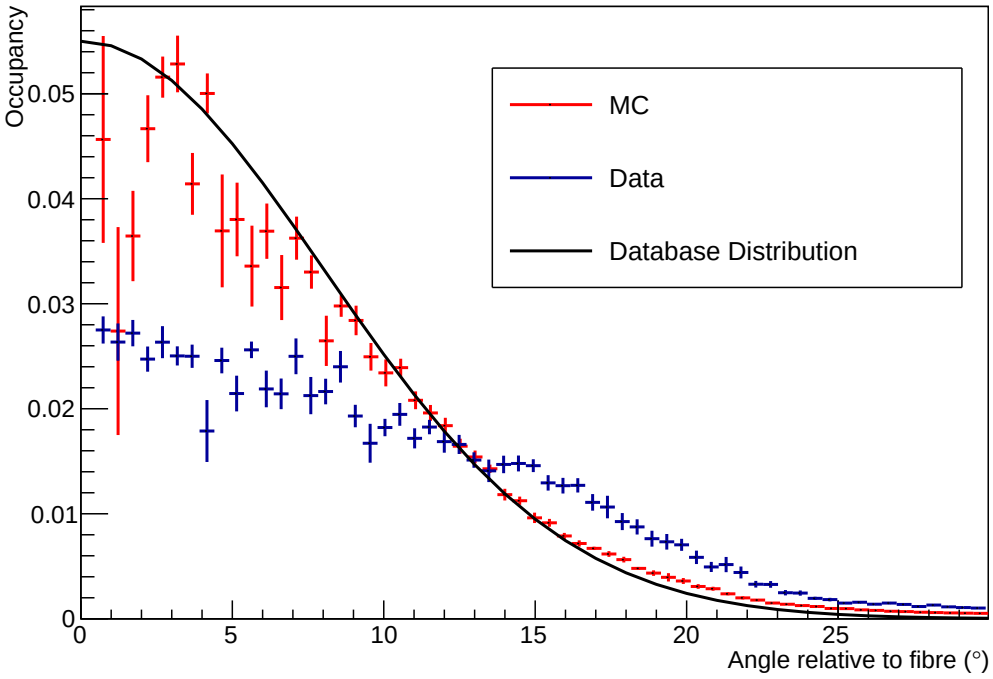

Figure 7.16: The angular distribution of light from data and simulations of TELLIE for fibre FT040A. Also shown is the angular distribution used within the simulation.

In the simulation Fibre FT040A was fired 1×10^6 times at an intensity of 1000 photons. The data is obtained from a TELLIE PCA run with 2×10^5 pulses. No scaling has been applied to either the simulation or data. The database distribution defines the angular distribution from the fibre in simulation. At small angles below 7° the error bars are quite large in MC and there is a large bin to bin variation, this is caused by the small number of PMTs existing this region resulting in large systematic differences due to PMT to PMT variation. At larger angular bins there are much more PMTs per bin reducing these systematics, the slight increase in the MC distribution is a result of refraction and scattering as light travels through the detector to the PMTs. There is a significant difference between the simulated angular distribution and the observed distribution. Several effects may be responsible for this difference including: dimples in the acyclic vessel from the panels are bonded, the surface of the AV not being perfectly smooth and a possible systematic difference between the assumed fibre angular distribution (which were measured ex-situ) and the true distribution. The collaboration is still working on determining the source of the difference between simulation and data.

7.5 Calculation of the TELLIE PCA offsets

Each TELLIE fibre has an intrinsic offset. As PMTs fall within multiple fibre beamspots in order to perform a time walk calibration using multiple fibres the offsets of these fibres relative to each other must be determined. The main contributor to these offsets is the trigger delay and fibre delay of each TELLIE channel, mode mixing within the fibre also contributes to the offset, this is performed using a separate analysis [179].

The PCA offset for a individual TELLIE channel O is defined via Eq. 7.4, D_{Trig} and D_{Fibre} are the hardware settings for the trigger and fibre delay for that particular run. T is the average time at which light leaves the fibre within the event window, the procedure to calculate this value is described below.

$$O = T + D_{\text{Trig}} - D_{\text{Fibre}} \tag{7.4}$$

The direct TELLIE beamspot is defined as the PMTs within who are illuminated by light emitted from the fibre at an angle smaller than 12°. PMTs within of the beamspot are used to perform the TELLIE PCA analysis. For all PMTs within the direct beamspot a histogram is filled with the hit times (which have been calibrated using the Laserball) of the PMT minus the time of flight to the PMT. A Gaussian is fitted to the peak of the histogram, the fitted mean and its error give the value of T and σ_T.

7.5.1 Effect of AV Position Shifts

As mentioned previously the AV is held in place with ropes, over time the position of the AV can change relative to the PSUP. The reflected light from TELLIE can be used to position the AV as described in the next chapter. However one also needs to understand how the unreflected light is altered due to shifts in the AV position and if this has any effect on the PMT calibrations.

Simulations were performed using fibre FT040A, the AV was shifted such that its offset away from the fibre ranged from -10 to 9 cm. The track length of photons reaching PMTs within the direct light beamspot (PMTs within 12° of the centre of the fibre beam) were stored. Figure 7.17 shows the path length of the direct light against the offset of the AV.

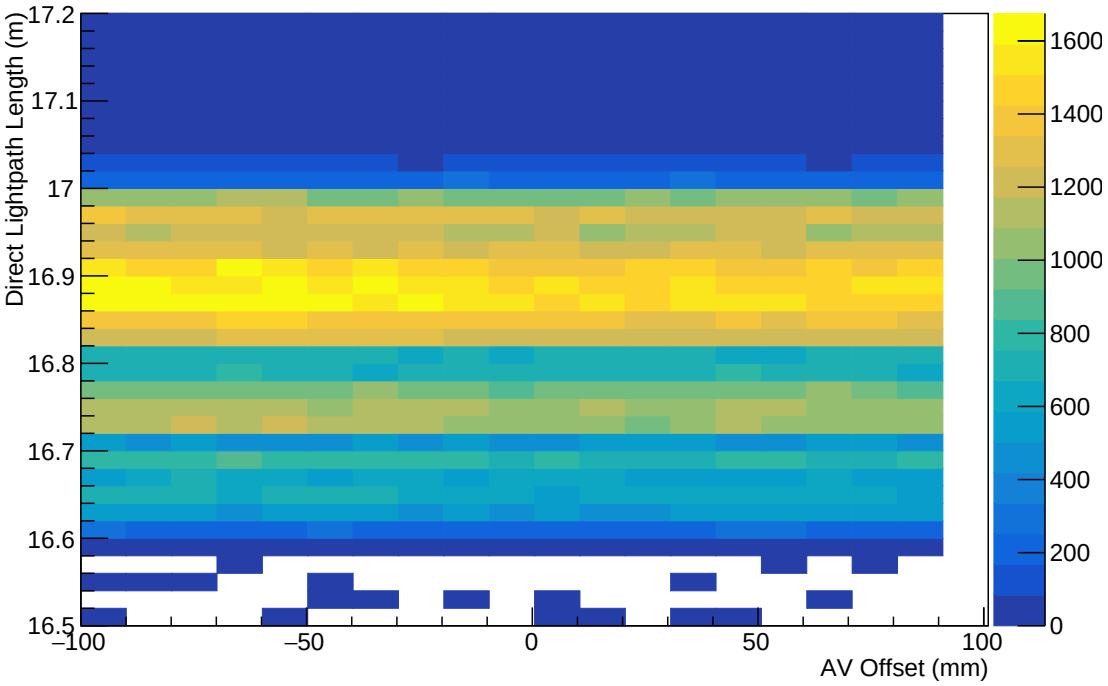

Figure 7.17: The distribution of lightpath lengths for photons from fibre FT040A to PMTs on the opposite side of the detector for varying AV offsets.

There is no correlation between the path length and the shift in AV position, any shifts in AV position throughout SNO+ should therefore leave the TELLIE PCA unaffected.

7.6 Ageing of the PMMA TELLIE fibres over the lifetime of SNO+

The initial measurements of the fibre ageing were made by an undergraduate student, the same undergraduate analysed these results a discussion of these results can be found in [180]. The connection error measurements described in were made by James Waterfield, and the experimental setup was designed by a technician at Sussex.

7.6.1 Motivation

Throughout the lifetime of the SNO+ experiment the TELLIE PMMA fibres will be submerged in UPW. Studies have shown that the main breakdown mechanism in fibres is caused by the oxidation of the polymers making up the core and cladding of the fibre [181]. It is important to understand the behaviour of the fibres over time, and ensure that fibres

will transmit light equally well throughout the entire lifetime of SNO+, and no noticeable optical degradation takes place.

7.6.2 Method

A heat bath was used to artificially age the fibre. The heat bath was set to 57.2 ± 0.2°C [180], a vessel was placed inside the heat bath containing a 45 m PMMA fibre submerged in UPW. A rough schematic of the setup is shown in Figure 7.18 The dry end of the fibre is left outside the heat bath while the wet end was submerged with the fibre. As the lab the setup was installed in was climate controlled there was a high rate of evaporation from both the heat bath and the UPW vessel. A reservoir ensured the heat bath was filled, the UPW vessel was topped up weekly manually. To reduce the effect of evaporation the heat bath and the UPW vessel were both covered.

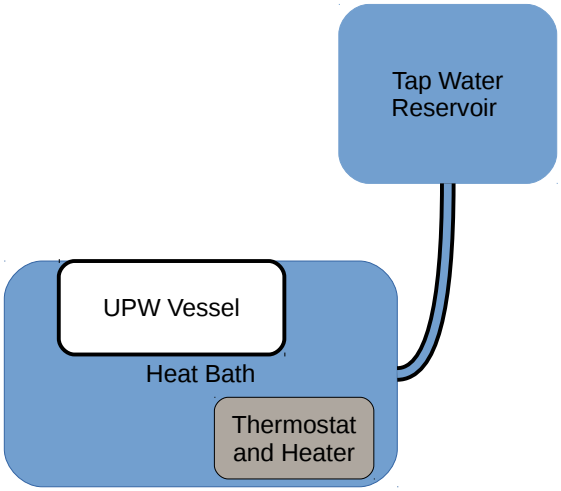

Figure 7.18: Simplified Schematic of the aging setup.

To calculate the effective aged time Arrhenius' principle was used as the degradation is chemical in nature. Arrhenius' principle states that the rate of reaction approximately doubles for each 10 °C raise. As the nominal running temperature of SNO+ is 10 °C, the rate of aging of the fibre relative to a SNO+ fibre R_A is given by Eq 7.5.

$$R_A = 2^{(57.2-10)/10} = 26.35 \tag{7.5}$$

To calculate the change in transmission coefficient, a second reference fibre is used.

This fibre is not artificially aged in any way and is stored in darkness at room temperature when a measurement is not being taken.

The dry end of the fibre is attached to a tungsten lamp, the wet end of the fibre was clipped into a spectrometer. The wet end is supported by a steel block to reduce the amount of error associated with the optical connection. A reading consisted of making a measurement of the dark current on the spectrometer, a measurement of the tungsten lamp spectrum through the reference fibre, and twenty readings of the tungsten lamp spectrum through the aged fibre. The transmission percentage of the aged fibre relative to the reference fibre is calculated using Eq. 7.6. Twenty values of the transmission percentage were taken to obtain a measure of the statistical error, which is obtained by taking the RMS of the individual measurements.

$$T_{\%}(\lambda) = \frac{I_{\text{Aged}}(\lambda) - I_D(\lambda)}{I_{\text{Ref}}(\lambda) - I_D(\lambda)} \tag{7.6}$$

Different wavelengths of light may be effected differently by degradation of the TELLIE fibres. In order to obtain a measurement of the transmission percentage, a weighted average is calculated across the TELLIE wavelength spectrum.

The wavelength weighted average value is given in Eq. 7.7 and the statistical error on this weighted average is shown in Eq.7.8.

$$\bar{T}_{\%} = \frac{\sum_\lambda T_{\%}(\lambda) I_{\text{LED}(\lambda)}}{\sum_\lambda I_{\text{LED}(\lambda)}} \tag{7.7}$$

$$\sigma(\bar{T}_{\%}) = \frac{\sqrt{\sum_\lambda (T_{\%}(\lambda) I_{\text{LED}}(\lambda))^2}}{\sum_\lambda I_{\text{LED}(\lambda)}} \tag{7.8}$$

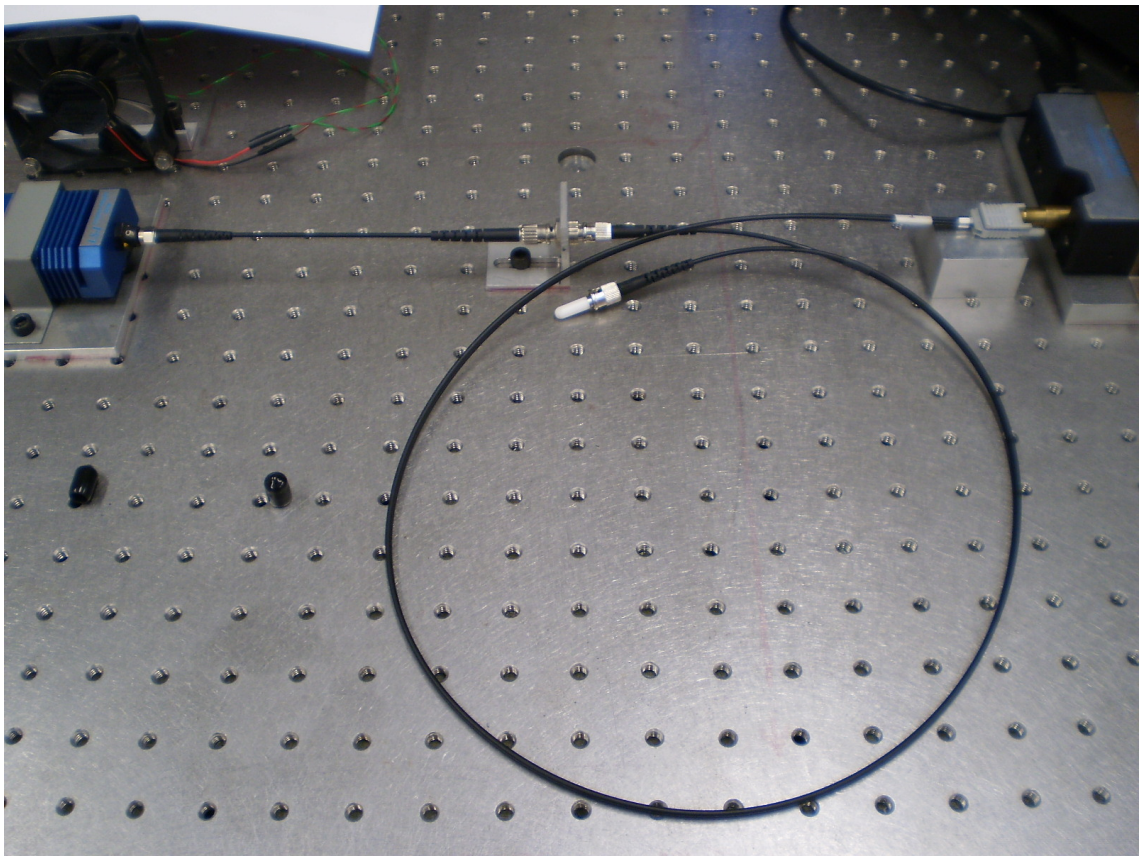

Figure 7.19: The experimental setup to make a transmission measurement of the reference fibre. The ST connector to the tungsten lamp via an optical patch fibre can be seen in the center of the image. The wet-end fibre connection to the spectrometer supported by the steel block can be seen on the right hand side of the image.

7.6.3 Uncertainties on the measurement of the transmission percentage

There are several sources of error associated with a measurement of the transmission percentage, the intensity of the Tungsten lamp and the response of the spectrometer can vary with time. By making a relative measurement between the two fibres, after subtracting the dark noise, the uncertainties caused by fluctuations in the spectrometers sensitivity and the tungsten lamp intensity are removed. Some systematic uncertainties, however, are not possible to remove. The two systematic uncertainties considered in the aging analysis are described below.

Error associated with the optical connection

Each time the fibre is connected and disconnected a different optical path is formed between the tungsten lamp and the spectrometer, this will produce a relative shift in the transmission of the fibre. The connection to the tungsten lamp is via a ST optical connector and is not thought to be a large source of uncertainty. The connection to the

spectrometer via the wet-end of the fibre is thought to be the main source of systematic error on the measurement.

In order to obtain an estimate of the connection error 15 transmission measurements were made over the course of a day. Figure 7.20 shows the distribution of transmission percentages weighed by the TELLIE LED spectrum. Two groupings can be seen within the transmission histogram in Figure 7.20. The majority of the measurements fall within the peak at 30 %. One measurement showed a reading significantly less than the other measurements, and is marked as the outlier in the figure. This outlier was included in the estimate of the error used within the fit.

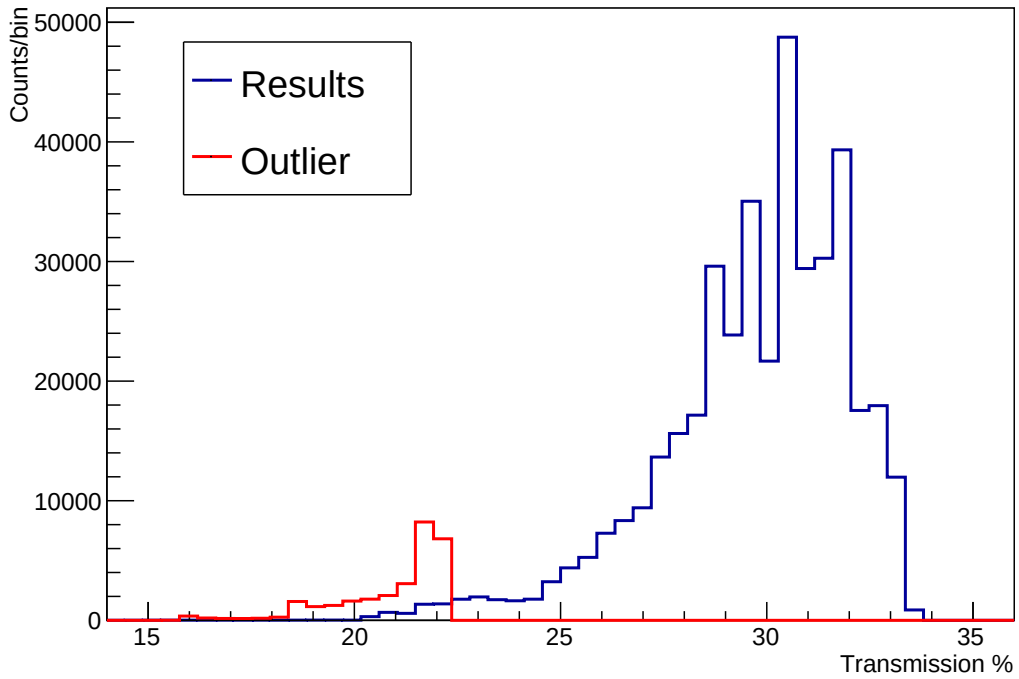

Figure 7.20: The transmission percentage distribution weighed using the TELLIE spectrum. The smaller distribution of events at a lower transmission percentage are from the 10th of the 15 transmission measurements.

The connection error was obtained by taking the standard deviation of the fifteen transmission percentages. Figure 7.21 shows the relative connection error as a function of wavelength with the TELLIE spectrum overlayed, the connection error causes an approximately constant uncertainty in the measurement of 8 % across the TELLIE spectrum.

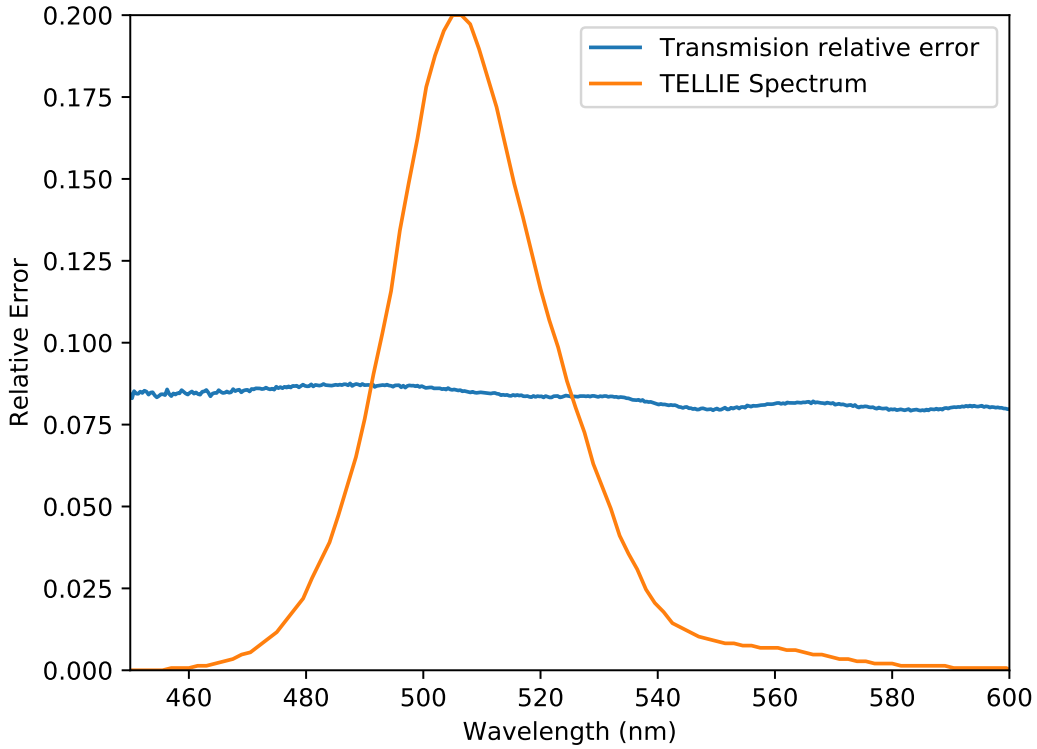

Figure 7.21: Uncertainty on the measurement of the transmission percentage due to the different optical path formed when the fibre is plugged and unplugged as a function of wavelength. Also shown is the TELLIE LED spectrum.

Error associated with the heat bath

Another source of error is due to the uncertainty in the temperature of the heat bath, the uncertainty in the heat bath temperature was found to be $\pm 0.2\,^{\circ}\mathrm{C}$. This results in an effective aging factor uncertainty of $^{+0.37}_{-0.36}$. The files produced during a measurement are timestamped. The uncertainty in the time between measurements was assumed to be negligible.

7.6.4 Results

A total of 27 transmission percentage measurements were taken between the 7th of April 2015 and, the 3rd of November 2015. The effective aging time of the fibre was calculated as 15.2 y, which is longer than the lifetime of the SNO+ experiment so fully covers the time at which the fibres are expected to not degrade within. Figure 7.22 shows the transmission percentage of the measurements against the effective aging time of the fibre. The figure also shows aging rates excluded at various confidence levels using the procedure described below. The error on the aging time is caused by the uncertainty on the heat bath

temperature and the error on the transmission percentage for each reading is obtained by adding the statistical uncertainty obtained with the systematic uncertainty due to the varying optical connection in quadrature.

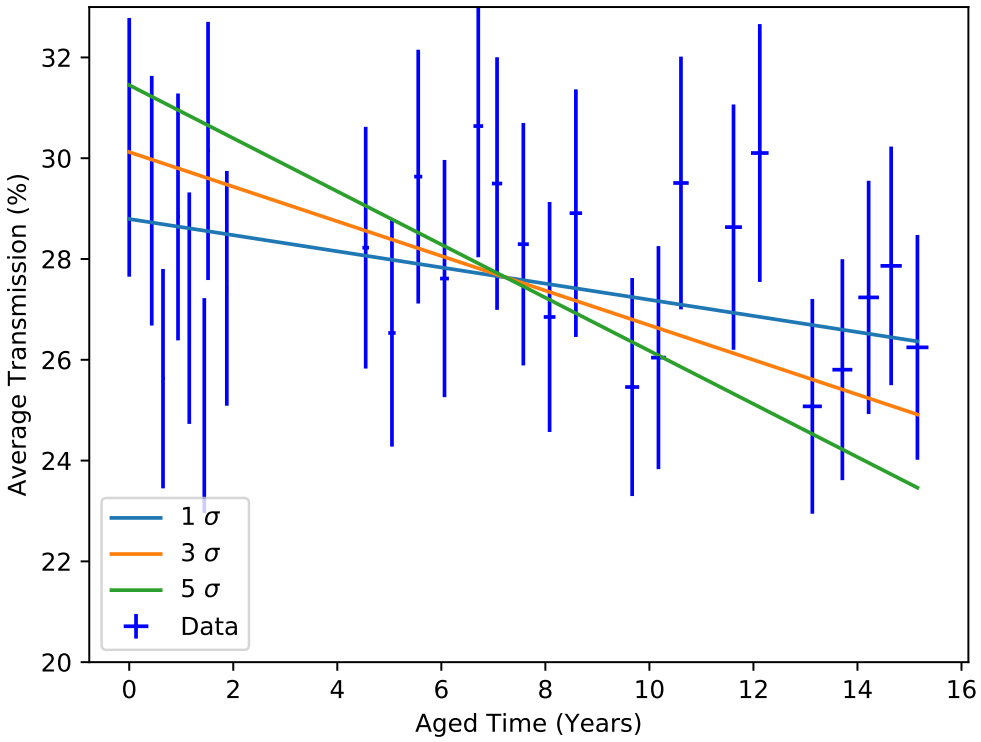

Figure 7.22: Calculated transmission percentage with error from connection and statistical error against the aged time of the fibre. Uncertainty on the aging time is caused by the uncertainty in the temperature of the heat bath. Aging rates excluded at various confidence levels are also shown.

Linear fits using the χ^2 function shown in Eq. 7.9 were made to the datapoints shown in Figure 7.22. In one fit both the gradient of the function a (the change in transmission percentage per year) was unconstrained, in another fit a is constrained below a limit $a < a_{\text{con}}$. In both fits the intercept b is unconstrained. Using Wilks' theorem shown in Eq 7.10, where n is the number of σ, χ^2_{Con} corresponds to the constrained fit and χ^2_{Un} corresponds to the unconstrained fit, a lower limit on the value of a can be obtained for a certain confidence level. The constraints on the lower value of a for 1σ, 3σ and 5σ confidence limits are shown in Table 7.1.

$$\chi^2 = \sum_i \frac{(y_i - (a * x_i + b))^2}{\sigma^2_{y_i} + a^2 * \sigma^2_{x_i}} \tag{7.9}$$

Sensitivity	a_{con} (%yr^{-1})
1σ	-0.160
3σ	-0.344
5σ	-0.527

Table 7.1: Constraints on the lower value of a (the change in transmission percentage per year) for given confidence levels.

$$n = \sqrt{\chi^2_{\text{Con}} - \chi^2_{\text{Un}}} \tag{7.10}$$

During standard TELLIE operation a fibre is required to emit 10^3 photons per pulse into the detector, a typical TELLIE driver board can emit up to 10^5 photons per pulse. Therefore, over the lifetime of SNO+ the increase in of attenuation of the fibre has to be less than a factor of 100 to leave the standard operation of TELLIE unaffected. Assuming an initial transmission percentage of 30% a increase of a factor 100 over the 15.2 years of artificial ageing corresponds to a reduction in the transmission percentage of 1.95% per year. As a aging rate of more than 0.527% per year is excluded at the 5σ level, it is very unlikely that the change in attenuation of will have any significant effect on the functionality of the TELLIE system.

7.6.5 Conclusion

A measurement of the aging of the TELLIE PMMA fibres was made. The measurement was dominated by systematic error caused by the connection between the wet end of the fibre and the spectrometer. This caused an approximate 8 % uncertainty in all measurements of the transmission percentage. A ageing rate of greater than 0.527 % per year was excluded at the 5σ level, this ageing rate can easily be compensated for by altering the intensity of the LED pulses.

Chapter 8

Positioning the AV Using TELLIE's Reflected Light

This chapter describes the development of a analytical analysis tool to determine the position of the SNO+ Acrylic Vessel by using the reflected light off of the AV from the external LED calibration system TELLIE. The chapter first describes the method used to determine the position of the AV. Systematic effects on the fits are then described by comparing the fit results with a known AV position in a full MC sim. Fibres least effected by systematic effects are used to fit to data to determine the offset of the AV in the Z axis. One systematic effect is backscattering of light in the external water, the amount of backscattered light is inversely proportional to the scattering length of the water. The chapter concludes with an analysis to determine the scattering length of the external water using this backscattered light.

Understanding the position of the Acrylic Vessel (AV) accurately is required to define a position cut in any $0\nu\beta\beta$ search due to AV surface backgrounds [164]. A continuous measurement of the AV position must be made throughout the lifetime of SNO+. Such a measument can be made using TELLIE reflected light. A small proportion of the light fired from TELLIE towards the other side of the detector will be reflected off of the AV back towards the PMTs surrounding the fibre. If the AV has shifted away from the position of the fibre then the path length of the reflected light will increase and the reflected light will arrive later after TELLIE has fired. Due to the precise timing of SNO+ the shift can be observed and used to fit the AV offset in the direction of the fibre. As TELLIE has a large number of fibres, multiple independent measurements can be made to obtain

an accurate position on the AV relative to the PSUP in three dimensions. AVLOC is designed to be a monitoring system of the AV position using an analytical expression to fit the AV position, rather than performing an computationally expensive comparison using Monte Carlo. The code exists as a RAT processor, and can be used to process data directly. AVLOC measurements can be made using the same data from a TELLIE PCA calibration. The original idea of using TELLIE reflected light was explored within Monte Carlo [164]. The method has been refined within this chapter to produce a fit to data.

During the AV positioning analysis it was found that backscattered light in the 3 m of external water was also observed by PMTs in the reflected region. A further analysis is presented at the end of this chapter to determine the scattering length of the external water using this backscattered light. Understanding the optics of the detector, including the scattering length within the external water, is important for accurate reconstruction of physics events.

This chapter first introduces the method behind the fitting procedure, after this the performance of the method on simulated data is shown, and systematic effects caused by changes in detector state and fibre are explored. A subset of fibres are selected based on their positions within the detector. Fits using these fibres were made to simulated data with the AV in two known positions. Any fibres showing any aforementioned systematics (due to AV belly plates and shadowing etc.) were removed. The remaining fibres were used to determine the AV position. The final section presents an analysis to determine the scattering length of the water, compared to the RAT default scattering length.

8.1 Method to Determine the AV Position

Figure 8.1 shows the possible light paths from a TELLIE fibre, the majority of light passes through the detector reaching the PMTs on the opposite side of the detector. Some is reflected back from the outer face of the AV towards the PMTs surrounding the fibre. To fit the offset of the AV both the direct light and the reflected light are used. Some light is scattered backwards in the various media of the detector, light that scatters backwards in the outer water of the detector arrives before the reflections off of the AV and forms a background to be considered in any position fits.

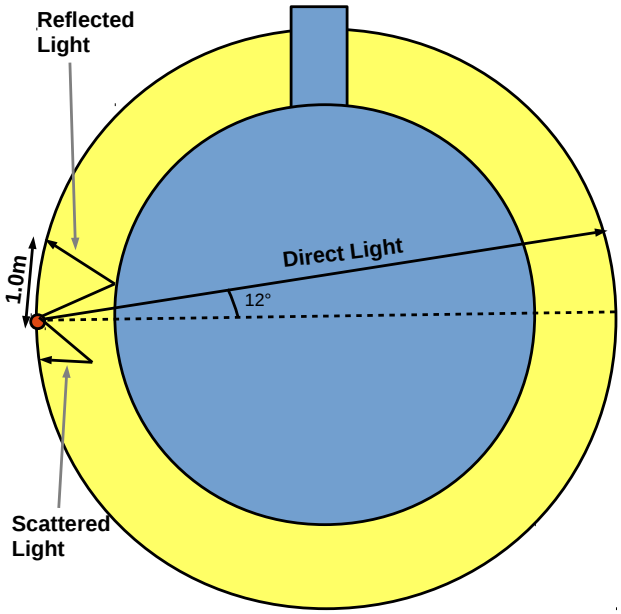

Figure 8.1: The various path lengths for light from a TELLIE fibre which considered in an AV position fit. Also shown are the nominal cut values used in the analysis to positioning the AV.

8.1.1 Time of Flight Calculations

To determine the time of flight, a tool known as 'lightpath calculator' is used [172]. When provided with a start and end point it calculates the path between the points taking into account any refraction at boundaries. When combining this with the group velocities of the detector media the total time of flight can be obtained. Lightpath calculator is also able to provide the initial light vector from the fibre and final light vector incident on the PMT. The final light vector is used to calculate the angle of entry to the PMT face which is used to calculate an additional time associated with the propagation through the PMT bucket and is responsible for a 0.45 ns to 0.70 ns increase in the total time of flight [172].

When a PMT is hit, there is no way to determine the position on the PMT bucket face where the photon has entered the bucket. In order to account for the spread in possible hit times because of this, the path to multiple positions on the PMT face are calculated.

33 positions on the PMT face are sampled: the central point on the face, and 32 positions corresponding to points separated by angle $\frac{\pi}{4}$ in angle and steps of $0.25R_{\text{Bucket}}$, where R_{Bucket} is the radius of the PMT bucket. The average time of flight for all positions is used as the time of flight to the PMT in the analysis. The error on the mean is used as the systematic error of the calculated time of flight to the PMT.

8.1.2 Direct Light: Determining the time when light enters the detector

The direct light from the fibre is used to determine the time in the trigger window when light leaves the wet end of the fibre. A cut is made on PMTs within an angular cut of the direction of the fibre such that only PMTs in the beam spot are considered (nominal value 12° [182]). For each PMT in the direct beam spot the hit time minus the time of flight is used to fill a histogram. The peak of the histogram (defined as the region bounded by the points at which the histogram crosses 10% of its maximum value) is fitted to a Gaussian, as shown in Figure 8.2.

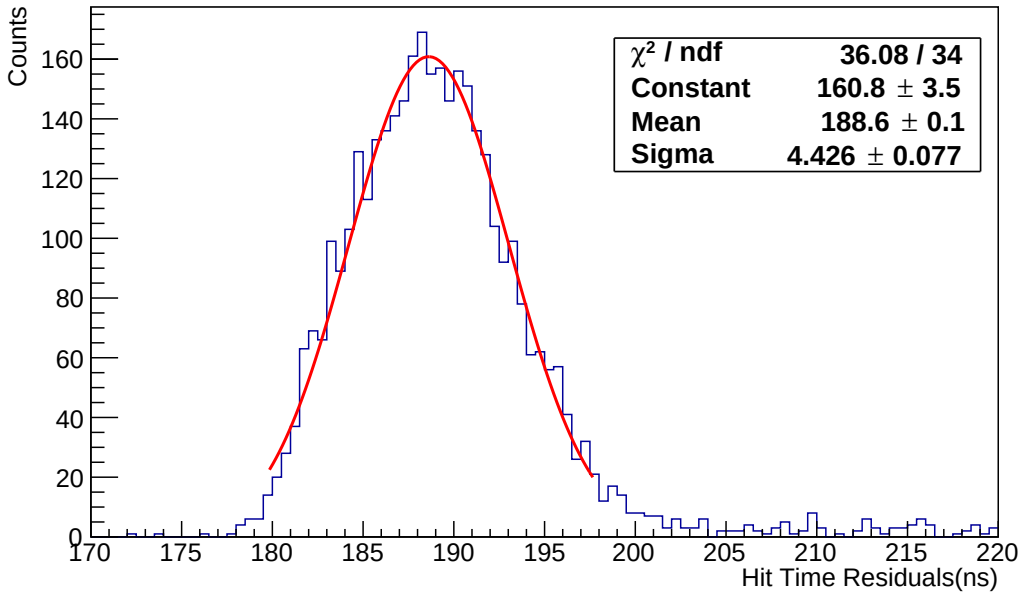

Figure 8.2: A fit of a single PMT in the direct beam spot using fibre FT079A. Run Number 101842.

Figure 8.3 shows a plot of the mean and error on the mean for the injection times obtained from the fits to individual PMTs against angle of injection. The spread on the individual channels is caused by bad timing calibrations on some channels. The later light injection time observed at higher angles in Figure 8.3 is a result of mode mixing within the fibre as shown in Section 7.2.4.

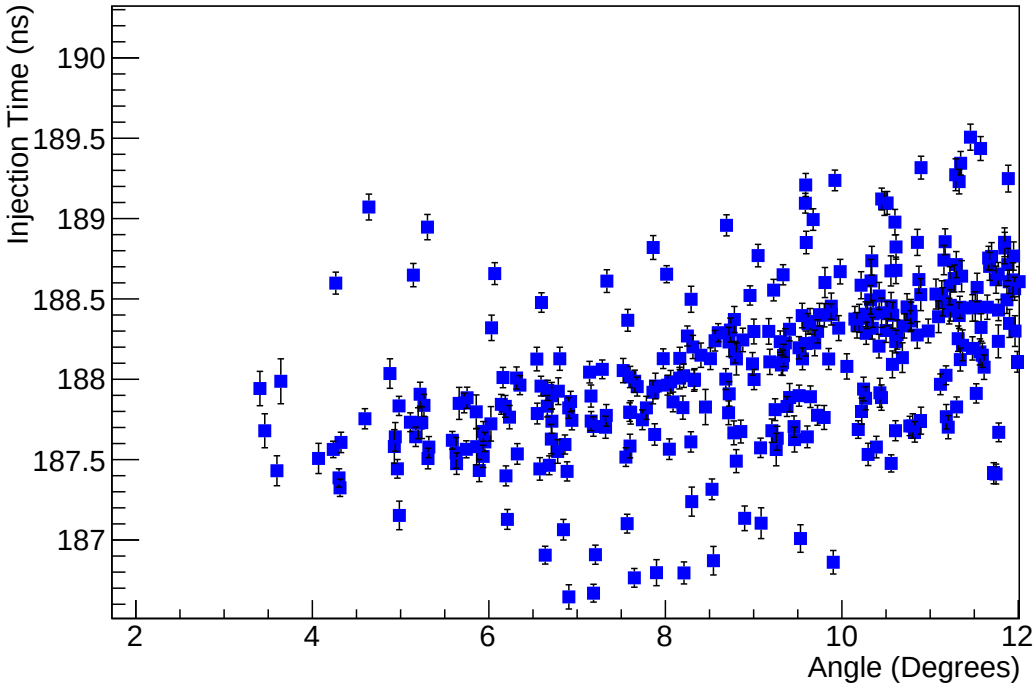

Figure 8.3: The mean and error on the mean of the fit results for the injection time for individual PMTs in the direct light beam spot. Using fibre FT079A, run 101842, which points upwards towards the neck, causing the lack of PMTs at low angles.

To obtain an estimate of the injection time against angle the PMTs are grouped in 0.5 degree bins. The total error on each bin is the combination of the individual PMT fit uncertainty and the uncertainty caused by not exactly knowing the light path from fibre to PMT. The error due to the uncertainty in the lightpath for each bin is obtained by calculating the weighted average of the light path uncertainty to each bin weighted by the number of hits on each PMT.

Figure 8.4 shows a comparison of the lightpath error and the error on the fit to each PMT, the former is a purely systematic error and on average does not vary significantly with angle. However, there is significant variation on this error from PMT to PMT. The error on the fit is statistical and increases with angle due to the beam profile of the fibre, shown in Figure 7.16.

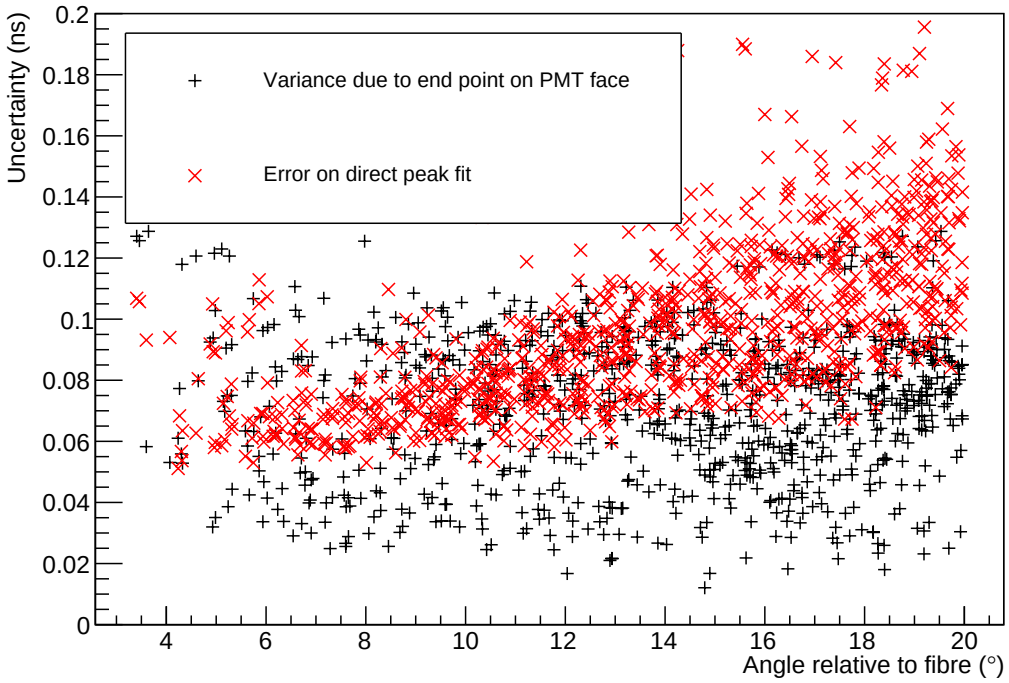

Figure 8.4: The errors on the analysis of the direct light. Two errors are shown, one due to the uncertainty on the fit of the individual PMTs and the other duue to the systematic uncertainty on the point at which the photon hits the PMT face. Data taken using fibre FT079A. Run Number 101842.

Figure 8.5 shows the averaged histogram used to calculate the injection time for a given angle.

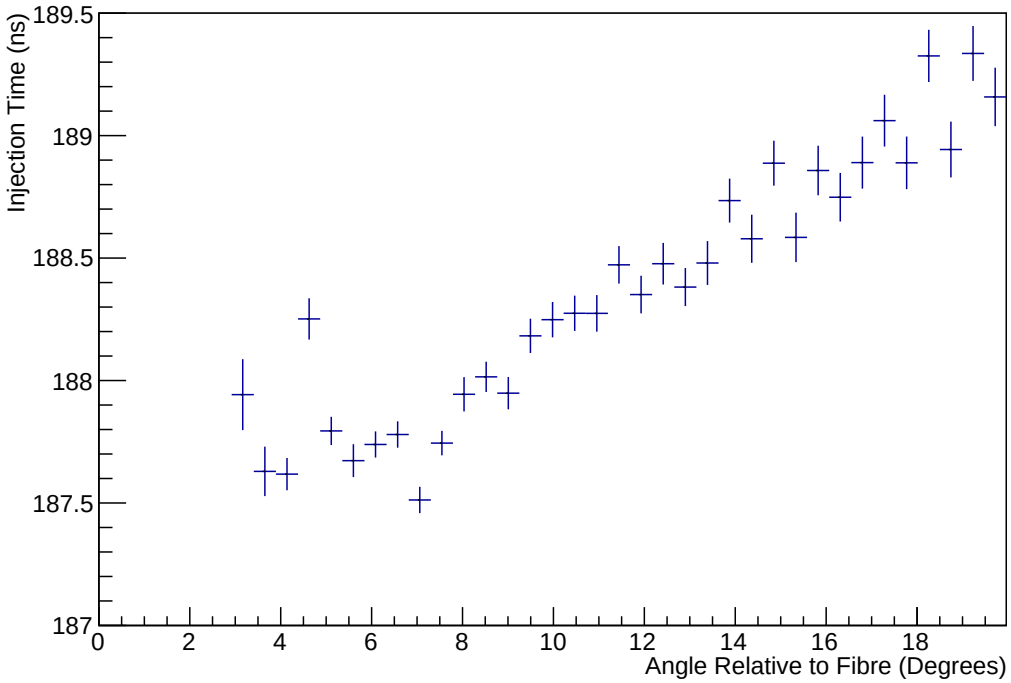

Figure 8.5: The histogram of injection time as a function of angle with error bars, the PMTs in Figure 8.3 have been grouped together into 0.5° bins.

8.1.3 Reflected Light: Determining the AV offset

The total path length taken by the reflected light is given by $|\overrightarrow{A}| + |\overrightarrow{B}|$ where $\overrightarrow{A}$ is the light incident on the AV from the fibre and is calculated using Eq. 8.1. $\overrightarrow{B}$ is the path of the light reflected from the AV onto the PMTs and is calculated using Eq. 8.2.

$$\overrightarrow{A} = \overrightarrow{P}_{ref} - \overrightarrow{P}_{fibre} \tag{8.1}$$

$$\overrightarrow{B} = \overrightarrow{P}_{PMT} - \overrightarrow{P}_{ref} \tag{8.2}$$

Obtaining the Point of Reflection

The point of reflection $\overrightarrow{P}_{ref}$ is determined using the method described in [183]. The calculation holds for a unit sphere positioned at the origin so a shift and scaling is applied to to scale to this coordinate system, after the calculation the transformation is undone to calculate the point of reflection in the coordinate system of the detector.

The transformation is applied using Eq. 8.3 to transform into the unit sphere at the origin where $\overrightarrow{O}$ is the offset vector of the AV and R_{AV} is the radius of the AV.

$$\overrightarrow{x}' = \frac{\overrightarrow{x} - \overrightarrow{O}}{R_{AV}} \tag{8.3}$$

Figure 8.6 shows the reflection after the transformation has been applied, I is the scaled point of injection, R is the scaled point of reflection, D is the scaled point of detection at the PMT and I' is the vector in the same direction as D but with the same magnitude as I.

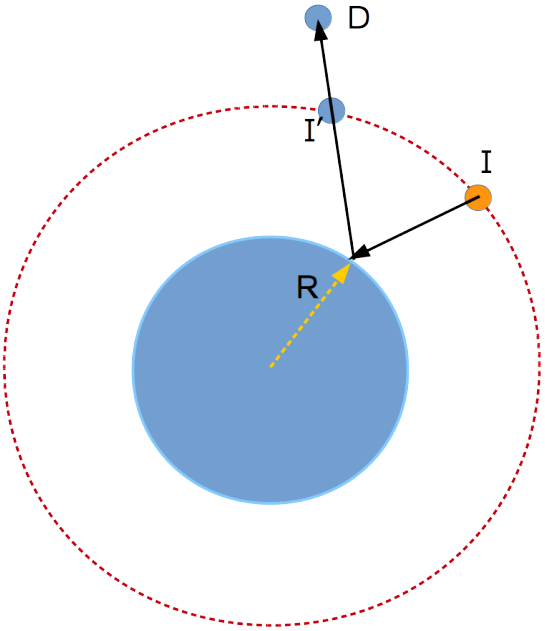

Figure 8.6: A schematic of the light path calculation after a transformation is applied to make the AV a unit sphere at the origin.

Approximating the reflection off the AV as specular, the angle of incidence of light relative to the AV normal at the is equal to the angle of reflection, this means the points I and I' can be written in the form seen in Eqs. 8.4 and 8.5, combining these and using the fact that $a = I \cdot R$ Eq. 8.6 is obtained.

$$I = aR + bR_{\text{Perp}} \tag{8.4}$$

$$I' = aR - bR_{\text{Perp}} \tag{8.5}$$

$$I' = 2(I \cdot R)R - I \tag{8.6}$$

The point of reflection on the AV can be written as the combination of where x and y are scalar values.

$$R = xI + yD \tag{8.7}$$

Eq. 8.8 is obtained using the fact that R is a point on a unit sphere.

$$1 = R \cdot R = x^2 I \cdot I + y^2 D \cdot D + 2xyI \cdot D \tag{8.8}$$

Another polynomial in x and y can be obtained by using the fact that $I' - R$ and $D - R$ are parallel so their cross product is 0. The second line of Eq. 8.6 The second polynomial is obtained from the final line of Eq. 8.9 as the only way $S \times I$ is 0 if the source is in the same direction as the point of detection.

$$\begin{aligned} 0 &= (D - R) \times (I' - R) \\ &= (D - R) \times ([2(I \cdot R)R - I] - R) \\ &= ([2xD \cdot I + 2yI \cdot I - 1]y - 1 + x)(S \times I) \end{aligned} \tag{8.9}$$

Combining these two equations leads to a fourth order polynomial in y which is solved analytically using the ROOT [184] polynomial class, the value of x can then be obtained from either of the polynomials. The values of x and y which are both positive give the point of reflection on the AV in the transformed geometry. $\overrightarrow{P}_{ref}$ is then found by applying the inverse of the transformation in Eq. 8.3.

Performing the Reflection Fit

PMTs within a certain distance of the fibre are used for the reflection fit (Nominal value 1 m). An optional angular cut can also be performed to check whether PMTs passing the distance cut also fall within the angular cut used for the direct light.

A time cut is performed on the PMTs to remove any hits resulting from 35 degree and PSUP reflections. 35 degree reflections are reflections off of the concentrators surrounding the PMTs. As these reflections occur on the far side of the detector any inclusion of PMT hits due to these will have a significant effect on the fitted AV position. The lower limit

of the time window is given by the value of the reflected time of flight when the AV is shifted downwards towards the fibre by its maximum possible distance. An additional user specified tolerance is also subtracted. The upper limit on the time window is set to the time of flight when the AV has been shifted in the maximum distance away from the fibre plus the user specified tolerance. In the following results the tolerance is set to 25 ns.

The initial guess on the injection time T_{inj} is obtained by performing a fit to the peak of the direct light residuals for all PMTs in the direct beam spot, the procedure is the same as the fit to the individual PMTs. For each reflected PMT hits passing the time cut are used to fill a histogram with the values $T_{\text{Hit}} - T_{\text{inj}}$. The histogram is then fitted to two Gaussian functions with a constant background, the earliest Gaussian represents the scattering in the external water, the later Gaussian is the near AV reflection. The histogram and the fit for a single PMT are shown in Figure 8.7.

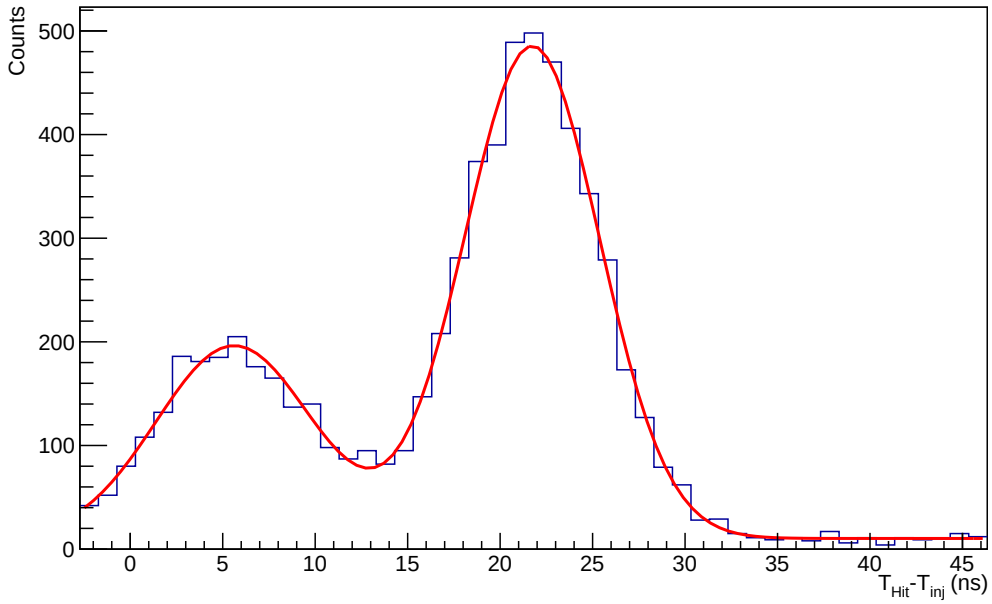

Figure 8.7: $T_{\text{Hit}} - T_{\text{inj}}$ for PMT 5663 from simulation using fibre FT079A. Also shown is the fit to the data, the fit function is made up of two Gaussians, one for the backscattered light and the other for the AV reflection, a constant backgrounds is also added. A schematic for the physics responsible for the two peaks is shown in Figure 8.1.

The fit to the histogram shown in Figure 8.7 contains a total of seven parameters: three for the scattered and reflected Gaussian peaks and one for the constant background. In order to correctly fit the data correctly, initial guesses and constraints need to be made to the fit parameters. The initial height of the Gaussian peaks is set to half the height of the histogram and allowed to vary between zero and three times this height. The width of both peaks is initially set to 2 ns and allowed to vary between 1.5 ns and 5 ns. The linear

background is set to the value of the last bin in the histogram and allowed to vary between zero and five times the initial guess.

For the reflected peak average time the initial guess of the peak is set to 29 ns with limits 20 ns to 30 ns, the limits were determined by examining the time of flight predicted by lightpath calculator. The scattering peak is set to have an initial value of 5 ns with range 0 ns to 15 ns. The initial values were chosen to separate the reflected and scattering peaks as much as possible to ensure a good fit.

The mean value of the AV reflection Gaussian $\bar{T}_{\mathrm{ref}}$ and its error $\sigma(\bar{T}_{\mathrm{ref}})$ are used in the AV position fit.

For a given AV offset, the reflected lightpath travelling to each PMT passing the distance cut is calculated using the calculation described in Section 8.1.3. The procedure of calculating the time of flight τ_{PMT} and its error $\sigma(\tau_{\mathrm{PMT}})$ of the reflected light to each PMT is the same as described in section 8.1.1.

Due to mode mixing within the fibre an angle dependent correction must be made to the injection time. The corrected time of injection of light T'_{inj} is obtained by calculating the angle of injection of light (obtained by taking the dot product of the fibre direction and the vector obtained from Eq. 8.1 normalised to 1) then finding the corresponding bin in Figure 8.5, the uncertainty on this value $\sigma(T'_{inj})$ is found from the error on the bin. It should be noted that as the AV position is varied in the fit, the angle of injection, and therefore the corrected injection time, can vary.

As multiple positions on each PMT bucket face are sampled there is the chance that a single PMT can span multiple angle bins in Figure 8.5. The injection time used in the fit is the average value of all the bin values for the sampled positions on the PMT face. If a angle is not covered by the direct light (i.e. in the case of the small angles in Figure 8.5) it is ignored. A conservative estimate of the error ($\sigma(T'_{inj})$) is made by taking the bin error bar with largest difference from the mean value and assuming this to be the bins error. The correction to the reflected time of flight is given by Eq. 8.10).

$$\bar{T}'_{\mathrm{ref}} = \bar{T}_{\mathrm{ref}} - T'_{\mathrm{inj}} + T_{\mathrm{inj}} \tag{8.10}$$

The total error on each reflected PMT is shown in Eq. 8.11. The second term corresponds to the spread in the calculated time of flight when sampling multiple positions on the PMT face, the final two terms correspond to the uncertainty added when applying the correction in Eq. 8.10.

$$\sigma_{\mathrm{PMT}} = \sigma(\bar{T}_{\mathrm{ref}}) + \sigma_{\tau_{\mathrm{ref}}} + \sigma(T'_{inj}) + \sigma(T_{inj}) \tag{8.11}$$

The χ^2 function used to fit the data is shown in Eq. 8.12.

$$\chi^2 = \sum_{\mathrm{PMT}} \frac{(\bar{T}'_{\mathrm{ref}} - \tau_{\mathrm{ref}}(\vec{O}))^2}{\sigma^2_{\mathrm{PMT}}} \tag{8.12}$$

8.1.4 Ideal Reflected Region Cut for AV Positioning

As the AV is 5 cm thick light reflecting off of both the inner and outer sides of the AV will be observed by the PMTs within the reflected region. Furthermore light reflected off of the inner face of the AV will be refracted twice, once when it enters the AV and a second time when it passes from the AV into the external water. A schematic of the reflections off of both the inner and outer face is shown in Figure 8.8.

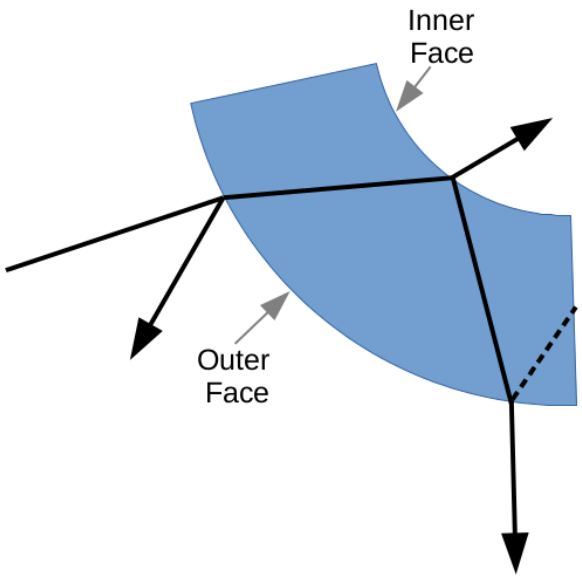

Figure 8.8: Possible light paths through the AV, the majority of the light passes through the AV. Some is reflected off of the inner and outer faces, a small amount can be reflected a second time on the outer face AV water boundary. Refraction also takes place within the AV.

The reflectivity between two surfaces of different refractive index for incident light normal to the surface is:

$$R = \left(\frac{n_1 - n_2}{n_1 + n_2}\right)^2 \tag{8.13}$$

In the water phase of SNO+, the inner face of the AV and the outer face of the AV will both reflect light. The refractive index of water is $n_{\text{water}} = 1.33$ and the refractive index of the AV $n_{\text{AV}} = 1.5$. During water phase the reflectivity off of both faces of the AV is approximately 0.4 %. As light reflected off the inner face of the AV will affect the fitted position of the AV a cut needs to be made to reduce the amount of light from inner AV reflections.

The refractive index of the scintillator used in SNO+ is 1.49 so during scintillator re-

flections off of the inner face of the AV are negligible compared to the outer face reflections. Therefore for the scintillator phase the distance cut on the reflected light can be relaxed.

A simple ray tracing program was written to see the reflected paths of light off of both sides of the AV. The reflection at both boundaries was obtained using the Fresnel equations shown in Eqs. 8.14 to 8.15. θ_i is the angle of incidence between the normal of the boundary and θ_t is the angle transmitted and can be calculated from Snells law. As the light from the LED is unpolarized Eq. 8.16 is used to determine the total reflectivity of the surface. Refraction in the AV was also considered for light reflecting off of the inner face of the AV. Both the AV and the PSUP were approximated as spheres. Figure 8.9 shows the distance between the start and end points of the reflected light from both faces of the AV when the AV is at the origin.

$$R_s = \left| \frac{n_1 cos\theta_i - n_2 cos\theta_t}{n_1 cos\theta_i + n_2 cos\theta_t} \right|^2 \tag{8.14}$$

$$R_s = \left| \frac{n_1 cos\theta_t - n_2 cos\theta_i}{n_1 cos\theta_t + n_2 cos\theta_i} \right|^2 \tag{8.15}$$

$$R = \frac{1}{2}(R_s + R_p) \tag{8.16}$$

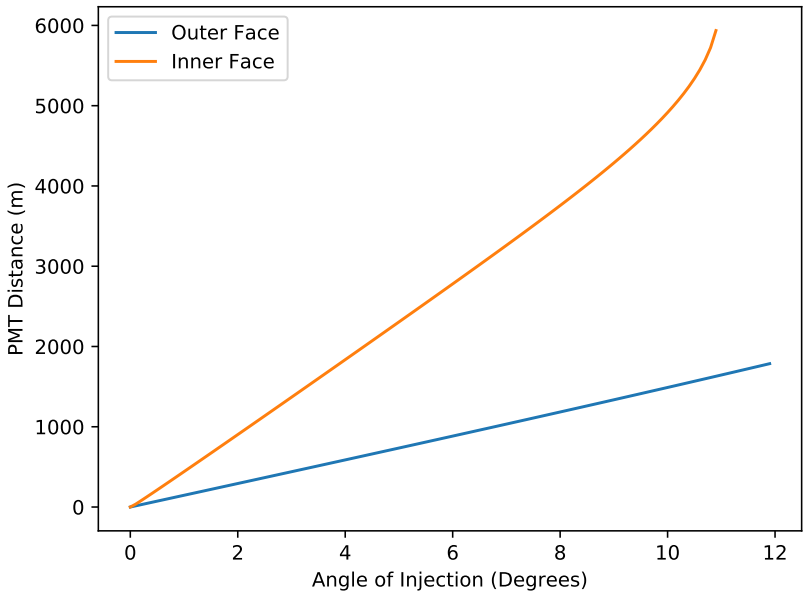

Figure 8.9: The distance between the fibre and detection position for light reflected off of both faces against the initial angle of injection from the fibre.

Figure 8.9 shows the justification of the use of the 1 m distance cut. Light reflected of the inner face of the AV is refracted within the AV causing it to arrive at PMTs further away from the fibre. For light emitted greater than 11° from the fibre total internal reflection takes place when the inner AV reflected light encounters the outer face of the AV.

The 1 m distance cut corresponds to a 2.3° angular cut on the TELLIE beam for light reflecting from the inner face of the AV. For light reflecting on the outer face of the cut corresponds to an angular beam profile cut of 6.8°. Using the measured beam profile of the TELLIE fibres the distance cut corresponds to the removal of 49 % of the light from the outer face and 88 % of the light reflected from the inner face when compared to no distance cut being applied.

8.2 Testing on Monte Carlo Simulation

Simulations using fibre FT079A which is situated at the bottom of the detector were run. This fibre was chosen as it points upwards through the bottom of the detector. The bottom of the AV is relatively featureless so this fibre is unaffected by many of the systematic effects in Section 8.3. Furthermore, the shift in AV position is expected to be mostly in the Z axis due to the buoyancy of the scintillator.

Two simulations were performed with the center of the AV at the origin and the AV shifted upwards by 10 cm. The channels online in the simulation reflect the detector state for run 101842, the last TELLIE run with this fibre at the time of writing. AVLOC was used with the MC hit times of the PMTs (the point at which the photoelectron is created at the cathode). Table 8.1 shows the results of the fit for the AV in both positions, both fits are accurate to within 1 cm of the true position.

AV Position (mm)	**Fitted offset (mm)**	**Error On Fitted Offset (mm)**
(0, 0, 0)	5.58	3.74
(0, 0, 100)	105.06	3.85

Table 8.1: AVLOC results with MC simulation of Run 101842.

8.3 Systematic Effects

8.3.1 Scattering In the External Water

The scattering in the external water causes an additional peak in the timing histogram of the reflected light. The peak is earlier in time than that of the AV reflection as shown in

Figure 8.7. The amount of scattered light on PMTs is larger for PMTs closer to the fibre. This is caused by the angular profile of light from the fibre. The AVLOC processor was run on a simulation of the detector without the AV. The time profile of the back scattered light for two PMTs can be seen in Figure 8.10.

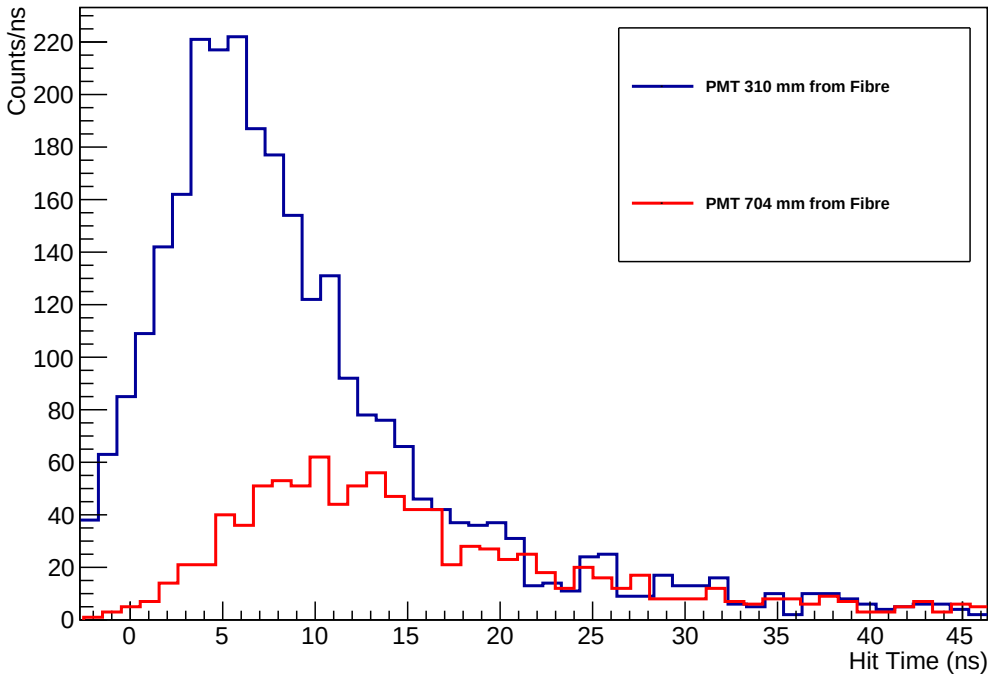

Figure 8.10: The time profile of scattered light to two PMTs at different distances from the fibre. In the simulation, the AV was removed from the detector.

8.3.2 Belly plates and Ropes

The belly plates can have a significant effect on the AV position fit. The fact that the belly plates produce regions of the AV surface that are not perfectly spherical (see Figure 5.1) effects both the direct and reflected light.

Several fibres near the equator of the detector are suitable for determining the offset of the AV in the X and Y directions. Figure 8.11 shows the direct light of fibres FT068A and FT069A. The respective positions of the fibres are (8279,5021,1289) and (8128,-1096, -1783) in PSUP coordinates. Both fibres are suitable to measure the offset in the X axis.

In Figure 8.11a the direct light from fibre FT068A is shown, the shadowed region is caused by a hold up rope, next to this shadowed region an area of high occupancy is seen. It appears that the belly plate is causing a lensing effect. The AV at the belly plates is also thicker than other parts of the AV, instead of 5 cm its thickness is 10 cm. The point at which light reflects off of the face of the AV is closer to the fibre by 5 cm.

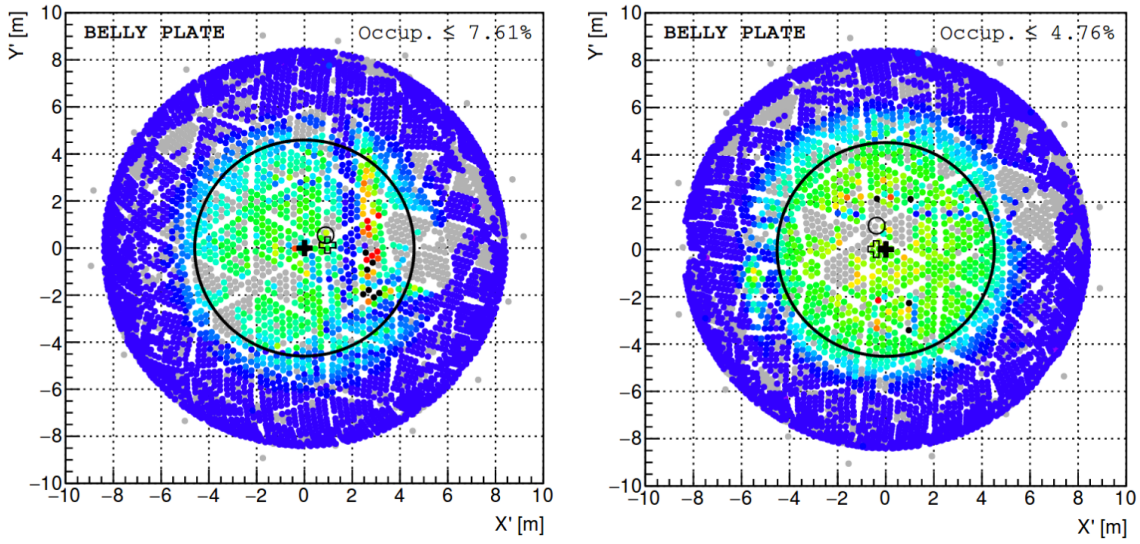

(a) FT068A run 101806.

(b) FT069A run 101809.

Figure 8.11: The direct light projections for fibre FT068A and FT069A. The direct light of fibre FT068A is effected by a belly plate [182].

The fit results for these fibres are shown in Table. 8.2 The runs for each fibre were directly after each other hence the offset must be caused by a systematic effect rather than a genuine shift in the AV position. The fibre with the belly plates shows a 12 cm shift from the nominal position. The fibre not effected by the belly plates shows results consistent with the expected zero offset. Any fibres with a beam spot that passes through the belly plates of the AV are not suitable for use with the AVLOC analysis.

Fibre	AV Offset (mm)	Error On AV Offset (mm)
FT068A	132.80	7.73
FT069A	-10.97	6.81

Table 8.2: AVLOC fit results for two TELLIE fibres. One fibre is effected by belly plates mounted on the AV, the other is not.

The line of low occupancy tubes passing through the beam spot in Figure 8.11b, is caused by a hold down rope shadowing the beam, based on the results shown in Table 8.2, the offset caused by hold down ropes is negligible.

8.3.3 Lateral Shifts in AV Position

Fibre FT040A is also near the equator of the detector with position (-744, 8177, -1556) the fibre mostly points in the negative Y direction, and is suitable for measuring offsets in that direction. Any shifts in the AV position perpendicular to the offset measured may cause a systematic effect on the fitted offset. Simulations were performed with the AV

positioned at the origin and the AV shifted up by 10.8 cm. The fit results for these two positions are listed in Table 8.3, in both fits the MC hit times of the PMTs were used.

AV Position (mm)	Fitted offset (mm)	Error On Fitted Offset (mm)
(0, 0, 0)	25.62	4.72
(0, 0, 108)	-6.63	3.28

Table 8.3: Fit results when the AV is shifted laterally to the fibre direction.

There is a 3.4 cm shift towards the fibre in the fitted AV offset, this could be caused by belly plates moving into the beam spot of the fibre affecting the fit. Another source of the shift may be caused by the fact the AV is a sphere. If this is the case fibres perpendicular to this fibre can measure the lateral offset, and the lateral offset could be used within the fitting procedure to remove this systematic.

8.3.4 The AV Neck

The AV neck region effects the light from the fibre in multiple ways. The AV geometry in this region can alter the path of the direct light, furthermore the neck region has much lower PMT coverage than other parts of the detector.

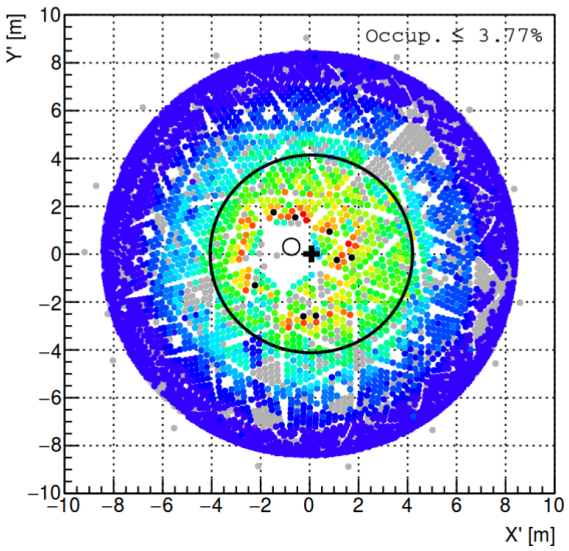

Figure 8.12: The direct light occupancy for fibre FT079A, the fibre is at the bottom of the detector pointing upwards [182].

8.3.5 Offline Channels

In Figures 8.11 and 8.12 some PMTs are marked grey: these PMTs were offline during the run. An earlier TELLIE run using FT079A was performed with more channels offline. Only 13 PMTs were online inside the reflected beam spot during this earlier run. A

simulation was run with these detector settings with the AV 0 cm and shifted upwards by 10 cm, the results are shown in Table 8.4. When compared to the fits in table 8.1, in which 29 PMTs were used to fit the AV position, a 3.5 cm to 4.5 cm shift can be seen. The offline channels have a significant effect on the fitted position of the AV.

AV Position (mm)	Fitted offset (mm)	Error On Fitted Offset (mm)
(0, 0, 0)	52.00	5.86
(0, 0, 100)	153.9	7.02

Table 8.4: AVLOC results with MC simulation of Run 100785.

8.4 Fitting to Data

8.4.1 Choosing Suitable Fibres

Fibres need to be chosen such that they lay close to an axis, for an accurate measurement in that axis. In total ten fibres were selected for use with AVLOC, the fibres and their positions are shown in Table 8.5. In the X direction two fibres were positioned on opposite sides of the detector. However in the case of the Y axis only one suitable fibre was found. Fibre FT058A can be used to position the offset in both the X and Y position, like the fibres used to position the X and Y offsets it is near the equator of the detector, but is positioned at approximately 49° from the X axis. Any offsets in the X and Y direction will be highly correlated for this fibre hence it is only suitable to verify the offset determined by the other fibres on the equator.

Five fibres can be used to position the Z offset of the fibre, they are all positioned at the bottom of the detector.

Fibre	Position	Axis
FT048A	(-8233.78, 1163.11, 1138.87)	X
FT075A	(7547.00, 3234.09, -1556.47)	X
FT033A	(-3311.18, 7645.50, -1025.51)	Y
FT058A	(-5406.61, -6176.89, -1566.62)	X & Y
FT090A	(2959.16, -550.74, -7834.87)	Z
FT079A	(-228.05, -326.13, -8383.14)	Z
FT084A	(-2717.72, -1293.81, -7834.87)	Z
FT087A	(390.66, -2984.50, -7834.87)	Z
FT080A	(-2070.30, 2184.89, -7834.87)	Z

Table 8.5: A list of selected fibres for determining the AV offset in various axes and their positions.

8.4.2 Verification of the Selected Fibres With MC

In order to verify that the fibres correctly identify the offset of the AV, RAT simulations were run with two known offsets for each fibre. For each fibre, offset combination a total of 100,000 TELLIE pulses were simulated with an intensity of 1,000 photons per pulse. The results of the fits are shown in Table 8.6. Several fibres show significant discrepancy from their MC fit values. Unfortunately no fibres in the X & Y axes were found to agree well enough with the truth values in MC to be suitable for use with data. However, as the ropenet constrains the AV in both the X and Y directions and there are no significant forces in either axis the offset in both axes is expected to remain zero, the focus is on the shift in the Z axis. Three fibres were chosen for use in the Z axis: FT090A, FT079A and FT087A.

Fibre	True offset (mm)	Fitted Offset (mm)	Fitted Error (mm)
FT048A	0	-14.95	8.24
	50	55.49	6.16
FT075A	0	-22.81	6.88
	50	39.82	7.15
FT033A	0	18.90	4.51
	50	74.25	5.00
FT058A	0	-38.26	6.88
	50	22.54	6.55
FT090A	0	6.62	7.87
	50	58.88	7.94
FT079A	0	12.75	7.17
	50	67.6	7.51
FT084A	0	-8.09	7.49
	50	67.4	7.64
FT087A	0	-0.34	9.15
	50	46.77	8.77
FT080A	0	-16.2	8.20
	50	40.0	7.73

Table 8.6: AVLOC fit results to a known AV offset from RAT simulation. The fit error is statistical only.

8.4.3 Results: Fits to Data

A full TELLIE PCA dataset was taken during the period May-June 2017. All three fibres had data taken. Each fibre's data set consisted of a total of 200,000 pulses, with an intensity setting to give an occupancy of less than 5% in the centre of the TELLIE beam spot. Table 8.7 shows the fitted results for all the fibres. Also shown is the calculated offset in the corresponding axis simply obtained via $O_X = O_F \cos\theta$ where O_X is the offset

in the axis, O_F is the offset relative to the fibre and θ is the angle between the fibre and the axis.

Fibre (Run Number)	**Axis**	**Fitted Offset (mm)**	**Fit Error (mm)**	**Reduced χ^2**	**Fitted Offset in Axis (mm)**	**Fit error in Axis (mm)**
FT090A (101910)	Z	114.1	4.67	1.34	106.5	4.36
FT079A (101842)	Z	95.2	21.9	0.279	95.2	21.9
FT087A (101898)	Z	190.2	2.11	4.61	177.6	1.9

Table 8.7: The AVLOC fit results for a selection of fibres to TELLIE PCA data taken in May-June 2017. The fit error is statistical only.

The three Z fibres found a positive offset in the Z axis, taking a weighted average of the offset in the Z direction the AV offset has been calculated as 106.1±4.3 mm. The third fibre (FT087A) had a much higher reduced χ^2 than the other fibres and was not used in the average fit. A direct measurement of the vertical offset of the detector using a ruler during commissioning of the detector found an offset of 109 mm which is within the uncertainty of the value obtained from TELLIE.

8.5 Measuring the Scattering Length of the External Water

Rayleigh scattering occurs when light scatters from particles much smaller than the wavelength of light [185], in the case of SNO+ this involves scattering from the water and scintillator molecules within the detector. Rayleigh scattering is strongly wavelength dependent, and is proportional to $1/\lambda^4$ where λ is the wavelength of light. Another type of scattering possible is Mie scattering [185]. This occurs when light scatters off of particles with a radius much larger or comparable to the wavelength of light. Mie scattering has no wavelength dependence, and also produces a different angular distribution to Rayleigh scattering.

As the scattering peak shown in Figure 8.7 arrives before the AV reflection peak, the back-scatterings occur within the external water volume of SNO+. The size of the scattering peak is inversely related to the scattering length of the external water. The smaller the scattering length in the external water, the larger the backscattered peak. The Rayleigh scattering length is altered in simulation by modifying the `RSLENGTH_value` fields within the `OPTICS` table of RATDB. Mie scattering is currently not simulated within RAT. The default scattering length used in RAT as a function of wavelength is shown in Figure 8.13.

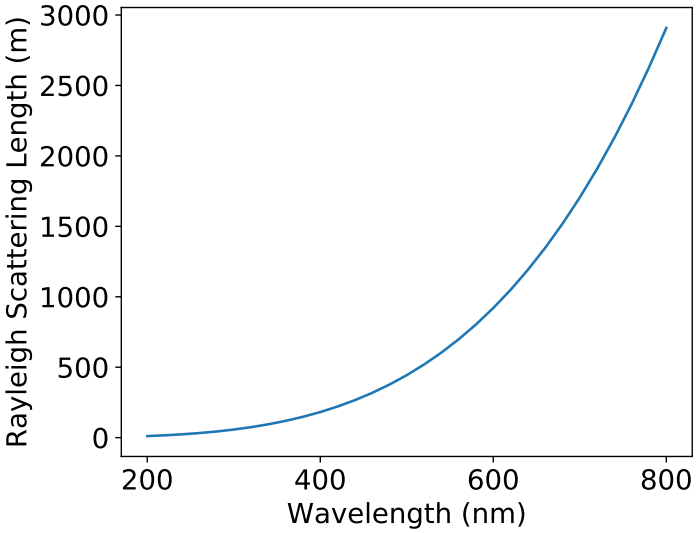

Figure 8.13: The default scattering length in water used in RAT shown as a function of wavelength.

Figure 8.14, shows the reflected light distributions produced by AVLOC for two simulations of fibre FT040A with varying scattering lengths. When the scattering length is smaller, more scattered light is observed. The distribution shown in Figure 8.14 is from PMT 2902, using fibre FT040A with 1,000,000 pulses and 1,000 photons per pulse (approximately 25 NHit per pulse).

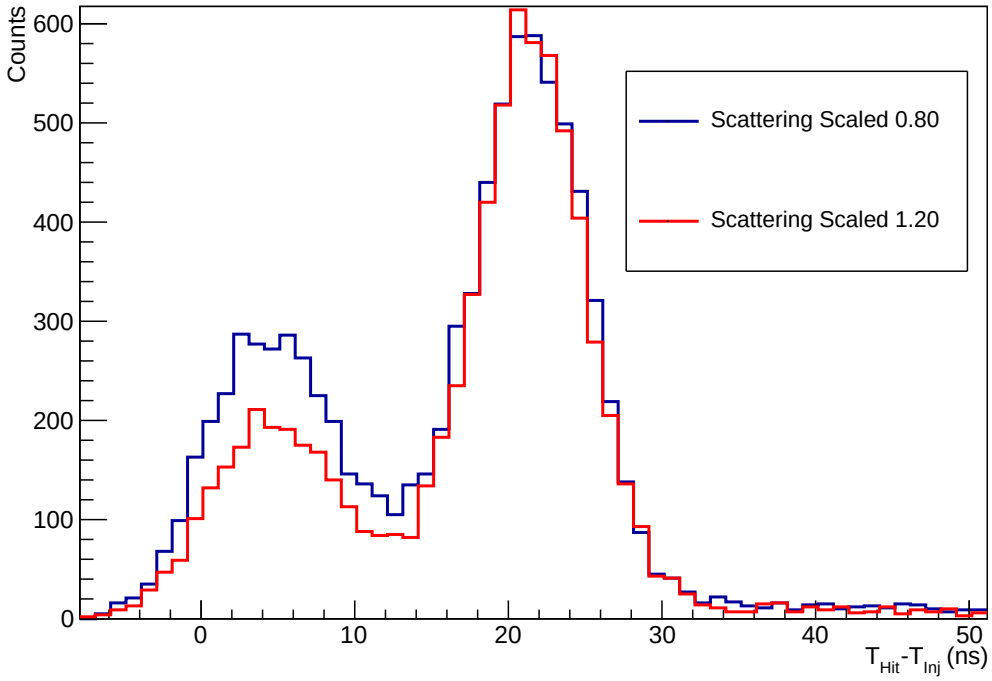

Figure 8.14: Variation of the time distribution of reflected light observed by a single PMT. The results of two simulations are shown, in one simulation the scattering length is set to 0.8 times the RAT default in the other simulation the scattering length is set to 1.2 times the rat default scattering length.

8.5.1 Procedure

A procedure was developed to determine the scattering length of the external water using the early scattered light. The method broadly follows three stages:

- The simulation of the fibre with varying scattering lengths.
- Running of the AVLOC processor on the simulations to obtain the histograms like those shown in Figure 8.14.
- Performing a χ^2 fit on the scattering peaks in the aforementioned histograms to data to determine the best scattering length.

Before the MC histograms can be fitted to data a normalisation step must take place. In simulation the number of photons emitted per pulse is fixed, in reality the number of photons emitted varies from pulse to pulse. To perform the normalization, the direct occupancy of the TELLIE PMTs is used. The direct occupancy does vary with scattering length, but it is insignificant compared to the variation in the reflected light with scattering. Figure 8.15 demonstrates that when the scattering length is changed from half the RAT

default to twice the RAT default the direct occupancy varies by only 4%. Realistically the scattering length is not expected to vary by more than 20% from the RAT default, in this case the direct occupancy varies by less than 1%.

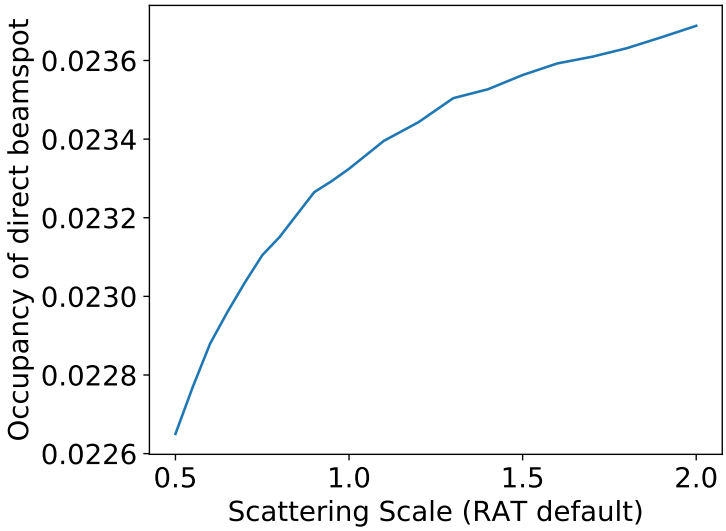

Figure 8.15: The direct light occupancy as a function of scattering length for simulations of fibre FT040A.

The ratio of the occupancies averaged over the entire direct beamspot is used to normalize the MC histograms to the data. Each PMT in the reflected beam spot region sees backscattered light from different angles from the fibre, as shown in Figure 8.16.

The normalization factor is shown in Eq. 8.17. The sum is made over the angular bins of the histograms shown in Figure 7.16, $D(\theta)$ is the direct occupancy for each bin. The error on the normalization is obtained using Eq. 8.18, where $\sigma(D)$ is simply the error on the mean of the bins.

$$N = \frac{\sum_\theta D_{\mathrm{Data}}(\theta)}{\sum_\theta D_{\mathrm{MC}}(\theta)} \tag{8.17}$$

$$\sigma_N = N \cdot \sqrt{\left(\frac{\sigma(\bar{D}_{\mathrm{Data}})}{\bar{D}_{\mathrm{Data}}}\right)^2 + \left(\frac{\sigma(\bar{D}_{\mathrm{MC}})}{\bar{D}_{\mathrm{MC}}}\right)^2} \tag{8.18}$$

In order to remove the AV reflection peak, a time cut (denoted by t_c in the following equations) is made, only hits arriving before 10 ns are considered. A small portion of AV reflected photons will arrive at the PMTs before the time cut. The fit to the AV reflection peak, shown in Figure 8.7, is used to perform background subtraction on the scattered light. The number of PMT hits due to scattered light for data is given by Eq. 8.19. The

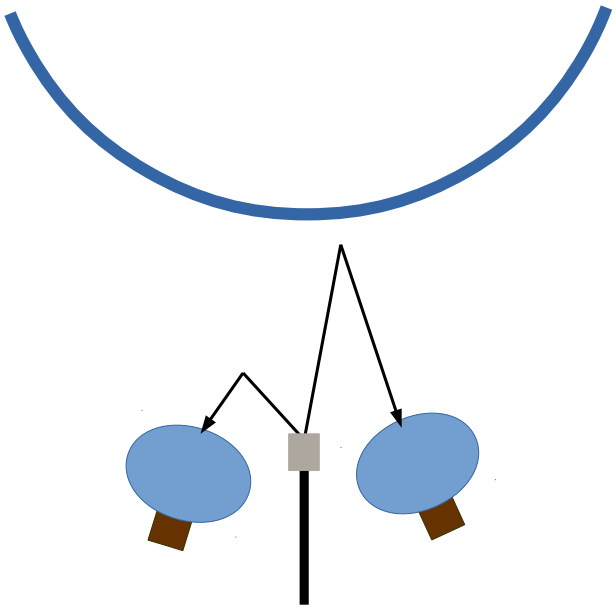

Figure 8.16: A schematic of the scattered light paths within the external water region of the detector. Scattering will take place at varying distances from the fibre and PMTs, resulting in the observed distribution of hit times for the scattered light

first term of Eq. 8.19 is a sum over the bins in the histogram shown in Figure 8.14 up to the time cut. The second term represents the removal of the AV reflection background, t_0 is the low edge of the first bin within the histogram.

$$A = \sum_{\tau<t_c} R(t) - \int_{t_0}^{t_c} AV_{\text{ref}}(t)dt \tag{8.19}$$

The uncertainty on the value of A is given by $\sigma_A = \sqrt{\sum_{t<t_c} R(t)}$. The uncertainty on the integral of the AV reflection peak is assumed to be negligible.

The number of hits due to scattering for Monte Carlo is given by Eq. 8.19, scaled by the normalization factor N, this case $R(t)$ is the histogram produced in RAT simulations. The error on the total number of hits must also take the uncertainty on the scaling factor into account, as shown in Eq. 8.20. The values of A' and σ'_A denote the unscaled values and uncertainties respectively.

$$\sigma_A(\text{MC}) = N \cdot A'_{\text{MC}} \cdot \sqrt{\left(\frac{\sigma_N}{N}\right)^2 + \left(\frac{\sigma'_{A(\text{MC})}}{A'_{\text{MC}}}\right)^2} \tag{8.20}$$

The occupancy of a PMT due to scattered light is obtained by dividing the total number of hits A due to scattered light by dividing the histograms by the number of shots

fired η. A χ^2 minimisation is then performed by summing over the PMTs in the reflected beamspot. The χ^2 function is defined by Eq. 8.21.

$$\chi^2 = \sum_{\text{PMT}} \frac{\left(\frac{A_{\text{Data}}}{\eta_{\text{Data}}} - \frac{A_{\text{MC}}}{\eta_{\text{MC}}}\right)^2}{\sigma^2_{A(\text{Data})} + \sigma^2_{A(\text{MC})}} \tag{8.21}$$

8.5.2 Performance with Monte Carlo Simulation

In order to fit the scattering length several simulations were run using fibre FT040A. The scattering length was varied from 0.5 times to two times its default value in RAT. Between 0.5 and 1.0 the scattering length is scaled in steps of 0.05, between 1.0 and 2.0 times the scattering length the scattering is scaled in steps of 0.1. At each step, 1,000,000 events were simulated with 1,000 photons per pulse. In addition, the detector state was simulated to be in the state of run 101553. This was done to match the detector configuration when the fibre was pulsed in reality. An additional 'fake' dataset with scattering length 1.0 was simulated in order to perform the fit to. The results of the fit are shown in 8.17.

The fitted value and the uncertainty on the measurement were obtained by fitting a fourth order polynomial to the χ^2 points, the point at which the polynomial satisfied the relation $\chi^2 = \chi^2_{\text{min}} + 1$ was used to determine the error on the fit.

The to the fake dataset is shown in Figure 8.17, the best fit and the estimated error on the fit are: $0.984^{+0.028}_{-0.027}$.

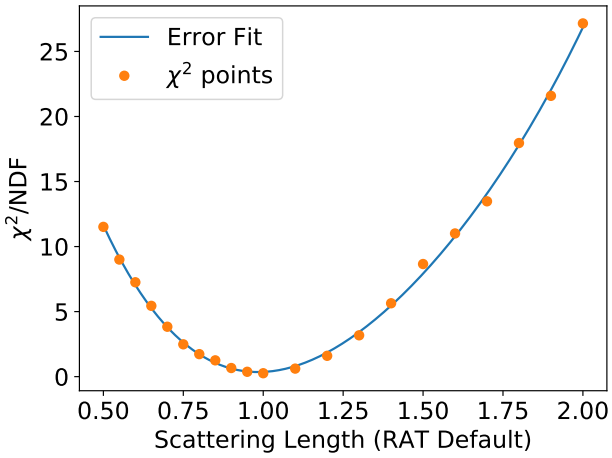

Figure 8.17: χ^2 values comparing simulation of TELLIE fibre FT040A to a fake (MC) data set in order to determine the functionality of the analysis procedure. Also shown are fits to the χ^2 evaluations used to determine the error on the fit.

8.5.3 Fit to data

The MC test results were also fitted to the TELLIE run 101553, taken in June 2017. This was a standard PCA run and had two hundred thousand pulses of TELLIE with an intensity of approximately 1,000 photons. Some triggers were missed by the detector during pulsing and only 196932 TELLIE events are used within the analysis. The χ^2 evaluation and the fits to determine the uncertainty on the measurement are shown in Figure 8.18.

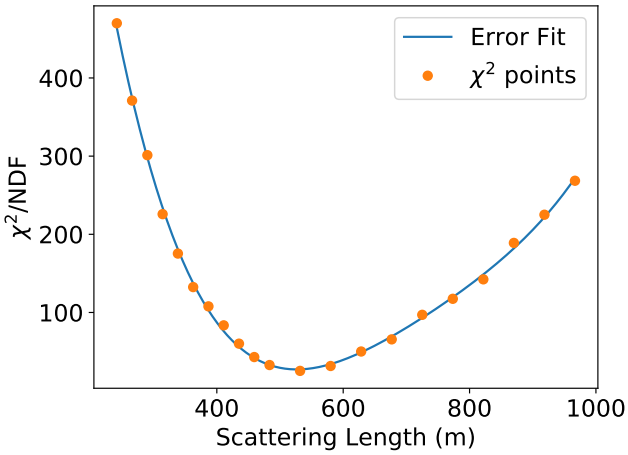

Figure 8.18: χ^2 values comparing simulation of TELLIE fibre FT040A to data in order to measure the scattering length of the external water. Also shown are fits to the χ^2 evaluations used to determine the error on the fit.

The polynomial fitted to the χ^2 points in order to estimate the best fit and error was a fourth order polynomial. The best fit and the error calculated using the fit function was $1.089 \pm^{0.041}_{0.039}$ times the default RAT scattering length..

Figure 8.19 shows the hit times on PMT 2900, which lies within the reflected beamspot of fibre FT040A. Only the region to the left of the dashed line is used within the scattering length fit, two simulated scattering lengths are shown in the figure. In Model A the default scattering length used in RAT (shown in Figure 8.13) is scaled by a factor 0.6. Model B is the best fitting simulation, where the scattering length is scaled 1.1 times the RAT default. The increase in the width of the AV reflection peak seen in data is thought to be caused by non specular reflections on the AV. Further work is in progress to fit roughness of the AV by using the width of the AV reflection peak.

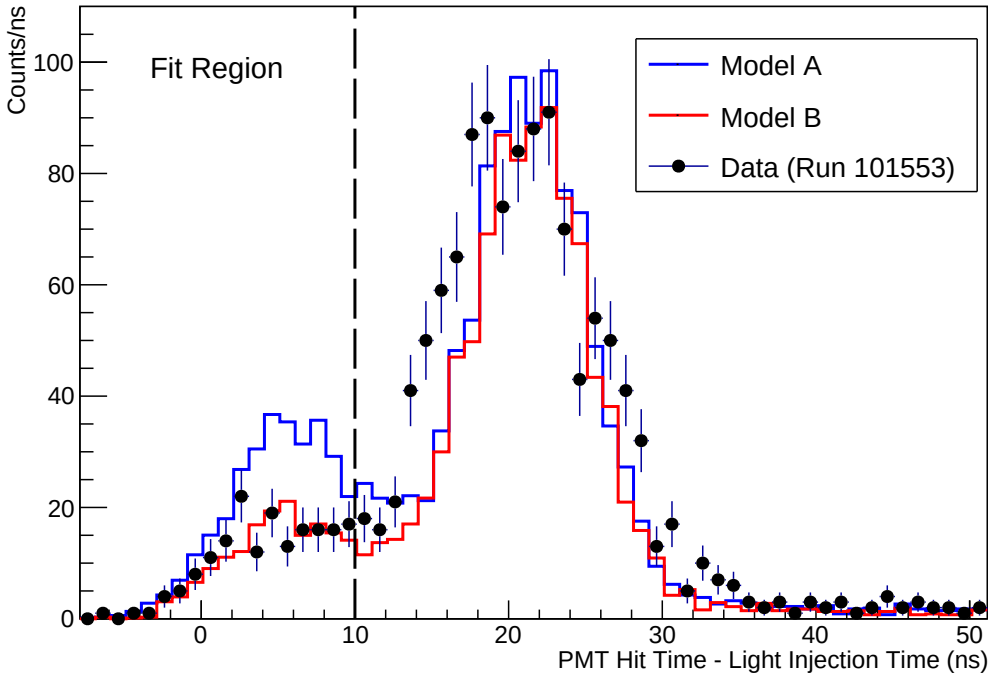

Figure 8.19: A comparison of the timing distributions of hits observed on a single PMT in the reflected beamspot region when the scattering length of water is varied in simulation. In Model A the RAT default scattering length is scaled by a factor 0.6. In model B the RAT default scattering length is scaled by a factor 1.1. Also shown is data taken using the same fibre.

8.5.4 Effect of Temperature Change on the Scattering Length

One possible explanation for the increase in scattering length observed is the water temperature of the cavity. The nominal operating temperature for the SNO+ detector is 10 °C, at the start of running during the time which the TELLIE PCA runs were taken the temperature of the cavity water was higher than this. Eq. 8.22 shows the Rayleigh scattering of length a liquid defined by the Einstein-Smoluchowski-Cabannes formula [186]. L_{Ray} is the Rayleigh scattering length, λ is the wavelength of the light, n is the refractive index, k is Boltzmanns constant, T is the temperature and κ_T is the isothermal compressibility of the material. δ is the depolarization ratio, for wavelengths around the TELLIE LED region and at room temperature this value is appears to be small, the value of the depolarization ratio was measured at 514.5 nm and found to be 0.039 [187]. This was significantly smaller than previous estimates which were effected by stray light causing a increase in the measured depolarization ratio. When δ is zero intermolecular forces are neglected and the media is approximated as an ideal gas. Any increase of the depolarization ratio results in a reduction of the predicted scattering length.

$$L_{\text{Ray}} = \left\{ \frac{8\pi^3}{3\lambda^4} \left[\frac{(n^2-1)(2n^2+0.8n)}{n^2+0.8n+1} \right]^2 kT\kappa_T \frac{6+3\delta}{6-7\delta} \right\}^{-1} \tag{8.22}$$

Figure 8.20 shows the TELLIE wavelength averaged Rayleigh scattering length in water as a function of temperature. The temperature dependence of n was obtained using the approximation described in [188], the values of κ_τ were obtained by interpolating between the values in [189], the value of δ was set to zero.

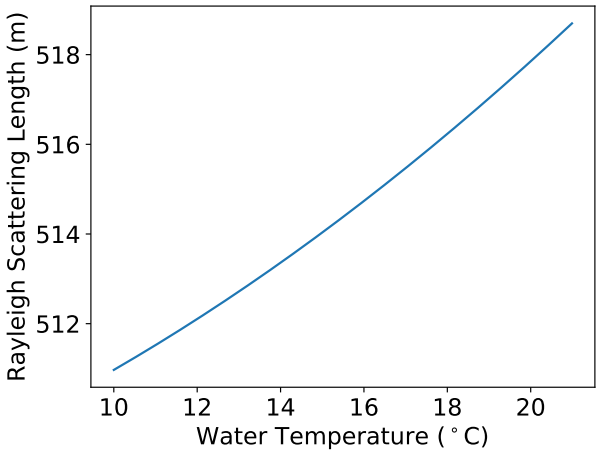

Figure 8.20: The Rayleigh scattering length of water as a function of temperature.

The TELLIE spectra weighted averaged Rayleigh scattering length currently used within RAT is 483.42 m, therefore the fitted value of the scattered (1.088 times this) is 527^{+20}_{-19} m. Run 101553 took place on the 9$^{\text{th}}$ June 2017. A measurement of the cavity water temperature was taken on the 11$^{\text{th}}$ of the same month and found the cavity temp to range between 15 °C and 18 °C. The theoretical result predicted using Eq. 8.22, and shown in Figure 8.20, predicts a scattering length of 514 to 516 m, this is agreement with the fitted value. When a value of $\delta = 0.039$ is used the theoretical prediction ranges from 479 to 483 m. However, as previously discussed, measurements of the depolarization ratio are effected by stray light which systematically increases the measured value of the depolarization ratio [187].

8.5.5 Systematic effects: Fibre Direction

One possible systematic effect on the scattering analysis is the fibre direction within the detector, an analysis was performed to fit the fibre positions and directions [182]. As the fibres are mounted to the PMTs the uncertainty on the fibre position was assumed to be negligible. The direction was fitted using the center of the direct light beamspot and the

Direction	u	v	w
RATDB	0.00014	-0.98	0.19
Fitted	0.029	-0.98	0.21

Table 8.8: The RATDB default and the fitted directions for fibre FT040A.

RATDB position. The fitted direction showed an approximate 2° [182] difference from the default value within RAT. The fitted direction and the RAT default are shown within Table 8.8.

Simulations were run with the fitted position and compared with the data, the scattering length of water was varied from 0.7 times the RAT default to 1.3 times the RAT default in steps of 0.03. Both datasets were processed using AVLOC with the new updated fibre direction. The results of the fit are shown in Figure 8.21.

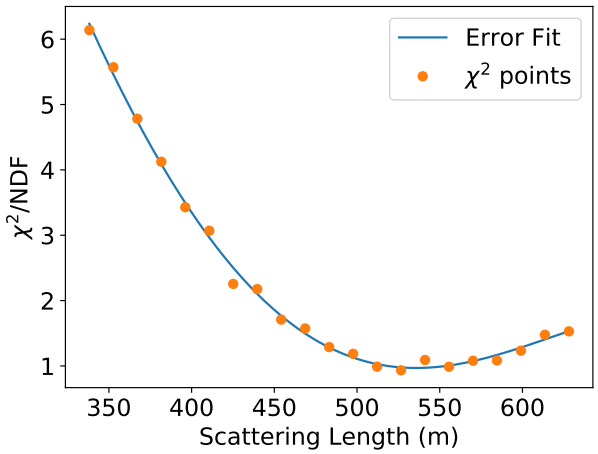

Figure 8.21: χ^2 values comparing simulation of TELLIE fibre FT040A to data in order to measure the scattering length of the external water. Also shown are fits to the χ^2 evaluations used to determine the error on the fit. A fitted value for the fibre direction is used.

The best fit value for the scattering length was $1.109\pm^{0.040}_{0.038}$ times the RAT default. This corresponds to a scattering length of $536\pm^{19}_{18}$ m. As the scattering length for the original fit was $527\pm^{20}_{19}$, a systematic error in the fibre direction of 2° is causes an approximate 11 m increase the measured scattering length of the external water. Any uncertainty in the fitted fibre direction is at the sub-degree level, therefore this systematic is smaller than the statistical error.

8.5.6 Systematic effects: LED Wavelength

Previously only the average LED wavelength distribution from all the TELLIE fibres was used to generate the simulation results. Each LED has a slightly different wavelength distribution, each LED had its wavelength distribution measured by a spectrometer during the commissioning of the hardware. The average distribution used in simulation and the distribution corresponding to LED 56, which was patched into fibre FT040A for run 101553, are shown in Figure 8.22. The average distribution is peaked at approximately 506 nm, whereas the LED attached to fibre FT040A is peaked at 501 nm. It should be noted that the LED peak wavelength increases with temperature [190], but as the spectrometer measurements and the SNO+ detector deck are both kept at 20 °C the effect of this systematic is expected to be negligible.

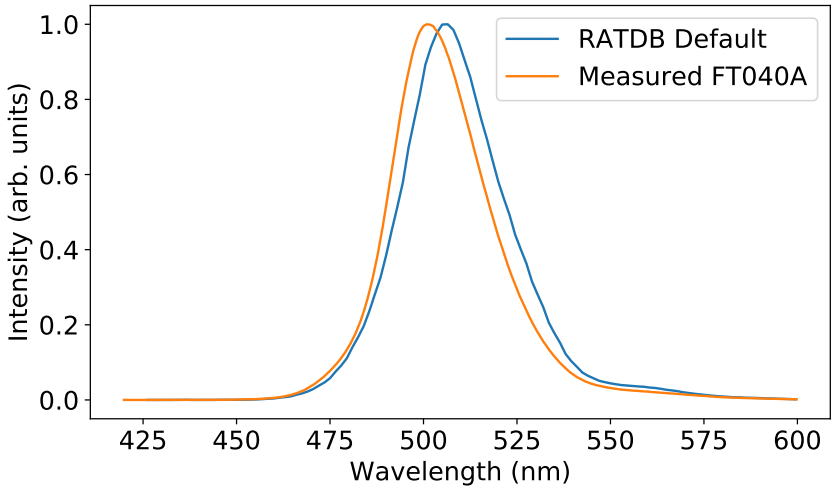

Figure 8.22: The LED wavelength distributions of the RAT default setting for TELLIE and LED 56, which is in use with FT040A.

The fit of the simulations to the data is shown in Figure 8.23. The best fitting scattering length was $1.075 \pm^{0.039}_{0.037}$ times the RAT default. This corresponds to a scattering length of $506 \pm^{18}_{17}$ m , this result takes into account alteration in the scattering length due to the change in LED wavelength. The theoretical prediction using Eq. 8.22 was between 465 and 470 m between water temperatures of 10 °C and 20 °C. The LED wavelength has the systematic effect of shifting the measured scattering length closer to the value used within RAT. If δ is set to zero the scattering length varies from 498 to 502 m when the water temperature is varied from 10 to 20 °C, in agreement with the predicted value.

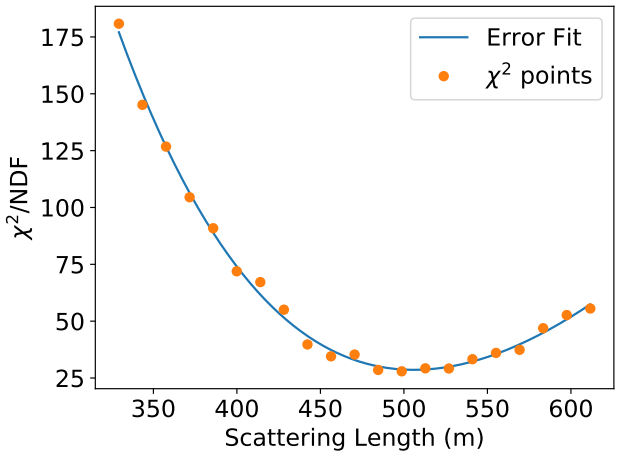

Figure 8.23: χ^2 values comparing simulation of TELLIE fibre FT040A to data in order to measure the scattering length of the external water. Also shown are fits to the χ^2 evaluations used to determine the error on the fit. The LED spectra used corresponds to the LED coupled with fibre FT040A during the run.

8.5.7 Conclusions

An in-situ measurement of the scattering length within the external water was made using a TELLIE fibre. The analysis procedure was verified using Monte Carlo. The best fitting scattering length within data is $1.088 \pm^{0.041}_{0.039}$ times the default value used within the RAT simulation. The fitted result agreed with the theoretical prediction for the Rayleigh scattering length, taking the cavity temperature into account and setting the depolarization ratio of water to zero. The measurement was made using a standard TELLIE PCA run.

As the analysis procedure requires the simulation of multiple scattering lengths, an analysis involving all fibres is not practically feasible. A smaller subset of fibres could be analysed to determine the scattering lengths at various heights within the detector however.

A combined fit of the AV position and external water scattering length could be made, however this would involve simulating over a two dimensional parameter space (AV position and scattering length) and may prove to be computationally prohibitive. Another alternative would be to develop and analytical model for the scattering within the external water and add this to the AVLOC processor.

To summarise the measured Rayleigh scattering length using the correct LED spectra was found to be $506 \pm^{18}_{17} \pm^{10}_{10}$ m, the first set of errors is the statistical error on the fit, the second set is the systematic error corresponding to a 2° shift in the fibre direction.

8.6 Summary

This chapter presents two analyses. One analysis used an analytical fit to determine the position of the AV based on the light reflected from the outer face of the AV. When the analysis was run on data a fitted offset consistent with no offset in the X or Y axes was found. In the Z axis two fibres found an average offset of 106.1 ± 4.3 mm upwards. This measurement was consistent with a direct measurement of the AV offset which found an offset of 109 mm upwards.

The second analysis involved fitting Monte Carlo simulation to data to determine the scattering length of the external water. Fibre FT040A, which is near the equator of the detector, was used to fit the scattering length of the external water. The best fitting of scattering length was $1.089 \pm^{0.041}_{0.039}$ times the RAT default (which is 483.42 m averaged over the TELLIE LED spectra), or $527 \pm^{20}_{19}$ m, this value is consistent with theoretical Rayleigh scattering predictions in water for the water temperatures measured two days after the data was taken if the value of δ is set to zero. The systematic effect of the uncertainty on the direction of the fibre was explored. When using the fitted direction of the fibre which deviated approximately 2° from the default direction a systematic shift to longer scattering lengths of approximately 10 m was observed. The systematic effect of the variance of the LED spectra was also considered, when the LED spectra that specifically corresponds to fibre FT040A was used the default scattering length within RAT showed a slightly better agreement with the data. Another possible systematic to be considered in future is the beam profile of the TELLIE fibre.

This chapter demonstrates that several detector properties can be determined using the TELLIE reflected light. The distance of the AV from the fibre can be measured using the AV reflection peak, the scattering length can be determined by the size of the backscattered peak. Future work to fit the width of the AV reflection peak can hopefully be used to determine the roughness of the AV surface.

Chapter 9

Sensitivity of SNO+ to Supernova Neutrinos

This chapter describes the sensitivity of the SNO+ detector to supernova. The first presents a study comparing the supernova signal to the detector backgrounds, the chapter then describes the burst trigger efficiency as a function of distance. The chapter then presents a toy study to the sensitivity of various neutrino detectors to the neutrino mass hierarchy using the neutrinos from a supernova burst. Only the matter (MSW) oscillation effects (which are described in Section 4.6.1) are considered. The sensitivity as a function of supernova distance is presented, these sensitivities are combined with the expected galactic supernova distance distribution shown in Figure 4.14 in order to obtain the probability of reaching a certain level of sensitivity given a galactic supernova occurs. The chapter concludes by making a comparison between the toy studies and the results of a full detector simulation in order to identify any systematic detector effects.

This chapter first describes the software that was used and further developed to convert the simulated neutrino fluences into input for the SNO+ detector simulation. The chapter then presents a series of cuts and an unblinding procedure should a supernova occur within the water phase of SNO+, the results of which are based on simulations. The chapter then continues with a study into the efficiency of the burst trigger, the lowest level of any potential supernova trigger, as a function of supernova distance. Full detector simulations are performed using an analytical expression for the supernova fluence, which has been used for previous SNO+ supernova sensitivity studies [48]. Next, the chapter presents the sensitivity of various detectors to the neutrino mass hierarchy, if a supernova

burst happens. First the sensitivity using a toy MC study for three detectors (SNO+, JUNO and Super-K) is presented. Also shown is a global fit combining the detectors, as well as the sensitivity assuming our current knowledge of the neutrino mass hierarchy as a prior. The sensitivity using a full detector simulation of SNO+ is also presented.

9.1 SNUGEN

The simulation software used to generate the following results is known as SNUGEN. The code was originally written by Belina von Krosigk and Torben Ferber. Several improvements have been made by the author to include additional cross sections, either in the GLoBES format [191] or as a ROOT TGraph. Functionality was also added to produce the summary plots shown in Figures 9.2 and 9.3. A separate library of python scripts was also written by the author to generate HEPEVT files from the SNUGEN output known as HEPEVTGEN using accurate kinematics of the interactions. The HEPEVT output was readable by RAT, enabling a full detector simulation of the supernova burst.

The input to SNUGEN is provided by the Garching supernova group [192]. The group performs simulations using the PROMETHEUS-VERTEX [193] code for various mass progenitors and equations of state. The results described in this chapter use a set of 10 1D models with progenitor masses ranging from $11.2M_{\odot}$ to $27.0M_{\odot}$ and use the Lattimer-Swesty [194] equations of state with a nuclear compressibility of 220 MeV.

9.1.1 SNUGEN Procedure

The input provided by the Garching group consists of four parameters sampled at different times during the supernova explosion. The time stepping is non-linear. In the regions surrounding the core bounce, the time stepping is small (approximately 10 µs). At later times the time step size is increased to approximately 100 µs. The supernovae were simulated between 0.17 s pre bounce until 0.5 s post bounce.

For each time step, four values are stored for each of ν_e, $\bar{\nu}_e$ and ν_x: the neutrino luminosity, and the averages of: the neutrino energy, the neutrino energy squared and the neutrino energy cubed. The four quantities are used to evaluate the neutrino spectra during that time step.

Generating the neutrino spectra

The values from the tables are used to construct the neutrino spectrum. The spectra are evaluated using Eq. 9.1. L_0 is the luminosity in MeV, $\langle E \rangle$ is the mean energy of the

neutrinos, and β is known as the pinching parameter, defined by Eq. 9.2 and $\langle E^2 \rangle$ being the average energy squared.

$$\frac{dL}{dE} = L_0 \frac{1.0}{\langle E \rangle^2} \frac{(1+\beta)^{1+\beta}}{\Gamma(1+\beta)} \frac{E}{\langle E \rangle}^{\beta} e^{\frac{-(1+\beta)E}{\langle E \rangle}} \tag{9.1}$$

$$\beta = \frac{2 - \frac{\langle E^2 \rangle}{\langle E \rangle^2}}{\frac{\langle E^2 \rangle}{\langle E \rangle^2} - 1} \tag{9.2}$$

SNUGEN produces the neutrino fluences for a fixed number of time bins specified by the user. Two time stepping methods exist to evaluate the spectra for these time bins. The first method treats the parameters Ł$_0$, β and $\langle E \rangle$ as continuous functions of time and evaluates the spectra at fixed time intervals by linearly interpolating between the points provided by the input. The second method evaluates the spectrum at each input time. The output spectra is provided by a average weighted by the bin width of the input.

In order to produce the spectrum Eq. 9.1 must be integrated with respect to energy. Two methods are in place to do this; the first method uses a GSL [195] integration library to numerically integrate Eq. 9.1 before binning, the second method uses a crude midpoint rule method to integrate the spectrum.

Calculating the number of interactions

After the spectrum has been calculated, it is convoluted with the cross sections for a set of user specified interactions to obtain the distribution of interacting neutrino energies in each time bin. Cross sections, which can be obtained analytically, such as those described in Sections 3.2, 3.3 and 3.4. Cross sections calculated numerically such as the ^{12}C interactions shown in Figure 3.9 are stored internally as a ROOT TGraph. Linear interpolation between the input points is used if necessary. The number of interactions occurring within the detector is obtained by applying a scaling factor given in Eq. 9.3. The first term is the scaling due to the distance from the supernova. The second term (the term in the brackets) corresponds to the number of targets within the detector, M is the fiducial mass of the detector, ρ is the density of the detector and η_{T} is the number of targets per cm^3.

$$S = \frac{1}{d^2} \times \left(\frac{\mathrm{M}}{\rho} \times \eta_{\mathrm{T}} \right) \tag{9.3}$$

SNUGEN also calculates the energy distribution of the outgoing particles for $\nu - p$, $\nu - e$ and IBD events using the kinematics described in Chapter 3. In the case of IBD events, only the energy of the outgoing positron is stored. The visible energy is defined

differently depending on the type of the detector as shown in Eq. 9.4, the liquid scintillator gains an additional $2m_e$ term due to the annihilation γ produced, which is not visible in water Cherenkov detectors.

$$\begin{aligned} E_{\text{vis}} &= E_\nu - \Delta - m_e \quad \text{(Water Cherenkov)} \\ &= E_\nu - \Delta + m_e \quad \text{(Liquid Scintillator)} \end{aligned} \tag{9.4}$$

Quenching, as described in section 5.2.2, can also be applied to the $\nu - p$ scattering events.

The analytical cross sections which can be calculated internally by SNUGEN are:

- Inverse Beta-Decay (IBD)
- Neutrino Electron Scattering ($\nu - e$)
- Neutrino Proton Scattering ($\nu - p$).

The nuclear cross-section tables included in SNUGEN are:

- ^{12}C tables [64]
- ^{16}O tables [56].

Cross sections for Tellurium are not available within literature, hence the following studies show the sensitivity for either the water phase or the pure scintillator phase of SNO+.

9.1.2 HEPEVTGEN Procedure

HEPEVTGEN consists of several python scripts to sample the output of SNUGEN and produce HEPEVT files for use within RAT. The code takes two SNUGEN files as input, one represents the events taking place in the inner AV region. The other is optional and represents events within the outer AV region. The direction of the supernova relative to the detector can also be controlled via an argument to the code.

The code parses the inputs of the SNUGEN file. For each SNUGEN time bin the interacting neutrino energy histograms are sampled to obtain the interacting neutrino energies within that time bin for that interaction. The time of each event is generated uniformly within the time bin.

The interacting neutrino energies and the direction to the supernova are used to calculate the kinematics of the interaction using the equations detailed in Chapter 3. The distribution of the ejecta energy and direction[1] is sampled to obtain the energy and direction of each event.

HEPEVTGEN is able to simulate the kinematics of three interactions:

- Inverse Beta Decay (including the kinematics of the neutron)
- Neutrino Proton Scattering
- Neutrino Electron Scattering

The interactions with nuclei are omitted due to a lack of literature on their kinematics and the possible final states the nuclei could end up in.

The positions of the events inside the inner AV region are generated uniformly within a 6 m radius. Events within the outer AV region are generated uniformly between 6.05 m and 9 m.

9.2 Supernova Analysis Plan for the Water Phase of SNO+

By the time a supernova happens it is important to have a robust analysis procedure set up such that a result of the energy and time distributions of a supernova signal can be published quickly for comparison with other experiments. As the main purpose of the water phase of SNO+ is to search for invisible nucleon decay, all events with energies between 5 MeV and 15 MeV are blinded. An unblinding procedure also must be developed in the case of a supernova burst to determine the background levels surrounding the burst time. This section describes a policy developed by the author to be undertaken in the case of a supernova burst during the water phase of SNO+.

To determine an analysis procedure, a conservative approach has been taken. Therefore, an electron core collapse supernova, which has lower core temperatures than an iron core collapse supernova, and in turn produces a cooler neutrino spectrum, has been used. The spectrum is shown in Figure 4.4.

9.2.1 Backgrounds to the Burst

The estimated backgrounds to a supernova signal are obtained by looking at seven days of data from the start of SNO+ water phase running. This data was fully unblinded to

[1] As an example see Figure 3.4, where the distribution must be calculated for each incoming neutrino energy and then sampled.

understand the background in the nucleon decay signal region. During the early stages of running the background levels were higher than nominal for water phase due to decaying backgrounds left over from commissioning. The standard data cleaning and reconstruction cuts were applied to the events within the detector, Figure 9.1 shows the energy and radial distribution of background events reconstructing within the AV. The band of events at the sub MeV level are made up of events below the PMT noise threshold of the detector and likely have these energies due to missreconstruction, all physics analyses in the water phase of SNO+ use a higher threshold than these events.

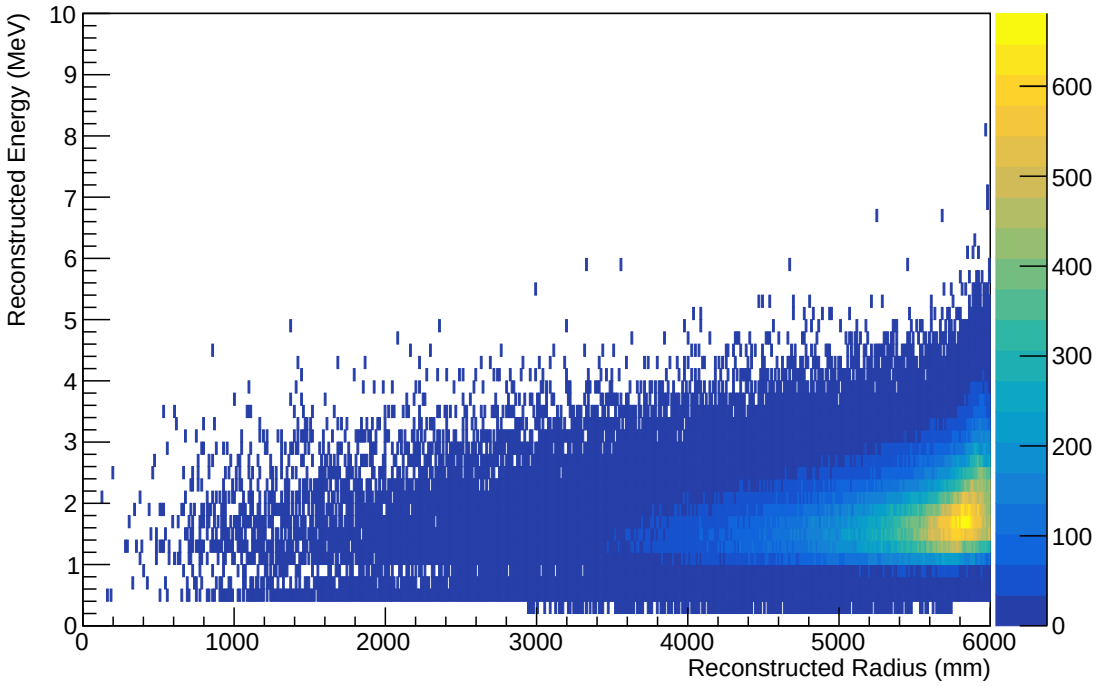

Figure 9.1: The distribution of background events within the SNO+ AV at the start of the water phase. The plot shows seven days of data and no blinding has been applied to the data.

9.2.2 Generating the Burst

The flux model shown in Figure 4.4 was combined with the interaction cross sections described in Chapter 3. Only the inverse beta decay interaction and neutrino electron elastic scattering were considered, proton scattering was omitted as SNO+ is unable to detect scattered protons in its water phase.

The energy spectrum of the neutrinos interacting in the first second of the supernova from Figure 4.4, at a distance of of 1 kpc and for the entire AV inner volume (mass 1 ktonne)

is shown in Figure 9.2. The timing distribution of events in the first second can be seen in Figure 9.3.

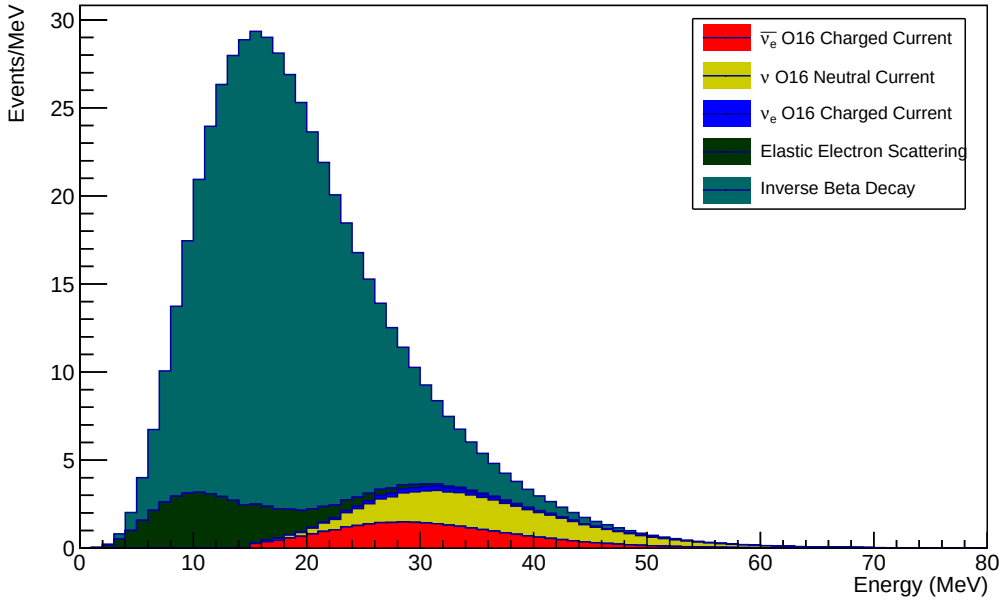

Figure 9.2: The energy distribution of neutrino events in the first second of a supernova burst for various interaction channels. The neutrino fluxes are obtained from the model shown in Figure 4.4. The supernova is simulated at a distance of 1 kpc and the detection medium is 1 ktonne (the mass of the inner AV region) of water.

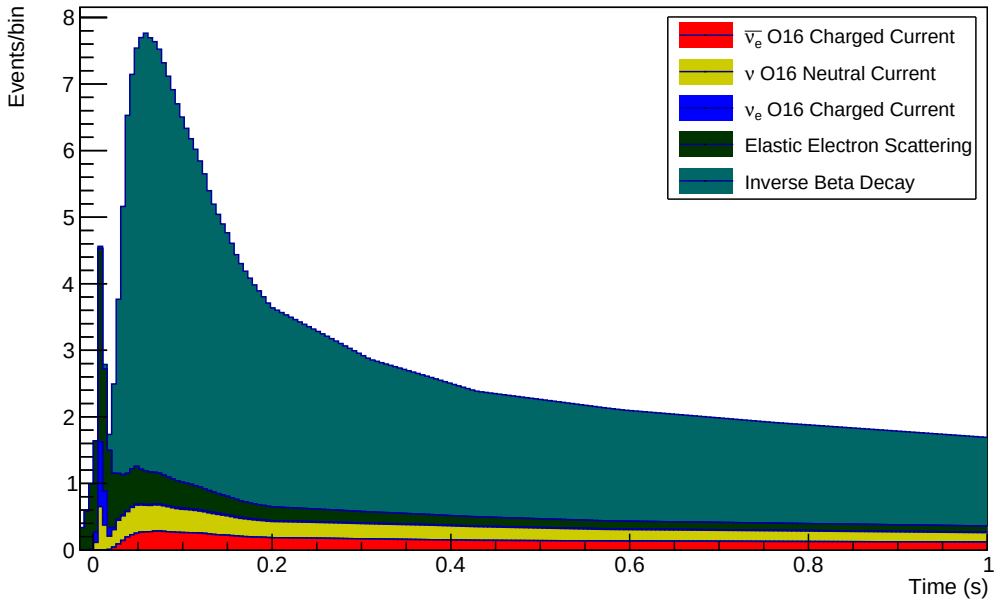

Figure 9.3: The time distribution of neutrino events in the first second of a supernova burst for various interaction channels. The configuration is the same as for Figure 9.2.

The histograms in Figures 9.2 and 9.3 were sampled to produce interaction energies for the neutrinos. These samples were then used to generate both the directions and energies of the outgoing particles of the neutrino interactions. When generating the directions, the supernova was assumed to occur in the negative x direction in the detector geometry, i.e. The neutrinos were incoming horizontally relative to the detector. In order to obtain a statistical measure of the detector response to the burst one hundred HEPEVT files were generated and simulated. Interactions with oxygen were not included due to a lack of understanding of the interaction kinematics. The lack of ^{16}O interactions will not effect the outcome of the cut regime study presented in the next section as the interactions produce isotopes which often decay with energies greater than 5 MeV. However, the burst trigger study will be effected as a proportion of the interactions will be missing reducing the efficiency of the burst trigger.

The HEPEVT files were then simulated in RAT, and the same data cleaning and reconstruction cuts were applied to the events as the backgrounds. The reconstructed energies and radii of the simulated events are shown in Figure 9.4.

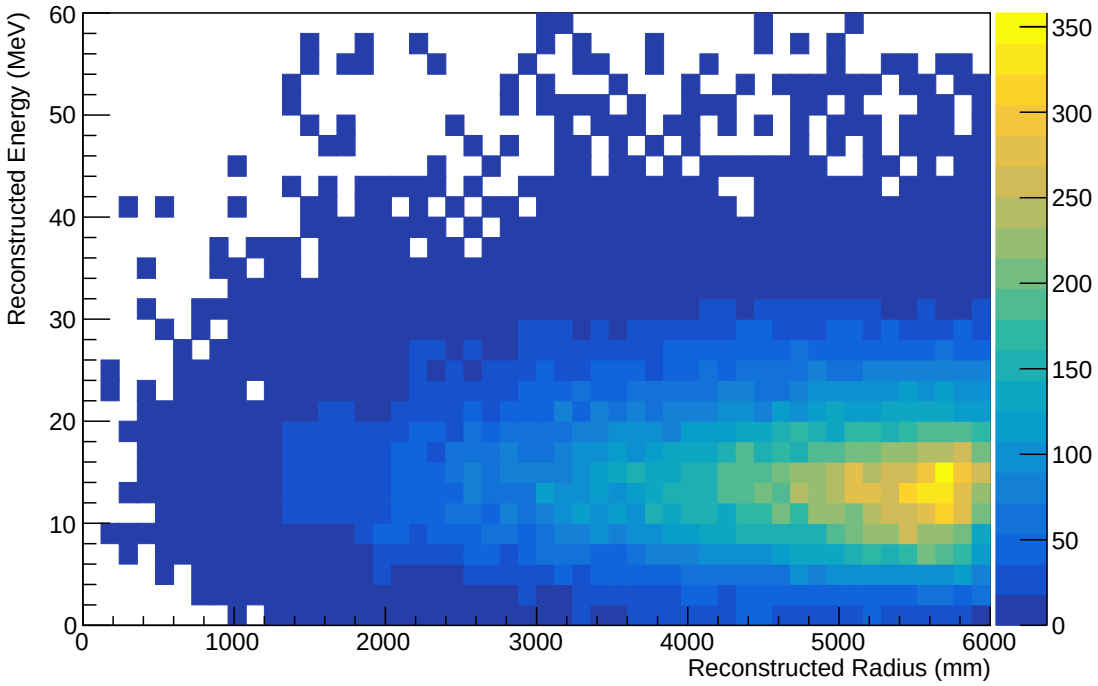

Figure 9.4: The distribution of reconstructed energies and radii of the 100 simulated supernovae bursts.

9.2.3 Defining an Unblinding and Cut Procedure

The cut procedure must be simple in order to allow the quick publication of results, additionally it must remove background events, whilst keeping the majority of the supernova burst signal. This section describes a cut regime which meets these criteria.

Figure 9.4 shows that many of the supernova events occur within the nucleon decay blindness region. Therefore, in the event of a burst the data should be unblinded. Furthermore, to understand the backgrounds of the detector around the time of the burst, the 24 hours before and after the burst should also be fully unblinded.

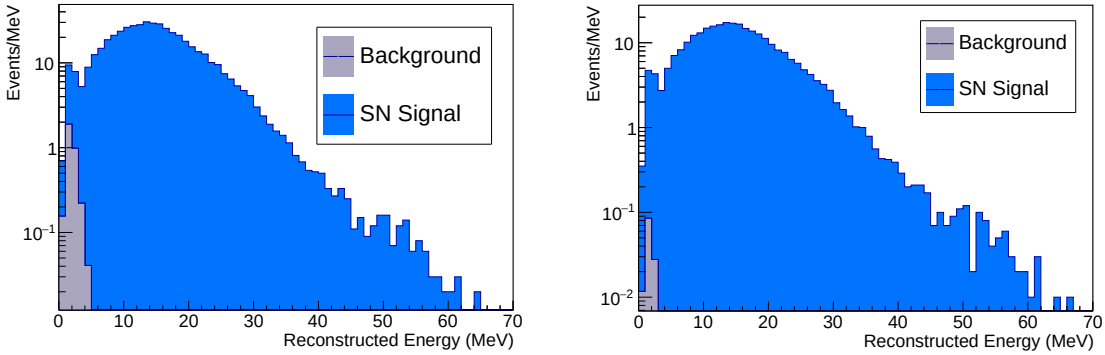

(a) No Radial Cut.

(b) 5 m Radial Cut.

Figure 9.5: Energy spectra of SN events and background events for two fiducial volumes.

Figure 9.5 shows the spectra of supernova and background events expected for a supernova at 1 kpc for two fiducial volumes. The majority of the background events occur in the region closest to the AV and have energies lower than 5 MeV. A conditional cut was developed to reduce the backgrounds to a supernova signal. The energy of the event was measured if it is above a certain energy threshold then no fiducial volume cut is applied. If the energy is below a certain energy threshold it is possible it is a background event, as most of the background events occur near the surface of the AV a fiducial volume cut is applied to events below the energy threshold.

Figure 9.6 shows the proportion of background and signal remaining for varying cut parameters. The most stringent cut, all events below 5 MeV must be reconstructed within a 5 m fiducial volume, removes approximately 60% of the backgrounds whilst keeping 98% of the signal.

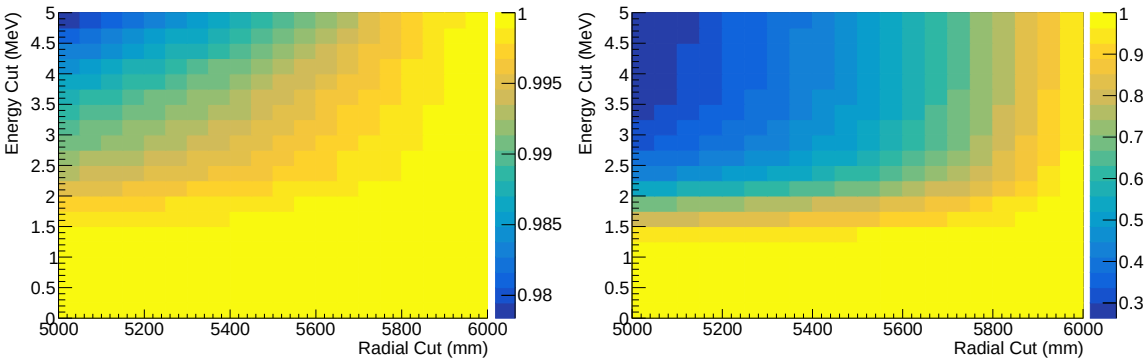

(a) Proportion of Remaining Signal.

(b) Proportion of remaining background events.

Figure 9.6: Proportion of background and signal events remaining as a result of varying the cut energy parameters.

9.3 Burst Trigger Efficiency as a Function of Distance

The burst trigger is the lowest level of trigger to identify a possible supernova. It is also used to study breakdowns in the detector electronics. The code runs nearline on the events as they are being built. If the criteria for a burst are met a burst file is produced. In the scintillator and $0\nu\beta\beta$ phases of the experiment software will analyse the burst file to see if the burst is a result of a supernova or a PMT breakdown.

The trigger looks for events with an NHit greater than 40. The code looks over a 10 s window counting the number of events meeting the NHit criteria. If more than 30 events are seen within a predefined time window the burst trigger is initiated, and the events passing the NHit criteria are written to a burst file. The burst trigger stops when the rate of events above 40 NHit drops below 10 Hz averaged over the last second.

The efficiency of the trigger was obtained for supernovae at varying distances. This represents an optimistic assessment of the efficiency of any future SNO+ supernova trigger. The burst trigger can only provide information on whether a large number of high NHit events over a short time period. To determine if the source of these events was due to a supernova further analysis needs to take place. The subsequent analysis will not be perfect and will not be able to correctly determine the cause of the burst 100% of the time.

The analytical flux was generated using Eq. 9.1. The values of $\langle E \rangle$, L_0 and β were obtained from [48] [196], and their values are shown in Table 9.1. No oscillations were applied to the neutrino spectra. The neutrino spectra are shown in Figure 9.7.

Neutrino Flavour	L_0 (10^{51} ergs)	$\langle E \rangle$ (MeV)	β
ν_e	50	12.0	3.0
$\bar{\nu}_e$	50	15.0	3.0
ν_x	50	18.0	3.0

Table 9.1: The parameters used to generate the analytical neutrino spectra for use in determining the trigger efficiency.

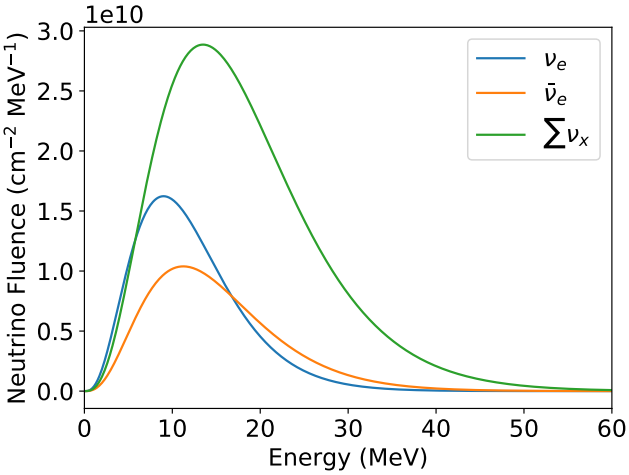

Figure 9.7: The analytical spectra of the neutrino fluence from a supernova used to determine the burst trigger efficiency.

The spectra were convoluted with the appropriate cross sections using SNUGEN to obtain the number of events in both the inner AV region and the external water region. Only inverse beta-decay events and electron scattering events were considered.

The histograms produced by SNUGEN were sampled by HEPEVTGEN. As the analytical spectra has no time dependence, the SN burst was assumed to last 10 s and the HEPEVT events were generated uniformly in a range 0 to 10 s. As the burst trigger counts events in a 10 s window, finer time binning will not have any effect on the burst efficiency.

One hundred SN were simulated at varying distances, with steps of 0.1 kpc from 20 kpc to 50 kpc. A model of the burst trigger is implemented into RAT, and the output of each simulation was studied to determine if the burst trigger had fired. The trigger efficiency and its error were determined using binomial statistics as shown in Eqs. 9.5 and 9.6. N_{trig} is the number of simulated supernovae that caused the burst trigger to fire, and N_{SN} is the total number of supernovae simulated.

$$E = \frac{N_{\text{trig}}}{N_{\text{SN}}} \tag{9.5}$$

$$\sigma(E) = \frac{1}{N_{\text{SN}}}\sqrt{N_{\text{trig}}(1-E)} \tag{9.6}$$

Figure 9.8 shows the trigger efficiency and its error as a function of distance. The burst trigger will fire more than 99% of the time for supernovae upto approximately 30 kpc. Past this the trigger efficiency begins to drop off reaching 50% efficiency at approximately 40 kpc. At 50 kpc the trigger efficiency is below 10%.

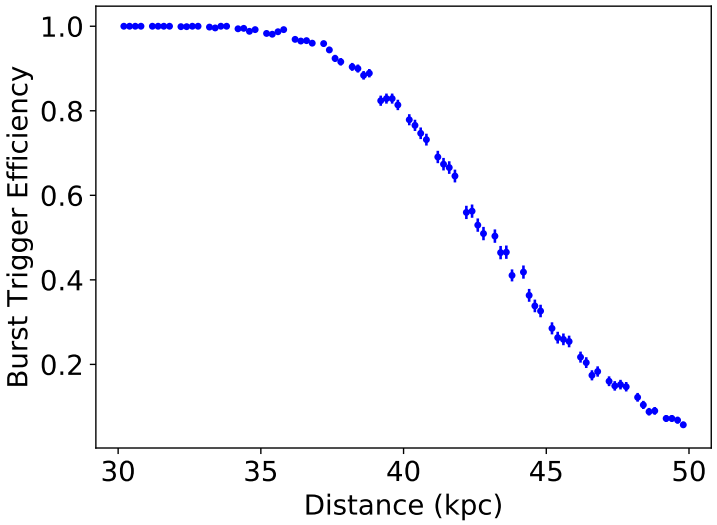

Figure 9.8: The proportion of simulations of supernovae at varying distances for which the burst trigger fired.

9.4 Determining the Mass Hierarchy Using Neutrinos From a Supernova

At early times during a supernova burst, the MSW matter effect plays a large role in determining the neutrino spectra seen at Earth. The core of the star is electron rich and any ν_e produced (mainly by electron capture processes between electrons and free protons) are created in the heaviest mass eigenstate. This is due to the adiabatic MSW effect described in Section 2.2. The heaviest mass eigenstate is denoted ν_3^m or ν_2^m, depending on whether the mass hierarchy is normal or inverted. It is suitable to consider the adiabatic effect at this point in time during a supernova burst, as a shockfront has not yet formed, and no large matter density discontinuities exist within the star. Depending on the hierarchy, the neutronization burst is completely or partially converted to ν_x (see Section 4.6.1).

As the sign of the MSW potential, is flipped for antineutrinos $\bar{\nu}_e$ are produced (via pair-production processes) in the lowest mass eiegenstate ν_1^m or ν_3^m depending on the hier-

archy. In the same way as neutrinos, the antineutrinos propagate out from the supernova adiabatically at early times. In the normal hierarchy the $\bar{\nu}_x$ will be produced in the ν_2^m and ν_3^m states, whereas in the inverted hierarchy the neutrinos will be produced in the ν_1^m and ν_2^m eigenstates. The unoscillatred ν_x flux has a quicker rise time than that of unoscillated $\bar{\nu}_e$ flux as the pair production of $\nu_e\bar{\nu}_e$ and e^+e^- pairs is Pauli blocked. Due to the increased mixing of $\bar{\nu}_e$ with ν_1 and ν_2, a quicker rise time of $\bar{\nu}_e$ is seen in the inverted hierarchy (See Section 4.6.1).

9.4.1 Analysis Procedure

The mass hierarchy analysis follows the procedure described in [197]. The analysis begins with the Bayes equation given by Eq. 9.7. $P(\text{Data}|\text{MH}, \text{M})$ is the likelihood of producing the data given a hierarchy MH (Which can either be the normal hierarchy (NH) or the inverted hierarchy (NH)) and a supernova model M. $\pi(MH)$ is the prior belief of a given hierarchy in nature. $P(\text{MH}|\text{Data})$ is the posterior probability of a certain mass hierarchy given the data, as there are only two possibilities, NH or IH, the sum of the posterior probabilities is equal to one $P(\text{NH}|\text{Data}) + P(\text{IH}|\text{Data}) = 1$.

$$P(\text{NH}|\text{Data}) = \frac{P(\text{Data}|\text{NH})\pi(\text{NH})}{P(\text{Data}|\text{NH})\pi(\text{NH}) + P(\text{Data}|\text{IH})\pi(\text{IH})} \tag{9.7}$$

By assuming a uniform prior on the hierarchy $\pi(IH) = \pi(NH) = 0.5$, Eq. 9.7 can be written in the form shown in Eq. 9.8, when $\Delta\chi^2$ is defined by Eq. 9.9.

$$P(\text{NH}|\text{Data}) = \frac{1}{1 + e^{-\frac{\Delta\chi^2}{2}}} \tag{9.8}$$

$$\Delta\chi^2 = -2\ln\frac{P(\text{Data}|\text{IH})}{P(\text{Data}|\text{NH})} \tag{9.9}$$

The overall likelihood for a certain mass hierarchy (MH) is found by summing up the likelihoods for each model as shown in Eq. 9.10. The value of $P(\text{MH}|\text{M})$, is the prior probability of a certain mass hierarchy given a certain supernova model as these values are independent this reduces to $P(\text{M})$, i.e. the probability of a supernova occurring with progenitor mass M. For the analysis considered in this chapter we assume a uniform prior on the mass of the progenitor, i.e. all models are equally likely.

$$
\begin{aligned}
P(\text{Data}|\text{MH}) &= \sum_M P(\text{Data}|\text{MH},\text{M})P(\text{M}|\text{MH}) \\
&= \sum_M P(\text{Data}|\text{MH},\text{M})\frac{P(\text{M}\cap\text{MH})}{P(\text{MH})} \\
&= \sum_M P(\text{Data}|\text{MH},\text{M})\frac{P(\text{M})P(\text{MH})}{P(\text{MH})} \\
&= \sum_M P(\text{Data}|\text{MH},\text{M})P(\text{M})
\end{aligned}
\tag{9.10}
$$

Three interaction channels are used in the procedure: Inverse Beta Decay (IBD), neutrino proton scattering ($\nu - p$) and neutrino electron scattering ($\nu - e$).

The $\nu - p$ and $\nu - e$ interaction channels are grouped into a single set of events, denoted as untagged events, they are indistinguishable from one another in the SNO+ detector. As $\nu - p$ scattering has the same cross section for all flavours of neutrino the number of $\nu - p$ scatter events seen in SNO+ will be independent of the mass hierarchy as shown in Figure 9.9a. The $\nu - e$ cross section varies with flavour as described in Section 3.3, the cross section for electron flavour neutrinos is larger than that of the other flavours. The enhancement of the $\nu - e$ scattering event rate is shown in Figure 9.9b. In the inverted hierarchy, the larger ν_e flux will result in more untagged events being seen relative to the normal hierarchy, as shown in Figure 9.10b. Figure 9.10a shows the expected counts of the number of IBD events for all models as a function of time for a supernova at 1 kpc. Equations 4.6 through to 4.11, are used to generate the oscillated fluences, the value of θ_{12} used is 33.89°.

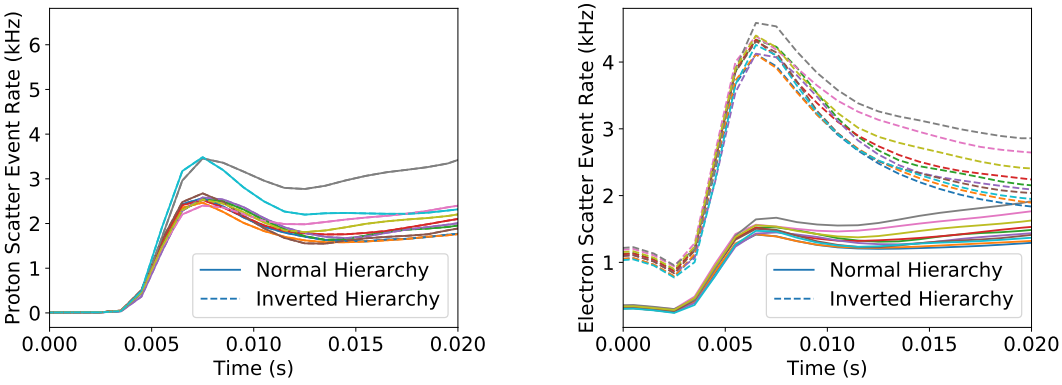

(a) $\nu - p$ Events

(b) $\nu - e$ Events

Figure 9.9: The event rates of $\nu - p$ and $\nu - e$ untagged events in the SNO+ detector (no fiducial volume cut) for a SN at 1 kpc. Each colour corresponds to a individual SN model. The color coding of each model is consistent with Figure 9.10 below.

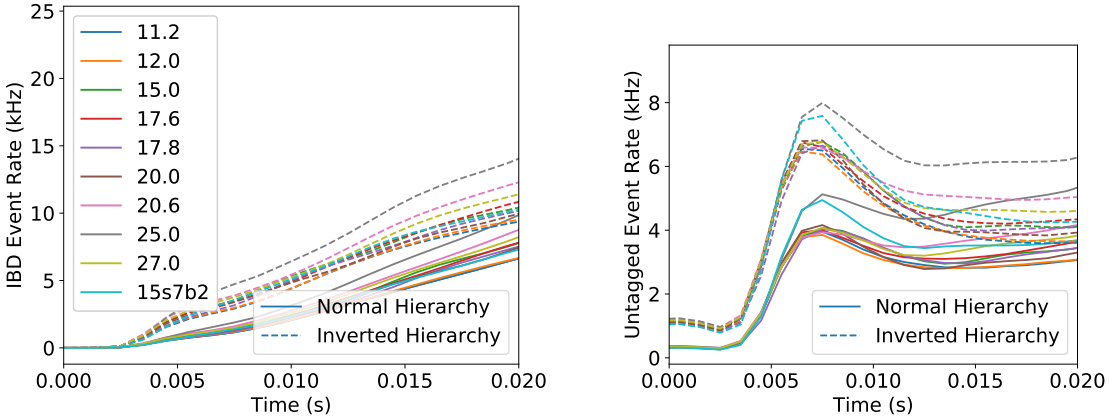

(a) IBD Events

(b) Untagged Events

Figure 9.10: The event rates of IBD and untagged events in the SNO+ detector (no fiducial volume cut) for a SN at 1 kpc. Each colour corresponds to a individual SN model.

9.4.2 Mistagging of Inverse Beta-Decay Events

Inverse beta-decay (IBD) events can be tagged by looking for a distinctive neutron capture signal after the prompt signal caused by the IBD interaction itself. The tagging process is not perfect and some IBD events will not be correctly identified. Neutrino detectors have a certain tagging efficiency that identifies the proportion of the time that a true IBD event will be identified as such. Scintillator detectors like KamLAND, SNO+ and Borexino have high tagging efficiencies (τ) in the order of 80-90% [198] [199]. Any events that are not correctly identified as inverse beta decay events will appear as untagged events. Depending on the threshold of the detector either only the prompt signal or both the prompt and delayed neutron capture signal may be observed. In both cases the misstagged events must be accounted for within the untagged interaction channel. If both the prompt and delayed signal are observable in the detector. A single mistagged IBD event will result in two untagged events. This must be taken into account during the analysis.

9.4.3 Generating the Fake Dataset

To generate the fake dataset, a model is first chosen at random. Next the histograms for the true number of IBD events and untagged events ($\nu - e + \nu - p$ in the case of scintillator detectors) created by SNUGEN are then scaled for the distance to the supernova and the fiducial volume of the detector. The expected number of IBD interactions within a bin is given by N_{IBD}, and the expected number of untagged interactions is given by N_{Un}. The fake dataset is obtained by Poisson sampling each bin as shown in Eqs. 9.11-9.12. Each

time bin will have a value of D_{Un} and D_{IBD} corresponding to the number of interactions occuring within that time bin within the dataset.

$$D_{\mathrm{IBD}} = \mathrm{Pois}(N_{\mathrm{IBD}}) \tag{9.11}$$

$$D_{\mathrm{Un}} = \mathrm{Pois}(N_{\mathrm{Un}}) \tag{9.12}$$

If the IBD tagging efficiency has zero error, then the number of IBD events is given by accept-reject [200] rounding to the nearest whole number, denoted in Eq. 9.13 as $\mathcal{R}$.

$$D^{\mathrm{O}}_{\mathrm{IBD}} = \mathcal{R}(\tau \cdot D_{\mathrm{IBD}}) \tag{9.13}$$

In the case that the tagging efficiency has some error on it (σ_τ), a true tagging efficiency (τ') is sampled from a normal distribution with mean τ and width σ_τ. The number of tagged IBD events is then obtained using Eq. 9.13 but with τ replaced with the true tagging efficiency τ'.

The remainder of IBD events will appear as untagged events, the total number of untagged events is given by Eq. 9.14. Where η is the number of untagged events resulting from a single misstagged IBD event. In detectors with a low energy threshold or ones that are Gd-doped, the delayed neutron capture will also be detected and $\eta = 2$. Otherwise only the prompt positron signal is observed and $\eta = 1$ Both the prompt signal and delayed signal are added to the same bin. Migration of the neutron capture to another bin later in time is not considered.

$$D^{\mathrm{O}}_{\mathrm{Un}} = D_{\mathrm{Un}} + \eta \cdot (D_{\mathrm{IBD}} - D^{O}_{\mathrm{IBD}}) + B \tag{9.14}$$

A fake background dataset is also generated. The background rate to IBD events is negligible [48]. This is not the case for untagged events, however, depending on the detector configuration[2], there is a fixed background count per time bin. The number of background events in a given time bin B is obtained by generating Poisson distributed random numbers with mean equal to expected count.

[2] i.e for SNO+ with a 5 m fiducial volume, the third column in Table 9.3 would be scaled to the bin width

9.4.4 Evaluating the Likelihood

The log-likelihood of the IBD events, $\ln \mathcal{L}_{\text{IBD}}$, is obtained by evaluating the Poisson log-likelihood using Eq. 9.15, where i is the bin index of the histogram, x_i is the observed data value seen in that bin, and μ_i^M is the expected bin content for a given model M. In the case of 100% IBD tagging efficiency, or $\eta = 1$, we can evaluate the log likelihood of the untagged events ($\ln L_{\text{Un}}$) in the same way.

$$\begin{aligned} \ln \mathcal{L}_{\text{Pois}}(x, \mu^M) &= \sum_i x_i \ln \mu_i^{\text{M}} - \mu_i^{\text{M}} - \ln(x_i!) \\ &= \sum_i x_i \ln \mu_i^{\text{M}} - \mu_i^{\text{M}} - \sum_{j \leqslant x_i} \ln(j) \end{aligned} \tag{9.15}$$

If the IBD tagging efficiency is not perfect then the evaluation of the log-likelihood becomes more complex for the number of untagged events in the case where $\eta = 2$. The untagged events are a combination of true untagged events and pairs of events resulting from untagged IBD events. The number of untagged events will be a convolution of two Probability Mass Functions (PMFs): a Poisson distribution representing the number of true untagged events and another Poisson-like distribution κ (shown in Eq. 9.16). κ is the Poisson distribution scaled by a factor two to account for both the prompt and delayed signal. α is the expected number of untagged IBD events $\alpha = (1 - \tau) \cdot N_{\text{IBD}}$. The PMF of κ when $\alpha = 5$ is shown in Figure 9.11.

$$\kappa(K; \alpha) = e^{-\alpha} \frac{\alpha^{K/2}}{(K/2)!} \tag{9.16}$$

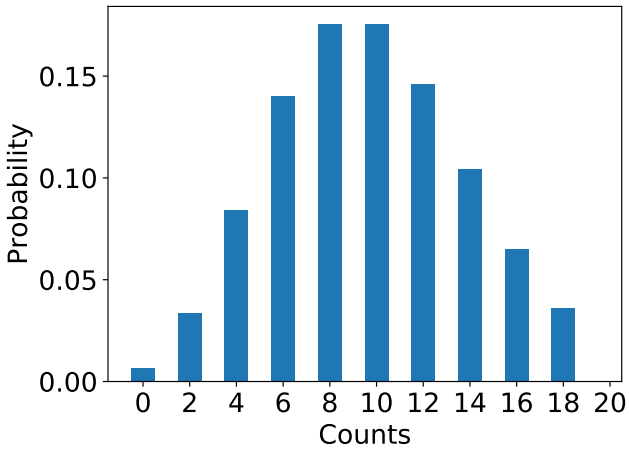

Figure 9.11: The distribution of κ shown in Eq. 9.16, which is used to model the distribution of additional untagged events due to untagged IBD events. The distribution shown has the value $\alpha = 5$.

The convolution of the two distributions is given in Eq. 9.17.

$$L_{\mathrm{Un}} = L(x;\alpha,N_{\mathrm{Un}}) = \sum_{K\leqslant x}^{K+2} \kappa(K;\alpha) L_{\mathrm{Pois}}(x-K;N_{\mathrm{Un}}) \tag{9.17}$$

As the convolution involves the sum of the likelihoods, the exponent of the log-likelihood must be taken. In order to avoid any issues due to floating point underflow, the log-likelihood is converted to an arbitrary precision decimal before the exponent and the sum are evaluated. After the sum, the logarithm is taken again and the number is converted back into a 64-bit float.

The overall log-likelihood for an individual model is given by the sum of the log-likelihoods over all the bins as shown in Eq. 9.18.

$$\ln P(\mathrm{Data}|\mathrm{MH},\mathrm{M}) = \sum_i \ln \mathcal{L}_{\mathrm{Un}}(i) + \ln \mathcal{L}_{\mathrm{IBD}}(i) \tag{9.18}$$

The overall likelihood of a given hierarchy is then obtained by marginalising over all the models as shown in Eq. 9.10. Once again the sum means the exponent of the log likelihood must be taken, and for this section of the calculation arbitrary precision arithmetic is used again.

The sensitivity plots (Figures 9.18, 9.19, 9.21, 9.23, 9.24, 9.25, 9.26, 9.27 and 9.43) show sensitivity levels in terms of $n\sigma$, the probability for $n\sigma$ sensitivity is given by Eq. 9.19. This corresponds to a one sided Gaussian fluctuation [197].

$$p = \frac{1}{2}\mathrm{Erfc}\left(\frac{n}{\sqrt{2}}\right) \tag{9.19}$$

9.4.5 Backgrounds

The radioactive decays likely to form a background to a SN burst signal have been extensively discussed in [48]. The backgrounds described below correspond to events that reconstruct within a 5 m (0.45 kt) fiducial volume.

The backgrounds to IBD events were found to be negligible across the time of the burst, with a random coincidence rate being of the order 10^{-5} Hz [48]. The main background to IBD events is caused by SN neutrinos interacting with ^{12}C releasing a neutron.

For untagged ($\nu - p$ and $\nu - e$) events the rate of events due to the detector (i.e. the ropes and the PMTs) were found to be negligible, with a total rate of 0.01 Hz.

The main backgrounds to a SN burst occur from intrinsic radioactivity in the scintillator and AV surface events.

The SNO experiment had much higher tolerances for low energy backgrounds than the SNO+ experiment due to the Cherenkov threshold. During construction of the detector the AV was exposed to radon rich mine air. One isotope in the radon decay chain is ^{210}Pb, which has a half life of 22.6 y and decays via β emission with an endpoint of 60 keV [201]. The long half life of the isotope means that a significant amount remains in the AV. Studies were made to investigate the removal of the embedded radon daughters by sanding the AV or using a EDTA solvent during the water phase of SNO+, but both were found to be cost and time prohibitive.

The daughter particle of ^{210}Pb is ^{210}Bi, which decays via β emission with a half-life of 5.01 d and endpoint energy of 1.16 MeV [201]. The ^{210}Po produced during the β decay then decays via the emission of an α particle with endpoint energy 5.30 MeV and half-life 138 d. The ^{206}Pb daughter produced is stable. The decay chain is shown in Figure 9.12.

^{210}Pb and its daughters form two types of background, inner AV surface backgrounds and internal backgrounds. The majority of the events are surface backgrounds. These events occur when one of the embedded ^{210}Rn daughters decays and depositing energy into the scintillator. They can be reduced significantly with a fiducial volume cut.

Table top experiments performed by members of the SNO+ collaboration found a significant rate of leeching from a test piece of of acrylic into the scintillator. Any nuclei that leech from the AV into the scinillator become internal backgrounds and are isotropically distributed within the scintillator volume.

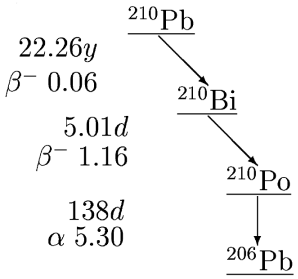

Figure 9.12: The end of the radon decay chain relevant to the backgrounds for the supernova analysis. [201]

The scintillator used in SNO+, LAB, is a hydrocarbon, a small proportion (10^{-18} g/g$_{\mathrm{LAB}}$) of the carbon atoms within the scintillator are the ^{14}C isotope. ^{14}C decays with and endpoint energy of 0.16 MeV [202] and has a half-life of 7730 y [203]. ^{14}C cannot be removed from the scintillator via chemical purification techniques. The decays form a low energy background, isotropically distributed within the scintillator volume.

The total predicted rates for background events occurring within the full scintillator

volume are shown in Table 9.2, bulk events indicate events which are caused by the intrinsic impurities in the scintillator and leaching from the AV. Surface events denote events which occur on the inner surface of the AV.

Isotope	Rate yr^{-1} (Hz)
^{14}C	4.08×10^9 (129.29)
Bulk ^{210}Pb	1.93×10^8 (6.12)
Bulk ^{210}Bi	1.93×10^8 (6.12)
Bulk ^{210}Po	2.03×10^8 (6.43)
Surface ^{210}Pb	3.04×10^{10} (963.34)
Surface ^{210}Bi	3.04×10^{10} (963.34)
Surface ^{210}Po	3.12×10^{10} (988.69)

Table 9.2: The raw expected background rates of relevance for a supernova burst for the pure scintillator phase of SNO+. Numbers obtained from [204], discussion of the backgrounds can be found in [35].

Table 9.3 shows the number of events which reconstruct within a various fiducial volumes for a period of 0.02 s, with an energy threshold of 0.2 MeV. The internal measurements of the radon daughters are the sum of the intrinsic rates due to imperfections in the purification process and the leaching.

Isotope	6 m Fiducial Cut	5.5 m Fiducial Cut	5 m Fiducial Cut
^{14}C	3×10^{-4}	2.9×10^{-5}	1.9×10^{-5}
Bulk ^{210}Pb	0.0	0.0	0.0
Bulk ^{210}Bi	0.084	0.066	0.050
Bulk ^{210}Po	0.14	0.108	0.082
Surface ^{210}Pb	0.0	0.0	0.0
Surface ^{210}Bi	4.46	0.006	3.4×10^{-4}
Surface ^{210}Po	8.87	0.073	0.02
Sum	13.55	0.253	0.152

Table 9.3: The reconstructed event counts occurring within a 0.02 s event window within varying fiducial volumes.

There is a factor of ten reduction in the event count of the ^{14}C background when the fiducial volume is changed from 6.0 m to 5.5 m. This is caused by the 0.2 MeV energy cut. Figure 9.13 shows the ^{14}C spectra for two fiducial volumes, when the larger fiducial volume is used the tail of the reconstructed energy extends to higher energies resulting in an increased event rate.

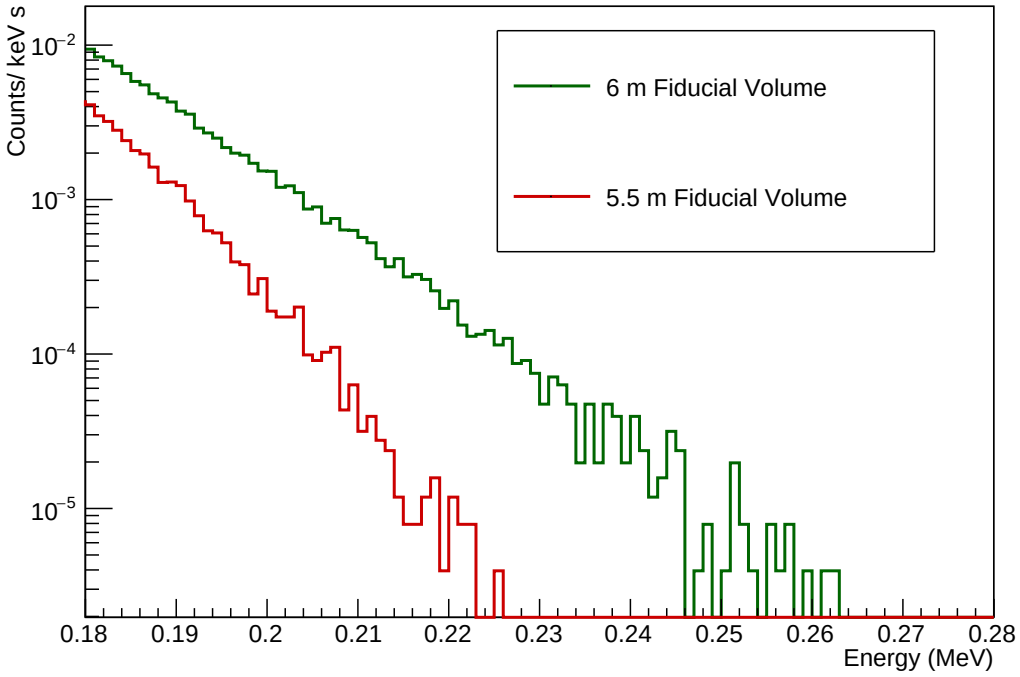

Figure 9.13: The endpoints of the reconstructed spectra of the ^{14}C background for two fiducial volumes. At larger radii the events reconstruct with higher energies.

The reconstructed energy spectrum of the bulk backgrounds occurring within a 5 m fiducial volume can be seen in Figure 9.14. The reconstructed spectra of the inner AV surface events are shown in Figure 9.15.

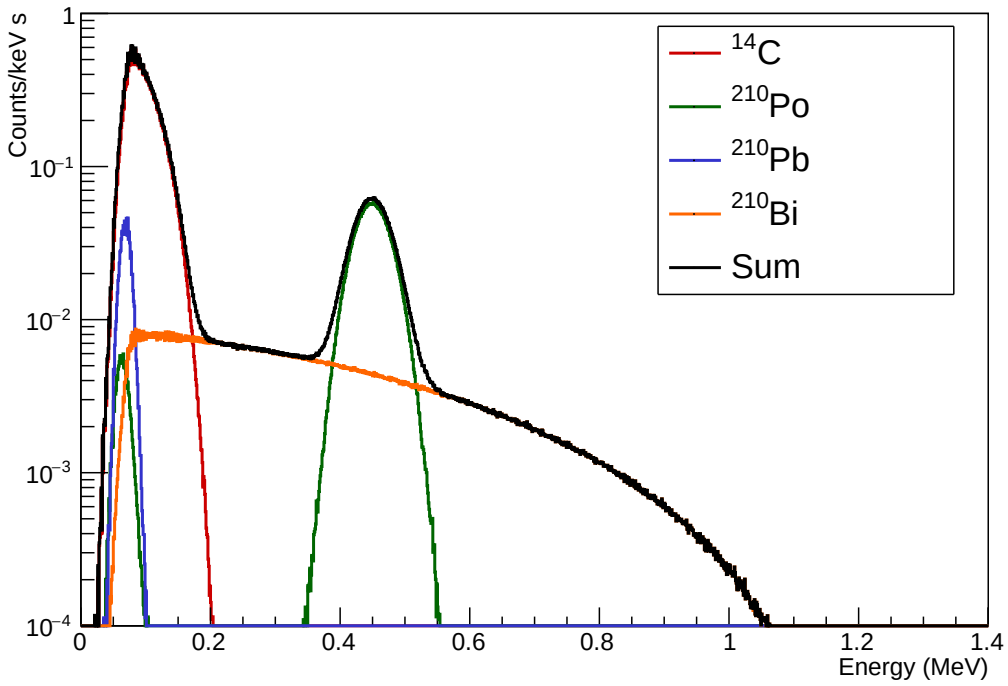

Figure 9.14: The reconstructed energies of the bulk backgrounds with high enough rate to be relevant to a supernova burst, which reconstruct within a 5 m fiducial volume.

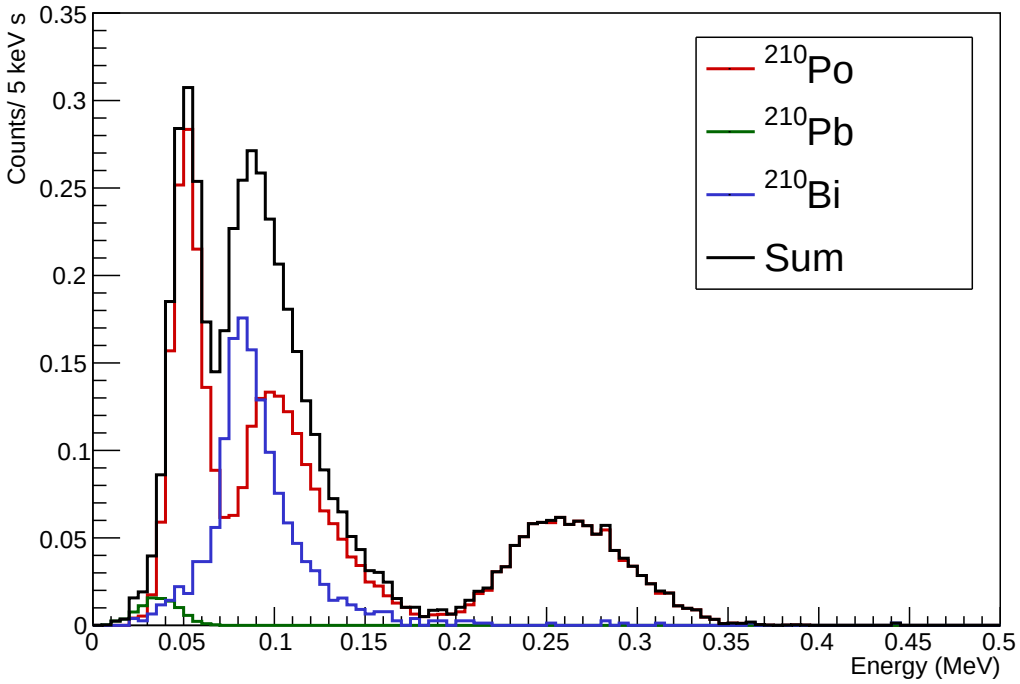

Figure 9.15: The reconstructed energies of the inner AV surface backgrounds which have a high enough rate to be relevent for a supernova burst, which reconstruct within a 5 m fiducial volume.

9.4.6 Results: Sensitivity to the Mass Hierarchy for various Neutrino Detectors

The histograms produced by SNUGEN are used to set a limit on the mass hierarchy. Figures 9.16 and 9.17 show the histograms for the number of IBD and untagged events as a function of time in for both mass hierarchies for a supernova at 1 kpc.

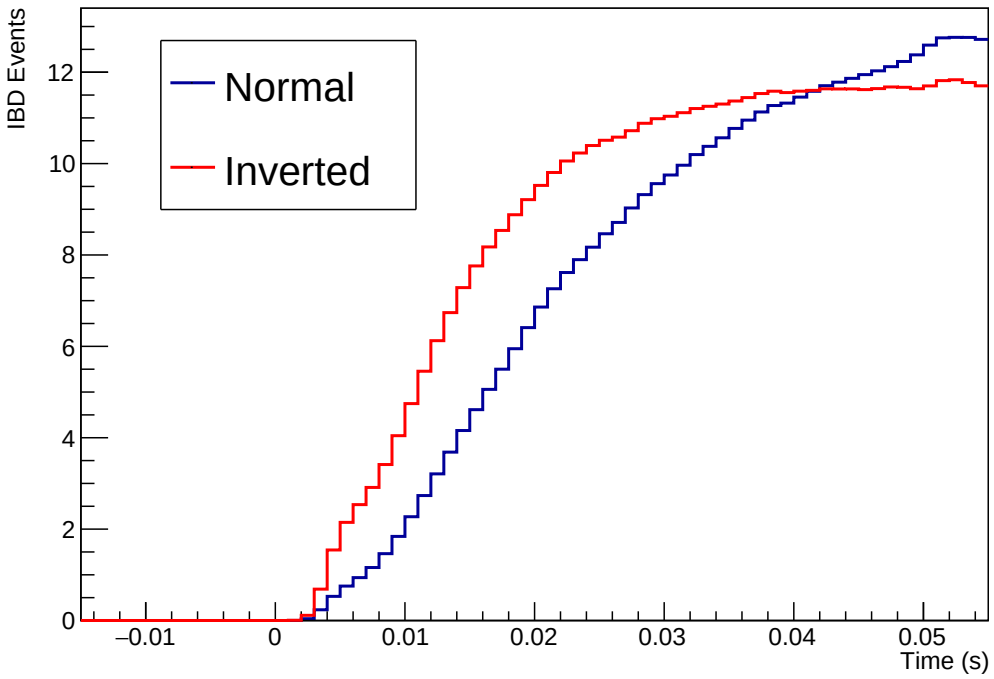

Figure 9.16: The number of IBD events inside the scintillator volume for a $11.2 M_{\odot}$ progenitor at 1 kpc for each mass hierarchy, perfect IBD tagging efficiency is assumed.

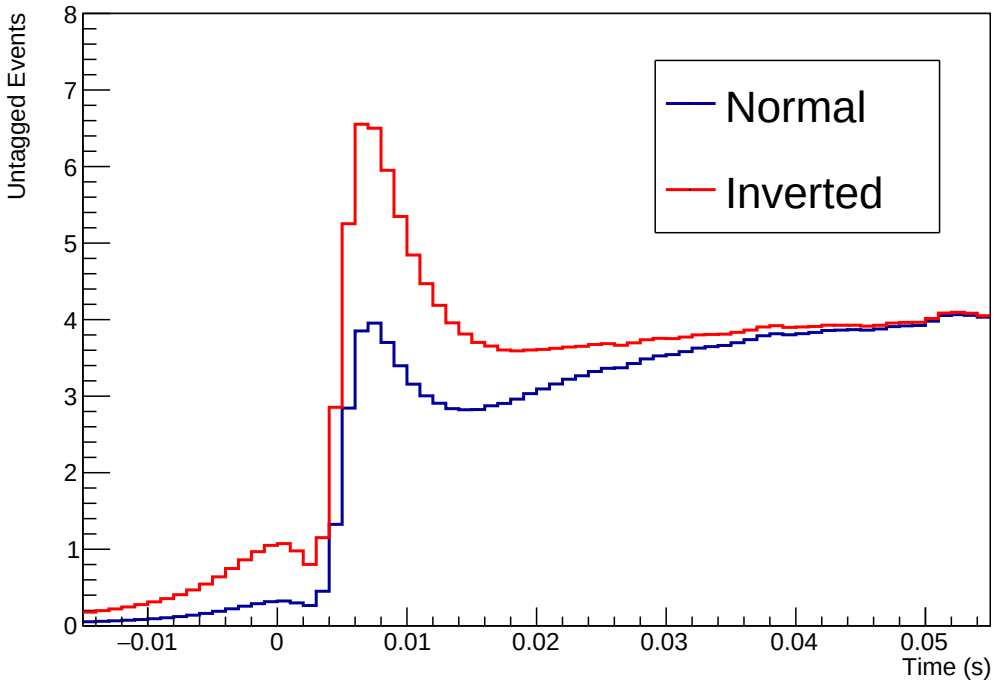

Figure 9.17: The number of untagged events inside the scintillator volume for a $11.2M_{\odot}$ progenitor at 1 kpc for each mass hierarchy a detector threshold of 0.2 MeV is assumed.

Adding Backgrounds

The background count is obtained by first calculating the expected number of events in a single time bin, the time resolution of the Garching input simulations results in 18 bins over the 0.02 s window. The average background count per bin is therefore given by the total background count for a given fiducial volume from Table 9.3 scaled by 1/18. A Poisson distribution with mean equal to the average background count is sampled to obtain a background count.

SNO+

Figure 9.18 shows the sensitivity to the neutrino mass hierarchy for the SNO+ detector as a function of supernova distance for various IBD tagging efficiencies. A 5 m fiducial volume is assumed as well as a 0.2 MeV threshold, no backgrounds are included. Supernovae were simulated between 0.5 and 3.0 kpc with a total of 10,000 simulations at each distance step. No rebinning of the dataset took place and the number of bins was fixed at 9.

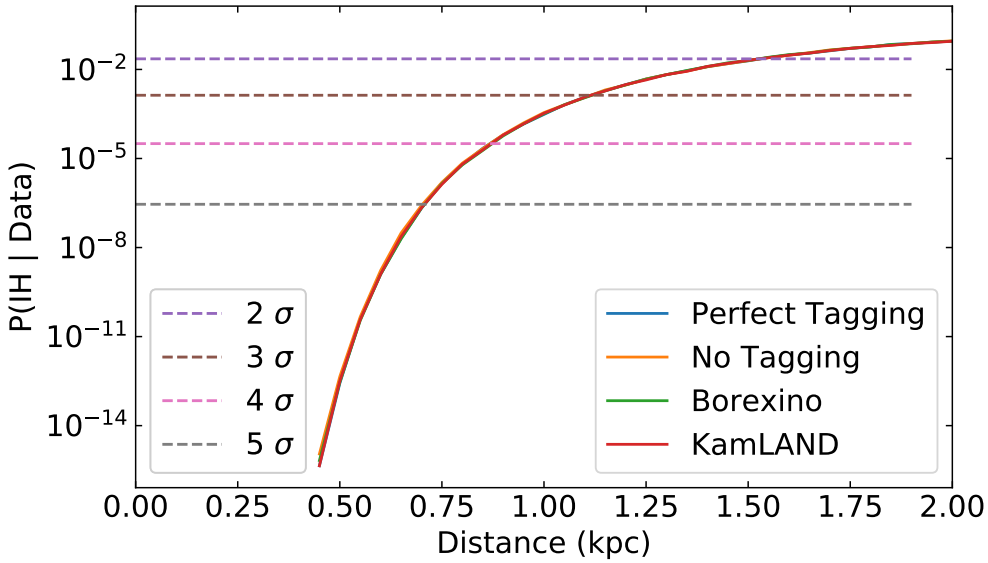

Figure 9.18: The sensitivity of SNO+ to the neutrino mass hierarchy as a function of supernova distance using the SNUGEN output. The IBD tagging efficiency has been varied. A fiducial volume of 5 m is assumed and no backgrounds are included. All results are very similar.

Figure 9.18 shows the sensitivity increases very slightly with an improvement in tagging efficiency. Four tagging efficiencies were simulated: no tagging, perfect tagging, KamLAND tagging (94 ± 0.6 %) and Borexino tagging (84 ± 1.0 %). Perfect IBD tagging shows the best limit. The limit set by KamLAND tagging efficiency is slightly better than when Borexino efficiency is used. Overall the change in sensitivity is minimal.

Figure 9.19 shows the sensitivity to the neutrino mass hierarchy for different fiducial volumes of the SNO+ detector. The backgrounds indicated within Table 9.3 are used, and two tagging efficiencies were used, the KamLAND efficiency and no tagging efficiency. A fixed number of bins (9) is used and a threshold of 0.2 MeV is assumed.

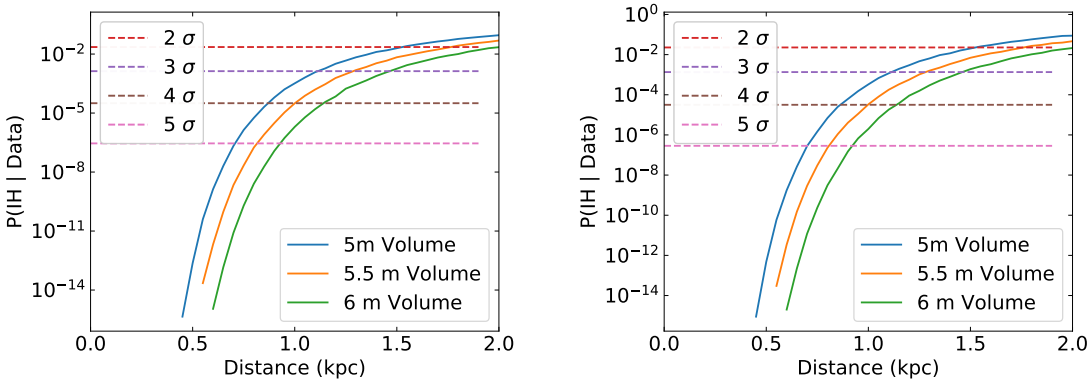

(a) KamLAND tagging efficiency

(b) No IBD Tagging

Figure 9.19: The sensitivity of the SNO+ experiment for varying fiducial volumes (taking into account backgrounds), for two IBD tagging efficiencies.

Figure 9.19 shows that in both cases the sensitivity is increased by increasing the fiducial volume, despite the higher background levels. This is likely caused by the fact that the time window of interest is small compared to the background rate. It should be noted that the KamLAND improvement is optimistic as the tagging efficiency is expected to decrease closer towards the AV.

After the generation of the fake dataset from the scaled histograms and the addition of the backgrounds a rebinning procedure can optionally applied to the data. The algorithm follows three stages:

1. Iterate through through the bins look for bins with less than five entries.

2. When a bin with less than five entries is found merge it with the adjacent bin with the fewest entries.

3. Repeat steps 1 and 2 until no bins have less than five entries or there is only one bin remaining.

Figure 9.20 shows a fake data set before and after the rebinning procedure, both the expected histograms (i.e. the histograms shown in Figures 9.16 and 9.17 after scaling) are binned in the same way to allow a comparison using Eq. 9.15.

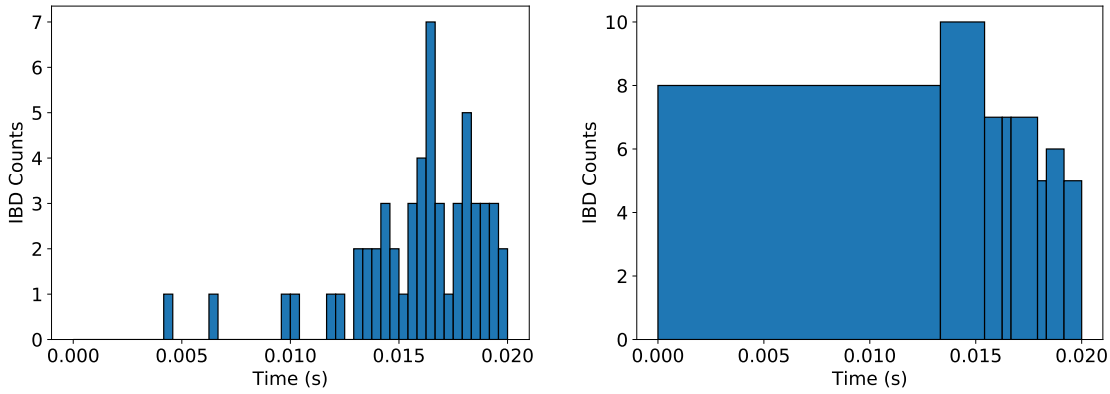

(a) Before Rebinning

(b) After Rebinning

Figure 9.20: Fake dataset generated for IBD events (within a 5 m fiducial volume) from the $11.2M_{\odot}$ model at 1 kpc, before and after rebinning.

The previous simulations all used fixed bin numbers. Figure 9.21 shows a comparison of the sensitivity achieved when using a fixed number of bins and applying the re-binning algorithm. A 5 m fiducial volume is assumed, with a 0.2 MeV threshold and KamLAND IBD tagging efficiencies. No improvement was seen when using the re-binning algorithm.

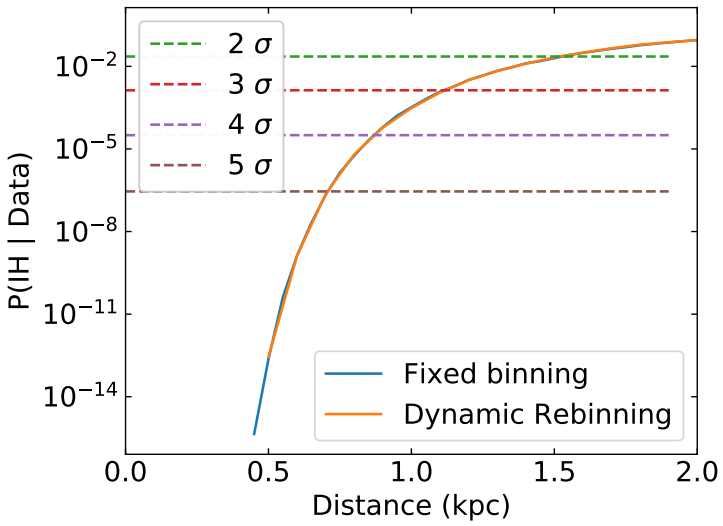

Figure 9.21: The sensitivity achieved when applying the re-binning algorithm to the data for SNO+.

The normalised visible energy spectra of the three interaction channels considered in the analysis is shown in Figure 9.22. The scattered protons experience quenching (as described in Section 5.2.2) and their visible energies are very low, almost all proton scatters fall below 1 MeV. Unlike the protons scattered, electrons are not quenched and have visible

energies up to 20 MeV. In the IBD interaction, the positron obtains the majority of the kinetic energy of the neutrino and can have energies of 30 MeV or higher.

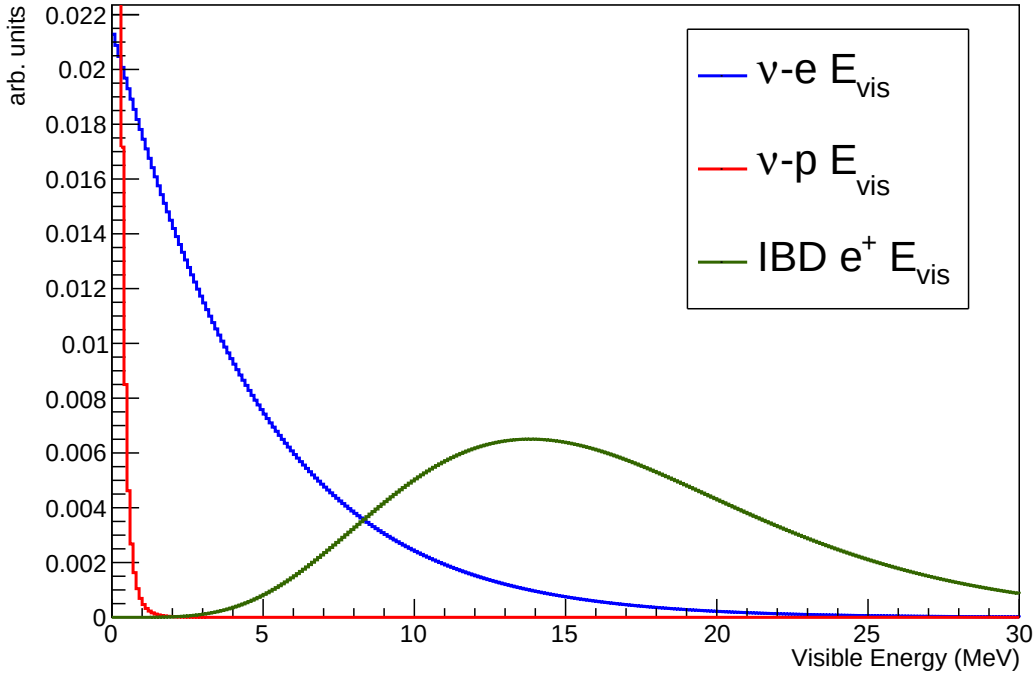

Figure 9.22: The visible energy distributions of the three interaction channels considered from a SN burst. The distributions were obtained using the $11.2 M_{\odot}$ model in the time region 0 to 0.02 s.

The effect of varying the energy cut on the limit of SNO+ is shown in Figure 9.23. The IBD tagging efficiency is assumed to be at KamLAND level, and a 5 m fiducial volume cut was made. Four thresholds are considered: 0.2 MeV is the standard threshold used for the other scintillator experiments and is included for reference, this threshold represents the lowest reasonable energy threshold of the SNO+ detector during nominal scintillator running. A threshold of 0.6 MeV corresponds to the point at which the ^{210}Po background is removed, 1 MeV is the energy threshold at which the large majority of all detector backgrounds are removed and 2 MeV is the energy cut which removes essentially all of the $\nu - p$ scatters.

Figure 9.23 shows initially as the energy cut is raised an improved sensitivity is observed, this is due to two effects: the reduction of intrinsic detector backgrounds and the removal of a portion of the low energy flavour insensitive $\nu - p$ scatters. An energy cut of 0.6 MeV and 1 MeV result in approximately the same sensitivity. The energy cut does not just remove $\nu - p$ scatters, some of the flavour-sensitive $\nu - e$ scatterings will also be removed, the 2 MeV cut removes a larger portion of these events, reducing the sensitivity.

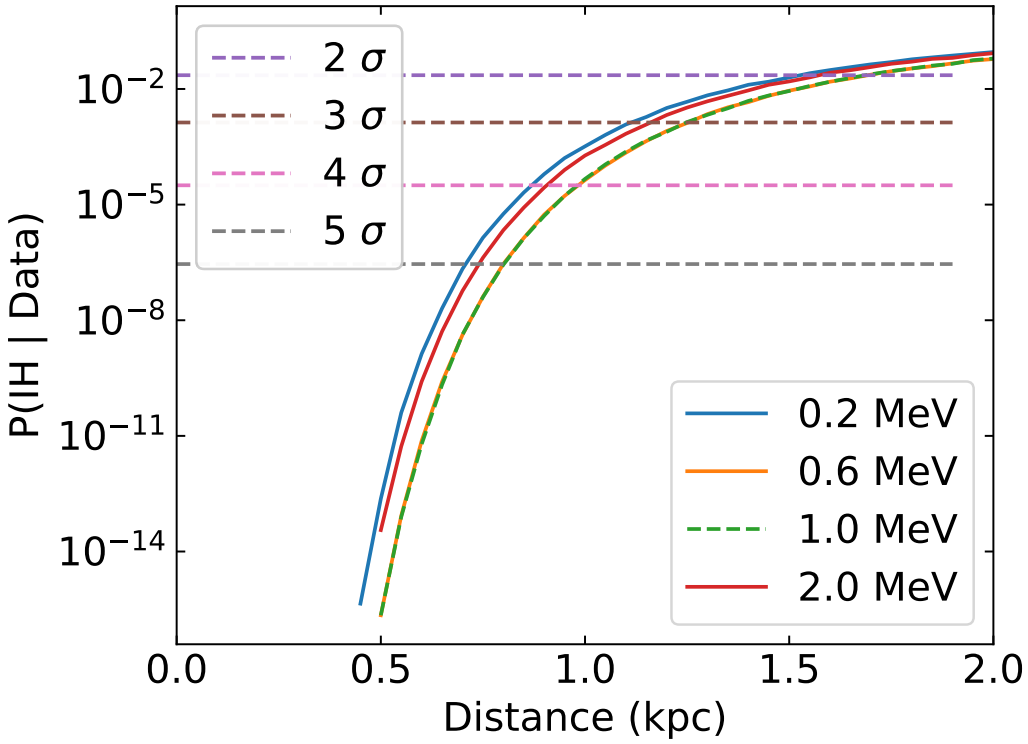

Figure 9.23: The limit on the mass hierarchy based on the SNO+ detector using varying energy thresholds.

It should be noted that a higher threshold producing a better limit just not justify the use of a higher detector threshold. The neutrino proton scattering channel is important to determine the total energy emitted by the supernova as well as the energies of the individual neutrino flavours [49] [48]. Furthermore, the neutrino proton scattering is crucial to determine the time profile of the burst as described in the next section. The variation of the threshold should be thought of as an analysis cut made on the data after the collection.

JUNO

JUNO is a 20 ktonne liquid scintillator detector similar in design to SNO+. The vessel used by JUNO has a radius of 17.25 m, a radial cut of 16.25 m is made to remove AV surface backgrounds. This results in an effective fiducial volume of 16.8 ktonne. The backgrounds for JUNO are assumed to be the same for SNO+ but scaled up to reflect the size disparity between SNO+ and JUNO. The backgrounds are scaled from those in the rightmost column of Table 9.3. The bulk backgrounds are scaled up by the ratio of their volumes within the detector. The inner surface AV backgrounds are scaled by a factor equal to the ratio between the surface areas of the inner surfaces of the vessels,

which are approximated as spherical. An energy threshold of 0.2 MeV is assumed [205] [3], except where noted. Another background for the JUNO experiment is cosmic muons that occur at a predicted rate of 3 Hz [205], resulting in a high level of cosmogenic backgrounds. It is hoped that these backgrounds can be significantly reduced [205]. Reactor and geo anti-neutrino events form a negligible background to a supernova with rates of 10^{-3} Hz and 2×10^{-5} Hz respectively.

Background	Scaling Factor	Background Rate (Hz)
Bulk Backgrounds	37.1	4.90
Surface Backgrounds	34.8	0.708

Table 9.4: Scaling of the SNO+ backgrounds to reflect the JUNO experiment.

The sensitivity of JUNO, assuming the backgrounds described above, is shown using Borexino and KamLAND tagging efficiencies in Figure 9.24. Also shown is the limit assuming KamLAND tagging efficiency and a 1.0 MeV energy cut on the events. The JUNO detector has a much larger range than SNO+ due to its increased size. It is sensitive to the MH at a two sigma level at distances up to approximately 7 kpc.

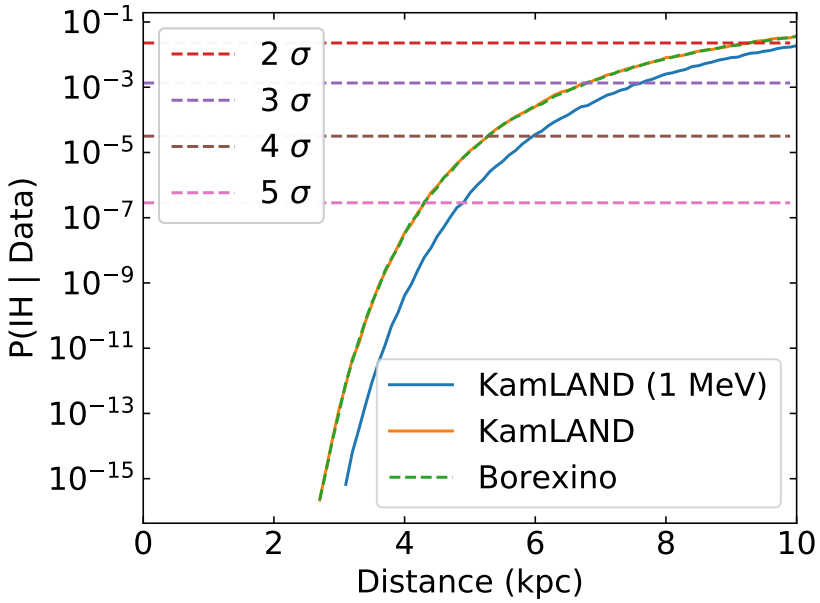

Figure 9.24: The sensitivity of JUNO to the neutrino mass hierarchy using the detected neutrinos from a supernova burst for two IBD tagging efficiencies.

[3] This is a very low threshold for a detector of JUNOs size. The minimum required for the JUNO reactor studies is 0.7 MeV

Super-K and Super-K+Gd

Super-K and Super-K+Gd, use the same 50 ktonne water Cherenkov detector based in Kamioka Mine in Japan. The original Super-K experiment is a pure water Cherenkov detector. The Super-K collaboration now plans to load the detector with 0.2% Gd by mass by disolving $Gd_2(SO_4)_3$ into the water. Gadolinium has a very large neutron capture section, after the capture it de-excites via a 8 MeV γ cascade [206]. Approximately 90% of the neutrons capture on a Gd nuclei, and the remaining 10% capture on a free proton emitting a 2.2 MeV γ [147]. The increased neutron capture signal can be used to tag $\bar{\nu}_e$ via the IBD interaction, the delayed signal is seen approximately 30 µs after the prompt signal [206]. The predicted IBD tagging efficiency of Super-K+Gd is 82.64% [206]. The increased tagging efficiency will aid in the search for the DSNB, as described in Section 4.10.

For the limit plots we use a energy threshold of 7 MeV and a fiducial volume of 22.5 ktonne is used. The background rate meeting these criteria is 0.0121 Hz [118]. Therefore, over the 0.02 second window of interest the expected background count is 2.42×10^{-4}, and is negligible. The tagged IBD events are assumed to be background free.

Unlike the scintillator detectors, the mistagged IBD events are assumed to appear as a single event rather than two observed in the scintillator detectors described above. The log-likelihood function for a given model M (shown in Eq. 9.20), is simply the sum of the Poisson log-likelihoods for the number of IBD and untagged events. x^{IBD} and x^{Un} are the number of observed IBD and untagged events respectively. $\mu^{\mathrm{M}}_{\mathrm{IBD}}$ and $\mu^{\mathrm{M}}_{\mathrm{Un}}$ are the expected number of IBD and untagged events respectively and are given in Eqs. 9.21 and 9.22, τ is the IBD tagging efficiency.

$$\ln \mathcal{L}_{\mathrm{SK,M}} = \ln \mathcal{L}_{\mathrm{Pois}}(x^{\mathrm{IBD}}, \mu^{\mathrm{M}}_{\mathrm{IBD}}) + \ln \mathcal{L}_{\mathrm{Pois}}(x^{\mathrm{Un}}, \mu^{\mathrm{M_{Un}}}) \tag{9.20}$$

$$\mu^{\mathrm{M}}_{\mathrm{IBD}} = \tau \cdot N^{\mathrm{M}}_{\mathrm{IBD}} \tag{9.21}$$

$$\mu^{\mathrm{M}}_{\mathrm{Un}} = N^{\mathrm{M}}_{\mathrm{Un}} + (1-\tau) \cdot N^{\mathrm{M}}_{\mathrm{IBD}} \tag{9.22}$$

24 time bins were used within the window for the analysis. Figure 9.25 shows the limit of Super-K and Super-K loaded with Gd. No improvement on the limit is seen with a Gd loaded detector. This is due to the fact that there is no flavour independent $\nu - p$ scattering. Furthermore the background for both $\nu - e$ and IBD interactions is negligible due to the high energy threshold and fiducial volume cut made within the detector. Untagged IBD

events were assumed to be caused by the neutron capturing on a proton releasing a 2.2 MeV γ ray rather than capturing on a Gd nuclei, and therefore unlike scintillator detectors two untagged events are not observed.

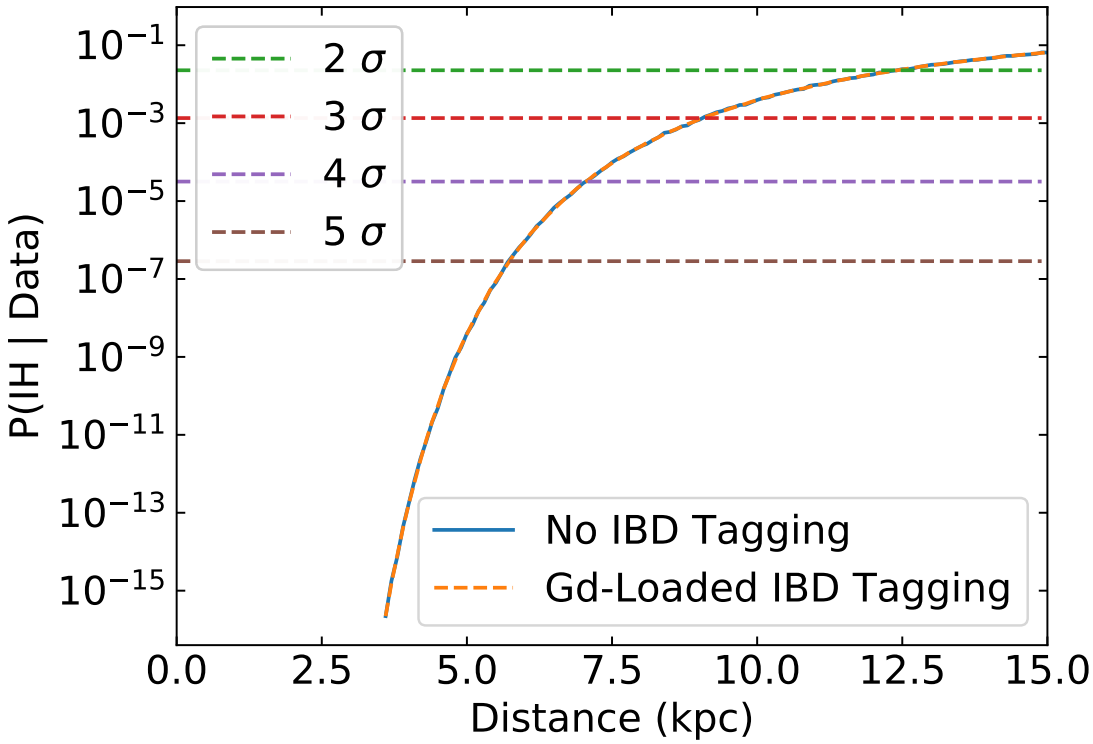

Figure 9.25: The limits on the neutrino mass hierarchy using neutrinos from a supernova burst for Super-K and Super-K+Gd.

Summary of Varying Detector Performances and a Global Limit

The predicted distribution of supernovae within the Milky Way is shown in Figure 4.14. The lower panel shows the cumulative probability, i.e. the probability that the next galactic supernova occurs within this distance. The limits obtained from the simulations described were convolved with this cumulative distribution to determine the probability of determining the neutrino mass hierarchy to a certain confidence level for a given detector given a galactic supernova occurs. The results are shown in Table 9.5

The results for the scintillator detectors assume a 1 MeV threshold, with 0.45 ktonne fiducial volume for SNO+ and a 16.80 ktonne fiducial volume for JUNO. KamLAND IBD tagging efficiencies were assumed. The limit for Super-K uses the non Gd loaded detector.

The global result is obtained by combining JUNO and Super-K limits, the log-likelihood for a given MH is given by Eq. 9.23, this is then put into Bayes' Equation (Eq. 9.8) to

obtain the posterior probability. At the point at which 5σ is crossed by Super-K (approximately 5 kpc) the posterior probability of SNO+ was calculated as 0.602, SNO+ is omitted from the global sensitivity as it will not add any sensitivity.

$$\ln P(\text{Data}_{\text{ Global}}|\text{MH}) = \ln P(\text{Data}_{\text{ Super-K}}|\text{MH}) + \ln P(\text{Data}_{\text{ JUNO}}|\text{MH}) \tag{9.23}$$

The global limit as a function of supernova distance is shown in Figure 9.26.

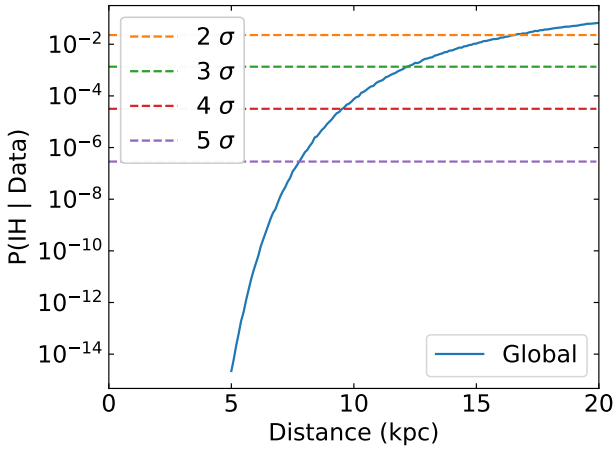

Figure 9.26: The sensitivity to the neutrino mass hierarchy using neutrinos from a supernova if the results of JUNO and Super-K are combined.

Experiment Name	2σ	3σ	4σ	5σ
SNO+	0.0096	0.0049	0.0040	0.0034
Super-K	0.75	0.44	0.23	0.14
JUNO	0.98	0.28	0.15	0.092
Global	0.93	0.74	0.49	0.29

Table 9.5: Table of the overall probability of determining the MH given a supernova occurs within the Milky Way for various experiments.

Determining the neutrino mass hierarchy using the MSW effect at early post bounce times is severely statistically limited. Larger fiducial mass detectors have much higher statistics than smaller detectors and are therefore able to set more stringent limits for supernova further away.

Scintillator detectors do not have an advantage over water Cherenkov detectors using this method. The $\nu - p$ scatterings observable in these detectors, form a background to the flavour dependent $\nu - e$ scatterings and a cut on low energy events improves the sensitivity of these detectors.

The best sensitivity achieved was with Super-K. If a Galactic supernova happens, it is expected to be able to determine the neutrino mass hierarchy using this method to the 5σ level with probability 0.14. A global fit combining the JUNO and Super-K detectors results in the probability of obtaining 5σ sensitivity of 0.29.

9.4.7 Adjusting the Prior

Our current knowledge of the neutrino mass hierarchy is better than simply guessing i.e. $\pi(IH) = \pi(NH) = 0.5$. The current global analysis of the neutrino mass hierarchy excludes the inverted hierarchy at $\Delta\chi^2 = 11.7$ [14] or 2.76σ[4] using Eq 9.19. Using Eq. 9.9 the prior ratio is calculated as 0.00288.

When assuming unequal priors Bayes' Equation shown in Eq. 9.7 becomes Eq. 9.24.

$$P(\text{NH}|\text{Data}) = \frac{1}{1 + \frac{\pi(\text{IH})}{\pi(\text{NH})}\frac{P(\text{Data}|\text{IH})}{P(\text{Data}|\text{NH})}} \tag{9.24}$$

Figure 9.27 shows the limits set by the three detectors and a global limit assuming the new adjusted prior.

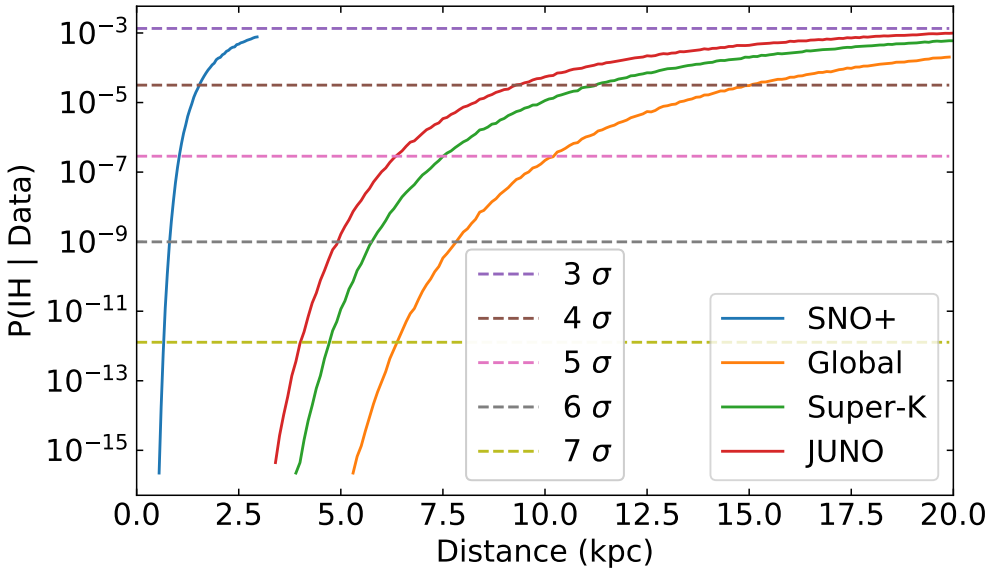

Figure 9.27: The sensitivity to the neutrino mass hierarchy as a function of SN distance. The plot assumes the current global level of sensitivity to the MH from accelerator experiments, which slightly favours the normal hierarchy. Also shown is the global sensitivity calculated by combining the Super-K and JUNO detectors using Eq. 9.23.

The limits within Figure 9.27 were convolved with the predicted Galactic supernova

[4]The literature uses Wilks theorem to calculate the number of sigma and quotes 3.4σ

distribution to determine the overall probability of obtaining $n\sigma$ sensitivity and are shown in Table 9.6. When adding the priors, the probability of global sensitivity to the MH to a 5σ level almost doubles to 0.56.

Experiment Name	4σ	5σ	6σ	7σ
SNO+	0.0079	0.0042	0.0034	0.0021
Super-K	0.66	0.27	0.14	0.083
JUNO	0.47	0.17	0.093	0.057
Global	0.90	0.56	0.30	0.18

Table 9.6: Table of the overall probability of determining the MH given a supernova occurs within the Milky Way for various experiments, assuming the current sensitivity as a prior.

9.4.8 Comparison with full SNO+ detector simulation

The following section presents the first sensitivity study using the HEPEVTGEN software. The histograms produced by SNUGEN and used in the studies described in the previous sections were sampled using the HEPEVTGEN code to generate a hundred SN interaction datasets for a SN at 1 kpc for each model. In total one thousand HEPEVT files were generated. The HEPEVT files were then used as input to RAT to simulate the detector response to the interactions. A pure scintillator filled detector was used and only events within the inner AV were generated. The output of the GEANT simulation was run through the reconstruction routines. The reconstructed events were used within the analysis.

For each progenitor model, 100 simulations were run in the normal hierarchy. The simulations were performed for a progenitor at 1 kpc, between -0.015 and 0.055 seconds during the burst. Each simulation took up to one week of CPU time. The simulated and processed events were then used to as input to the sensitivity studies. The sampling of the events follows three stages described below. The sampling takes place on physics events, one physics event can correspond to multiple events within the detector.

- A simulation of the model is chosen at random. The number of individual physics events within this model (N_{Ev}) gives the unscaled number of physics events
- N_{Ev} is scaled for the supernova distance to obtain $N_{\mathrm{Ev}}(d)$.
- Physics events from all simulations of the same model are sampled, ensuring the same events are not sampled twice, until $N_{\mathrm{Ev}}(d)$ events have been chosen.

After the events are sampled, an IBD tagging procedure is applied, and the events are binned in time as IBD or untagged events. The core bounce time T_0 is crucial to this

analysis and discussed below. The log-likelihood for each interaction channel is given by Eq. 9.15 for each interaction channel. The time of the IBD event is determined by the interaction time of the prompt signal.

Identifying Inverse Beta Decay interactions

The IBD events are identified by using a tagging method similar to the one described in [24]. A window of events stored within τ_{cut} before the current event are stored. If the current event has energy in the range $1.8 < \text{E} < 2.6$ MeV (the energy region for neutron capture on a proton) or $4.0 < \text{E} < 5.8$ (the energy released due to a capture on a carbon nucleus) then the previous stored events are iterated through to try and find the prompt positron signal. The prompt signal search involves several cuts. A distance cut of 2 m is applied (i.e. the delayed and prompt signal must be within 2 m of each other). The prompt signal must also occur more than 0.5 µs after the delayed signal. An energy cut is also made on the prompt positron energy with the requirement that $E_{\text{p}} > 5$ MeV. The prompt energy cut is much higher than the cut described in [24], due to the higher energy of supernova neutrinos compared to reactor neutrinos and the high rate neutrino proton scattering, which can result in misstagging of events.

Figure 9.28 shows the distribution scattered neutron energies produced in the IBD reaction during a SN burst. Some neutrons will be produced with an energies higher than the 0.2 MeV energy threshold. These neutrons may then subsequently scatter off of protons which will then deposit their energy within the scintillator volume producing fake untagged events. Any events occurring in between the prompt and delayed signal, and within the distance cut are therefore not counted as untagged events. This will create a spherical dead region within the detector 2 m in radius and 600 µs in length, for supernova at closer distances when the rate of events is high enough a greater proportion of events will be lost.

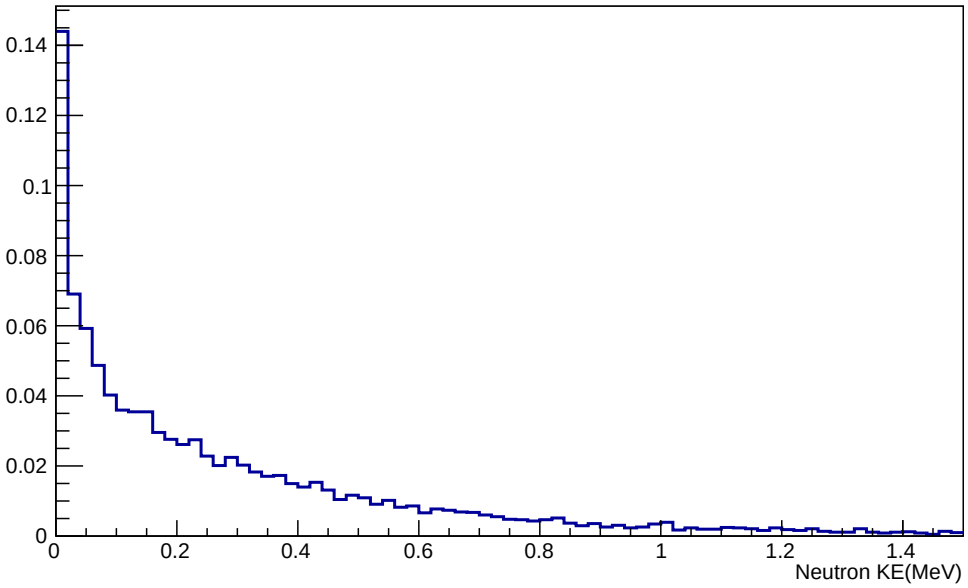

Figure 9.28: Distribution of the neutron kinetic energies produced via the IBD interaction channel for the $11.2M_{\odot}$ model using the normal hierarchy.

The IBD tagging efficiency was calculated for each of the SN simulations using Eq 9.25, N_{IBD} is the number of tagged IBD events within the fiducial volume using the algorithm above, N_{True} is the true number of IBD events within the fiducial volume. Figure 9.29a shows the distribution of the efficiencies for two values of τ_{cut}, 600 µs and 1000 µs.

$$\epsilon = \frac{N_{\text{IBD}}}{N_{\text{True}}} \times 100\% \tag{9.25}$$

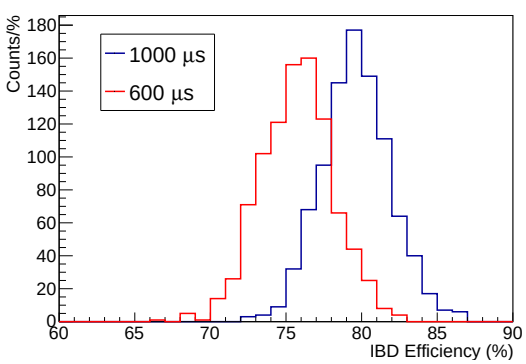

(a) The tagging efficiencies of the IBD interactions during a Supernovae burst for two cut regimes.

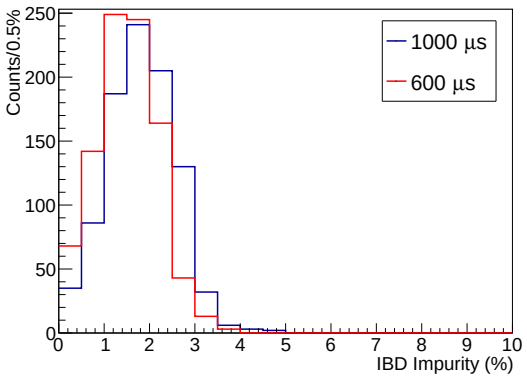

(b) The tagging impurities of the IBD interactions during a Supernovae burst for two cut regimes.

A Gaussian fit was made to the two histograms, the average and spread on the tagging efficiencies are shown in Table 9.7.

τ_{cut}	ϵ	σ_ϵ
600 µs	75.8%	2.28%
1000 µs	79.6%	2.26%

Table 9.7: The tagging efficiencies of the IBD interaction for SN at 1 kpc, determined using MC.

The algorithm described above was used to search for anti-neutrinos from reactors. During a supernova burst, the rate of events will be much higher, and there is a chance random coincidences from supernova neutrinos interactions could be misstagged as genuine IBD events. The same dataset was used to measure the signal impurity arising from these false coincidences. The IBD impurity is defined using Eq. 9.26, where N_{Fake} is the number of tagged IBD events where either the prompt or delayed signal is not from a true IBD event. As the rate of events varies strongly with distance to the progenitor, the impurity of the IBD signal due to random coincidences of other supernova events by will also vary. For supernovae at further distances the signal impurity is expected to be significantly reduced. Figure 9.29b shows the impurities of the IBD signal for the two cut regimes. The mean and RMS of the impurities is shown in Table 9.8

$$I = \frac{N_{\text{Fake}}}{N_{\text{True}}} \times 100\% \tag{9.26}$$

τ_{cut}	$\bar{I}$	RMS(I)
600 µs	1.51%	0.66%
1000 µs	1.83%	0.74%

Table 9.8: The IBD tagging impurities for two different tagging regimes.

Reconstruction Efficiency and systematic effects associated with misreconstruction

A certain proportion of events within the detector will not successfully reconstruct. In the toy MC studies described in the previous section the reconstruction efficiency was assumed to be perfect, in reality however some events will fail to reconstruct. With improved algorithms the reconstruction efficiency should be increased.

The reconstruction efficiency was determined in a similar way to the true IBD efficiency. The efficiency is defined as the number of events reconstructing within a 5 m fiducial volume, divided by the true number of events within within the fiducial volume. Only the

initial scatterings are considered, any subsequent scatterings are likely to be removed with a retrigger cut described within the next section. The distribution of the reconstruction efficiency for untagged events from the simulations is shown in Figure 9.30.

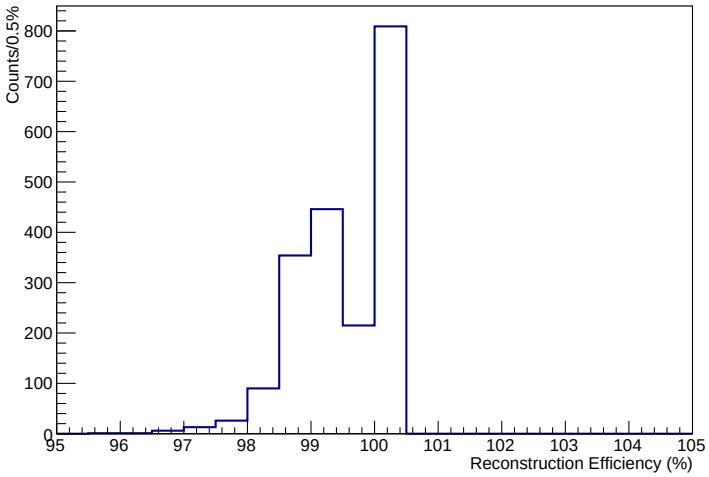

Figure 9.30: The reconstruction efficiency for untagged events within the fiducial volume of SNO+, only the initial scattering event is considered, a 0.2 MeV visible energy cut is made on the events.

The reconstruction efficiency varies strongly with energy. Figure 9.31 shows the reconstruction efficiency as a function of energy. Below 0.2 MeV the reconstruction efficiency begins to sharply drop off. Above 0.2 MeV the average reconstruction efficiency was found to be 99.54%

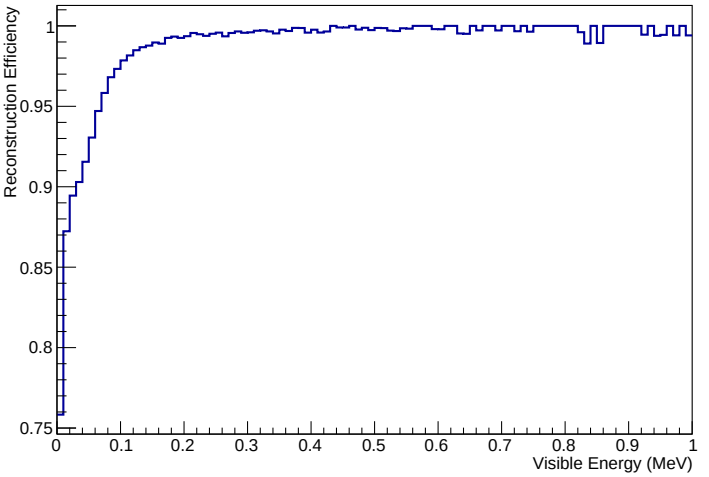

Figure 9.31: The reconstruction efficiency as a function of deposited energy within the detector.

Due to the higher visible energy of the IBD events the reconstruction energy of both the positron and the neutron was found to be essentially 100%.

Some events may also misreconstruct within the fiducial volume from a region external to the fiducial volume and vice versa. Figure 9.32a shows the proportion of untagged events external to the fiducial volume which reconstruct within it for the $11.2M_{\odot}$ model. Figure 9.32b shows the opposite, the proportion of untagged events which occur within the fiducial volume and go on to reconstruct outside it.

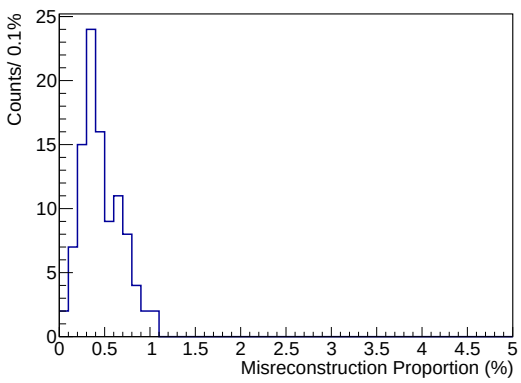

(a) The proportion of untagged events external to the fiducial volume which mistakenly reconstruct within it and have reconstructed energy greater than 0.2 MeV.

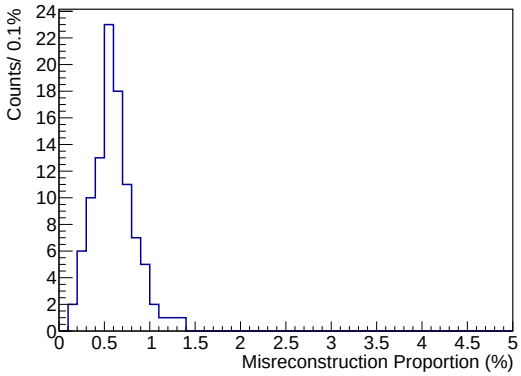

(b) The proportion of untagged events inside the fiducial volume which mistakenly reconstruct outside it, with reconstructed energy greater than 0.2 MeV.

The relative change in the number of untagged events will be given by Eq. 9.27, where $\mathcal{F}$ is the proportion of the detector making up the fiducial volume, p_I is the proportion of external events which propagate into the fiducial volume and p_O is the proportion of events which propagate out of the fiducial volume.

$$\frac{\Delta N}{N_{\text{True}}} = (1-\mathcal{F})p_I - \mathcal{F}p_O \tag{9.27}$$

Assuming the average values of the histograms in Figures 9.32a and 9.32b the relative change in the number of untagged events is -0.16%. The systematic effect of event propagation of untagged is much smaller than the statistical uncertainty.

The proportion of IBD events external to the fiducial volume where either the neutron or the positron reconstructs within the fiducial volume is shown in Figure 9.33a for the $11.2M_{\odot}$ model. The number of events internal to the fiducial volume and propagate outside it is shown in Figure 9.33b. It should be noted that this is not just due to misreconstruction of events, as the delayed neutron capture signal could propagate into the fiducial volume.

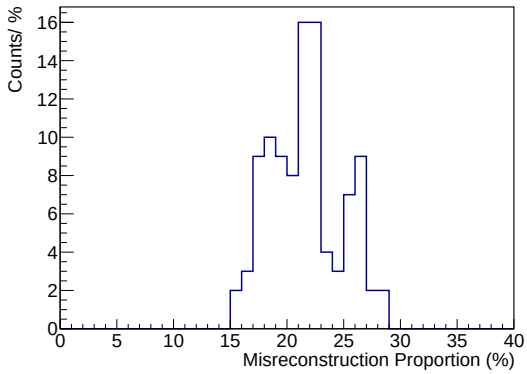

(a) The proportion of IBD events external to the fiducial volume which mistakenly reconstruct within it and have reconstructed energy greater than 0.2 MeV.

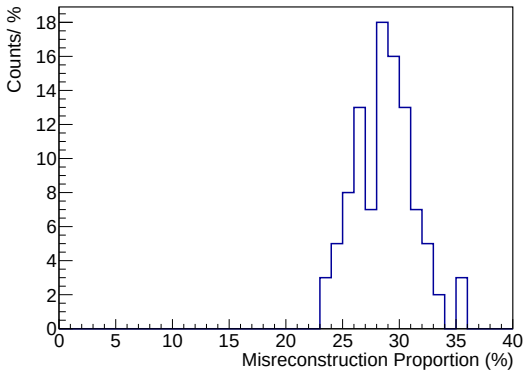

(b) The proportion of IBD events inside the fiducial volume which mistakenly reconstruct outside it, with reconstructed energy greater than 0.2 MeV.

When inserting the average values of the two IBD histograms into Eq. 9.27, the total observed change in the number of observed events is -7.5%.

Table 9.9 summarises the reconstruction efficiencies and the misstagging proportions for the interaction channels.

Value	**Mean (%)**	**RMS** (%)
Reconstruction Efficiency (Untagged)	99.54	0.73
Reconstruction Efficiencies (IBD)	99.99	0.02
Event Propagation(Untagged)	-0.157	-
Event Propagation (IBD)	-7.5	-

Table 9.9: The averages and the RMS' of the reconstruction efficiencies, and the relative change in the number of events as a result of propagation within and outside it.

Removal of Retriggers

Approximately 40% of $\nu - e$ events generate multiple detector events. The majority of these events are retrigger events, the event occurs over multiple detector trigger windows and a second global trigger is issued immediately after the first. The definition of a retrigger event in SNO+ is an event which occurs less than 600 ns after the previous global trigger. As the limit setting procedure involves counting the number of events any physics events that generate multiple detector events can skew the result, any retrigger events are therefore removed. Figure 9.34a shows the distribution of triggered detector events for single $\nu - e$ scattering events before and after the retrigger cut. The removal of retriggers significantly reduces the number of physics events generating multiple triggers. The retrigger cut essentially generates a 1 µs region of dead time for the entire detector, 400 ns corresponding to the width of the original trigger window plus 600 ns due to the

retrigger cut. If the supernova is close enough and therefore the rate of events is high enough events will be lost due to random coincidences.

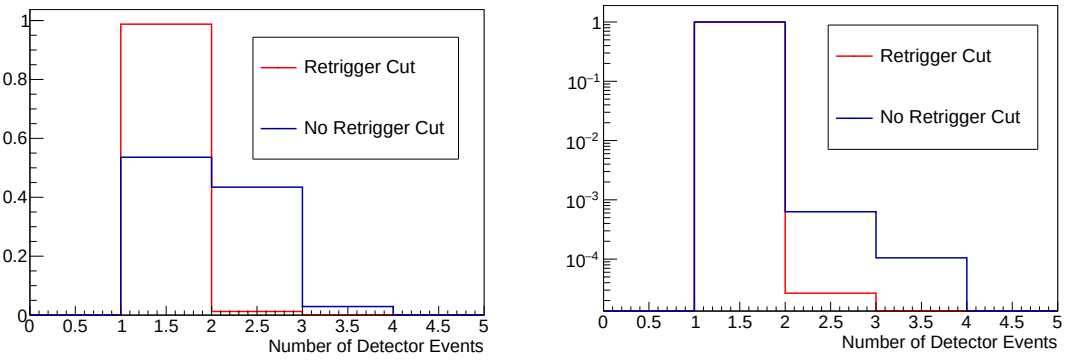

(a) The distribution of detector events caused by $\nu - e$ scattering before and after retriggers have been cut.

(b) The distribution of detector events caused by $\nu - p$ scattering before and after retriggers have been cut.

Figure 9.34b shows the distribution of the number detector events for $\nu - p$ scattering events. Only a small proportion of $\nu - p$ scatters generate retriggers.

Figure 9.35 shows the distribution of the number of detector events for inverse beta-decay events. Several events are observed for a single IBD interaction, after the retrigger cut the majority of IBD events generate two detector events as expected.

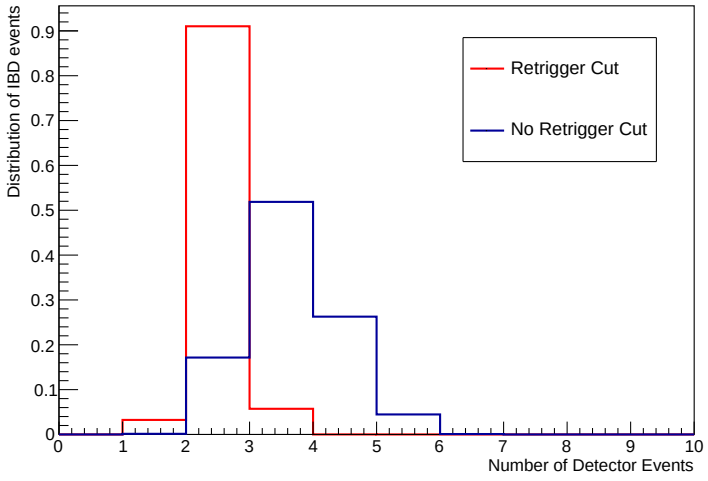

Figure 9.35: The distribution of detector events caused by IBD events before and after retriggers have been cut.

Systematic effects associated with the scintillator response

Figure 9.36 shows the predicted, and true number of untagged events as a function of time, the points from the simulation use the MC truth times of the events. There is a slight

difference between the number of events observed in simulation and the number predicted by SNUGEN.

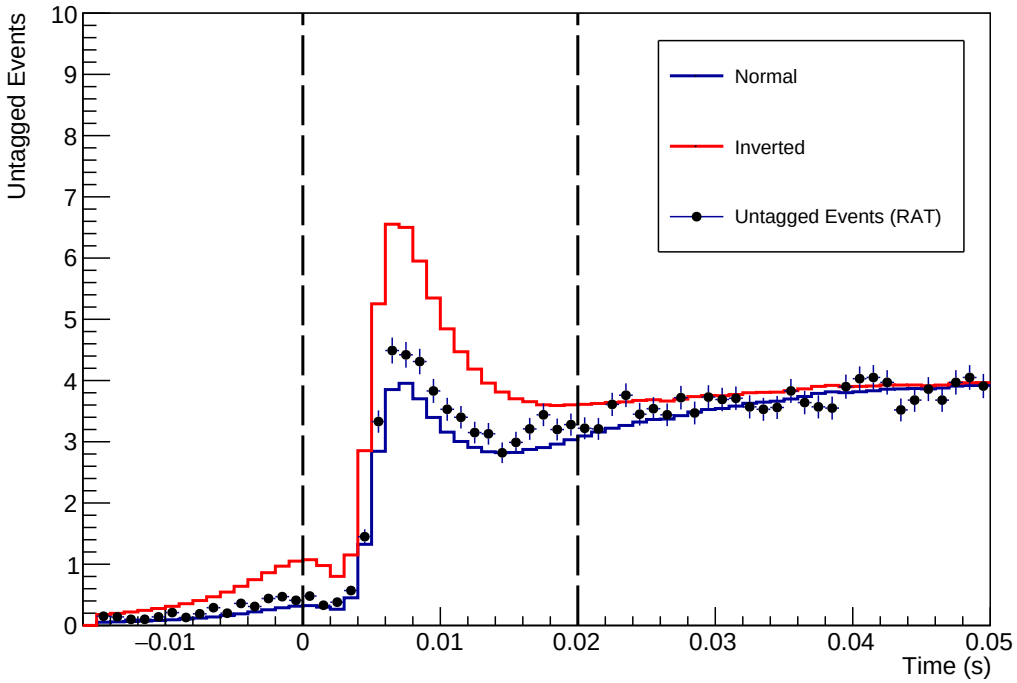

Figure 9.36: The number of untagged events as predicted by SNUGEN and obtained from the full RAT simulations (The simulations are run in the normal hierarchy, the datapoints show the average of the true untagged events in the 1000 simulations). The true MC times of the events are used from the RAT simulations. A 0.2 MeV energy cut is made on the events.

The difference is due to the differences in the scintillator response for protons. SNUGEN models the scintillator response using Birks' law given by Eq. 5.4, the Birks' constant used for the scintillator was 0.0096 cm/MeV. A comparison of the reconstructed energy of as a function of true proton energy is shown between the RAT simulations and the prediction from Birks' law in Figure 9.37. The reconstructed energy is slightly higher than the prediction from Birks' law resulting in the slightly increased number of events in Figure 9.36. The scintillator response has been verified to be correctly modelled in simulation. The difference between the reconstructed energy and the proton true energy is caused by an approximately 10% upwards shift in the reconstructed energy vs true visible energy. Understanding the response of the scintillator and the detector to low energy protons is crucial, especially as it is expected to change significantly when the Tellurium loading begins. A fit of Birks' law was made to the results of the RAT simulations, the

fitted Birks' constant was found to be 0.0082 cm/MeV. The following results use SNUGEN results with the fitted Birks' constant in the comparison with the RAT results.

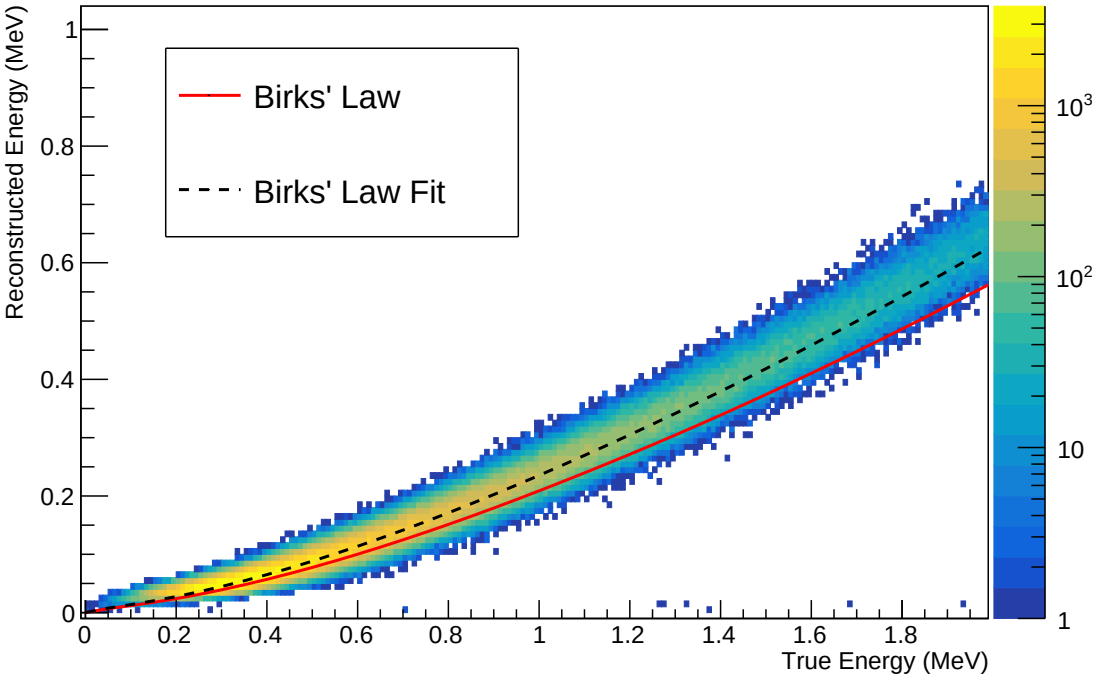

Figure 9.37: The reconstructed energy against the true proton energy from the supernova simulations. The red line is theoretical prediction from Birks' law when the measured value of Birks' constant is used. The dashed black line is the fit of the theoretical function to the simulation data.

The visible number of IBD events observed in the fiducial volume will be given by Eq. 9.28 where τ is the tagging efficiency, $\mathcal{I}$ is the impurity of the IBD signal and $\mathcal{F}$ is the proportion of the detector making up the fiducial volume. N_{IBD} is the true number of IBD events within the detector volume. The reconstruction efficiency of IBD events is not included in the equation and is assumed to be one as per Table 9.9. The observed IBD events from the 100 simulations of the $11.2M_{\odot}$ model and predicted values of IBD events are shown in Figure 9.38.

$$N_{\mathrm{IBD}}^{\mathrm{O}} = \mathcal{F} \cdot (\tau + \mathcal{I}) \cdot N_{\mathrm{IBD}} \tag{9.28}$$

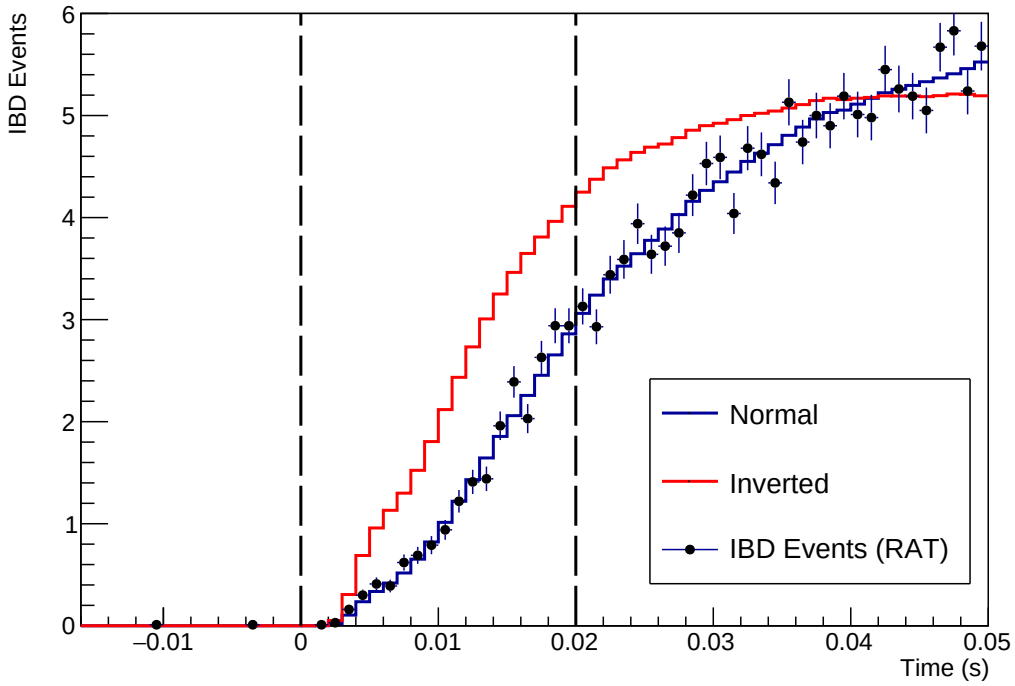

Figure 9.38: The predicted number of IBD events for the $11.2M_{\odot}$ model from SNUGEN and Eq. 9.28 and the average of the RAT simulations using the MC truth times of the events.

The visible number of untagged events observed in the fiducial volume will be given by Eq. 9.29. $\mathcal{R}$ is the reconstruction efficiency for untagged events ΔN is the change in the number of events due to propagation inside and outside the fiducial volume, only the propagation of IBD events is considered as the propagation of untagged events was found to be at the sub-percent level. The observed average number of events from the 100 simulations of the $11.2M_{\odot}$ model and the predicted number from SNUGEN when using Eq. 9.29 are shown in Figure 9.39. At later times a slight excess of untagged events is seen compared to the predicted value. One effect not considered in Eq. 9.29, is the fact that neutrons propagating from outside of the fiducial volume may create multiple events within the fiducial volume, this could be responsible for the slight discrepancy observed.

$$N_{\mathrm{Un}}^{\mathrm{O}} = \mathcal{F} \cdot (\mathcal{R} N_{\mathrm{Un}} + 2(1 - \tau - \mathcal{I}) N_{\mathrm{IBD}}) + \Delta N_{\mathrm{IBD}} \tag{9.29}$$

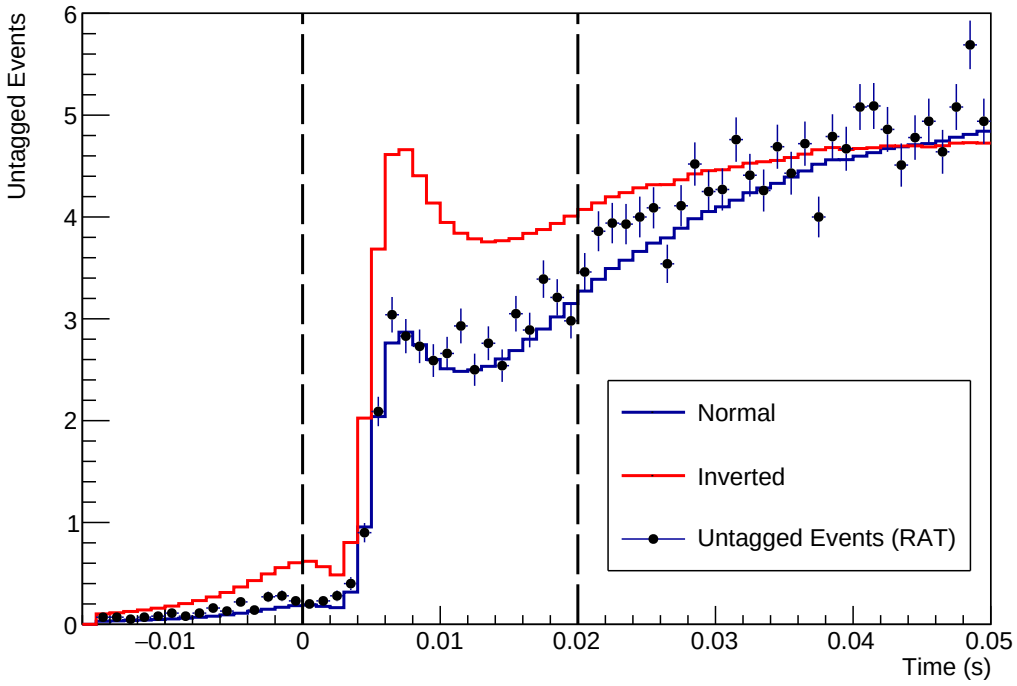

Figure 9.39: The predicted number of untagged events for the $11.2M_{\odot}$ model from SNU-GEN and Eq. 9.29 and the average of the RAT simulations using the MC truth times of the events and the tagging/cut procedures described at the start of this section.

Determining T_0

As the true time profile of the supernova is not known one must use the detected neutrinos to predict the time profile of the burst. A simple algorithm was developed to determine the time profile of the burst. The algorithm first identifies the time of the first IBD event a histogram is then filled with untagged events between 0.015 seconds before this time to 0.005 seconds after this time. This window was chosen as it is likely to contain the neutronisation burst, furthermore the time window is short enough after the first IBD event such that untagged IBD events cannot enhance the number of untagged events enough to mask the neutronisation burst. The most filled bin in the histogram is then used to define the peak of the neutronisation burst. A fixed time is then subtracted from this time, the time is set to 0.007 s and determined from simulation as the time offset from the core bounce to the neutronisation burst as shown in Figure 9.9b.

The algorithm was applied to the simulations of the $11.2M_{\odot}$ model. The distribution of the offsets from the true zero time can be seen in Figure 9.40. On average there is a good agreement with the true value of the burst. There is a large uncertainty on the

burst, however. This could be remedied by obtaining the value of T_0 from other, larger, experiments.

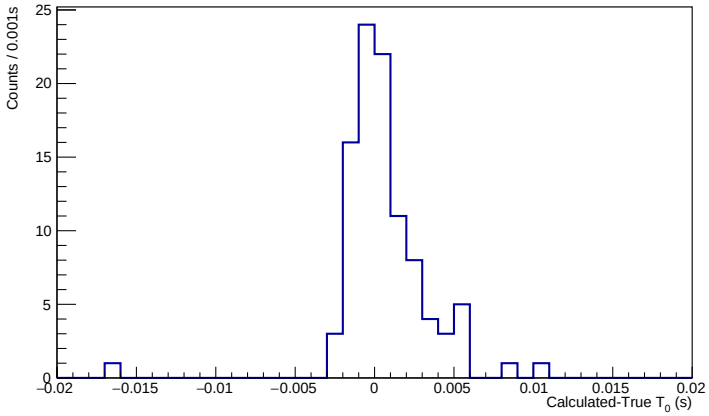

Figure 9.40: The offset of the calculated value of T_0 relative to the true value of T_0 for the 100 simulations of the $11.2M_{\odot}$ model at 1 kpc.

The distribution of untagged events is shown in Figure 9.41, some variation is seen from Figure 9.39 due to the shifting of the times by the algorithm.

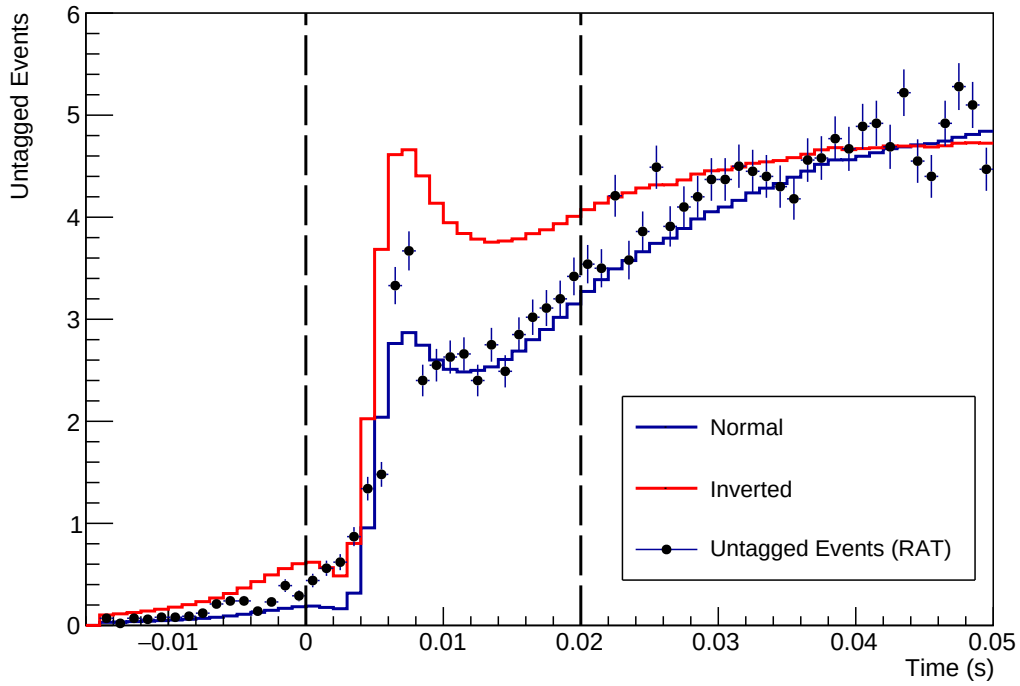

Figure 9.41: The average time profile of the untagged events for the 100 simulations of the $11.2M_{\odot}$ model when the full analysis procedure is performed, including identifying the core bounce time.

The distribution of IBD events is shown in Figure 9.42. There is a slight increase in

the number of IBD events at early times as the algorithm appears to favour a later T_0 than truth in some simulations.

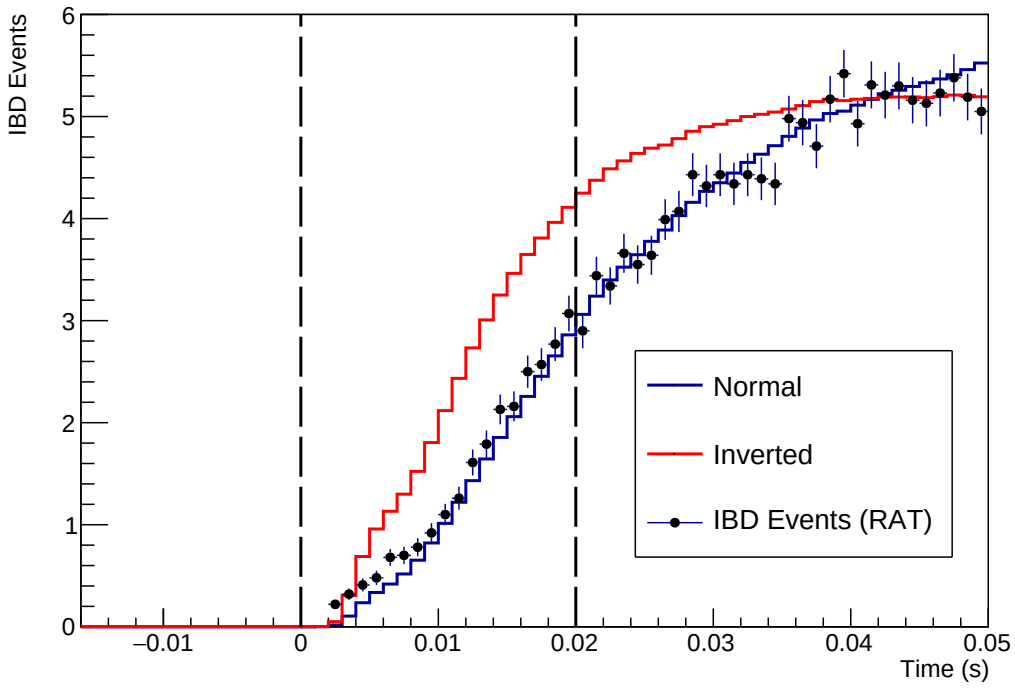

Figure 9.42: The average time profile of the IBD events for the 100 simulations of the $11.2M_{\odot}$ model when the full analysis procedure is performed, including identifying the core bounce time.

Summary of Systematics

In summary the measurement of both the untagged and IBD events as a function of time is effected by several systematics associated with the detector listed below:

- Misconstruction of the energies of low energy events
- The reconstruction efficiency of the detector as a function of energy.
- Multiple detector events caused by a single physics event.
- Events lost due to the retrigger cut.
- Events lost due to the IBD neutron cut.
- The effect of the misreconstruction of events inside the fiducial volume to outside the fiducial volume and vice versa.
- Uncertainties in the determination of T_0.

Results

The limit from the RAT simulations is shown in Figure 9.43; for comparison the sensitivity from the toy study with the same IBD tagging efficiency (75.8%) is also shown.

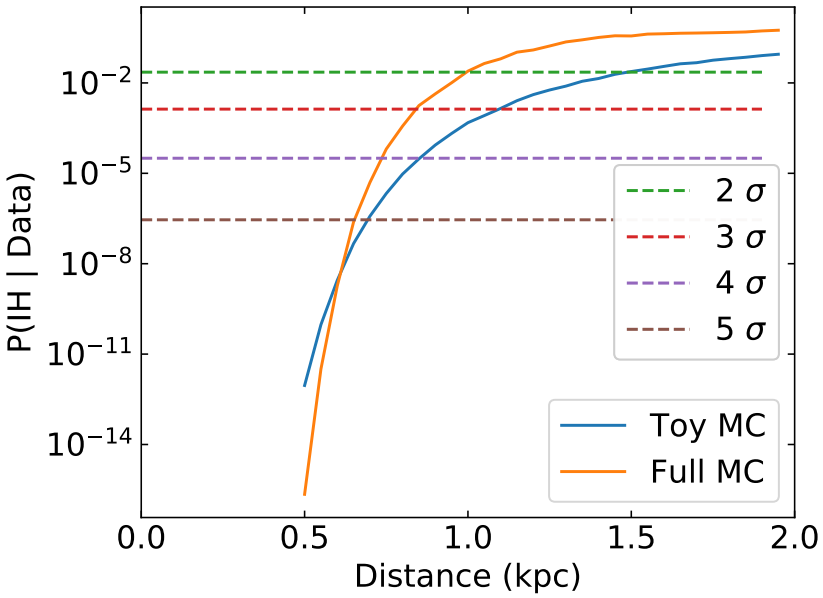

Figure 9.43: The sensitivity of SNO+ to the neutrino mass hierarchy as determined by the toy MC for SNO+. Also shown is the predicted sensitivity from performing a full analysis on the RAT simulations.

The limit obtained from the full simulations is initially much worse than the prediction from the toy study, this is likely due to the large uncertainty in the value of T_0 which is not considered in the toy model. For distances closer than approximately 0.6 kpc an enhanced sensitivity is seen for the full simulations. This increased limit is completely false and caused by the shift of T_0 with distance, the change in the IBD tagging impurity and efficiency with supernova distance and the removal of events by the retrigger cut and IBD neutron scatter removal.

The offset of T_0 as a function of distance is shown in Figure 9.46 for the majority of the distances the average offset was 0. At closer distances however, the estimated value of T_0 shows a systematically underestimated.

Figures 9.44 and 9.45 show the average number of IBD and untagged events respectively from the simulations at 0.5 kpc, also shown is the average of the 10 SNUGEN models. The IBD events agree reasonably well with the prediction, whereas the untagged events show significantly less events than expected.

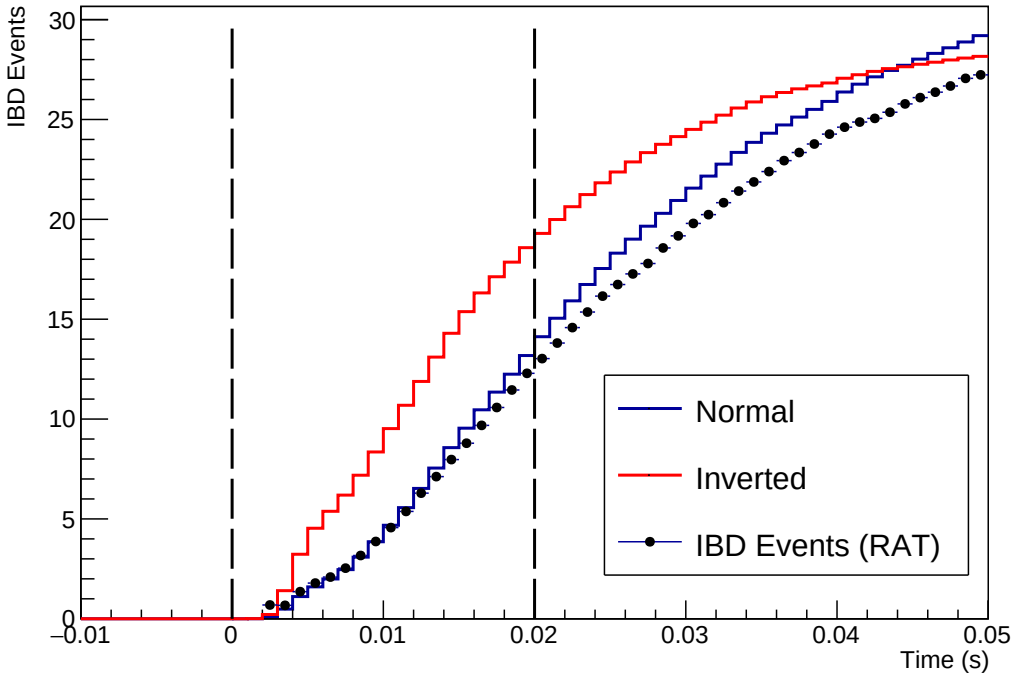

Figure 9.44: The expected average and observed number of IBD events when performing the analysis procedure as a function of time for a supernova at 0.5 kpc.

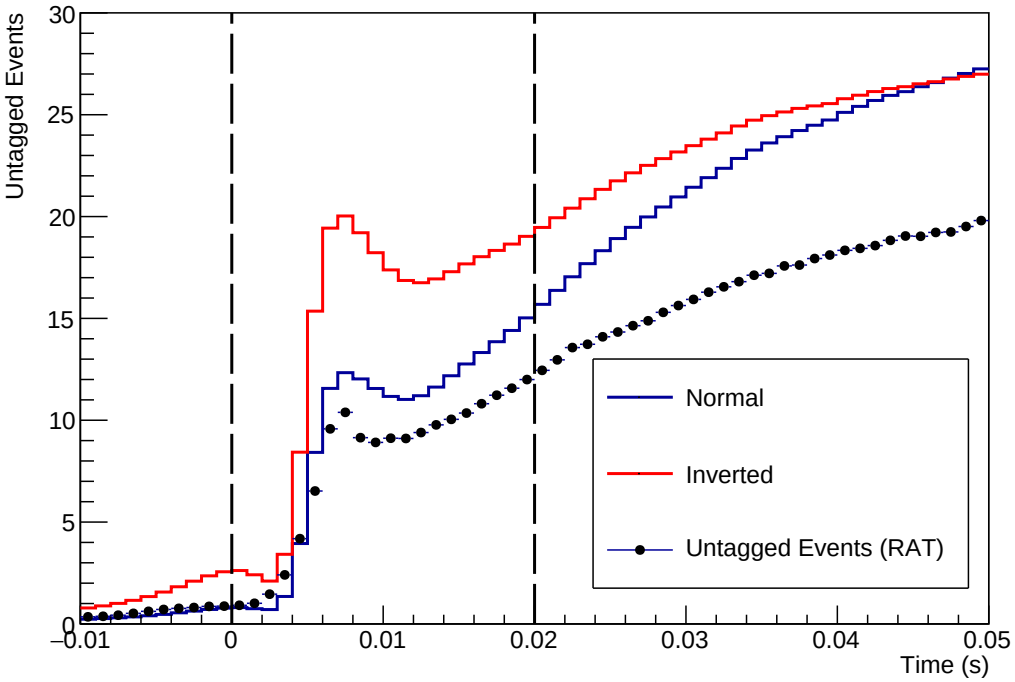

Figure 9.45: The expected average and observed number of untagged events when using the analysis procedure as a function of time for a supernova at 0.5 kpc.

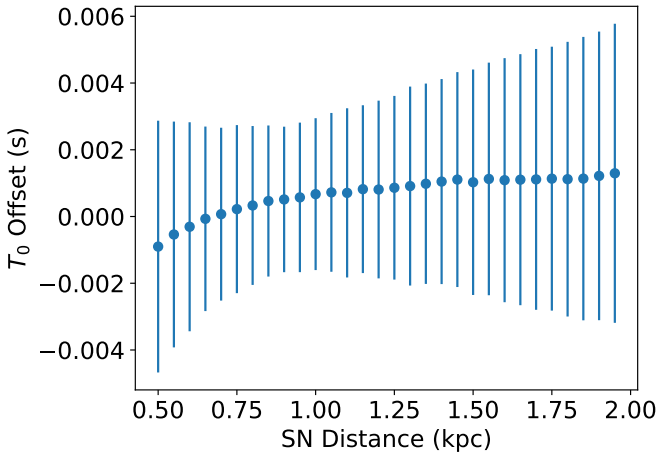

Figure 9.46: The change in the average estimate of T_0, the point of core bounce, with distance relative to the true value of T_0.

An earlier value of T_0 means the rise time of IBD events will appear to occur slightly later. This in turm produces a limit which slightly overfavours the normal hierarchy.

As well as the change in T_0 both the IBD impurity and tagging efficiency change significantly. Figure 9.47 shows the variation in the IBD tagging efficiency as a function of distance, as the distance to the supernova is reduced the tagging efficiency is reduced. The impurity of the IBD signal is shown as a function of distance in Figure 9.48, as the distance to the supernova is reduced the signal impurity of IBD events is significantly increased, this is due to random coincidences between events within the detector.

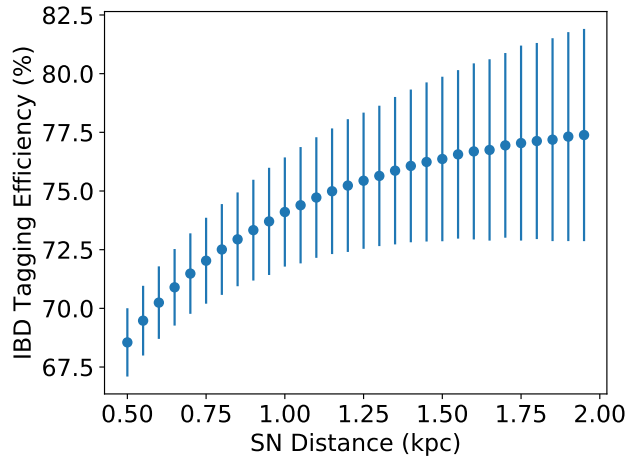

Figure 9.47: The change in the IBD tagging efficiency with distance. At closer distances the tagging efficiency is reduced due to random coincidences between events in the detector mimicking an IBD event.

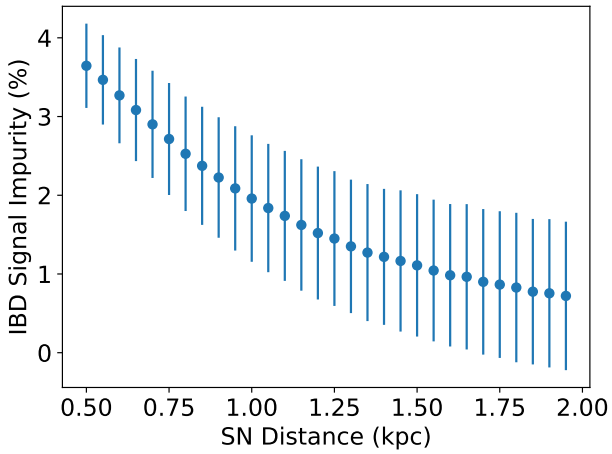

Figure 9.48: The change in the IBD tagging impurity with distance. At closer distances the tagging impurity is increased due to random coincidences between events in the detector mimicking an IBD event.

A number of events are also lost to the retrigger removal and the IBD neutron scatter removal. Figure 9.49 shows the number of events removed by the retrigger cut and the IBD neutron scatter cut relative to the true number of physics events within the detector. If the cuts were perfect a fixed proportion of events would be removed as a function of distance. However, the figure shows an increase in the proportion of events removed at shorter distances. At closer distances random coincidences cause additional genuine physics events to be removed, this results in fewer events being observed than expected and contributes to the false improved sensitivity observed in Figure 9.43. This also explains the reduced number of events observed in Figure 9.45. This systematic can likely be reduced with a more advanced analysis.

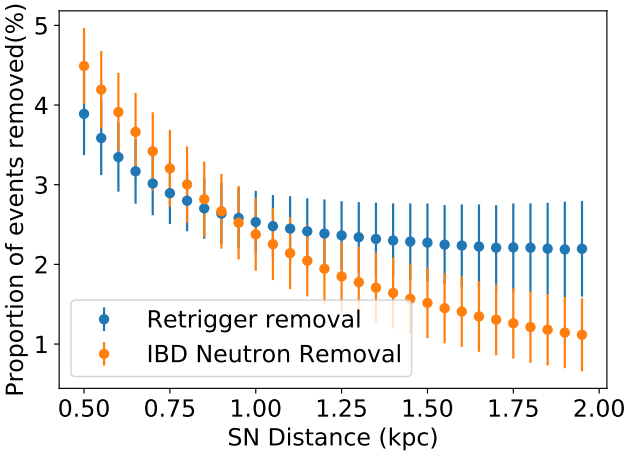

Figure 9.49: The proportion of events removed relative to the true number of events within the detector for the retrigger cut and the IBD neutron cut.

9.5 Summary

This chapter discusses the sensitivity of SNO+ to a supernova. It first presents the development of software to simulate a supernova burst within the simulation framework used by SNO+. A procedure to follow in the case of a burst during the water phase of SNO+ is presented using this software, by making a comparison between the supernova signal and the detector intrinsic backgrounds. A study on the sensitivity of the burst trigger, the lowest level component of any supernova trigger, to a burst in the water phase of SNO+ was presented. It was found the trigger was fully sensitive up to approximately 30 kpc, after this the trigger efficiency drops off, at 50 kpc the burst trigger only triggered approximately 5% of the time.

A sensitivity study to the neutrino mass hierarchy using supernova neutrinos was presented. At early times in the burst the oscillations are driven by the adiabatic MSW effect, this results in distinct differences in the number of IBD and untagged events depending on the neutrino mass hierarchy. First a toy MC study was presented for various detectors. As expected detectors with larger fiducial volumes did significantly better than smaller detectors, due to their higher statistics. Furthermore, it was found that water Cherenkov detectors had a slight advantage over scintillator detectors for this analysis, as they are not sensitive to the neutrino proton scattering, which forms a mass hierarchy independent flat background to the neutrino-electron scattering interaction channel. A global limit was obtained by combining the sensitivities of the JUNO and Super-K detectors. By combining the predicted sensitivities with the predicted distance distribution of galactic supernovae, the overall probability of a supernova giving a level of sensitivity to the neutrino mass hierarchy can be found. When no prior was assumed the probability of reaching a 5σ sensitivity to the neutrino mass hierarchy given a supernova occurs was found to be 0.29. When adjusting the prior to reflect the current favouring to the NH the probability of obtaining 5σ sensitivity increases to 0.56.

In order to quantify the detector systematics not considered within the toy study the software developed was used to simulate bursts for all models in both hierarchies. An analysis procedure was developed and performed on the bursts. The procedure followed two stages, the identification of the core bounce time T_0 and the binning of the events in time. On average good agreement was observed with the true core bounce time but a large uncertainty on the value of T_0 was found, this value could be reduced by using an estimate from a larger experiment with more statistics. Cuts were made on the events to account for systematic effects such as detector retriggers and additional events caused by multiple

neutron scatters. The algorithm developed to determine the core bounce time was found to underestimate the value of T_0 for supernova at closer distances. Both the IBD tagging efficiency and impurity were also found to vary with supernova distance. For supernova at closer distances the tagging efficiency is reduced and the signal impurity is increased. Finally the retrigger and neutron scatter cut were found to have an effect on the number of events observed. Both of these cuts create a dead zone, a region of the detector which is insensitive to any additional events. When the supernova is close enough and the rate of events is high enough events are lost due to random coincidences with these dead zones, a more advanced analysis would likely be able to reduce the size and impact of these dead zones.

Chapter 10

Conclusions

Supernovae are infrequent events which produce short bursts of neutrinos over periods of O(10) s. The large matter densities and the high neutrino flux, unique to supernova, can induce large oscillation effects observable at Earth. One such effect is analogous to the MSW effect within the Sun. Depending on the neutrino mass hierarchy the expected observed neutrino spectra differ.

This thesis presents the development of a software package to convert a supernova burst into input for full detector simulation using accurate kinematics of the various interactions. The package was used to study the burst trigger efficiency, the lowest stage of any potential supernova trigger, as a function of distance for the water phase of SNO+. It was found that the trigger was efficient to approximately 30 kpc, past this point the efficiency dropped off. At 50 kpc the efficiency was approximately 5%.

An toy MC analysis was developed to determine the neutrino mass hierarchy for various neutrino detectors. The overall probability of determining the neutrino mass hierarchy was found by convolving the observed sensitivities from the toy MC with a predicted distance distribution of galactic supernova [119]. A global sensitivity was obtained by combining the Super-K and JUNO detectors. With an unbiased prior the probability of obtaining 5σ sensitivity given a galactic supernovae occurs was found to be 0.29. The same analysis was performed with an adjusted prior to reflect the current knowledge of the neutrino mass hierarchy[1], when using the adjusted priors the probability of a supernova increasing the sensitivity to 5σ increases to 0.56.

The toy MC study did not take into account the systematic effect of the time profile of the burst not being known exactly. Furthermore other systematics associated with the detector were not included. In order to quantify this effect full detector simulations were

[1]The current sensitivity favours the normal hierarchy at $\Delta\chi^2 = 11.7$

performed for a supernova at 1 kpc. Tagging algorithms for IBD events were implemented from the ones used within KamLAND [24]. The number of untagged events was also affected by IBD events occurring external to the fiducial volume reconstructing within it. A simple algorithm was developed to determine the point of core bounce of the supernova, the algorithm was found to underestimate the bounce time at shorter distances, producing a systematic offset in the rise time of the IBD events. The IBD efficiency and impurity were also found to vary with distance. Untagged events were lost due to the retigger cut and IBD neutron scatter cut made on events. The removal of the events caused a overestimated sensitivity relative to the toy study.

The RAT simulations used to verify the mass hierarchy study were also used to study the IBD tagging efficiency of the detector during a supernova. When using the KamLAND IBD tagging procedure [24] two different Δt cuts (the time between the prompt e^+ and the delayed neutron capture) were investigated. With a 1000 µs cut the tagging efficiency was 79.6±2.3% the impurity of the IBD signal was found to be $1.83 \pm 0.74\%$ for a SN at 1 kpc. With a 600 µs cut the tagging efficiency was $75.8 \pm 2.28\%$ the signal impurity at 1 kpc was $1.51 \pm 0.66\%$. The signal impurity was found to increase at shorter distances, and the tagging efficiency was found to decrease.

The main physics goal of the SNO+ experiment is the search for neutrinoless double-beta decay ($0\nu\beta\beta$) in ^{130}Te. In order to set a competitive limit the detector response must be accurately understood. Any calibration scan must cover the entire angular range of physics events within the detector. Chapter 6 shows the proposed scans cover the entire angular range of physics events in the detector. New hardware is being developed for the scintillator phase of SNO+. One of these pieces of hardware is a new laserball with thinner neck, resulting in less shadowing of PMTs at the top of the detector. Simulations using the new laserball indicated a reduction in the error of the measurement of the angular response by approximately 10-15% compared to the old laserball.

Any deployment of calibration sources within the detector risks radioactive contamination, increasing the backgrounds for any $0\nu\beta\beta$ search. In order to reduce the probability of radioactive contamination an external LED/Laser calibration system was developed to enable calibration without the requirement of deployment of a source. Chapter 7 describes the commissioning activities I undertook to ensure correct operation. The performance of the system during early commissioning runs is also shown. The results of a study to determine the rate of aging the PMMA TELLIE fibres in UPW were also shown, the study indicated no significant aging of the fibres would occur over the lifetime of SNO+.

The optics of the detector must also be under to undertake a successful $0\nu\beta\beta$ search, the AV position will effect the optics of the detector, furthermore any changes to the AV position will also change the fiducial volume as AV surface backgrounds form a background to $0\nu\beta\beta$. A analysis procedure is shown in Chapter 8 to position the AV by using the reflected light off of the AV to position it. The offset was measured in the Z axis of the detector, systematic effects such as ropes and belly plates on the AV affected the measurement in the X and Y axes In the Z axis an offset of 105.7 ± 4.9 mm was found, this was consistent with direct measurements of the AV height, which was found to lie at 109 mm. A background to the AV position fit was as a result of backscattering of light in the external water region of the detector, the amount of backscattered light is inversely proportional to the scattering length of the external water. A fit to Monte Carlo found a scattering length of $527\pm^{19}_{20}$ m, this was 1.088 times the RAT default scattering length. The systematic uncertainty associated with the fibre direction was considered, it was found to cause an approximate 10 m shift upwards in the measured scattering length.

Appendix A

Laserball and ^{16}N Angular Response

A.1 Original Laserball Scan positions

The first three columns indicate the position within the detector. The fourth column represents the orientation of the laserball, by rotating the laserball any systematics associated with the ϕ asymmetry of the Laserball are removed. The final column represents the number of simulated events described in Section 6.4.2 and is proportional to the amount of time the source spends at each position.

X	**Y**	**Z**	**Orientation**	**Number of Events**
0.0	0.0	0.0	3	1440
0.0	0.0	0.0	1	720
0.0	0.0	0.0	0	720
0.0	0.0	0.0	2	720
0.0	1500.0	1500.0	3	360
0.0	-1500.0	1500.0	3	360
0.0	1500.0	-1500.0	3	360
0.0	-1500.0	-1500.0	3	360
0.0	3000.0	3000.0	3	360
0.0	-3000.0	3000.0	3	360
0.0	3000.0	-3000.0	3	360
0.0	-3000.0	-3000.0	3	360
1500.0	0.0	1500.0	0	360
1500.0	0.0	-1500.0	0	360

-1500.0	0.0	1500.0	0	360
-1500.0	0.0	-1500.0	0	360
3000.0	0.0	3000.0	0	360
3000.0	0.0	-3000.0	0	360
-3000.0	0.0	3000.0	0	360
-3000.0	0.0	-3000.0	0	360
0.0	1900.0	-4600.0	3	360
0.0	-1900.0	-4600.0	3	360
0.0	2300.0	-5000.0	3	360
0.0	-2300.0	-5000.0	3	360
1900.0	0.0	-4600.0	0	360
-1900.0	0.0	-4600.0	0	360
2300.0	0.0	-5000.0	0	360
-2300.0	0.0	-5000.0	0	360
0.0	4000.0	0.0	3	360
0.0	-4000.0	0.0	3	360
4000.0	0.0	0.0	0	360
-4000.0	0.0	0.0	0	360
0.0	0.0	-5000.0	3	360
0.0	0.0	-5500.0	3	360
0.0	0.0	5500.0	3	360
0.0	0.0	5750.0	3	360
0.0	0.0	6000.0	3	360
0.0	0.0	6250.0	3	360
0.0	0.0	6500.0	3	360
0.0	0.0	6750.0	3	360
-5861.1	-2524.1	-5000.0	3	360
-5861.1	-2524.1	-4500.0	3	360
-5861.1	-2524.1	-4000.0	3	360
-5861.1	-2524.1	-3500.0	3	360
-5861.1	-2524.1	-3000.0	3	360
-5861.1	-2524.1	-2500.0	3	360
-5861.1	-2524.1	-2000.0	3	360
-5861.1	-2524.1	-1500.0	3	360

-5861.1	-2524.1	-1000.0	3	360
-5861.1	-2524.1	-500.0	3	360
-5861.1	-2524.1	0.0	3	360
-5861.1	-2524.1	500.0	3	360
-5861.1	-2524.1	1000.0	3	360
-5861.1	-2524.1	1500.0	3	360
-5861.1	-2524.1	2000.0	3	360
-5861.1	-2524.1	2500.0	3	360
-5861.1	-2524.1	3000.0	3	360
-5861.1	-2524.1	3500.0	3	360
-5861.1	-2524.1	4000.0	3	360
-5861.1	-2524.1	4500.0	3	360
-5861.1	-2524.1	5000.0	3	360

Table A.1: List of positions and orientations for the Laserball scan

A.2 Angular response for PMTs

Figure A.1 shows the angular response calculated for various sets of PMTs grouped by height.

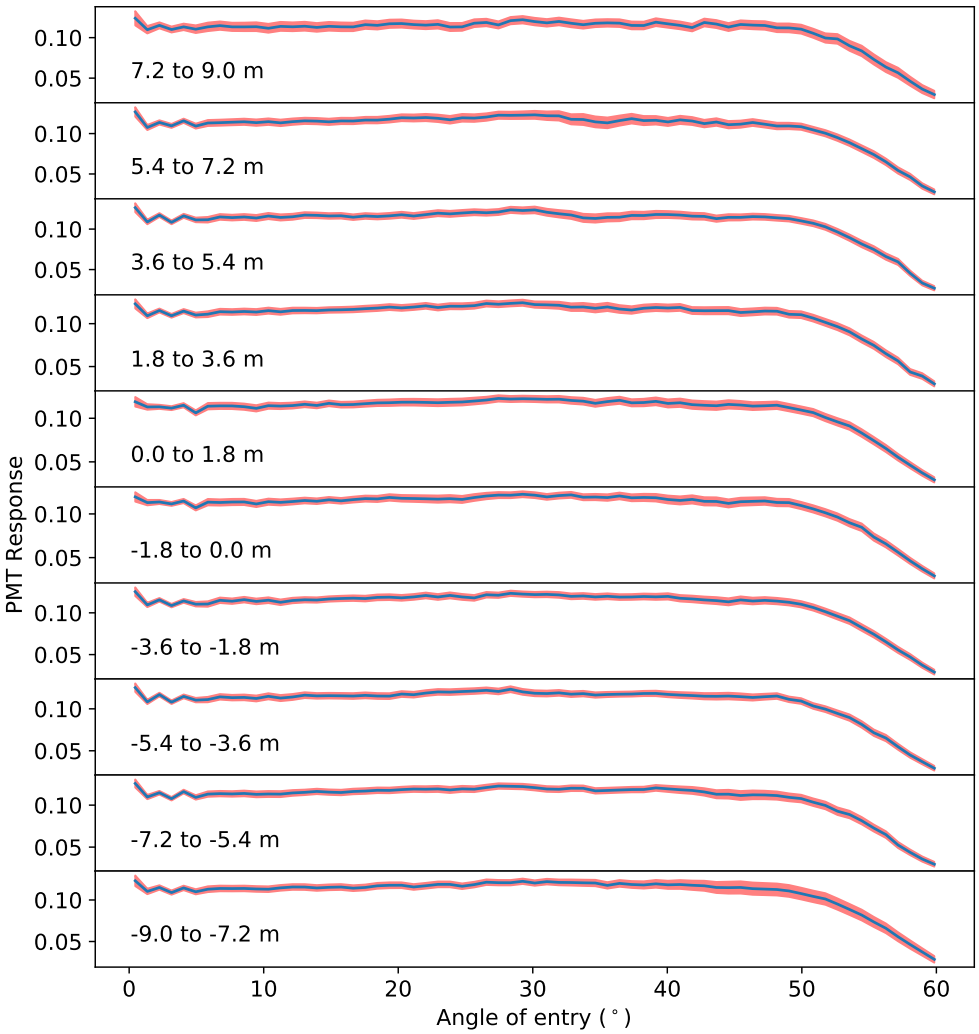

Figure A.1: Angular response of the PMTs grouped by their height in the detector. The red bar indicates the uncertainty on the measurement scaled up by a factor 10.

A.3 Original ^{16}N Scan positions

X	Y	Z
-5500.0	0.0	0.0
-5000.0	0.0	0.0
-4500.0	0.0	0.0
-4000.0	0.0	0.0
-3500.0	0.0	0.0

-3000.0	0.0	0.0
-2500.0	0.0	0.0
-2000.0	0.0	0.0
-1500.0	0.0	0.0
-1000.0	0.0	0.0
-500.0	0.0	0.0
0.0	0.0	0.0
500.0	0.0	0.0
1000.0	0.0	0.0
1500.0	0.0	0.0
2000.0	0.0	0.0
2500.0	0.0	0.0
3000.0	0.0	0.0
3500.0	0.0	0.0
4000.0	0.0	0.0
4500.0	0.0	0.0
5000.0	0.0	0.0
5500.0	0.0	0.0
0.0	-5500.0	0.0
0.0	-5000.0	0.0
0.0	-4500.0	0.0
0.0	-4000.0	0.0
0.0	-3500.0	0.0
0.0	-3000.0	0.0
0.0	-2500.0	0.0
0.0	-2000.0	0.0
0.0	-1500.0	0.0
0.0	-1000.0	0.0
0.0	-500.0	0.0
0.0	500.0	0.0
0.0	1000.0	0.0
0.0	1500.0	0.0
0.0	2000.0	0.0
0.0	2500.0	0.0

0.0	3000.0	0.0
0.0	3500.0	0.0
0.0	4000.0	0.0
0.0	4500.0	0.0
0.0	5000.0	0.0
0.0	5500.0	0.0
0.0	0.0	-5500.0
0.0	0.0	-5000.0
0.0	0.0	-4500.0
0.0	0.0	-4000.0
0.0	0.0	-3500.0
0.0	0.0	-3000.0
0.0	0.0	-2500.0
0.0	0.0	-2000.0
0.0	0.0	-1500.0
0.0	0.0	-1000.0
0.0	0.0	-500.0
0.0	0.0	500.0
0.0	0.0	1000.0
0.0	0.0	1500.0
0.0	0.0	2000.0
0.0	0.0	2500.0
0.0	0.0	3000.0
0.0	0.0	3500.0
0.0	0.0	4000.0
0.0	0.0	4500.0
0.0	0.0	5000.0
0.0	0.0	5500.0
-5861.1	-2524.1	-5000.0
-5861.1	-2524.1	-4500.0
-5861.1	-2524.1	-4000.0
-5861.1	-2524.1	-3500.0
-5861.1	-2524.1	-3000.0
-5861.1	-2524.1	-2500.0

-5861.1	-2524.1	-2000.0
-5861.1	-2524.1	-1500.0
-5861.1	-2524.1	-1000.0
-5861.1	-2524.1	-500.0
-5861.1	-2524.1	0.0
-5861.1	-2524.1	500.0
-5861.1	-2524.1	1000.0
-5861.1	-2524.1	1500.0
-5861.1	-2524.1	2000.0
-5861.1	-2524.1	2500.0
-5861.1	-2524.1	3000.0
-5861.1	-2524.1	3500.0
-5861.1	-2524.1	4000.0
-5861.1	-2524.1	4500.0
-5861.1	-2524.1	5000.0
2309.0	0.0	2309.0
2309.0	0.0	-2309.0
0.0	2309.0	2309.0
0.0	2309.0	-2309.0
-2309.0	0.0	2309.0
-2309.0	0.0	-2309.0
0.0	-2309.0	2309.0
0.0	-2309.0	-2309.0
3000.0	0.0	3000.0
3000.0	0.0	-3000.0
0.0	3000.0	3000.0
0.0	3000.0	-3000.0
-3000.0	0.0	3000.0
-3000.0	0.0	-3000.0
0.0	-3000.0	3000.0
0.0	-3000.0	-3000.0

Table A.2: List of positions for the ^{16}N scan, for the plots produced in Section 6.4.4 a total of 1×10^5 events were simulated at each position.

Figure A.2 shows the angular response calculated from the ^{16}N scan for various sets of PMTs grouped by height.

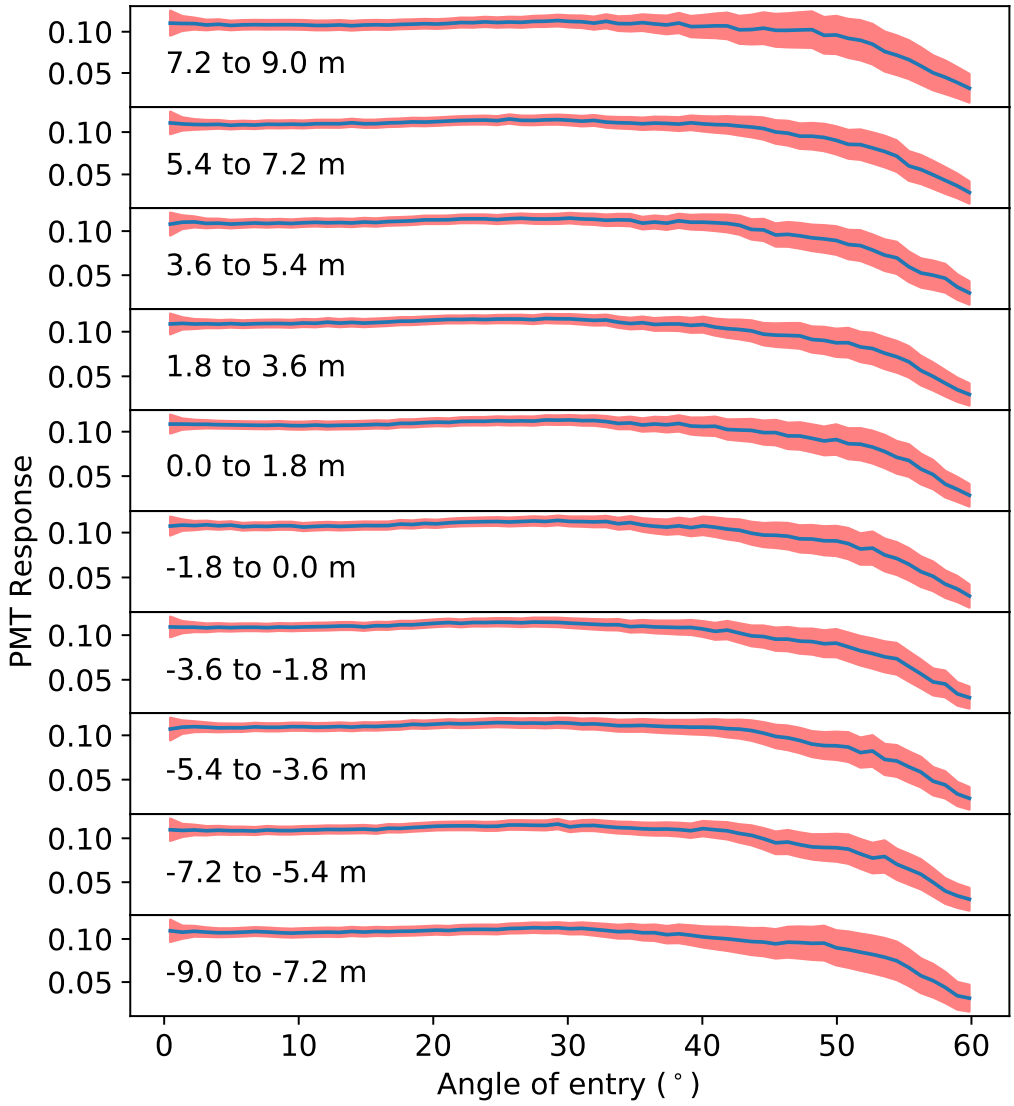

Figure A.2: Angular response of the PMTs determined by the ^{16}N scan grouped by their height in the detector. The red bar indicates the uncertainty on the measurement scaled up by a factor 10.

Appendix B

List of Acronyms

PMT PhotoMultiplier Tube

ELLIE Embedded Laser/LED Light Injection Entity

UFO Umbilical Flasher Object

AV Acrylic Vessel

FTXXX Numbering scheme for TELLIE fibres

FSXXX Numbering scheme for SMELLIE fibres

FAXXX Numbering scheme for AMELLIE fibres

DQ Data Quality

PSUP PMT Support Structure

RAT RAT is an Analysis Tool: The software package used to simulate the SNO+ detector.

BAO Baryon Acoustic Oscillation

IBD Inverse Beta Decay

$\boldsymbol{\nu - e}$ Neutrino Electron Scattering

$\boldsymbol{\nu - p}$ Neutrino Proton Scattering

SN Supernovae

NS Neutron Star

BH Black Hole

$M_{\odot}$ Solar Mass

PNS Proto Neutron Star

EOS Equation Of State

LAB Linear Alkyl Benzene

TTL Transistor Type Logic

ECL Emitter Coupled Logic

UPW Ultra Pure Water

OCA Optical Calibration

PCA PMT Calibration

NHit Number of PMTs hit in a single detector event

Bibliography

[1] Fred L. Wilson. Fermi's theory of beta decay. *American Journal of Physics*, 36(12):1150–1160, 1968. Cited on

[2] C. L. Cowan, F. Reines, F. B. Harrison, et al. Detection of the free neutrino: a confirmation. *Science*, 124(3212):103–104, 1956. Cited on

[3] G. Danby, J-M. Gaillard, K. Goulianos, et al. Observation of high-energy neutrino reactions and the existence of two kinds of neutrinos. *Phys. Rev. Lett.*, 9:36–44, Jul 1962. Cited on

[4] DONUT Collaboration. Observation of tau neutrino interactions. *Physics Letters B*, 504:218–224, April 2001. Cited on

[5] Q. R. Ahmad, R. C. Allen, T. C. Andersen, et al. Measurement of the rate of $nu_e + d \rightarrow p + p + e^-$ Interactions Produced by ^{8}b solar neutrinos at the sudbury neutrino observatory. *Physical Review Letters*, 87(7):071301, August 2001. Cited on

[6] Y. Fukuda, T. Hayakawa, E. Ichihara, et al. Evidence for oscillation of atmospheric neutrinos. *Phys. Rev. Lett.*, 81:1562–1567, Aug 1998. Cited on

[7] Boris Kayser. Neutrino physics. *eConf*, C040802:L004, 2004. Cited on

[8] Feng Peng An et al. Measurement of electron antineutrino oscillation based on 1230 days of operation of the Daya Bay experiment. *Phys. Rev.*, D95(7):072006, 2017. Cited on

[9] L. Wolfenstein. Neutrino Oscillations in Matter. *Phys. Rev.*, D17:2369–2374, 1978. Cited on

[10] S. P. Mikheev and A. Yu. Smirnov. Resonance Amplification of Oscillations in Matter and Spectroscopy of Solar Neutrinos. *Sov. J. Nucl. Phys.*, 42:913–917, 1985. [Yad. Fiz.42,1441(1985)]. Cited on

[11] H. A. Bethe. Possible explanation of the solar-neutrino puzzle. *Phys. Rev. Lett.*, 56:1305–1308, Mar 1986. Cited on

[12] Boris Kayser. Neutrino Oscillation Phenomenology. In *Neutrinos in particle physics, astrophysics and cosmology. Proceedings, 61st Scottish Universities Summer School in Physics, SUSSP61, St. Andrews, UK, August 8-23, 2006*, pages 51–64, 2008. Cited on

[13] Martin Freund. Analytic approximations for three neutrino oscillation parameters and probabilities in matter. *Phys. Rev.*, D64:053003, 2001. Cited on

[14] P. F. de Salas, D. V. Forero, C. A. Ternes, M. Tortola, and J. W. F. Valle. Status of neutrino oscillations 2017. 2017. Cited on

[15] J. N. Bahcall, A. M. Serenelli, and S. Basu. New solar opacities, abundances, helioseismology, and neutrino fluxes. *apjl*, 621:L85–L88, March 2005. Cited on

[16] Carlo Bemporad, Giorgio Gratta, and Petr Vogel. Reactor based neutrino oscillation experiments. *Rev. Mod. Phys.*, 74:297, 2002. Cited on

[17] R. N. Cahn, D. A. Dwyer, S. J. Freedman, et al. White Paper: Measuring the Neutrino Mass Hierarchy. In *Proceedings, 2013 Community Summer Study on the Future of U.S. Particle Physics: Snowmass on the Mississippi (CSS2013): Minneapolis, MN, USA, July 29-August 6, 2013*, 2013. Cited on

[18] DUNE Collaboration. Long-Baseline Neutrino Facility (LBNF) and Deep Underground Neutrino Experiment (DUNE) Conceptual Design Report Volume 2: The Physics Program for DUNE at LBNF. *ArXiv e-prints*, December 2015. Cited on

[19] Mark Thomson. *Modern particle physics*. Cambridge University Press, New York, 2013. Cited on

[20] Raymond Davis. A review of the homestake solar neutrino experiment. *Progress in Particle and Nuclear Physics*, 32:13 – 32, 1994. Cited on

[21] C. Giunti and C.W. Kim. *Fundamentals of Neutrino Physics and Astrophysics*. OUP Oxford, 2007. Cited on

[22] J. Hosaka, K. Ishihara, J. Kameda, et al. Solar neutrino measurements in Super-Kamiokande-I. *PRD*, 73(11):112001, June 2006. Cited on

[23] B. Aharmim, S. N. Ahmed, A. E. Anthony, et al. Electron energy spectra, fluxes, and day-night asymmetries of ^{8}B solar neutrinos from measurements with NaCl dissolved in the heavy-water detector at the Sudbury Neutrino Observatory. *prc*, 72(5):055502, November 2005. Cited on

[24] S. Abe, T. Ebihara, S. Enomoto, et al. Precision Measurement of Neutrino Oscillation Parameters with KamLAND. *Physical Review Letters*, 100(22):221803, June 2008. Cited on

[25] F. An, G. An, Q. An, et al. Neutrino physics with JUNO. *Journal of Physics G Nuclear Physics*, 43(3):030401, March 2016. Cited on

[26] S.-B. Kim. New results from RENO and prospects with RENO-50. *ArXiv e-prints*, December 2014. Cited on

[27] L. Zhan, Y. Wang, J. Cao, and L. Wen. Determination of the neutrino mass hierarchy at an intermediate baseline. *prd*, 78(11):111103, December 2008. Cited on

[28] K. Abe, Y. Haga, Y. Hayato, et al. Limits on sterile neutrino mixing using atmospheric neutrinos in super-kamiokande. *Phys. Rev. D*, 91:052019, Mar 2015. Cited on

[29] T. Kajita, E. Kearns, and M. Shiozawa. Establishing atmospheric neutrino oscillations with super-kamiokande. *Nuclear Physics B*, 908:14 – 29, 2016. Neutrino Oscillations: Celebrating the Nobel Prize in Physics 2015. Cited on

[30] M. Fukugita and T. Yanagida. Barygenesis without grand unification. *Physics Letters B*, 174(1):45 – 47, 1986. Cited on

[31] Michael Dine and Alexander Kusenko. The Origin of the matter - antimatter asymmetry. *Rev. Mod. Phys.*, 76:1, 2003. Cited on

[32] B. Pritychenko. Systematics of evaluated half-lives of double-beta decay. *Nuclear Data Sheets*, 120:102 – 105, 2014. Cited on

[33] Juris Meija, Tyler B Coplen, Michael Berglund, et al. Isotopic compositions of the elements 2013 (iupac technical report). *Pure and Applied Chemistry*, 88(3):293–306, 2016. Cited on

[34] Boris Kayser. Are neutrinos their own antiparticles? *Journal of Physics: Conference Series*, 173(1):012013, 2009. Cited on

[35] S. Andringa et al. Current Status and Future Prospects of the SNO+ Experiment. *Adv. High Energy Phys.*, 2016:6194250, 2016. Cited on

[36] S. Dell'Oro, S. Marcocci, M. Viel, and F. Vissani. Neutrinoless double beta decay: 2015 review. *ArXiv e-prints*, January 2016. Cited on

[37] Steven R. Elliott and Petr Vogel. Double beta decay. *Annual Review of Nuclear and Particle Science*, 52(1):115–151, 2002. Cited on

[38] J. R. Alonso et al. Advanced Scintillator Detector Concept (ASDC): A Concept Paper on the Physics Potential of Water-Based Liquid Scintillator. 2014. Cited on

[39] J. Caravaca, F. B. Descamps, B. J. Land, et al. Experiment to demonstrate separation of Cherenkov and scintillation signals. *Phys. Rev.*, C95(5):055801, 2017. Cited on

[40] K. Alfonso, D. R. Artusa, F. T. Avignone, et al. Search for neutrinoless double-beta decay of $^{130}mathrmTe$ with cuore-0. *Phys. Rev. Lett.*, 115:102502, Sep 2015. Cited on

[41] M. Auger, D. J. Auty, P. S. Barbeau, et al. Search for Neutrinoless Double-Beta Decay in Xe136 with EXO-200. *Physical Review Letters*, 109(3):032505, July 2012. Cited on

[42] R. Arnold, C. Augier, J. Baker, et al. First Results of the Search for Neutrinoless Double-Beta Decay with the NEMO 3 Detector. *Physical Review Letters*, 95(18):182302, October 2005. Cited on

[43] Susanne Mertens. Status of the katrin experiment and prospects to search for kev-mass sterile neutrinos in tritium *beta*-decay. *Physics Procedia*, 61:267 – 273, 2015. 13th International Conference on Topics in Astroparticle and Underground Physics, TAUP 2013. Cited on

[44] A. J. Cuesta, V. Niro, and L. Verde. Neutrino mass limits: Robust information from the power spectrum of galaxy surveys. *Physics of the Dark Universe*, 13:77–86, September 2016. Cited on

[45] S. M. Bilenky and C. Giunti. Neutrinoless Double-Beta Decay: a Probe of Physics Beyond the Standard Model. *Int. J. Mod. Phys.*, A30(04n05):1530001, 2015. Cited on

[46] G. Bellini et al. Observation of Geo-Neutrinos. *Phys. Lett.*, B687:299–304, 2010. Cited on

[47] Alessandro Strumia and Francesco Vissani. Precise quasielastic neutrino/nucleon cross-section. *Physics Letters B*, 564(1–2):42 – 54, 2003. Cited on

[48] Belina von Krosigk. *Measurement of proton and alpha–particle quenching in LAB based scintillators and determination of spectral sensitivities to supernova neutrinos in the SNO+ detector*. PhD thesis, TU Dresden. Cited on

[49] John F. Beacom, Will M. Farr, and Petr Vogel. Detection of supernova neutrinos by neutrino proton elastic scattering. *Phys. Rev.*, D66:033001, 2002. Cited on

[50] L. A. Ahrens, S. H. Aronson, P. L. Connolly, et al. Measurement of neutrino-proton and antineutrino-proton elastic scattering. *Phys. Rev. D*, 35:785–809, Feb 1987. Cited on

[51] Katherine Woodruff. Exploring Nucleon Spin Structure Through Neutrino Neutral-Current Interactions in MicroBooNE. In *22nd International Symposium on Spin Physics (SPIN 2016) Urbana, IL, USA, September 25-30, 2016*, 2017. Cited on

[52] Rafael F. Lang, Christopher McCabe, Shayne Reichard, et al. Supernova neutrino physics with xenon dark matter detectors: A timely perspective. *Phys. Rev.*, D94(10):103009, 2016. Cited on

[53] Matteo Biassoni. *THE CUORE POTENTIAL AS A COHERENT INTERACTION BASED OBSERVATORY FOR SUPERNOVA NEUTRINOS*. PhD thesis, Milan Bicocca U., 2013. Cited on

[54] M. Biassoni and C. Martinez. Study of supernova *nu*-nucleus coherent scattering interactions. *Astroparticle Physics*, 36:151–155, August 2012. Cited on

[55] D. Akimov et al. Observation of Coherent Elastic Neutrino-Nucleus Scattering. *Science*, 357(6356):1123–1126, 2017. Cited on

[56] E. Kolbe, K. Langanke, and P. Vogel. Estimates of weak and electromagnetic nuclear decay signatures for neutrino reactions in super-kamiokande. *Phys. Rev. D*, 66:013007, Jul 2002. Cited on

[57] E Kolbe, K Langanke, G Martínez-Pinedo, and P Vogel. Neutrino–nucleus reactions and nuclear structure. *Journal of Physics G: Nuclear and Particle Physics*, 29(11):2569, 2003. Cited on

[58] David E. Alburger. Beta decay of N^{16}. *Phys. Rev.*, 111:1586–1591, Sep 1958. Cited on

[59] K. Langanke, P. Vogel, and E. Kolbe. Signal for supernova *ensuremath*ν_μ and ν_τ neutrinos in water Čerenkov detectors. *Phys. Rev. Lett.*, 76:2629–2632, Apr 1996. Cited on

[60] F. Ajzenberg-Selove. Energy levels of light nuclei a = 11-12. *Nuclear Physics A*, 506(1):1 – 158, 1990. Cited on

[61] B.E. Bodmann, N.E. Booth, G. Drexlin, V. Eberhard, J.A. Edgington, K. Eitel, M. Ferstl, E. Finckh, H. Gemmeke, W. Grandegger, J. Hößl, M. Kleifges, J. Kleinfeller, W. Kretschmer, R. Maschuw, P. Plischke, J. Rapp, F. Schilling, B. Seligmann, O. Stumm, J. Wolf, S. Wölfle, and B. Zeitnitz. Neutrino interactions with carbon: recent measurements and a new test of ν_e, ν_μ universality. *Physics Letters B*, 332(3):251 – 257, 1994. Cited on

[62] Richard Imlay. New results on electron-neutrino carbon scattering and muon-neutrino carbon scattering at lsnd. *Nuclear Physics A*, 629(1):531 – 537, 1998. Quark Lepton Nuclear Physics. Cited on

[63] B Armbruster, I Blair, B.A Bodmann, et al. Measurement of the weak neutral current excitation 12c($\nu_\mu\nu'_\mu$)12c*(1^+,1;15.1mev) at e_{ν_μ}=29.8 mev. *Physics Letters B*, 423(1):15 – 20, 1998. Cited on

[64] T. Yoshida, T. Suzuki, S. Chiba, et al. Neutrino-Nucleus Reaction Cross Sections for Light Element Synthesis in Supernova Explosions. *Astrophys. J.*, 686:448–466, 2008. Cited on

[65] A. Gando, Y. Gando, K. Ichimura, et al. Search for extraterrestrial antineutrino sources with the kamland detector. *The Astrophysical Journal*, 745(2):193, 2012. Cited on

[66] K. Hirata, T. Kajita, M. Koshiba, et al. Observation of a neutrino burst from the supernova sn1987a. *Phys. Rev. Lett.*, 58:1490–1493, Apr 1987. Cited on

[67] R. M. Bionta, G. Blewitt, C. B. Bratton, et al. Observation of a neutrino burst in coincidence with supernova 1987a in the large magellanic cloud. *Phys. Rev. Lett.*, 58:1494–1496, Apr 1987. Cited on

[68] E.N. Alexeyev, L.N. Alexeyeva, I.V. Krivosheina, and V.I. Volchenko. Detection of the neutrino signal from sn 1987a in the lmc using the inr baksan underground scintillation telescope. *Physics Letters B*, 205(2):209 – 214, 1988. Cited on

[69] E. Margaret Burbidge, G. R. Burbidge, William A. Fowler, and F. Hoyle. Synthesis of the elements in stars. *Rev. Mod. Phys.*, 29:547–650, Oct 1957. Cited on

[70] S. Chandrasekhar. On stars, their evolution and their stability. *Science*, 226(4674):497–505, 1984. Cited on

[71] Gregory Laughlin, Peter Bodenheimer, and Fred C. Adams. The end of the main sequence. *The Astrophysical Journal*, 482(1):420, 1997. Cited on

[72] A. Mirizzi, I. Tamborra, H.-T. Janka, et al. Supernova neutrinos: production, oscillations and detection. *Nuovo Cimento Rivista Serie*, 39:1–112, 2016. Cited on

[73] H.-T. Janka. Explosion Mechanisms of Core-Collapse Supernovae. *Annual Review of Nuclear and Particle Science*, 62:407–451, November 2012. Cited on

[74] S. Wanajo, K. Nomoto, H.-T. Janka, et al. Nucleosynthesis in Electron Capture Supernovae of Asymptotic Giant Branch Stars. *apj*, 695:208–220, April 2009. Cited on

[75] K. Nomoto. Evolution of 8-10 solar mass stars toward electron capture supernovae. II - Collapse of an O + Ne + Mg core. *apj*, 322:206–214, November 1987. Cited on

[76] L. H"udepohl, B. Müller, H.-T. Janka, et al. Neutrino signal of electron-capture supernovae from core collapse to cooling. *Phys. Rev. Lett.*, 104:251101, Jun 2010. Cited on

[77] T. Fischer, S. C. Whitehouse, A. Mezzacappa, et al. Protoneutron star evolution and the neutrino-driven wind in general relativistic neutrino radiation hydrodynamics simulations. *aap*, 517:A80, July 2010. Cited on

[78] A. Odrzywolek, Marcin Misiaszek, and M. Kutschera. Detection possibility of the pair - annihilation neutrinos from the neutrino - cooled pre-supernova star. *Astropart. Phys.*, 21:303–313, 2004. Cited on

[79] K. Asakura et al. KamLAND Sensitivity to Neutrinos from Pre-Supernova Stars. *Astrophys. J.*, 818(1):91, 2016. Cited on

[80] The KamLAND Collaboration. Kamland sn monitor. url-http://www.awa.tohoku.ac.jp/kamland/SNmonitor/regist/index.html, 2015. Cited on

[81] Pasquale D. Serpico, Sovan Chakraborty, Tobias Fischer, et al. Probing the neutrino mass hierarchy with the rise time of a supernova burst. *Phys. Rev. D*, 85:085031, Apr 2012. Cited on

[82] R. Bollig, H. Th. Janka, A. Lohs, et al. Muon Creation in Supernova Matter Facilitates Neutrino-driven Explosions. *Phys. Rev. Lett.*, 119(24):242702, 2017. Cited on

[83] C. J. Horowitz. Weak magnetism for anti-neutrinos in supernovae. *Phys. Rev.*, D65:043001, 2002. Cited on

[84] Hans-Thomas Janka, K. Langanke, A. Marek, et al. Theory of Core-Collapse Supernovae. *Phys. Rept.*, 442:38–74, 2007. Cited on

[85] T. Totani, K. Sato, H. E. Dalhed, and J. R. Wilson. Future detection of supernova neutrino burst and explosion mechanism. *The Astrophysical Journal*, 496(1):216, 1998. Cited on

[86] T. Fischer, G. Mart'ınez-Pinedo, M. Hempel, and M. Liebendörfer. Neutrino spectra evolution during protoneutron star deleptonization. *Phys. Rev. D*, 85:083003, Apr 2012. Cited on

[87] S. E. Woosley. Pulsational Pair-Instability Supernovae. *Astrophys. J.*, 836(2):244, 2017. Cited on

[88] Alexander Heger, C. L. Fryer, S. E. Woosley, et al. How massive single stars end their life. *Astrophys. J.*, 591:288–300, 2003. Cited on

[89] A. Heger and S. E. Woosley. The nucleosynthetic signature of population III. *Astrophys. J.*, 567:532–543, 2002. Cited on

[90] D. Kasen, S. E. Woosley, and A. Heger. Pair Instability Supernovae: Light Curves, Spectra, and Shock Breakout. *apj*, 734:102, June 2011. Cited on

[91] C. L. Fryer, S. E. Woosley, and A. Heger. Pair instability supernovae, gravity waves, and gamma-ray transients. *Astrophys. J.*, 550:372–382, 2001. Cited on

[92] B. Müller. The Status of Multi-Dimensional Core-Collapse Supernova Models. *Publ. Astron. Soc. Austral.*, 33:48, 2016. Cited on

[93] H. A. Bethe. Supernova mechanisms. *Rev. Mod. Phys.*, 62:801–866, Oct 1990. Cited on

[94] R. I. Epstein. Lepton-driven convection in supernovae. *mnras*, 188:305–325, August 1979. Cited on

[95] Florian Hanke, Bernhard Müller, Annop Wongwathanarat, et al. Sasi activity in three-dimensional neutrino-hydrodynamics simulations of supernova cores. *The Astrophysical Journal*, 770(1):66, 2013. Cited on

[96] J. M. Blondin, A. Mezzacappa, and C. DeMarino. Stability of Standing Accretion Shocks, with an Eye toward Core-Collapse Supernovae. *apj*, 584:971–980, February 2003. Cited on

[97] Thierry Foglizzo, Fr'edéric Masset, Jérôme Guilet, and Gilles Durand. Shallow water analogue of the standing accretion shock instability: Experimental demonstration and a two-dimensional model. *Phys. Rev. Lett.*, 108:051103, Jan 2012. Cited on

[98] John M. Blondin and Anthony Mezzacappa. Pulsar spins from an instability in the accretion shock of supernovae. *Nature*, 445:58, 2007. Cited on

[99] A. Marek and H.-Th. Janka. Delayed neutrino-driven supernova explosions aided by the standing accretion-shock instability. *The Astrophysical Journal*, 694(1):664, 2009. Cited on

[100] R. Fern'andez. Three-dimensional simulations of SASI- and convection-dominated core-collapse supernovae. *mnras*, 452:2071–2086, September 2015. Cited on

[101] Irene Tamborra, Florian Hanke, Bernhard Müller, et al. Neutrino signature of supernova hydrodynamical instabilities in three dimensions. *Phys. Rev. Lett.*, 111(12):121104, 2013. Cited on

[102] Irene Tamborra, Florian Hanke, Hans-Thomas Janka, and Andreas others. Self-sustained asymmetry of lepton-number emission: A new phenomenon during the supernova shock-accretion phase in three dimensions. *Astrophys. J.*, 792(2):96, 2014. Cited on

[103] James Pantaleone. Dirac neutrinos in dense matter. *Phys. Rev. D*, 46:510–523, Jul 1992. Cited on

[104] Amol S. Dighe and Alexei relax Yu. Smirnov. Identifying the neutrino mass spectrum from the neutrino burst from a supernova. *Phys. Rev.*, D62:033007, 2000. Cited on

[105] M. Kachelriess, Ricard Tomas, R. Buras, et al. Exploiting the neutronization burst of a galactic supernova. *Phys. Rev.*, D71:063003, 2005. Cited on

[106] Lorenz Hudepohl. *Neutrinos from the Formation, Cooling and Black Hole Collapse of Neutron Stars*. PhD thesis, Technische Universitat Munchen. Cited on

[107] Bronson Messer. Supernova models: neutrino signals and gravitational waves. SNOBS, 2017. Cited on

[108] Sovan Chakraborty, Tobias Fischer, Alessandro Mirizzi, et al. No collective neutrino flavor conversions during the supernova accretion phase. *Phys. Rev. Lett.*, 107:151101, Oct 2011. Cited on

[109] Richard C. Schirato and George M. Fuller. Connection between supernova shocks, flavor transformation, and the neutrino signal. 2002. Cited on

[110] Enrico Borriello, Sovan Chakraborty, Alessandro Mirizzi, et al. (Down-to-)Earth matter effect in supernova neutrinos. *Phys. Rev.*, D86:083004, 2012. Cited on

[111] Amol S. Dighe, Mathias T. Keil, and Georg G. Raffelt. Identifying earth matter effects on supernova neutrinos at a single detector. *JCAP*, 0306:006, 2003. Cited on

[112] Steen Hannestad, Georg G. Raffelt, Gunter Sigl, and Yvonne Y. Y. Wong. Self-induced conversion in dense neutrino gases: Pendulum in flavour space. *Phys. Rev.*, D74:105010, 2006. [Erratum: Phys. Rev.D76,029901(2007)]. Cited on

[113] Andreu Esteban-Pretel, Sergio Pastor, Ricard Tomas, et al. Decoherence in supernova neutrino transformations suppressed by deleptonization. *Phys. Rev.*, D76:125018, 2007. Cited on

[114] Sovan Chakraborty and Alessandro Mirizzi. Multi-azimuthal-angle instability for different supernova neutrino fluxes. *Phys. Rev.*, D90(3):033004, 2014. Cited on

[115] Christopher Jones. *Future Searches for Rare Astrophysical Signals and Detector Commissioning in SNO+*. PhD thesis, University of Oxford, UK. Cited on

[116] J. Bland-Hawthorn and O. Gerhard. The Galaxy in Context: Structural, Kinematic, and Integrated Properties. *araa*, 54:529–596, September 2016. Cited on

[117] C A Duba, F Duncan, J Farine, et al. Halo – the helium and lead observatory for supernova neutrinos. *Journal of Physics: Conference Series*, 136(4):042077, 2008. Cited on

[118] K. Abe et al. Real-Time Supernova Neutrino Burst Monitor at Super-Kamiokande. *Astropart. Phys.*, 81:39–48, 2016. Cited on

[119] Scott M. Adams, C. S. Kochanek, John F. Beacom, et al. Observing the next galactic supernova. *The Astrophysical Journal*, 778(2):164, 2013. Cited on

[120] S. van den Bergh. Supernova rates: A progress report. *physrep*, 204:385–400, June 1991. Cited on

[121] G. A. Tammann, W. Loeffler, and A. Schroeder. The Galactic supernova rate. *apjs*, 92:487–493, June 1994. Cited on

[122] Roland Diehl et al. Radioactive Al-26 and massive stars in the galaxy. *Nature*, 439:45–47, 2006. Cited on

[123] E. F. Keane and M. Kramer. On the birthrates of galactic neutron stars. *Monthly Notices of the Royal Astronomical Society*, 391(4):2009–2016, 2008. Cited on

[124] Weidong Li, Ryan Chornock, Jesse Leaman, et al. Nearby supernova rates from the lick observatory supernova search – iii. the rate–size relation, and the rates as a function of galaxy hubble type and colour. *Monthly Notices of the Royal Astronomical Society*, 412(3):1473–1507, 2011. Cited on

[125] K. Scholberg. The SuperNova Early Warning System. *Astron. Nachr.*, 329:337–339, 2008. Cited on

[126] Pietro Antonioli et al. SNEWS: The Supernova Early Warning System. *New J. Phys.*, 6:114, 2004. Cited on

[127] Andrea Gallo Rosso, Francesco Vissani, and Maria Cristina Volpe. Measuring the neutron star compactness and binding energy with supernova neutrinos. *JCAP*, 1711(11):036, 2017. Cited on

[128] H. A. Bethe and G. E. Brown. Observational constraints on the maximum neutron star mass. *apjl*, 445:L129–L132, June 1995. Cited on

[129] K. Sumiyoshi, S. Yamada, and H. Suzuki. Dynamics and neutrino signal of black hole formation in non-rotating failed supernovae. 1. EOS dependence. *Astrophys. J.*, 667:382–394, 2007. Cited on

[130] H. Shen, H. Toki, K. Oyamatsu, and K. Sumiyoshi. Relativistic equation of state of nuclear matter for supernova and neutron star. *Nucl. Phys.*, A637:435–450, 1998. Cited on

[131] W. David Arnett, John N. Bahcall, Robert P. Kirshner, and Stanford E. Woosley. Supernova 1987a. *Annual Review of Astronomy and Astrophysics*, 27(1):629–700, 1989. Cited on

[132] M. Aglietta, G. Badino, G. Bologna, et al. On the event observed in the mont blanc underground neutrino observatory during the occurrence of supernova 1987 a. *EPL (Europhysics Letters)*, 3(12):1315, 1987. Cited on

[133] M. Aglietta, G. Badino, G. Bologna, et al. Analysis of the data recorded by the mont blanc neutrino detector and by the maryland and rome gravitational-wave detectors during sn1987a. *Il Nuovo Cimento C*, 12(1):75–103, Jan 1989. Cited on

[134] P. Galeotti and G. Pizzella. Galileo versus aristotle: the case of supernova 1987a. *Astrophysical Bulletin*, 72(3):251–256, Jul 2017. Cited on

[135] P. Galeotti and G. Pizzella. New analysis for the correlation between gravitational wave and neutrino detectors during SN1987A. *Eur. Phys. J.*, C76(8):426, 2016. Cited on

[136] C. A. Dickson and Bernard F. Schutz. Reassessment of the reported correlations between gravitational waves and neutrinos associated with sn 1987a. *Phys. Rev. D*, 51:2644–2668, Mar 1995. Cited on

[137] V. S. Imshennik and O. G. Ryazhskaya. A rotating collapsar and possible interpretation of the lsd neutrino signal from sn 1987a. *Astronomy Letters*, 30(1):14–31, Jan 2004. Cited on

[138] J. N. Bahcall and S. L. Glashow. Upper limit on the mass of the electron neutrino. *Nature*, 326:476 EP –, Apr 1987. Cited on

[139] Michael J. Longo. Tests of relativity from sn1987a. *Phys. Rev. D*, 36:3276–3277, Nov 1987. Cited on

[140] H. E. Jørgensen, V. M. Lipunov, I. E. Panchenko, et al. Evolution of supernova explosion rates in the universe. *The Astrophysical Journal*, 486(1):110, 1997. Cited on

[141] John F. Beacom. The Diffuse Supernova Neutrino Background. *Ann. Rev. Nucl. Part. Sci.*, 60:439–462, 2010. Cited on

[142] Shunsaku Horiuchi and John F. Beacom. Revealing Type Ia supernova physics with cosmic rates and nuclear gamma rays. *Astrophys. J.*, 723:329–341, 2010. Cited on

[143] Shunsaku Horiuchi, John F. Beacom, Christopher S. Kochanek, et al. The cosmic core-collapse supernova rate does not match the massive-star formation rate. *The Astrophysical Journal*, 738(2):154, 2011. Cited on

[144] S. Mattila, T. Dahlen, A. Efstathiou, et al. Core-collapse supernovae missed by optical surveys. *The Astrophysical Journal*, 756(2):111, 2012. Cited on

[145] C. S. Kochanek, J. F. Beacom, M. D. Kistler, et al. A Survey About Nothing: Monitoring a Million Supergiants for Failed Supernovae. *Astrophys. J.*, 684:1336–1342, 2008. Cited on

[146] K. Bays, T. Iida, K. Abe, et al. Supernova relic neutrino search at super-kamiokande. *Phys. Rev. D*, 85:052007, Mar 2012. Cited on

[147] Mark R. Vagins. Dsnb: Experimental challenges. urlhttps://indico.mitp.uni-mainz.de/event/77/contribution/22/material/slides/0.pdf, 2017. SNOBS 17. Cited on

[148] John F. Beacom. Dsnb theory. urlhttps://indico.mitp.uni-mainz.de/event/77/contribution/21/material/slides/0.pdf, 2017. SNOBS 17. Cited on

[149] John F. Beacom and Mark R. Vagins. GADZOOKS! Anti-neutrino spectroscopy with large water Cherenkov detectors. *Phys. Rev. Lett.*, 93:171101, 2004. Cited on

[150] Fraser Duncan. Overview of the snolab facility and current programme evolution. urlhttps://indico.cern.ch/event/439062/, 2015. Future Projects Planning Workshop 2015, SNOLAB. Cited on

[151] J. Boger et al. The Sudbury neutrino observatory. *Nucl. Instrum. Meth.*, A449:172–207, 2000. Cited on

[152] S. N. Ahmed et al. Constraints on nucleon decay via 'invisible' modes from the Sudbury Neutrino Observatory. *Phys. Rev. Lett.*, 92:102004, 2004. Cited on

[153] H. Ejiri. Nuclear deexcitations of nucleon holes associated with nucleon decays in nuclei. *Phys. Rev. C*, 48:1442–1444, Sep 1993. Cited on

[154] T. Araki et al. Search for the invisible decay of neutrons with KamLAND. *Phys. Rev. Lett.*, 96:101802, 2006. Cited on

[155] C. Patrignani and Particle Data Group. Review of particle physics. *Chinese Physics C*, 40(10):100001, 2016. Cited on

[156] I. B. Nemchenok, V. I. Babin, V. B. Brudanin, et al. Liquid scintillator based on linear alkylbenzene. *Physics of Particles and Nuclei Letters*, 8(2):129–135, Mar 2011. Cited on

[157] J B Birks. Scintillations from organic crystals: Specific fluorescence and relative response to different radiations. *Proceedings of the Physical Society. Section A*, 64(10):874, 1951. Cited on

[158] B. von Krosigk, L. Neumann, R. Nolte, et al. Measurement of the proton light response of various LAB based scintillators and its implication for supernova neutrino detection via neutrino-proton scattering. *Eur. Phys. J.*, C73(4):2390, 2013. Cited on

[159] G. Bellini et al. Neutrinos from the primary proton–proton fusion process in the Sun. *Nature*, 512(7515):383–386, 2014. Cited on

[160] Richard J. Ford. A Scintillator Purification Plant and Fluid Handling System for SNO+. *AIP Conf. Proc.*, 1672:080003, 2015. Cited on

[161] J. Argyriades et al. Measurement of the Double Beta Decay Half-life of Nd-150 and Search for Neutrinoless Decay Modes with the NEMO-3 Detector. *Phys. Rev.*, C80:032501, 2009. Cited on

[162] C. Alduino et al. Measurement of the two-neutrino double-beta decay half-life of ^{130}Te with the CUORE-0 experiment. *Eur. Phys. J.*, C77(1):13, 2017. Cited on

[163] Tanner Kaptanoglu. Getting HQE (R5912-100) PMTs Detector Ready. *SNO+ Internal DocDB*, DocDB-3843, 2016. Cited on

[164] James R. Sinclair. *Positioning and Timing Calibration of SNO+*. PhD thesis, University of Sussex, UK. Cited on

[165] James R. N. Cameron. *The Photomultiplier Tube Calibration of the Sudbury Neutrino Observatory*. PhD thesis, University of Oxford, UK. Cited on

[166] James R. Sinclair. *Optical Calibration System for SNO+ and Sensitivity to Neutrinoless Double-Beta Decay*. PhD thesis, University of Sussex, UK. Cited on

[167] Richard J. Bonventre. *Neutron Multiplicity in Atmospheric Neutrino events at the Sudbury Neutrino Observatory*. PhD thesis, University of Pennsylvania, USA. Cited on

[168] Liz Fletcher, Szymon Manecki, and Sean Takahaski. Umbilical #6 Log. *SNO+ Internal DocDB*, DocDB-3431, 2015. Cited on

[169] B.A. Moffat, R.J. Ford, F.A. Duncan, et al. Optical calibration hardware for the sudbury neutrino observatory. *Nucl.Instrum.Meth.*, A554:255–265, 2005. Cited on

[170] Bryce Anton Moffat. *The optical Calibration of the Sudbury Neutrino Observatory*. PhD thesis, Queens University, Canada. Cited on

[171] Nuno Filipe Fiúza de Barros. *Precision Measurement of Neutrino Oscillation Parameters: Combined Three-phase Results of the Sudbury Neutrino Observatory*. PhD thesis, University of Lisbon. Cited on

[172] Robert Stainforth. *Characterising the Optical Response of the SNO+ Detector*. PhD thesis, University of Liverpool, UK. Cited on

[173] M. R. Dragowsky et al. The N-16 calibration source for the Sudbury Neutrino Observatory. *Nucl. Instrum. Meth.*, A481:284–296, 2002. Cited on

[174] Chris Jackson. Photographs of aged concentrators. *SNO+ Internal DocDB*, DocDB-3518, 2016. Cited on

[175] B. E. Berger, J. Busenitz, T. Classen, et al. *Journal of Instrumentation*, 4:04017, April 2009. Cited on

[176] E. Falk, J. Lidgard, M. I. Stringer, and E. Turner. Commissioning of ELLIE for SNO+. *ArXiv e-prints*, April 2017. Cited on

[177] R. Alves et al. The calibration system for the photomultiplier array of the SNO+ experiment. *JINST*, 10(03):P03002, 2015. Cited on

[178] Hamamatsu h10721-210 datasheet. https://www.hamamatsu.com/resources/pdf/etd/H10720_H10721_TPMO1062E.pdf. Cited on

[179] Martti Nirkko. Angular systematic evaluation using TELLIE PCA data. *SNO+ Internal DocDB*, DocDB-4748, 2017. Cited on

[180] Hebba Zedan. Optical transmission stability for polyethylene methacrylate fibres for use in the calibration of sno+ experiment. Cited on

[181] Anilkumar Appajaiah, Volker Wachtendorf, and Werner Daum. Climatic exposure of polymer optical fibers: Thermooxidative stability characterization by chemiluminescence. *Journal of Applied Polymer Science*, 103(3):1593–1601, 2007. Cited on

[182] Martti Nirkko. TELLIE fibre position validation. *SNO+ Internal DocDB*, DocDB-4442, 2017. Cited on

[183] David Eberly. Computing a point of reflection on a sphere. urlhttps://www.geometrictools.com/Documentation/SphereReflections.pdf, 2008. Cited on

[184] *ROOT - An Object Oriented Data Analysis Framework*, Nucl. Inst. & Meth. in Phys. Res. A 389 81-86, 1997. Cited on

[185] Wilford Zdunkowski, Thomas Trautmann, and Andreas Bott. *Light scattering theory for spheres*, pages 333–377. Cambridge University Press, 2007. Cited on

[186] Qian Liu et al. Rayleigh scattering and depolarization ratio in linear alkylbenzene. *Nucl. Instrum. Meth.*, A795:284–287, 2015. Cited on

[187] Raymond S. Farinato and Robert L. Rowell. New values of the light scattering depolarization and anisotropy of water. *The Journal of Chemical Physics*, 65(2):593–595, 1976. Cited on

[188] A. N. Bashkatov and E. A. Genina. Water refractive index in dependence on temperature and wavelength: a simple approximation. In V. V. Tuchin, editor, *Saratov Fall Meeting 2002: Optical Technologies in Biophysics and Medicine IV*, volume 5068 of *procspie*, pages 393–395, October 2003. Cited on

[189] Martin Chaplin. Water structure and science. urlhttp://www1.lsbu.ac.uk/water/data1.html, 2015. Cited on

[190] K.J. Reynolds, J.P. De Kock, L. Tarassenko, and J.T.B. Moyle. Temperature dependence of led and its theoretical effect on pulse oximetry. *British Journal of Anaesthesia*, 67(5):638 – 643, 1991. Cited on

[191] Patrick Huber, M. Lindner, and W. Winter. Simulation of long-baseline neutrino oscillation experiments with GLoBES (General Long Baseline Experiment Simulator). *Comput. Phys. Commun.*, 167:195, 2005. Cited on

[192] Garching core collapse archive. urlhttps://wwwmpa.mpa-garching.mpg.de/ccsnarchive/archive.html. Accessed: 2018-01-30. Cited on

[193] Markus Rampp and H.-Thomas Janka. Spherically symmetric simulation with boltzmann neutrino transport of core collapse and postbounce evolution of a 15 $m_\odot$ star. *The Astrophysical Journal Letters*, 539(1):L33, 2000. Cited on

[194] James M. Lattimer and F. Douglas Swesty. A generalized equation of state for hot, dense matter. *Nuclear Physics A*, 535(2):331 – 376, 1991. Cited on

[195] M. Galassi et al. *GNU Scientific Library Reference Manual (3rd Ed.)*. Cited on

[196] Basudeb Dasgupta and John F. Beacom. Reconstruction of supernova ν_μ, ν_τ, anti-ν_μ, and anti-ν_τ neutrino spectra at scintillator detectors. *Phys. Rev.*, D83:113006, 2011. Cited on

[197] Emilio Ciuffoli. Statistical Methods for the Neutrino Mass Hierarchy. In *Proceedings, Prospects in Neutrino Physics (NuPhys2016): London, UK, December 12-14, 2016*, 2017. Cited on

[198] A. Gando et al. A study of extraterrestrial antineutrino sources with the KamLAND detector. *Astrophys. J.*, 745:193, 2012. Cited on

[199] G. Bellini et al. Measurement of geo-neutrinos from 1353 days of Borexino. *Phys. Lett.*, B722:295–300, 2013. Cited on

[200] John von Neumann. Various techniques used in connection with random digits. In A.S. Householder, G.E. Forsythe, and H.H. Germond, editors, *Monte Carlo Method*, pages 36–38. National Bureau of Standards Applied Mathematics Series, 12, Washington, D.C.: U.S. Government Printing Office, 1951. Cited on

[201] Helen Mary O'Keeffe. *Low Energy Background in the NCD Phase of the Sudbury Neutrino Observatory*. PhD thesis, University of Oxford, UK. Cited on

[202] G. Audi, A. H. Wapstra, and C. Thibault. The AME2003 atomic mass evaluation . (II). Tables, graphs and references. *Nuclear Physics A*, 729:337–676, December 2003. Cited on

[203] H. Godwin. Half-life of Radiocarbon. *nat*, 195:984, September 1962. Cited on

[204] Mark Chen, Valentina Lozza, and Helen O'Keeffe. Expected radioactive backgrounds in SNO+. *SNO+ Internal DocDB*, DocDB-507, 2018. Cited on

[205] Fengpeng An et al. Neutrino Physics with JUNO. *J. Phys.*, G43(3):030401, 2016. Cited on

[206] P. Fernández. Status of gadzooks!: Neutron tagging in super-kamiokande. *Nuclear and Particle Physics Proceedings*, 273-275:353 – 360, 2016. 37th International Conference on High Energy Physics (ICHEP). Cited on